CFD and Reduced-Order Modeling of Ram Air Duct for the Elysian E9X Battery-Electric Aircraft

G.B.J. Galenkamp

MSc Thesis
Aerospace Engineering: Flight Performance & Propulsion
Delft University of Technology

Delft University of Technology

TUDelft

CFD and Reduced-Order Modeling of Ram Air Duct for the Elysian E9X Battery-Electric Aircraft

by

Gertjan Bastian Jelier Galenkamp

in partial fulfillment of the requirements for the degree of
Master of Science
in Aerospace Engineering
at the Delft University of Technology,
to be defended publicly on Thursday, January 22, 2026 at 13:30 PM.

Student number: 4684354

Thesis committee:

Dr. ir. M. Pini	TU Delft	Supervisor
Dr. ir. A. Giuffré	Elysian Aircraft	Supervisor
Dr. ir. C.M. De Servi	TU Delft	Chairman
Dr. ir. T. Michelis	TU Delft	External Committee Member

Cover image courtesy of Elysian Aircraft.

An electronic version of this thesis is available at http://repository.tudelft.nl/.

PREFACE

This research has been both challenging and rewarding, marking the culmination of my Bachelor's and Master's studies in Aerospace Engineering at TU Delft. Over these years, I have had an exceptional learning experience that allowed me to pursue my childhood fascination with aircraft while developing a strong interest in fluid dynamics. Working on this project in collaboration with Elysian Aircraft has therefore been particularly meaningful.

I would like to express my sincere gratitude to Dr. Matteo Pini for his guidance throughout this work. I am also very grateful to Andrea for offering me the opportunity to work on this project in collaboration with Elysian Aircraft and for his excellent supervision. I wish Elysian Aircraft every success in the further development of the E9X. It is encouraging to see such an innovative company emerging in the Netherlands. Additionally, I would like to thank Dr. Carlo De Servi and Dr. Theo Michelis for joining my graduation committee.

Finally, I would like to thank my family, and in particular my parents Henk and Anja, for their endless support throughout my life and especially during my studies. I am also grateful to my brothers and to all my friends, both long-time friends and those I met during my time in Delft, for their support and encouragement along the way.

Basthian Galenkamp
Delft, November, 2025

ABSTRACT

The Elysian E9X, a 90-seat battery-electric aircraft with a useful range of 800 km, offers the potential to reduce aviation-sector CO_2 emissions by up to 14%, with future range extensions up to 2000 km targeting a segment responsible for 43% of emissions [1]. Achieving this potential requires, among other aerospace technology advancements, an efficient thermal management system (TMS), since battery-electric aircraft rely on active cooling that may introduce significant weight and drag penalties.

This thesis presents a systematic methodology to optimize and evaluate the design of condenser and radiator heat exchangers arranged in series within the E9X ram air ducts, which strongly influence both cooling and aerodynamic performance. The work comprises three interconnected components: development of a multi-point optimization framework for sequential condenser-radiator configurations using reduced order models (ROMs), implementation of a computational fluid dynamics (CFD) methodology for representing heat exchangers within ram air ducts using a porous media model (PMM), and application of these models to study the impact of heat exchanger design parameters on overall TMS performance.

A multi-objective, multi-point optimization framework is developed in *Python* using the in-house finite-volume heat exchanger code *HeXacode* coupled with the NSGA-II genetic algorithm. The optimization minimizes both heat exchanger mass and weighted air-side pressure drop across eight operating points spanning the E9X mission profile, including extreme hot-day conditions. Air-side pressure drop is converted to an equivalent battery mass through its impact on ram air duct drag, enabling system-level optimization that balances heat exchanger structural mass with aerodynamic penalties.

A 2D RANS CFD approach is implemented in *Ansys Fluent* where the heat exchangers are represented using a PMM with calibrated momentum and energy source terms following the Darcy-Forchheimer formulation for pressure drop and Nusselt number-based correlations for heat transfer. Key methodological contributions include the development of wall temperature correlations to enable off-design heat transfer prediction and improvements to the momentum source term calibration that address the consistent pressure drop deviations observed in earlier TU Delft studies. ROM and CFD predictions agree within 1–5% for system-level metrics including total pressure loss, heat transfer, and net drag.

The methodology is applied in three studies assessing system-level performance trade-offs. First, the effect of air-side fin topology is assessed by comparing offset strip fins (OSF) and louvered fins (LF). OSF consistently outperform LF for the boundary conditions and thermal constraints of this study. Selecting OSF over LF reduces total equivalent system mass by approximately 100 kg.

Second, the effect of heat exchanger inclination is systematically evaluated for angles from 0° to 60°. Inclination increases the effective frontal area, reducing inlet velocity and enabling denser fin configurations without excessive pressure drop penalties. However, CFD simulations reveal that inclination introduces additional pressure losses due to flow turning, with total pressure loss over the heat exchangers increasing by approximately 15% at 60° inclination. A pressure loss correction factor correlation is developed from CFD data and incorporated into the ROM. Despite this inclination penalty, increasing inclination from 0° to 60° reduces total equivalent system mass by 60 kg.

Third, two TMS architectures are compared: a series configuration with eight ram air ducts each containing both condenser and radiator, and a separate-duct configuration with 16 total ducts (eight for condensers, eight for radiators). Despite suboptimal radiator performance due to receiving preheated air in the series configuration, it reduces total equivalent system mass by 213 kg compared to the separate-duct architecture, primarily by having only half the number of ram air ducts and thereby reducing frontal area and external drag.

The combined effects of heat exchanger topology selection (OSF), inclination optimization (60°), and series-architecture choice yield cumulative total equivalent system mass savings of approximately 326 kg, leading to roughly a 10 km (+1%) increase in nominal range, underscoring the significant influence of TMS mass and drag characteristics on battery-electric aircraft performance.

The developed methodology can be readily extended to alternative TMS architectures, different operating conditions, and 3D CFD analysis coupling internal duct flow with external aerodynamics.

CONTENTS

LIST OF FIGURES

LIST OF TABLES

NOMENCLATURE

ACRONYMS

ACARE	Advisory Council for Aeronautics Research in Europe
ASHRAE	American Society of Heating, Refrigerating & Air Conditioning Engineers
CFD	Computational Fluid Dynamics
CR	Cruise
CS	Certification Specification
ECS	Environmental Control System
EM	Empty Mass
EPU	Electric Power Unit
ESDU	Engineering Sciences Data Unit
FAR	Federal Aviation Regulations
FV	Finite Volume
HEOS	Helmholtz Equation of State
HX	Heat Exchanger
ICAO	International Civil Aviation Organization
ISA	International Standard Atmosphere
LF	Louvered Fins
LMTD	Log Mean Temperature Difference
MAE	Mean Absolute Error
MAPE	Mean Absolute Percentage Error
MB	Moving Boundary
MEG	Mono Ethylene Glycol
MFR	Mass Flow Ratio
MTOM	Maximum Take-Off Mass
NACA	National Advisory Committee for Aeronautics
NIST	National Institute of Standards and Technology
NSGA-II	Non-dominated Sorting Genetic Algorithm II
NTU	Number of Transfer Units
ORC	Organic Rankine Cycle
OSF	Offset Strip Fins
PCHIP	Piecewise Cubic Hermite Interpolating Polynomials
PEMFC	Proton Exchange Membrane Fuel Cell
PIV	Particle Image Velocimetry
PMAD	Power Management and Distribution
PMM	Porous Media Model
RANS	Reynolds-Averaged Navier–Stokes
RES	Reserve Energy System
REV	Representative Elementary Volume
ROM	Reduced-Order Model
RSM	Reynolds Stress Model
RQ	Research Question
SAF	Sustainable Aviation Fuel
SOC	State of Charge
SST	Shear Stress Transport
TMS	Thermal Management System
TO	Take-Off
TOC	Top of Climb
TOD	Top of Descent
TRL	Technology Readiness Level
UDF	User Defined Function
VCC	Vapor-Compression Cycle
WHR	Waste Heat Recovery

Roman Symbols

A	Area [m^2]
a	Nusselt correlation coefficient [-]
AR	Aspect ratio [-]
b	Nusselt correlation exponent [-]
C	Heat capacity rate [$\mathrm{W\,K^{-1}}$]
c	Nusselt correlation exponent [-]; Univariate wall temperature correlation coefficient
C_2	Inertial resistance coefficient [$\mathrm{m^{-1}}$]
C_d	Discharge coefficient [-]
C_D	Drag coefficient [-]
C_p	Static pressure recovery coefficient [-]; Specific heat capacity [$\mathrm{J\,kg^{-1}\,K^{-1}}$]
D	Drag force [N]
d	Diameter [m]; Depth [m]
E	Energy [J]
e_{bat}	Battery energy density [$\mathrm{Wh\,kg^{-1}}$]
F	Correction factor [-]
$\mathbf{F}$	Vector of objective functions [-]
f	Friction factor [-]
$\mathbf{G}$	Vector of constraints [-]
g	Gravitational acceleration [$\mathrm{m\,s^{-2}}$]
h	Specific enthalpy [$\mathrm{J\,kg^{-1}}$]; Heat transfer coefficient [$\mathrm{W\,m^{-2}\,K^{-1}}$]; Height [m]
j	Colburn factor [-]
K	Permeability [m^2]
k	Thermal conductivity [$\mathrm{W\,m^{-1}\,K^{-1}}$]; Turbulence kinetic energy [$\mathrm{m^2\,s^{-2}}$]
K_c	Entrance loss coefficient [-]
K_e	Exit loss coefficient [-]
L, l	Length [m]
M	Mach number [-]
m	Mass [kg]
$\dot{m}$	Mass flow rate [$\mathrm{kg\,s^{-1}}$]
N	Number of cells [-]; Diffuser length [m]
n	Number [-]; Polynomial order [-]; Cell index [-]
Nu	Nusselt number [-]
P	Pressure [Pa]; Power [W]
p	Pitch [m]
Pr	Prandtl number [-]
q	Dynamic pressure [Pa]
$\dot{Q}$	Heat transfer rate [W]
R	Range [km]
Re	Reynolds number [-]
s	Specific entropy [$\mathrm{J\,kg^{-1}\,K^{-1}}$]
S_e	Energy source term [$\mathrm{W\,m^{-3}}$]
S_m	Momentum source term [$\mathrm{N\,m^{-3}}$]
T	Temperature [K]
t	Thickness [m]; Time [s]; Bivariate wall temperature correlation coefficient
U	Overall heat transfer coefficient [$\mathrm{W\,m^{-2}\,K^{-1}}$]
V	Volume [m^3]
v	Velocity [$\mathrm{m\,s^{-1}}$]
w	Width [m]; Weight [-]
$\mathbf{x}$	Design vector [-]
Y	Nozzle loss factor [-]
y^+	Normalized wall distance [-]

GREEK SYMBOLS

α	Inclination angle [°]	η	Efficiency [-]
β	Surface area density compactness [m^{-1}]	θ	Diffuser divergence angle [°]
γ	Ratio of specific heats [-]	μ	Dynamic viscosity [Pa s]
Δ	Difference [-]	π	Pressure ratio [-]
δ	Convergence tolerance [-]	ρ	Density [kg m^{-3}]
δ^*	Boundary layer displacement thickness [m]	σ	Ratio of core free-flow to frontal area [-]
ε	Porosity [-]; Effectiveness [-]	ω	Turbulence specific dissipation rate [s^{-1}]
ϕ	Mass flow ratio [-]		

SUBSCRIPTS

0	Reference condition	lm	Logarithmic mean
amb	Ambient	max	Maximum
bat	Battery	mc	Microchannel
c	Cold side	min	Minimum
cond	Condenser/condensation	net	Net
crit	Critical	noz	Nozzle
dsh	Desuperheating	out	Outlet
epu	Electric power unit	p	Propulsive
eq	Equivalent	pmad	Power management and distribution
ext	External	proj	Projected
fin	Fin	rad	Radiator
fr	Frontal	ram	Ram air
ft	Flat tube	req	Required
h	Hot side	s	Static
ht	Heat transfer	sc	Subcooling
HX/hx	Heat exchanger	t	Total
i	Mission segment index; Iteration index	us	Usable
in	Inlet	wf	Working fluid
int	Internal	∞	Freestream
j	Operating point index		

SUPERSCRIPTS

$*$	Optimal value	k	Coupling iteration number
i	Iteration number	n	Cell index
j	Operating point		

1

INTRODUCTION

1.1. BACKGROUND AND MOTIVATION

As global temperatures rise and extreme weather events become more frequent, it has become increasingly urgent to reduce humanity's environmental impact. In 2022, the aviation sector was responsible for approximately 1.9% of global greenhouse gas emissions, 2.5% of global CO_2 emissions, and about 3.5% of effective radiative forcing when accounting for additional non-CO_2 effects such as contrail-induced cloud formation [2]. Aircraft have undergone continuous improvements in fuel efficiency, primarily through increases in engine efficiency. However, the rate of efficiency improvement is slowing. Between 2000 and 2010, average aircraft fuel efficiency increased by 2.4% per year, while between 2010 and 2019 this dropped to 1.9% per year [3]. In contrast, passenger demand grew by more than 5% annually from 2000 to 2019 [4], and global air travel demand is expected to increase further as global populations become wealthier [2]. This implies that current improvements in fuel efficiency are insufficient to meet long-term climate targets, such as those set by the European Union's Advisory Council for Aeronautics Research in Europe (ACARE) in Flightpath 2050 [5]. These goals include reducing NO_x emissions by more than 90%, CO_2 emissions by more than 75%, and noise emissions by more than 65% from commercial aircraft in 2050 compared to a year 2000 baseline aircraft [6].

Several technological pathways are currently being explored to reduce aviation's climate impact. Fully battery-electric propulsion has traditionally been considered limited to small, short-range aircraft with limited payload [7, 8, 9]. However, recent studies [10] have challenged this assumption, and building on these insights, the Dutch company Elysian Aircraft developed the E9X concept: a 90-seat battery-electric aircraft with a full-electric useful range of 800 km. Replacing flights up to 800 km could reduce the sector's CO_2 emissions by up to 14%, while continued advances in battery technology and operations could extend the range up to 2000 km, a segment responsible for 43% of emissions [1].

Unlike conventional aircraft, battery-electric aircraft such as the E9X require active cooling, which may introduce significant weight and drag penalties. The thermal management system (TMS) is therefore critical to the viability of battery-electric propulsion. In the E9X, the ram-air duct houses two heat exchangers arranged in series: a condenser that rejects heat from the battery cooling loop and a radiator that cools the electrical power unit. The aircraft features eight ducts located beneath the distributed propulsion units. Since every additional kilogram directly reduces range and payload capacity, the trade-off between heat exchanger mass and aerodynamic drag is a central design challenge for the E9X and for battery-electric aircraft more broadly.

1.2. RESEARCH SCOPE AND OBJECTIVES

This thesis presents a methodology for the design and optimization of compact heat exchangers in ram air ducts, with specific application to the Elysian E9X. The work addresses gaps in the literature regarding sequential heat exchanger configurations, multi-point mission analysis, and CFD analysis of inclined heat exchangers. The detailed research gaps and specific research questions motivating this work are presented in Section 2.5 following the literature review in Chapter 2.

The research comprises three interconnected components. First, a multi-point, multi-objective optimization framework using reduced-order models (ROM) is developed for sequential condenser-radiator configurations. The optimization framework enforces sequential coupling where condenser outlet conditions, i.e., air mass flow rate, static pressure, and static temperature, become fixed inlet conditions for radiator optimization at each operating point. System-level performance is evaluated by translating air-side pressure drop into an equivalent battery mass required to overcome ram air duct drag, enabling true system-level optimization.

Second, a computational fluid dynamics (CFD) methodology is developed to model compact heat exchangers in ram air ducts using porous media modeling with calibrated momentum and energy source terms. The methodology builds on prior work within the TU Delft Propulsion and Power group [11, 12, 13] and incorporates methodological improvements to address consistent pressure drop deviations observed in earlier studies. A key contribution is the development of wall temperature correlations as functions of mass flow rate and inlet temperature, enabling off-design heat transfer predictions particularly important for the downstream radiator receiving preheated air from the condenser.

Third, the combined optimization and CFD methodology is applied to perform three system-level design studies. Two heat exchanger fin topologies are compared to assess their impact on system-level performance. The effect of heat exchanger inclination from 0° to 60° is systematically quantified, and correction factors are developed to account for additional pressure losses due to heat exchanger inclination not captured by the reduced-order model. Finally, two thermal management system architectures are compared: a series configuration with both heat exchangers in the same duct versus a separate-duct configuration with independent condenser and radiator ducts.

1.3. RESEARCH QUESTIONS

This thesis addresses four main research questions, each supported by specific sub-questions that are detailed in Section 2.5 following the literature review:

- **RQ1:** How can a multi-point, multi-objective optimization framework be developed for sequential condenser-radiator configurations that accounts for thermal coupling while balancing heat exchanger mass and aerodynamic penalties?

- **RQ2:** How can compact heat exchangers be accurately represented in CFD using porous media modeling with off-design capability?

- **RQ3:** How accurately does the reduced-order model predict ram air duct performance when compared to CFD simulations?

- **RQ4:** What additional pressure losses arise from heat exchanger inclination, and how do these losses affect system-level performance?

1.4. THESIS OUTLINE

This thesis is organized as follows. First, Chapter 2 provides background information on the TMS of the E9X aircraft, reviews heat exchanger modeling approaches, and presents relevant literature. Specific research gaps are identified, leading to the formulation of detailed research questions in Section 2.5. Subsequently, Chapter 3 outlines the methodology, beginning with the problem formulation and E9X mission data, followed by descriptions of the reduced-order models for all ram air duct components (intake, diffuser, heat exchangers, and nozzle), the multi-objective optimization framework, and the CFD methodology. Chapter 4 then presents the results in two parts. The first part discusses the heat exchanger optimization outcomes, including comparisons of fin topologies, inclination angles, and thermal management system architectures. The second part provides CFD–ROM comparisons and quantifies the effect of heat exchanger inclination on pressure drop. Finally, Chapter 5 summarizes the conclusions and provides recommendations for future work.

2

BACKGROUND

This chapter presents the background for this thesis and is structured as follows. First, Section 2.1 introduces the E9X battery-electric aircraft and its thermal management system, including the ram air duct. Section 2.2 then covers the fundamentals of compact heat exchangers, followed by Section 2.3 which examines modeling approaches for heat exchangers. Subsequently, Section 2.4 provides a comprehensive literature review. Finally, Section 2.5 presents research gaps and formulates the research questions addressed in this work.

2.1. THERMAL MANAGEMENT OF THE ELYSIAN E9X AIRCRAFT

2.1.1. THE CASE FOR BATTERY-ELECTRIC AIRCRAFT

Multiple pathways are currently being explored to reduce the climate impact of aviation, including the use of Sustainable Aviation Fuel (SAF), hydrogen, and batteries for hybrid or fully-electric aircraft. Battery-electric aircraft have already entered operation at small scale, such as the two-seater Pipistrel Velis Electro[1]. Battery-electric flight is widely perceived as feasible only for short-range aircraft (below 400 km) with small payloads, even considering future battery energy densities in the range of 300–500 Wh/kg [7, 8, 9]. As a result, battery-electric propulsion is often dismissed as unsuitable for CS-25-category aircraft. This prevailing conclusion is based on the well-established fact that batteries have a substantially lower gravimetric energy density than kerosene, which results in heavier onboard energy storage, and that battery mass does not decrease during flight, thereby imposing a persistent weight penalty.

Nevertheless, a recent study [7] challenges the assumption that battery-electric aircraft are inherently limited to small payloads and short ranges by identifying four common misconceptions:

1. An energy mass fraction, defined as the ratio of empty mass (EM) to maximum take-off mass (MTOM), of approximately 50% is feasible for battery-electric tube-and-wing aircraft without relying on advanced engineering or immature materials. This contrasts with the commonly assumed 20-25%, but is achievable with a clean-sheet design [10].

2. A $(L/D)_{max}$ greater than 20 can be achieved due to the inherently lower wetted-area-to-reference-area ratio of battery-electric aircraft. Therefore, the E9X should not be constrained by the typical $(L/D)_{max}$ values of 14–18 observed for current regional or turboprop aircraft, as its configuration enables significantly higher aerodynamic efficiency without requiring low-TRL innovations [7].

---

[1] Pipistrel Velis Electro: `https://www.pipistrel-aircraft.com/products/velis-electro/`

3. The assumption that aviation reserve requirements render battery-electric aircraft impractical is misleading. While current regulations mandate contingency, alternate, and final reserve energy, these reserves can be provided by a fuel-based Reserve Energy System (RES) rather than by additional battery capacity. This approach significantly reduces overall mass, allows more battery energy to be allocated to the nominal mission, and has no impact on day-to-day emissions [7].
4. It is often argued that negative scaling effects, such as a reduction in maximum range with increasing aircraft size, preclude battery-electric propulsion for CS-25-category aircraft. However, no such effects have been observed. In fact, for the same energy efficiency, a higher passenger count can even increase maximum range. This indicates that battery-electric propulsion is not inherently limited to the 9–23 seat CS-23 commuter segment but can scale to larger aircraft without a fundamental performance penalty [7].

Taken together, these insights demonstrate that battery-electric aircraft in the CS-25/FAR Part 25 category are technically feasible and can reach ranges exceeding 1000 km with an usable pack-level energy density approaching 400 Wh/kg [7]. This suggests that battery-electric propulsion could play a more substantial role in climate-neutral aviation than previously assumed. Replacing flights up to 800 km could reduce the sector's CO_2 emissions by up to 14%, while continued advances in battery technology and operations could extend the range up to 2000 km, a segment responsible for 43% of emissions [1].

Figure 2.1 shows the distribution of flights below 1000 km and the number of passengers carried over that distance for several major airlines. The figure highlights that a majority of flights are shorter than 1000 km. As such, the introduction of battery-electric aircraft in this segment would address a significant portion of current airline operations.

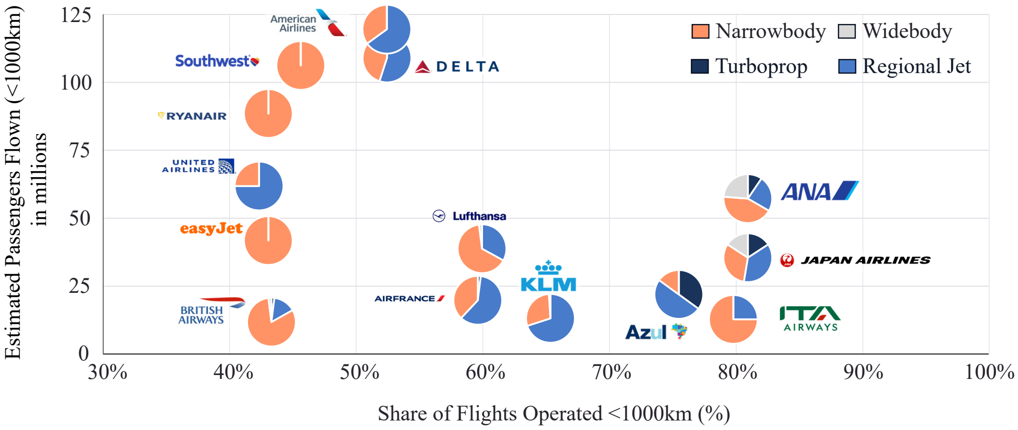

Figure 2.1: Share of flights and absolute number of passengers flown below 1000 kilometers for several major airlines according to Elysian's internal analysis. Reproduced from [10].

2.1.2. The Elysian E9X Concept

Based on these new considerations, a first conceptual design was developed: a 90-passenger battery-electric aircraft with a useful range of 800 km for a pack-level energy density of 360 Wh/kg [1]. This design later became the starting point for the Dutch company Elysian Aircraft[2] , where the aircraft program was named E9X. The initial design of the E9X is shown in Figure 2.2 and Figure 2.3.

Figure 2.2: Render of the E9X. Courtesy: Elysian Aircraft.

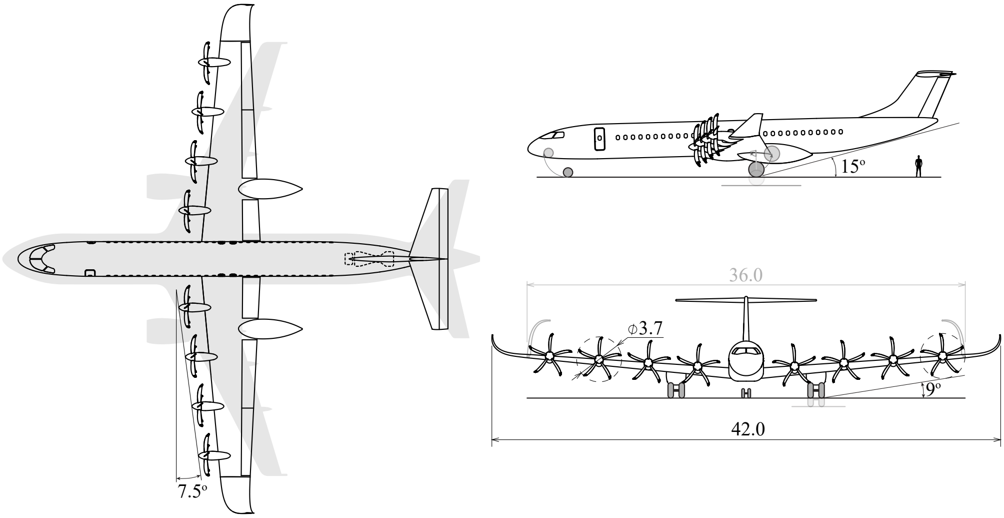

Figure 2.3: Three-view drawing of the first conceptual design of the E9X 90-seater battery-electric aircraft with a gas-turbine based reserve energy system shown with dotted lines. Top view includes Airbus A320 planform for reference. Dimensions in meters. Reproduced from [1].

The E9X features a conventional tube-and-wing layout with a T-tail configuration, eight

---

[2] Elysian Aircraft's website: `https://www.elysianaircraft.com`

distributed propellers, and a SAF-fueled gas turbine-based reserve energy system (RES) to cover required reserves. The batteries are placed in the wing to provide bending-moment alleviation and thereby reducing the structural weight of the wing. The aircraft uses a low-wing configuration to enable a shorter and therefore lighter main landing gear. Folding wing tips are applied to meet the ICAO category C-gate span constraints of 36 meters.

The assumptions underlying the aircraft's conceptual design were examined through dedicated research conducted over the past two years in ten key technical areas. These so-called hot potato studies addressed the most critical design drivers, including wing–battery pack integration, battery cell development for aviation applications, and the sizing of the thermal management system. The results of these investigations are summarized in [10]. A more detailed analysis of the Thermal Management System (TMS), which is of particular relevance to this thesis, is presented in [14]. Overall, the findings indicate that the concept is both technically and commercially viable, with no fundamental show-stoppers.

The range of a battery-electric aircraft is naturally highly dependent on the assumed pack-level energy density. This relationship is illustrated for the E9X in Figure 2.4. The latest redesign achieves a 750 km full-electric range at 320 Wh/kg, but range may increase significantly over the aircraft's operational lifetime depending on advances in battery technology.

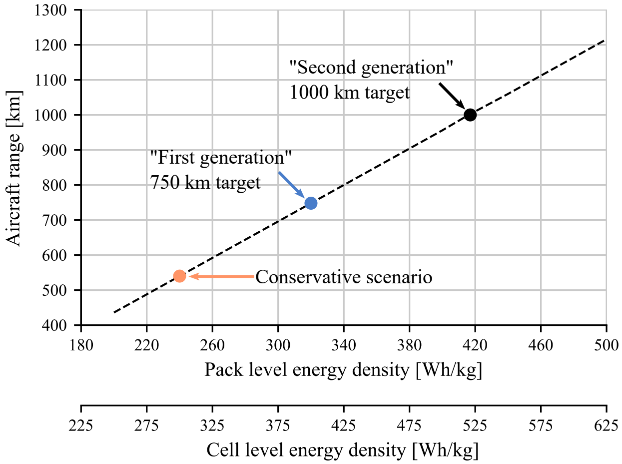

Figure 2.4: Evolution of usable range of the E9X as battery technology evolves, assuming a 25% mass overhead for packaging to go from cell to pack level energy density. Energy densities refer to 100% SOC at start of life; meaning usable energy densities are lower. Reproduced from [10].

2.1.3. Thermal Management

Thermal Management in Battery-Electric Aircraft

The Thermal Management System (TMS) ensures that onboard systems remain within their allowable temperature limits across all operating conditions. It provides thermal control for critical subsystems such as avionics, flight-control units, electric motors, batteries, and the high-voltage power distribution system, while minimizing penalties in weight, aerodynamic drag, and auxiliary power consumption.

For conventional turbofan-powered aircraft, thermal management is typically less critical. Much of the waste heat is rejected as part of the open Brayton cycle, and additional thermal loads are managed through engine-driven oil, fuel, and bleed-air circuits. Ram-air ducts with heat exchangers are also used, particularly for the Environmental Control System (ECS). Because these systems typically operate at relatively high temperatures, they benefit from larger temperature differences with the ambient air, enabling more effective convective heat transfer.

In battery-electric aircraft, however, thermal management becomes substantially more challenging. While electric powertrains have higher overall efficiency, all waste heat must be actively rejected through heat exchangers to ambient air. Unlike turbofan-powered aircraft, they do not benefit from natural heat rejection through the open Brayton cycle, nor do they have fuel available as a heat sink. Electric motors, inverters, battery packs, and high-voltage components generate significant thermal loads, yet operate at much lower allowable temperatures than combustion-based systems. As a result, the temperature difference relative to the environment is smaller, which limits the effectiveness of convective heat transfer [15]. These factors together necessitate more active and carefully integrated cooling strategies in electric architectures.

Coutinho et al. [16] reviewed various TMS architectures for hybrid and fully electric aircraft and concluded that active liquid-cooling loops combined with ram air heat exchangers remain the most viable approach with current technology.

In such architectures, nearly all waste heat must be extracted and rejected through dedicated cooling loops and compact heat exchangers, as no alternative sinks are available. The battery is particularly critical, because its cells must be kept within a narrow temperature window to ensure performance, safety, and limited degradation. Depending on the mission phase and ambient conditions, the TMS must therefore provide both active cooling (e.g., during take-off on a hot day) and active heating (e.g., during descent in cold environments). Ram-air ducts may also exploit the *Meredith effect* [17], in which the heated airflow leaving the duct produces a small net thrust. This can partially offset the drag of the intake and internal duct losses [15].

The importance of these considerations is highlighted by Sain et al. [18], who showed in the conceptual design of a nacelle-integrated fuel-cell TMS that ducted heat exchangers are the largest and most critical components affecting system drag.

THERMAL MANAGEMENT SYSTEM ARCHITECTURE OF THE E9X AIRCRAFT

The preliminary sizing of the Thermal Management System (TMS) architecture for the Elysian E9X aircraft is presented in [14]. This preliminary design focuses on the thermal control of the primary electric powertrain components, namely the battery packs, inverters, and electric motors. Other heat sources such as avionics, the ECS, ice protection, PMAD systems, and the fuel-based reserve energy system are acknowledged but were not included in the TMS sizing for this study.

Two TMS configurations were evaluated. The baseline consisted of separate ram-air ducts for the EPU liquid-to-air radiator and the battery condenser. A second configuration, in which both heat exchangers are placed in series within a single ram-air duct, was found to provide lower overall weight and drag penalties. The reduction in external drag results from combining the condenser and radiator in one duct, thereby reducing the total frontal intake area and wetted surface [14].

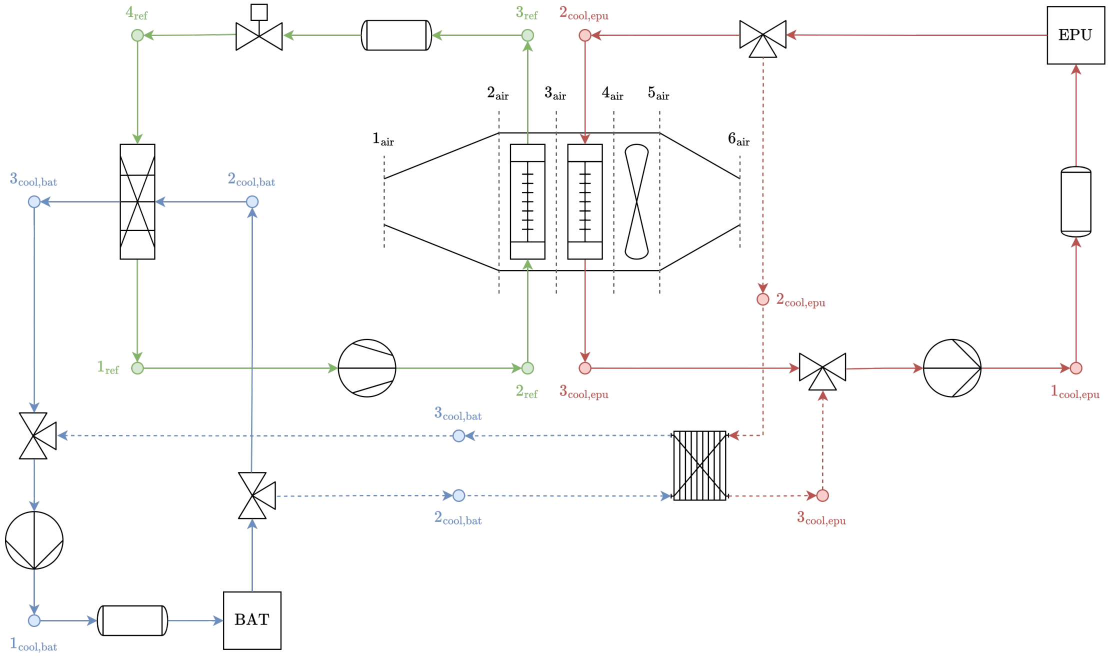

Figure 2.5: E9X TMS architecture integrating the heat rejection systems of two coolant loops (i.e., the battery condenser and the EPU radiator) into the same ram air duct.
Red: EPU coolant loop. Blue: battery coolant loop. Green: refrigerant loop of the Vapor-Compression Cycle (VCC). Dashed lines: bypass system. Reproduced from [14].

This series architecture is shown in Figure 2.5 and forms the basis of the analysis in this thesis. Its key features include:

- **A mechanically pumped liquid cooling loop for the EPUs**, which rejects heat through a radiator located within the ram-air duct. A water–ethylene glycol mixture is used as the coolant.
- **A single-stage vapor-compression cycle (VCC) dedicated to the battery pack,** which rejects heat through a condenser placed in the same ram-air duct. The VCC, based on the inverse Rankine cycle, consists of an evaporator, compressor, condenser, and expansion valve. Using a refrigerant such as R1234yf, it provides active cooling when ambient temperatures exceed the target battery temperature.
- **A shared ram-air duct containing both the condenser and radiator in series.** Although less conventional than using separate ducts, this arrangement reduces drag and system mass. Placing the radiator downstream of the condenser exploits the higher operating temperature of the EPU loop and increases total heat addition to the airstream, which can generate additional thrust in the nozzle via the Meredith effect.
- **A bypass system connecting the two liquid loops via controllable valves**, allowing the battery to serve as a heat sink for the EPU cooling loop under specific operating

conditions. This can be used, for example, to preheat the battery during cruise in cold environments, reducing or eliminating active heating during descent.

As suggested by Rheaume et al. [19], the thermal load during takeoff and initial climb, when ram air dynamic pressure is relatively low and ambient temperatures are high, can be mitigated by exploiting the thermal inertia of the battery pack. This is achieved by pre-cooling the battery prior to takeoff to a temperature below its maximum permissible operating value [14].

Role of the Ram-Air Duct in the TMS

Components The general layout of the ram-air duct used in the E9X TMS is shown in Figure 2.6. It consists of an intake, diffuser, condenser and radiator arranged in series, a puller fan, and a variable-area nozzle. Air enters through the intake, is decelerated and compressed in the diffuser, passes sequentially through the condenser and radiator cores, and is then accelerated through the nozzle. The diffuser reduces flow velocity and increases static pressure, thereby lowering the pressure drop across the heat exchanger cores. Through the condenser and radiator, pressure losses occur due to viscous dissipation, while heat addition raises the air temperature. The subsonic nozzle then accelerates the heated flow back toward ambient pressure, producing a thrust force. This thrust can partially offset the cooling-system drag through the Meredith effect. The puller fan shown in Figure 2.6 is not included in the analyses of this thesis.

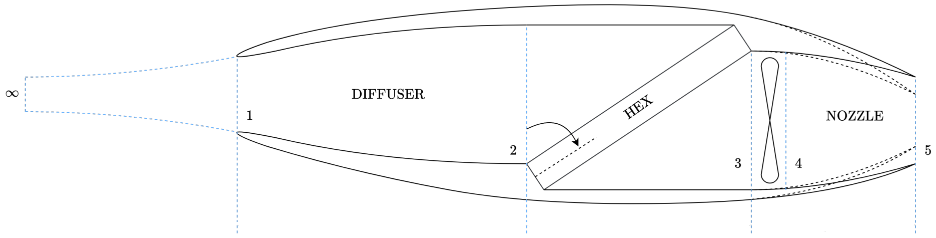

Figure 2.6: Schematic of ram air duct with inclined heat exchanger and puller fan. Reproduced from [14].

The ram air duct strongly influences both the available cooling mass flow and the system's aerodynamic penalties. The TMS is sized for the most critical condition, i.e., takeoff on a hot day, when ram air dynamic pressure is low and ambient temperatures are high [14]. Under these conditions, a puller fan may be required to maintain sufficient mass flow. Prior studies have also proposed the use of a smaller fan to avoid oversizing the TMS for extreme cases [15], though this introduces additional weight, complexity, and windmilling drag when the fan is inactive.

The mass flow through the ram air duct is regulated using a variable-area nozzle. Actuators adjust the outlet area to meet heat rejection requirements at each operating point. The E9X integrates one ram air duct beneath each distributed propulsion unit, with the scoop intake located below the nacelle, similar to turboprop aircraft such as the ATR-72 (Figure 3.5b). Operating in the propeller slipstream increases dynamic pressure and may reduce the need for a puller fan. However, the non-axial inflow induced by propeller swirl requires careful intake and diffuser design to avoid flow separation, as investigated by Kirz et al. [20].

Historical Context The aerodynamic impact of ducted heat exchangers was already recognized during World War II, leading to extensive NACA research on their drag characteristics [21, 22, 23]. These studies were motivated by the need to cool piston engines efficiently by means of radiators while minimizing the aerodynamic penalty.

Drela [24] derived an analytical expression for the drag power associated with a heat-exchanger core, $D_{\mathrm{HX\ core}}$, explicitly accounting for the effect of heat addition, which can partially offset the drag through the Meredith effect:

$$D_{\mathrm{HX\ core}} v_\infty \simeq \frac{\dot{m}}{2} v_\infty^2 \frac{\Delta p_{\mathrm{HX}}}{q_1} \left(\frac{v_1}{v_\infty}\right)^2 - \dot{H}\left(\gamma - \tfrac{1}{2}\right) M_\infty^2 . \tag{2.1}$$

Here, $\dot{m}$ is the mass flow through the core, v_∞ and M_∞ are the freestream velocity and Mach number, v_1 and q_1 are the velocity and dynamic pressure at the HX inlet, and γ is the ratio of specific heats. Equation 2.1 shows the benefit of decelerating the flow before the core (by means of a diffuser) and minimizing the core's pressure drop. If the rejected heat rate $\dot{H}$ is sufficiently large, the thrust term may even yield negative net core drag.

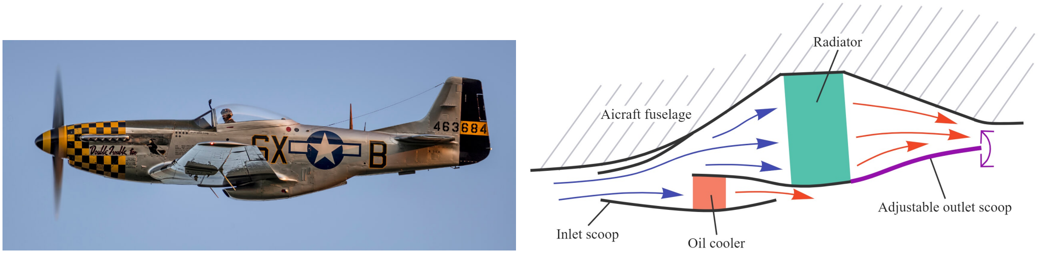

(a) P-51 Mustang aircraft. Photo courtesy of the Military Aviation Museum, Virginia Beach [25].

(b) Sketch of the P-51 Mustang radiator duct leveraging the Meredith effect. Reproduced from [13], adapted from [26].

Figure 2.7: P-51 Mustang ram air duct exploiting the Meredith effect for thrust recovery.

A classic example is the P-51 Mustang shown in Figure 2.7a, whose ducted radiator, sketched in Figure 2.7b, dissipated heat from its liquid-cooled piston engine. The outlet scoop could be fully opened to maximize mass flow during high cooling demand, or partially closed during cruise to exploit heat addition for thrust generation via the Meredith effect.

As turbojet and turbofan engines became prevalent, much of the waste heat was rejected directly through the open Brayton cycle, reducing the need for such actively optimized cooling ducts. The current shift toward more-electric and fully electric aircraft has renewed interest in ram-air-duct aerodynamics and in leveraging the Meredith effect to offset cooling-system drag.

2.2. COMPACT HEAT EXCHANGERS

2.2.1. FUNDAMENTALS OF COMPACT HEAT EXCHANGERS

DEFINITIONS

A heat exchanger is a heat transfer device that exchanges heat between two or more fluid streams. In the present work, heat exchangers with two fluid streams are considered. The fluid stream that rejects heat is referred to as the *hot side* or *working fluid*, while the stream that functions as the heat sink is referred to as the *cold side*. In this work, the cold side corresponds specifically to the ram air stream. This can involve single-phase sensible heat transfer, but may also include latent heat transfer due to phase change processes such as evaporation or condensation. Heat transfer occurs through convection between the fluids and the heat exchanger walls, and conduction through the walls themselves. Heat exchangers are designed to meet a required heat duty while minimizing mass and pressure losses in both fluids.

There are many possible classifications of heat exchangers, as outlined in textbooks [27, 28, 29]. A fluid stream can pass once or multiple times relative to the other stream, leading to single-pass or multi-pass configurations. Both fluids can be liquid or gas, resulting in liquid-to-liquid, gas-to-gas, or liquid-to-gas exchangers. Moreover, there are different flow arrangements including parallel flow, counter flow, and cross flow. Counter flow offers the highest thermal effectiveness, while parallel flow provides the lowest [28]. Cross flow heat exchangers offer intermediate thermodynamic effectiveness compared to counter flow and parallel flow configurations, but they are frequently used in practice.

Compact heat exchangers are characterized by a large heat transfer surface area per unit volume. A heat exchanger is considered compact if the surface area density β, defined as the ratio of heat transfer area to heat exchanger volume, is $\beta \geq 700\,\mathrm{m^2/m^3}$ [28]. Compact heat exchangers are widely used in automotive and aerospace applications due to their high effectiveness and low mass, with compactness in the order of $\beta = 1100\,\mathrm{m^2/m^3}$ [28].

When a working fluid undergoes a phase change, the device is categorized as a multiphase heat exchanger. An *evaporator* is a heat exchanger where the working fluid enters as a liquid, absorbs heat, and evaporates, while a *condenser* is where the working fluid rejects heat, entering as a vapor and condensing. An evaporator and condenser are typically part of the same thermodynamic process, for example in the vapor compression cycle (VCC) of the E9X system shown in Figure 2.5. A liquid-to-air heat exchanger, in which the working fluid rejects heat without a phase change, is typically referred to as a *subcooler* or a *radiator*. Its working fluid is called a *coolant*, such as a water–glycol mixture or oil. In contrast, in evaporators and condensers the working fluid undergoes phase change and is referred to as a *refrigerant*, for example a fluid from the R1234 family.

In this work, the ram air duct contains both the condenser and the radiator arranged in series as part of the system visualized in Figure 2.5. This configuration leverages the fact that the working fluid in the radiator is at a higher temperature than in the condenser, allowing the ram air to act as a common heat sink for both components. Consequently, the outlet temperature of the air from the condenser becomes the inlet temperature for the radiator.

Figure 2.8 illustrates this series configuration using example thermal diagrams for a single operating point corresponding to take-off (TO) at ISA+35 conditions, representing a hot day. In Figure 2.8a, the temperature–heat flow (T–$\dot{Q}$) diagram clearly shows how the same ram air stream first cools the condenser and then the radiator. In the condenser most of the heat transfer occurs through the condensation process. The condenser section displays three thermodynamic regions: *desuperheating*, where the refrigerant vapor is cooled to its saturation temperature; *condensation*, where phase change occurs at constant temperature; and *subcooling*, where the liquid refrigerant is cooled below its saturation temperature. In contrast, the radiator operates entirely in a single-phase region with only sensible heat transfer (subcooling). Figure 2.8b shows the corresponding temperature–entropy (T–s) diagram for the condenser, which highlights the two-phase region and the transitions between the three thermodynamic regions described above.

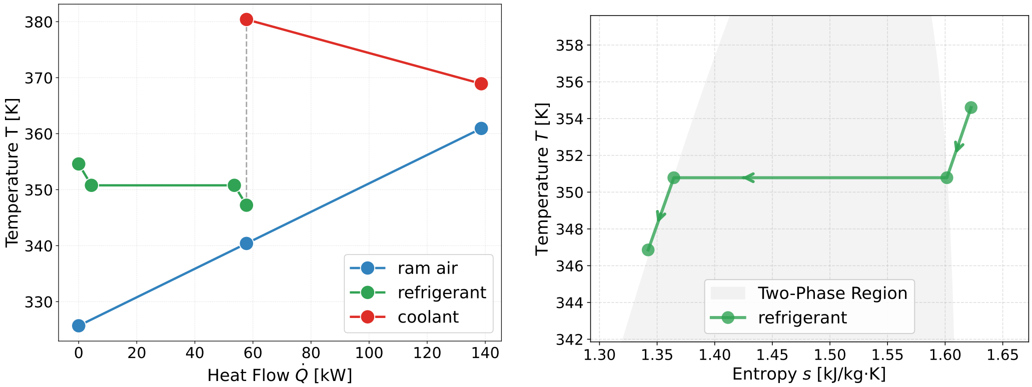

(a) Temperature–heat flow (T–$\dot{Q}$) diagram showing condenser and radiator in series arrangement.

(b) Temperature–entropy (T–s) diagram for the condenser showing desuperheating, condensation, and subcooling.

Figure 2.8: Example thermal diagrams for the considered condenser and radiator in the ram air duct at TO ISA+35 conditions.

TOPOLOGIES

Compact heat exchangers can be configured in multiple topologies depending on their application. Two common types in aerospace applications are plate-fin and flat-tube microchannel designs. Plate-fin exchangers are widely used in environmental control systems (ECS) [30] and engine oil coolers [31], while flat-tube exchangers are typical for condensers and radiators in propulsion and thermal management systems [11, 13].

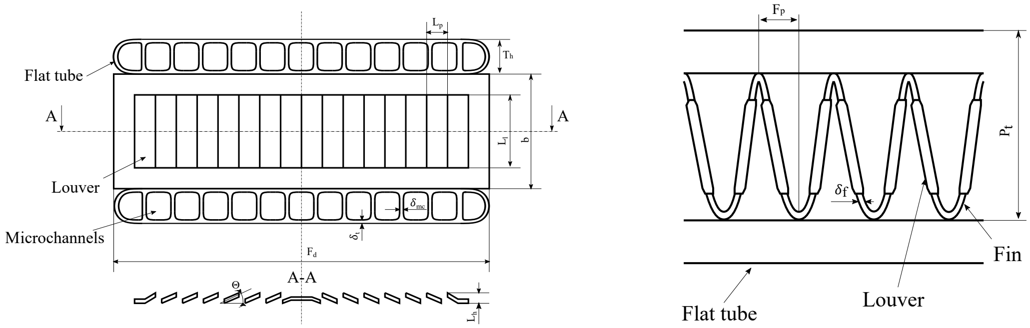

(a) Side view with cross-section A-A of louver fin geometry

(b) Front view

Figure 2.9: Schematic view of the internal geometry of a heat exchanger featuring flat tubes with microchannels and multi-louvered fins. Adapted from [30]

Modern flat-tube designs feature microchannels that divide the working fluid into many parallel rectangular passages, increasing the internal heat-transfer surface area. An example of such a flat-tube heat exchanger with louvered fins is shown in Figure 2.9. Fins on the air side further enlarge the effective area, which is essential because the convective heat-transfer coefficient of air is typically an order of magnitude lower than that of the liquid working fluid. Common fin geometries, such as triangular, offset-strip, and louvered fins, enhance heat transfer by disrupting boundary layers and promoting mixing, though this comes at the cost of increased pressure drop [29].

2.2.2. PERFORMANCE METRICS

HEAT TRANSFER

The convective heat transfer coefficient h is a key parameter in evaluating the thermal performance of a heat exchanger. It is typically obtained from empirical correlations involving nondimensional parameters that capture the effects of geometry, flow regime, and fluid properties.

A common approach employs the Colburn factor j, which is widely used for air-side correlations. It relates the heat transfer coefficient to fluid properties and mass velocity as:

$$h = j \frac{C_p G}{Pr^{2/3}} \tag{2.2}$$

where j is the Colburn heat transfer factor, C_p the specific heat at constant pressure, G the mass flux, and Pr the Prandtl number. The Prandtl number expresses the ratio of momentum diffusivity to thermal diffusivity, while the Colburn factor characterizes the air-side heat transfer capability for a given flow condition.

Alternatively, the heat transfer coefficient can be expressed using the Nusselt number Nu, which represents the ratio of convective to conductive heat transfer:

$$h = \frac{\mathrm{Nu}\, k}{d_{\mathrm{hyd}}} \tag{2.3}$$

where k is the thermal conductivity and d_{hyd} the hydraulic diameter. Nusselt-based correlations are commonly expressed as functions of the Reynolds and Prandtl numbers and can be applied to both the air and liquid sides of the heat exchanger. In this thesis, such Nusselt correlations are also used to define the heat transfer coefficient for the porous-media energy source term in the CFD model described in Subsection 3.4.5.

PRESSURE DROP

Core Friction Pressure losses in heat exchangers arise primarily from wall friction and inertial effects, and generally scale with the square of the velocity [32]. For this reason, a diffuser is typically placed upstream of a heat exchanger to reduce inlet velocity and associated losses. The pressure drop ΔP in the heat exchanger core is given by [27]:

$$\Delta P = f \frac{l}{d_{\mathrm{hyd}}} \cdot \frac{\rho v^2}{2} \tag{2.4}$$

where f is the Fanning friction factor, l the flow length, d_{hyd} the hydraulic diameter, ρ the density, and v the average velocity. The friction factor accounts for viscous shear as well as inertial effects within the heat exchanger geometry [18]. It is typically expressed as a function of Reynolds number, fluid phase, and surface roughness.

Pressure Drop Breakdown When air enters a heat exchanger, it experiences four main pressure changes: a sudden contraction at the inlet, frictional losses within the core, acceleration due to heating, and a sudden expansion at the outlet. These contributions are illustrated in Figure 2.10.

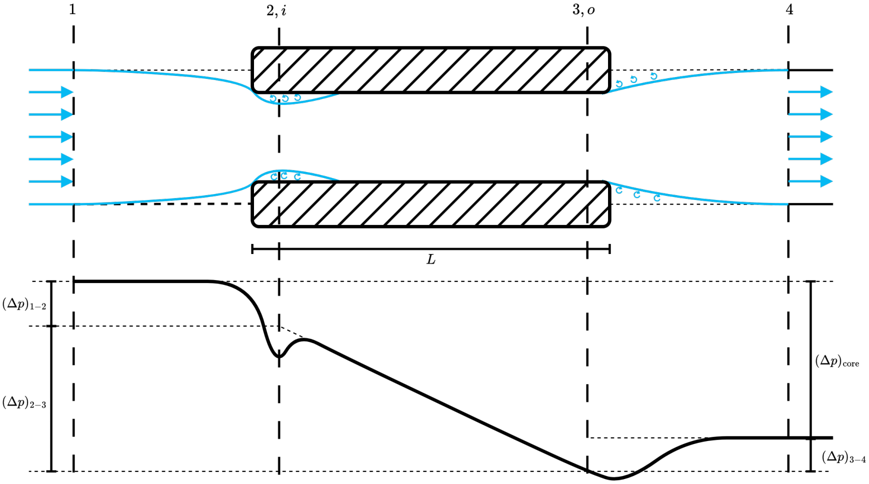

Figure 2.10: Pressure drop components associated with one passage of a compact heat exchanger. Reproduced from [12], adapted from [27].

A commonly used expression that includes all four contributions is given by [27]:

$$\frac{\Delta P}{P_{\text{in}}}=\frac{(\dot{m}/A_o)^2}{2\rho_{\text{in}}P_{\text{in}}}\left[\underbrace{1-\sigma^2+K_c}_{\text{entrance effect}}+2\left(\underbrace{\frac{\rho_{\text{in}}}{\rho_{\text{out}}}-1}_{\text{momentum effect}}\right)+\underbrace{f\,\frac{l}{d_{\text{hyd}}}\rho_{\text{in}}\left(\frac{1}{\rho}\right)_m}_{\text{core friction}}-\underbrace{(1-\sigma^2-K_e)\frac{\rho_{\text{in}}}{\rho_{\text{out}}}}_{\text{exit effect}}\right] \tag{2.5}$$

Here, P denotes static pressure, ρ the density (subscripts in, out, and m for inlet, outlet, and mean, respectively), and $\sigma = A_o/A_{\text{frontal}}$ the ratio of core free-flow to frontal area. K_c and K_e are contraction and expansion loss coefficients, respectively, and $\dot{m}/A_o$ is the core mass velocity.

The entrance and exit terms each include a reversible contribution, $(1-\sigma^2)$, which arises from static pressure changes due to flow acceleration through an area reduction (entrance) and deceleration through an area increase (exit). The irreversible contribution, represented by K_c or K_e, accounts for additional losses caused by the sudden contraction or sudden expansion, including secondary flows and potential flow separation. These coefficients depend on heat exchanger geometry, porosity, and Reynolds number, and are tabulated in [27]. The momentum term accounts for acceleration due to density changes as the air is heated within the core, while the core friction term represents viscous and form drag losses similar to Equation 2.4.

For air flows in compact heat exchangers, friction typically contributes about 90% of the total pressure loss [27], whereas entrance and exit effects become significant for short cores (small l) or low free-flow area ratios (σ). The working fluid on the hot side also experiences pressure losses, but these are generally secondary compared to the air side: air-side losses directly translate into aerodynamic drag, whereas hot-side losses only increase pump or compressor work [28].

Effect of Inclination The inclination of a heat exchanger within a duct can significantly affect pressure losses. Tilting the core reduces its frontal area, which lowers the inlet velocity and thereby decreases the overall pressure drop. However, the inclined configuration introduces additional losses due to flow turning across the core and misalignment between the incoming stream and the fin orientation. These incidence effects can cause flow separation and local maldistribution, particularly at higher inclination angles.

Experiments by Nichols [33] show a rapid rise in losses for inclination angles above 70°, which is therefore a typical design limit. A more recent CFD study [34] confirm that the inclined heat exchanger can account for up to 60% of total duct pressure loss , though optimized fin alignment or curved fins can mitigate this effect. A near total loss of the kinetic energy of the velocity component perpendicular to the direction of the fins was observed due to incidence of the flow relative to the fins [34].

2.3. MODELING APPROACHES FOR COMPACT HEAT EXCHANGERS

2.3.1. ANALYTICAL AND DISCRETIZATION METHODS

LMTD METHOD

The Logarithmic Mean Temperature Difference (LMTD) method is a classical approach for analyzing heat exchanger performance. It relates the total heat transfer rate q between two fluids to the overall heat transfer coefficient U, the total heat transfer surface area A, and the logarithmic mean temperature difference ΔT_{lm}:

$$q = UA\Delta T_{\mathrm{lm}} = UA\frac{\Delta T_2 - \Delta T_1}{\ln(\Delta T_2/\Delta T_1)}. \tag{2.6}$$

The quantity ΔT_{lm} represents an effective mean temperature difference driving the heat transfer, analogous to the temperature difference in Newton's law of cooling. It depends on the temperature differences between the two fluids at each end of the heat exchanger (points 1 and 2). A detailed derivation is provided in standard textbooks [27, 28].

The method assumes steady-state operation, constant fluid properties (in particular, specific heat), and a uniform overall heat transfer coefficient U along the heat exchanger length.

For standard parallel- and counter-flow configurations, Equation 2.6 applies directly. More complex geometries (e.g.,cross-flow or multi-pass arrangements) require correction factors F, such that $q = UAF\Delta T_{\mathrm{lm}}$, where $F<1$ accounts for the reduced effectiveness compared to the counter-flow configuration.

When outlet temperatures are unknown, the LMTD method requires iterative solution in combination with energy balances. Moreover, it provides no direct indication of the maximum achievable heat transfer for a given set of inlet conditions.

THE ε–NTU METHOD

The ε–NTU method provides an alternative approach that is particularly useful when only the inlet temperatures of the two fluids are known, eliminating the iterative procedure required by the LMTD method. It introduces two key dimensionless parameters: the effectiveness ε and the number of transfer units (NTU).

The effectiveness ε quantifies the thermal efficiency of a heat exchanger as the ratio between the actual heat transfer rate and the maximum possible heat transfer rate. Here, subscripts h and c denote the hot and cold fluids, respectively, while subscripts "in" and "out" denote inlet and outlet conditions:

$$\varepsilon = \frac{q_{\text{actual}}}{q_{\max}} = \frac{C_h(T_{h,\text{in}} - T_{h,\text{out}})}{C_{\min}(T_{h,\text{in}} - T_{c,\text{in}})} = \frac{C_c(T_{c,\text{out}} - T_{c,\text{in}})}{C_{\min}(T_{h,\text{in}} - T_{c,\text{in}})} \tag{2.7}$$

where the heat capacity rates are defined as $C_h = \dot{m}_h C_{p,h}$ and $C_c = \dot{m}_c C_{p,c}$ for the hot and cold fluids, respectively. The minimum heat capacity rate $C_{\min}$ is the smaller of C_h and C_c, and the heat capacity ratio is defined as $C_r = C_{\min}/C_{\max}$.

The number of transfer units (NTU) represents a dimensionless measure of the heat exchanger size relative to its heat capacity rate:

$$\text{NTU} = \frac{UA}{C_{\min}} \tag{2.8}$$

The overall heat transfer coefficient UA accounts for both convection and conduction in the heat exchanger [3]. The relationship between effectiveness and NTU depends on both the heat capacity ratio and the flow configuration, such that

$$\varepsilon = f(\text{NTU}, C_r, \text{flow arrangement})$$

Analytical expressions and graphical correlations for common configurations (e.g.,counter-flow, cross-flow) are widely available in the literature [27, 28].

For heat exchanger sizing problems, when the required heat duty and inlet temperatures are known, the desired effectiveness can be determined first. Using the known ε and C_r, the corresponding NTU is obtained from the inverse relationship $\text{NTU} = f^{-1}(\varepsilon, C_r, \text{flow arrangement})$, and the required heat transfer area follows from Equation 2.8.

Conversely, for rating of an existing heat exchanger, NTU and C_r are computed from the known geometry and operating conditions. The effectiveness is then determined, allowing calculation of the actual heat transfer rate as

$$q = \varepsilon\, C_{\min}(T_{h,\text{in}} - T_{c,\text{in}})$$

and subsequently the outlet temperatures.

The method shares the same assumptions as the LMTD approach—steady-state operation, constant fluid properties, and a uniform overall heat transfer coefficient, but it offers clearer physical insight into heat exchanger performance. In particular, the ε–NTU formulation reveals that, as NTU increases, the effectiveness ε asymptotically approaches a maximum value determined by the flow arrangement and heat capacity ratio. Consequently, the ε–NTU method enables straightforward assessment of how a given heat exchanger performs relative to its theoretical limit.

DISCRETIZATION METHODS (MB AND FV)

The analytical methods discussed above assume constant fluid properties and uniform heat transfer coefficients, which becomes inaccurate when large temperature variations or phase changes occur. To address this, the heat exchanger can be represented using numerical discretization.

Two widely applied approaches are the moving boundary (MB) and finite volume (FV) methods. Both divide the heat exchanger into a series of control volumes and evaluate the local thermodynamic state, heat transfer, and pressure losses for each segment.

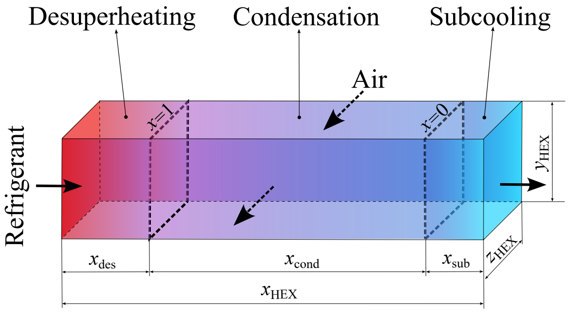

Figure 2.11: Schematic of the three thermodynamic regions in a condenser using the MB method. Adapted from [30].

In the MB method, a condenser is divided into its three thermodynamic regions, as shown in Figure 2.11: desuperheating (superheated vapor), condensation (liquid–vapor equilibrium), and subcooling (subcooled liquid). The length of each region is determined by the refrigerant phase and its enthalpy change, and a linear distribution of thermodynamic properties is often assumed within each control volume. This approach enables the estimation of the heat transfer coefficients and pressure drops using the most appropriate correlations for each phase. The total heat transfer rate can be obtained using either the LMTD or ε–NTU formulation, while the pressure losses are evaluated using phase and geometry dependent correlations.

An example of a model combining the MB approach with ε–NTU applied to flat-tube heat exchangers with louvered fins in an electrically driven vapor compression cycle (VCC) for aircraft is presented in [30].

The MB formulation can be extended to a finite volume (FV) approach by dividing each thermodynamic region into multiple cells, allowing for finer spatial resolution and a more detailed representation of distribution of fluid properties. The choice between MB and FV methods represents a trade-off between computational efficiency and model fidelity [35]. Although this discretization is naturally suited to two-phase condensers or evaporators, it can be applied to single-phase exchangers as well, where it typically reduces to a single control volume.

Within the TU Delft Propulsion and Power Group, an in-house heat exchanger sizing and rating tool named *HeXacode* [36, 37] has been developed based on the finite volume method. This tool will be employed in the present work and is described in detail in Subsection 3.2.6. It uses the correlations listed in Table 3.8.

2.3.2. POROUS-MEDIA AND SOURCE-TERM APPROACHES IN CFD

GEOMETRY-RESOLVED SIMULATIONS

While CFD methods are capable of resolving the complete geometry of compact heat exchangers, including conjugate heat transfer between the two fluid streams and the wall, this approach is generally prohibitively expensive due to the large difference in geometric scales: the overall heat exchanger size is on the order of meters, whereas the fins and channels are typically on the order of millimeters. Resolving these small features results in dense meshes and large computational demands [38].

For example, Sain et al.[39] studied air-to-liquid cross-flow heat exchangers with various fin topologies for a nacelle-integrated fuel-cell system. Using 3D RANS on unit cell geometries, they resolved conjugate heat transfer between coolant and air, with meshes ranging from 12–44 million cells per unit cell. Scaling the unit cell to a full radiator geometry would require hundreds of millions of cells, making such simulations prohibitively expensive.

To reduce computational cost, simplified geometric representations are sometimes used. Patrao [34], for instance, simulated a 2D finned flat-tube heat exchanger with 151 discrete fins using a mesh of 5.1 million cells. Similarly, Sain et al. [40] modeled a ducted plate-fin heat exchanger as an array of flat tubes with prescribed wall temperature, neglecting fin details. These simplifications can reduce computational cost significantly but may not be appropriate for every topology.

SOURCE-TERM AND POROUS-MEDIA MODELING

An alternative to explicitly meshing and resolving the heat exchanger geometry is to represent its macroscopic effects through momentum and energy source terms added to the RANS equations. This is conceptually similar to the actuator-disk approach used in turbomachinery. Source-term formulations reproduce the pressure drop and heat transfer with significantly reduced computational cost.

Momentum Source Terms In its simplest form, the pressure loss across a heat exchanger can be prescribed as a fixed value. However, this approach is inaccurate since pressure drop strongly depends on velocity. A more realistic representation expresses the pressure drop across a heat exchanger as a second-order polynomial in velocity, as demonstrated experimentally and applied successfully in CFD by Missirlis et al. [32]. This representation is consistent with fundamental fluid dynamic principles and the analytical formulation in Equation 2.4. A more general approach represents the pressure drop as a function of both flow velocity and local fluid properties using the Darcy–Forchheimer law:

$$\frac{\Delta P}{L} = \frac{\mu}{K}v + C_2\frac{1}{2}\rho v^2 \tag{2.9}$$

where μ is the dynamic viscosity, K the permeability, v the velocity, ρ the fluid density, and C_2 the inertial coefficient associated with form drag losses. The first term represents viscous (Darcy) resistance, while the second accounts for inertial losses.

This formulation forms the basis of the porous media modeling (PMM) approach, in which the heat exchanger is represented as a porous zone characterized by direction-dependent permeability and inertial coefficients. Missirlis et al. [41] extended this model for aero-engine applications using an anisotropic Darcy–Forchheimer formulation with non-zero off-diagonal terms to better capture the effects of flow incidence. While more accurate, this model requires additional empirical calibration based on experimental data which is not always available.

The benefits of PMM are illustrated by Patrao et al. [34], who compared a full 2D finned flat-tube heat exchanger simulation (5.1 million cells) with a porous-zone representation (300,000 cells). The PMM predicted the total pressure loss within 1% of the detailed CFD result, confirming its ability to reproduce the macroscopic flow effects at a fraction of the computational cost.

Energy Source Terms For heat transfer, the most straightforward energy source formulation is to specify a uniform volumetric heat source, equal to the total added heat divided by the heat exchanger volume. This heat flow can be obtained from experiments or precomputed using analytical methods such as the ε–NTU approach, as demonstrated by Patrao et al. [34, 31]. However, this treatment assumes a fixed heat transfer rate, whereas in reality it varies with operating conditions such as mass flow rate, temperature, and flow distribution.

To address these limitations, more advanced formulations have been proposed. One option is to employ velocity-dependent correlations for the heat flow, as applied by Maho [42]. Similarly, Kirz [43] coupled a one-dimensional lookup-table model to CFD, allowing iterative evaluation of heat transfer and pressure drop as functions of the local flow conditions. An alternative strategy is to embed an ε–NTU model directly within CFD, allowing the heat transfer between the two fluid streams to be solved simultaneously. Adler [44] integrated a one-dimensional heat exchanger model directly within CFD, where inlet properties were mass-averaged to provide representative boundary conditions. Although these methods improve accuracy under varying operating conditions, they still rely on a uniform heat source distribution within the porous zone.

In reality, heat addition within a heat exchanger is non-uniform. The temperature difference between the air and the hot side decreases along the flow direction, and the axial distribution depends on local flow conditions and the flow arrangement (e.g.,crossflow or counterflow). To capture these effects, Kirz et al. [20] introduced an energy source term dependent on local temperature and velocity. Likewise, Missirlis et al. [41] proposed a model based on a Nusselt-number correlation expressed as a function of local Reynolds and Prandtl numbers. This enables off-design simulations when an average wall temperature is prescribed for the porous zone and has shown good agreement with experimental data. The approach has been successfully applied to several ducted heat exchanger configurations [11, 13].

Rather than considering only one fluid side with a prescribed wall temperature, the PMM from Missirlis et al. [41] was extended by Yakinthos et al. [45] to include both the hot and cold streams simultaneously. Additional transport equations for the total specific enthalpy and total pressure of the secondary stream are coupled with the RANS equations, enabling calculation of three-dimensional temperature fields and pressure losses on both sides of the heat exchanger. Compared to detailed conjugate heat transfer CFD simulations resolving both streams and tube walls, this advanced PMM required more than 80 times fewer computational cells while maintaining comparable accuracy. This method has been successfully applied to study innovative air-to-air heat recuperation concepts in aero-engine nozzles [46].

Validation of Porous-Media Modeling Several validation studies confirm the effectiveness of the PMM approach in representing the macroscopic behaviour of heat exchangers. Yang et al. [47] performed numerical simulations of a rod-baffle shell-and-tube heat exchanger using four different modeling strategies and compared the results to experimental data. The porous-medium approach provided results comparable to the full-geometry simulations, with deviations of 6–12% for heat transfer and 4–12% for pressure drop.

Similarly, Li et al. [48] applied a PMM to simulate the pressure drop over 3D finned-tube heat exchangers. The model accurately captured the flow resistance of a single finned tube, with deviations below 10% across different Reynolds numbers. The predicted pressure drop closely matched that of the geometry-resolved simulation, while the mesh size was fifteen times smaller.

Zhao et al. [49] further validated the PMM experimentally by comparing CFD predictions of a tubular heat exchanger in an aero-engine intercooler duct with pressure and Particle Image Velocimetry (PIV) measurements. The porous-media model successfully reproduced the flow distribution within the heat transfer units, and total pressure contours at the intercooler outlet showed good agreement with the PIV data.

These results highlight that PMM can accurately capture the macroscopic flow behavior of heat exchangers while reducing computational cost by one to two orders of magnitude, provided appropriate correlations are available for the heat exchanger geometry.

2.4. LITERATURE REVIEW

Having established the fundamentals of compact heat exchangers, their performance metrics, and the available modeling approaches ranging from analytical methods to porous media CFD, this section reviews recent applications of these methodologies in aerospace thermal management systems. The focus is on optimization studies and integrated system analyses relevant to the present work, concluding with a discussion of research gaps specific to battery-electric aircraft.

Beltrame et al. [37] applied *HeXacode* to optimize compact ORC condensers for waste heat recovery in aircraft auxiliary power units. The study employed multi-objective optimization using the NSGA-II genetic algorithm [50] to minimize both heat exchanger mass and air-side pressure drop while satisfying heat duty requirements. A key finding was that the optimal fin topology depends on system-level objectives and constraints. For high net power output applications, flat-tube microchannel condensers with offset strip fins achieved lower mass than louvered fin designs at equivalent pressure drops. However, louvered fins could yield lighter configurations if higher air-side pressure losses were acceptable. This topology-dependence demonstrates that fin selection must be evaluated within the specific operating envelope rather than being determined a priori. The same methodology was subsequently applied to a combined-cycle turboshaft case study for the turbo-electric ONERA Dragon aircraft [36].

Frey et al. [51] performed multi-objective optimization of a fan-fed ducted radiator dissipating 1 MW from a Proton Exchange Membrane Fuel Cell (PEMFC), demonstrating that drag can be offset by heat dissipation via the Meredith effect. A genetic algorithm minimized radiator pressure loss for a louvered fin-and-tube topology.

Beltrame et al. [11] modeled ram air ducts housing compact heat exchangers, applied to a bottoming ORC condenser. The study concluded that optimal heat exchanger design is primarily driven by pressure loss minimization and can be decoupled from optimal duct design. This decoupling supports the present study's approach of optimizing heat exchanger geometry within a fixed duct configuration. Beltrame et al. also compared *HeXacode* predictions against 2D RANS CFD simulations using the porous media methodology of Missirlis et al. [41], revealing close agreement but consistent deviations in the order of 5% in pressure drop predictions. The present work will identify methodological improvements to reduce these discrepancies.

Patrão et al. [34] performed conceptual design and optimization of compact heat exchangers for hydrogen-fueled aero-engine intercooling and recuperation. Following initial sizing using the ϵ-NTU method, duct shape optimization was conducted with 2D axisymmetric RANS CFD. The heat exchanger was modeled as a porous zone with a constant volumetric energy source term, and the duct geometry, heat exchanger location, and inclination angle were optimized using NSGA-II on a metamodel. A follow-up study [52] extended this methodology to curved fins by implementing a spatially-varying transformation matrix for the resistance vectors in the PMM. Curved fin heat exchangers reduced total pressure losses and exhibited less sudden flow deceleration at the inlet compared to straight fin designs, with benefits most pronounced for shorter diffusers. However, total pressure loss within the heat exchanger itself was higher for curved designs due to longer flow paths and higher local velocities.

Adler et al. [44] achieved a 70% reduction in cruise drag for a ducted radiator through a coupled 3D optimization. The study considered three operating points with variable nozzle area to regulate mass flow and cooling capacity, using gradient-based optimization that coupled RANS CFD with an ϵ-NTU heat exchanger model.

Maho [42] studied the aerodynamics of a wing-integrated ram air duct with a heat exchanger for a hydrogen fuel cell powered propeller aircraft by applying a PMM in RANS CFD with a velocity-dependent energy source term. A 2D design-of-experiments study revealed that heat exchanger characteristics, particularly porosity and depth, have a more pronounced impact on aerodynamic performance than external duct geometry.

Wessendorp [13] investigated condenser integration into the bypass duct of a turbofan engine as part of a combined-cycle configuration. 2D axisymmetric RANS CFD simulations with porous zone modeling following Missirlis et al. [41] quantified the effect on bypass stream performance and net thrust. Gradient-based optimization was then used to refine the bypass duct geometry and reduce the drag penalty.

2.5. RESEARCH GAPS AND RESEARCH QUESTIONS

RESEARCH GAPS

The literature review shows different methodologies and applications of heat exchanger optimization and CFD modeling of ducted heat exchangers. However, several research gaps remain unaddressed:

- **Application context:** No prior work addresses the thermal management requirements of fully battery-electric aircraft. Existing studies focus on heat exchangers in applications such as fuel cells or ORC heat recuperation. For battery-electric aircraft, it is essential to translate heat exchanger performance accounting for both structural weight and aerodynamic drag penalties to system-level aircraft performance.

- **Sequential thermal coupling:** The reviewed studies consider single heat exchangers with independent inlet conditions. In a sequential configuration, the upstream condenser directly determines the mass flow rate, static pressure, and outlet temperature of the air entering the downstream radiator. This coupling introduces interdependencies that cannot be captured by optimizing each component in isolation. The effect of condenser-preheated air on radiator performance and the system-level implications remain unexplored.
- **Multi-point optimization framework:** Most existing studies optimize for a single operating point or at most three conditions. In this work, the E9X mission profile has been discretized into eight operating points, including four extreme cases corresponding to hot-day conditions. This necessitates a multi-point optimization framework that ensures thermal requirements are met across the entire mission profile while minimizing system-level penalties.
- **CFD methodology for sequential heat exchangers:** Earlier studies within the TU Delft Propulsion and Power group [11, 12, 13] showed consistent pressure drop deviations in the order of 5% between porous media CFD predictions and *HeXacode* predictions. Additionally, previous work employed constant wall temperature assumptions in the energy source terms, which cannot capture off-design heat transfer. This limitation is particularly present for the downstream radiator receiving preheated air from the condenser, where heat transfer varies significantly with operating conditions. Methodological improvements are needed to reduce these discrepancies and enable accurate off-design heat transfer predictions.
- **Inclination quantification for sequential configurations:** While most reference work [11, 13, 34] applied inclined porous media CFD for inclined heat exchangers, no study has systematically quantified the additional pressure losses due to inclination. A systematic CFD study is needed to quantify inclination penalties and develop a correlation that can be incorporated into reduced-order models.

RESEARCH QUESTIONS

This thesis addresses the following research questions (RQs), grouped into four main areas addressing the identified gaps:

- **RQ1: How can a multi-point, multi-objective optimization framework be developed for sequential condenser-radiator configurations that accounts for thermal coupling while balancing heat exchanger mass and aerodynamic penalties?** This addresses both framework development and application to key design decisions. Specific sub-questions include:
  - How should the optimization handle the physical constraint that condenser outlet conditions define radiator inlet conditions?
  - How to perform a system level trade-off between heat exchanger mass and pressure drop?
  - Which heat exchanger fin topology (offset strip fins versus louvered fins) provides superior system-level performance?
  - What is the optimal thermal management system architecture: series or separate-duct configuration?

  - How does thermal coupling between the upstream condenser and downstream radiator constrain the radiator design space?

- **RQ2: How can compact heat exchangers be accurately represented in CFD using porous media modeling with off-design capability?**
  This addresses the development of a CFD methodology using calibrated porous media models. Specific sub-questions include:
  - How can momentum and energy source terms be calibrated to accurately reproduce heat exchanger pressure drop and heat transfer characteristics predicted by *HeXacode*?
  - What wall temperature correlations can be developed to enable off-design heat transfer predictions for both heat exchangers, particularly for the radiator which depends on condenser outlet conditions?
  - What methodological improvements can reduce the consistent pressure drop deviations observed in prior TU Delft studies [11, 12]?

- **RQ3: How accurately does the reduced-order model predict ram air duct performance when compared to CFD simulations?**
  With the porous media heat exchangers calibrated to *HeXacode*, CFD provides verification of the ROM predictions for the remaining duct components, namely the diffuser and nozzle. Specific sub-questions include:
  - How well does the ROM predict system-level metrics (total pressure loss, net drag) compared to CFD?
  - Which duct components contribute most to prediction differences?
  - What are the sources of discrepancies?

- **RQ4: What additional pressure losses arise from heat exchanger inclination, and how do these losses affect system-level performance?**
  This quantifies inclination penalties through CFD simulations and assesses their impact on optimal system design. Specific sub-questions include:
  - How can inclination-induced pressure losses be quantified through CFD and incorporated into the reduced-order model?
  - Up to what inclination angle can heat exchangers be safely operated without excessive pressure drop penalties or flow maldistribution?
  - How does the system-level benefit of inclination compare to the penalty of increased pressure loss due to flow turning?

These research questions are addressed through the methodology detailed in Chapter 3, with results presented in Chapter 4 and conclusions summarized in Chapter 5.

3

METHODOLOGY

This chapter presents the methodology for this thesis and is structured as follows. First, Section 3.1 introduces the methodology and presents the input data for the E9X. Subsequently, Section 3.2 outlines the reduced-order models for all ram air duct components (intake, diffuser, heat exchangers, nozzle). Section 3.3 then details the multi-objective optimization framework, including the sequential coupled approach for the condenser-radiator system. Finally, Section 3.4 describes the CFD methodology to model the ram air duct with heat exchangers using a porous media approach with momentum and energy source terms.

3.1. PROBLEM FORMULATION

3.1.1. OVERVIEW AND DESIGN OBJECTIVES

Overview This work is an extension of Elysian's thermal management system study [14], but focuses specifically on heat exchanger optimization and developing a methodology to model the ram air duct with heat exchangers in CFD. The ram air cooling system plays a critical role in the E9X thermal management system, as heat is rejected from both the condenser and radiator to the ram air, as visualized in Figure 2.5. Given the thermal load requirements for the condenser (battery cooling loop) and radiator (electrical power unit cooling loop), while simultaneously minimizing system-level penalties such as weight and drag, the design of the heat exchangers must be carefully optimized.

The purpose of this work is to develop a methodology to optimize the condenser and radiator as serially arranged heat exchangers within the thermal and spatial constraints of the E9X aircraft. Heat exchanger inclination will be exploited to maximize the effective frontal area for a given geometric frontal area. The duct geometry is fixed but must be modeled, as the boundary conditions and performance of the heat exchangers depend on the upstream (intake, diffuser) and downstream (nozzle) components. These reduced-order models form the basis for a multi-point, multi-objective optimization framework and will later be verified against CFD simulations.

In this work, the in-house finite-volume heat exchanger code *HeXacode* will be used for heat exchanger sizing and rating. Moreover, the porous media methodology by Missirlis et al. [41] will be employed, as similarly performed in earlier studies within the TU Delft Propulsion and Power group [11, 12, 13]. Several methodological improvements and additions in terms of pressure drop modeling and heat transfer (wall temperature representation)are will be proposed. By performing coupled heat exchanger optimizations with *HeXacode* and developing a porous media-based CFD methodology for heat exchangers with different inclination angles, this work provides a systematic framework to design, evaluate, and optimize compact heat exchangers as part of the E9X battery-electric aircraft thermal management system.

Design Objectives The heat exchanger optimization addresses a multi-objective design problem with two competing objectives: (i) minimize total heat exchanger mass and (ii) minimize weighted air-side pressure drop assessing the performance across multiple operating points. These objectives are evaluated subject to heat duty constraints, i.e., the condenser must meet the required heat rejection $\dot{Q}_{\mathrm{cond},j}$ exactly at all operating points $j \in \Omega$, while the radiator must meet or exceed $\dot{Q}_{\mathrm{rad},j}$. Using Equation 3.35, the effect of pressure drop and drag is translated to system-level impact by computing the additional battery energy required to overcome ram air duct drag over the mission, which is then converted to an equivalent battery mass. This approach will used throughout this project to make design trade-offs and draw conclusions.

3.1.2. E9X MISSION PROFILE AND THERMAL REQUIREMENTS

Operating Points The first iteration of the E9X aircraft introduced in Subsection 2.1.2 is considered in this analysis. The aircraft layout is illustrated in Figure 2.3, while the thermal management system architecture was presented in Subsection 2.1.3 and is visualized in Figure 2.5. This work focuses specifically on the ram air duct configuration featuring the condenser and radiator arranged in series.

The operating conditions analyzed in this study are obtained by discretizing the nominal mission phases (take-off, climb, cruise, and descent) visualized in Figure 3.1 into four operating points as summarized in Table 3.1: take-off (TO), top of climb (TOC), cruise (CR), and top of descent (TOD).

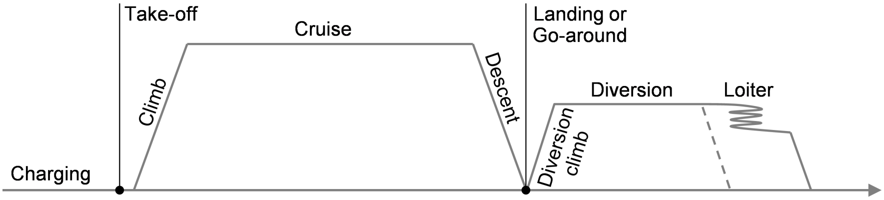

Figure 3.1: E9X mission profile [14].

Each operating point is evaluated under both standard International Standard Atmosphere (ISA) conditions and a hot-day scenario defined as ISA+35°C, resulting in a total of eight operating points. The mission phase durations Δt_i in Table 3.1 indicate that the climb and descent phases are of similar magnitude as the cruise phase, which is typically not the case for conventional aircraft. The time-averaged freestream velocity $\bar{v}_{\infty,i}$ in Table 3.1 is used in later analysis.

In Table 3.1, the index i refers to the four nominal ISA mission phases (TO, TOC, CR, TOD). In subsequent sections, the index j is instead used to denote the full set of operating points:

$$j \in \Omega, \quad \Omega = \{\text{TO ISA, TOC ISA, CR ISA, TOD ISA, TO ISA+35, TOC ISA+35, CR ISA+35, TOD ISA+35}\}$$

Table 3.1: E9X mission segment discretization

Phase	**Operating Point** i	**Duration** Δt_i [min]	**Time-Averaged Velocity** $\bar{v}_{\infty,i}$ [m/s]
Take-Off	TO	3.0	75.0
Climb	TOC	23.8	138.0
Cruise	CR	35.4	185.8
Descent	TOD	27.4	127.0

Heat Duties The detailed specifications for each operating point are presented in Table 3.2. Referring to the TMS architecture in Figure 2.5, the battery heat rejection ($\dot{Q}_{\text{bat}}$) is achieved through a vapor-compression cycle (VCC) loop, which ultimately dissipates heat via the condensers located within the ram air ducts. Similarly, the electrical power unit heat load ($\dot{Q}_{\text{epu}}$) is dissipated via a single-phase coolant loop through the radiators to the ram air. The altitude, Mach number, and ISA deviation at each operating point determine the corresponding ambient static and total conditions, as listed in Table 3.2. The available ram air dynamic pressure (q_{ram}) determines whether a given combination of duct mass flow and pressure drop is feasible, and it becomes particularly limiting at TO ISA+35, where elevated ambient temperatures and increased heat duties drive the need for higher mass flow and therefore larger pressure drops.

Table 3.2: Mission operating points, heat duties, ambient conditions, and ram pressure

Operating Point	$\dot{Q}_{\text{bat}}$ [kW]	$\dot{Q}_{\text{epu}}$ [kW]	M_∞ [-]	h [km]	p_{amb} [kPa]	$p_{\text{amb},t}$ [kPa]	q_{ram} [kPa]	T_{amb} [K]	$T_{\text{amb},t}$ [K]
TO ISA	300.0	635.0	0.200	0.00	101.3	104.16	2.87	288.15	290.5
TOC ISA	500.0	528.0	0.565	7.62	37.6	46.69	9.09	238.65	253.9
CR ISA	450.0	324.0	0.565	7.62	37.6	46.69	9.09	238.65	253.9
TOD ISA	400.0	324.0	0.565	7.62	37.6	46.69	9.09	238.65	253.9
TO ISA+35	315.0	667.0	0.200	0.00	101.3	104.16	2.87	323.15	325.7
TOC ISA+35	525.0	554.0	0.565	7.62	37.6	46.69	9.09	273.65	291.0
CR ISA+35	472.5	340.0	0.565	7.62	37.6	46.69	9.09	273.65	291.0
TOD ISA+35	420.0	340.0	0.565	7.62	37.6	46.69	9.09	273.65	291.0

The heat loads presented in Table 3.2 represent system-level heat rejection requirements for both the battery and EPU. Given the distributed propulsion architecture of the E9X aircraft, which incorporates eight propellers as described in Subsection 2.1.2, the aircraft features eight individual ram air ducts positioned beneath each propeller nacelle. The heat duties are assumed to be distributed equally among the eight ducts and corresponding heat exchangers.

The appropriate individual heat exchanger heat duties ($\dot{Q}_{\text{cond}}$, $\dot{Q}_{\text{rad}}$) and corresponding working fluid inlet conditions: hot-side mass flow rate ($\dot{m}_{\text{h}}$), inlet temperature ($T_{\text{h,in}}$), and inlet pressure ($P_{\text{h,in}}$), are given in Table 3.3, computed by Elysian's *Modelica* model using thermodynamic cycle calculations and are considered constant in this work. It is acknowledged that in a follow-up study one might want to couple the heat exchanger optimization with the thermodynamic cycle optimization.

For the radiator, this results in $\dot{Q}_{\text{rad}} \approx \dot{Q}_{\text{epu}}/8$ (Table 3.3b), being slightly smaller as determined by Elysian's heat transfer computations, particularly due to some heat transfer from the engine nacelle to the environment. However, it is important to note that for the condenser, $\dot{Q}_{\text{cond}}$ (Table 3.3a) consistently exceeds $\dot{Q}_{\text{bat}}/8$ for all operating points, with differences ranging from +10% to even +48% for TO ISA+35. This is a direct consequence of the thermodynamic characteristics of the vapor-compression cycle, where the condenser must reject both the heat absorbed from the battery at the evaporator and the compressor work input.

Table 3.3: Hot-side heat exchanger input data for each operating point per heat exchanger

(a) Condenser

OP	$\dot{Q}_{\mathrm{cond}}$ [kW]	$\dot{m}_{\mathrm{h}}$ [kg/s]	$T_{\mathrm{h,in}}$ [K]	$P_{\mathrm{h,in}}$ [kPa]
TO ISA	45.6	0.351	331.2	1200
TOC ISA	71.1	0.498	321.2	900
CR ISA	62.9	0.430	317.5	850
TOD ISA	55.0	0.367	313.4	700
TO ISA+35	58.2	0.592	354.6	2400
TOC ISA+35	82.0	0.662	337.1	1600
CR ISA+35	73.2	0.584	335.6	1550
TOD ISA+35	64.6	0.509	334.2	1450

(b) Radiator

OP	$\dot{Q}_{\mathrm{rad}}$ [kW]	$\dot{m}_{\mathrm{h}}$ [kg/s]	$T_{\mathrm{h,in}}$ [K]	$P_{\mathrm{h,in}}$ [kPa]
TO ISA	77.0	2.00	380.1	300
TOC ISA	64.0	2.00	361.5	300
CR ISA	39.0	2.00	338.4	300
TOD ISA	39.0	2.00	337.7	300
TO ISA+35	81.0	2.00	380.4	300
TOC ISA+35	67.2	2.00	359.4	300
CR ISA+35	41.0	2.00	344.3	300
TOD ISA+35	41.0	2.00	345.6	300

3.1.3. RAM AIR DUCT AND HEAT EXCHANGER GEOMETRY

Baseline Geometry Considering the eight distributed propellers of the E9X as presented in Subsection 2.1.2, there are eight ram air ducts located under each propeller nacelle. In order to enable comparison with 2D CFD simulations in the second part of this work, a rectangular ram air duct with constant out-of-plane width is selected. While aircraft intake geometries are frequently non-rectangular (e.g., elliptical) and diffusers typically expand in both width and height, the present work adopts a rectangular, constant-width duct. This choice facilitates the development of 2D reduced-order models and enables direct comparison with 2D CFD simulations.

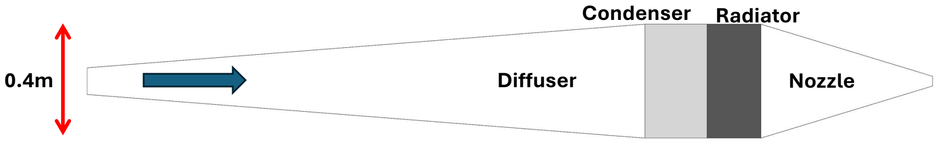

Figure 3.2: Ram air duct 2D reference geometry for the baseline configuration (0° inclination) with vertical height constraint of 0.4 m, showing the main duct components: intake, diffuser, heat exchangers, and nozzle.

The ram air duct sketched in Figure 3.2 features a rectangular cross-section with constant width of 560 mm. The intake area is fixed at 0.0523 m^2 (93.4 mm height × 560 mm width), which Elysian has sized to accommodate a maximum mass flow of 3.9 kg/s under the most demanding operating conditions.

The diffuser has a total divergence angle of $2\theta = 9°$ and a length of 1.950 m, connecting the intake to a heat-exchanger inlet area of 0.224 m^2 (400 mm × 560 mm), resulting in a diffuser area ratio of AR = 4.283. Although a value of $2\theta \approx 14°$ is commonly recommended as a guideline [53], CFD simulations showed that such a divergence angle leads to flow separation at the diffuser walls for large heat-exchanger inclination angles. Therefore, a smaller divergence angle of $2\theta = 9°$ is used to maintain attached flow across all inclination angles and enable consistent comparison between configurations.

The height of the duct is constrained to 0.4 m due to space limitations in the nacelle as defined by Elysian. By maintaining constant width throughout the duct, the intake has a relatively large aspect ratio compared to typical designs. In practice, the intake would have a larger height-to-width ratio, which would naturally reduce the vertical expansion required between the intake and diffuser outlet. The complete ram air duct geometry parameters are listed in Table 3.4.

Table 3.4: Ram air duct geometry parameters. The inclination angle α is the parametric variable studied in this work.

Parameter	**Symbol**	**Value**	**Unit**
Intake			
Height	–	93.4	mm
Width	w_{hx}	560.0	mm
Area	A_{in}	0.0523	m^2
Diffuser			
Length	–	1950	mm
Divergence angle	2θ	9.0	deg
Area ratio	AR	4.283	–
Normalized length	N/W_1	20.9	–
Heat Exchanger			
Width	w_{hx}	560	mm
Height	h_{hx}	400–800	mm
Geometric area	$A_{frontal}$	0.224	m^2
Inclination angle	α	**0–60**	**deg**
Nozzle			
Width	w_{hx}	560.0	mm
Height	h_{noz}	variable	mm
Variable exit area	A_{noz}	variable	m^2

Table 3.5: Heat exchanger inclination effect on physical height and effective frontal area. Projected height is fixed at $h_{proj} = 400$ mm.

Inclination Angle α [°]	**Physical Height** h_{hx} [mm]	**Effective Frontal Area** $A_{frontal}$ [m^2]	**Area Increase** vs. baseline [%]
0	400.0	0.224	0.0
15	414.2	0.232	+3.5
30	461.9	0.259	+15.5
45	565.7	0.317	+41.4
60	800.0	0.448	+100.0

Heat Exchanger Inclination To maximize heat transfer performance within the vertical constraint of 0.4 m, the heat exchangers can be inclined at angle α to increase their effective frontal area. While the geometric duct cross-section remains 0.224 m^2, the heat exchanger's projected frontal area normal to the flow direction scales with the inclination factor $1/\cos(\alpha)$, as does the physical heat exchanger height, with values given in Table 3.5. The effect of heat exchanger inclination is studied for five inclination angles: $\alpha \in \{0°, 15°, 30°, 45°, 60°\}$. As visualized in Figure 3.3, the diffuser and nozzle geometry remain constant across inclination angles. This inclination strategy allows for significant heat exchanger frontal area enhancement while respecting the 0.4 m vertical constraint. At α = 60, both the physical height and effective frontal area double compared to the baseline horizontal configuration (Table 3.5).

Note that this inclination strategy results in longer ram air ducts for larger inclination angles, incurring a potential drag and weight penalty from increased wetted surface area that is not considered in this work.

(a) Baseline ($\alpha = 0°$).

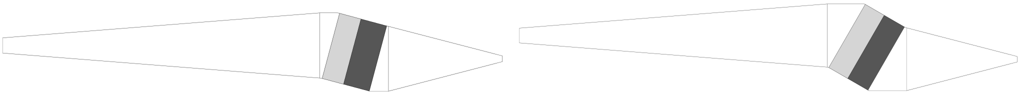

(b) $\alpha = 15°$.

(c) $\alpha = 30°$.

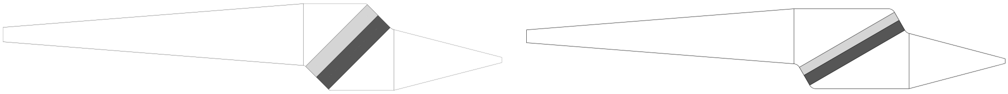

(d) $\alpha = 45°$.

(e) $\alpha = 60°$.

Figure 3.3: Ram air duct geometry configurations for the five considered heat exchanger inclination angles. The diffuser area ratio remains constant at AR = 4.283 across all configurations.

Heat Exchanger Geometry The heat exchanger topology considered for both the condenser and radiator is a flat-tube microchannel with two air-side fin configurations: (i) louvered fins and (ii) offset strip fins, as visualized in Figure 3.4. The air and the working fluid flow according to an unmixed, single-pass, cross-flow arrangement. This topology promotes compact and lightweight designs and is widely used in automotive and aerospace applications. These heat exchangers feature high compactness ($\beta \approx 1100\ \mathrm{m}^2/\mathrm{m}^3$) and thermal efficiency [28]. In both configurations, the working fluid flows inside rectangular microchannels within the flat tubes, while air flows externally through the fins where the boundary layer is continuously disrupted, thereby enhancing the heat transfer rate but also increasing the pressure drop [29].

The geometrical parameters referred to in Figure 3.4 and the corresponding bounds used in the optimization are presented in Table 3.6. The duct and therefore the heat exchanger width is fixed at $w_{\mathrm{hx}} = 560$ mm, while the heat exchanger height h_{hx} varies depending on the inclination angle (Table 3.5).

The louvered fins correlations [54, 55] and offset strip fins correlations [56] are given in terms of non-dimensional ratios, and the bounds in Table 3.6 are chosen to be within the validity range of these correlations and based on engineering judgment. Note that fin thicknesses are kept constant at 0.15 mm and the flat tube wall thickness at 0.2 mm due to manufacturing constraints. The complete set of optimization variables is given by the design vectors in Equation 3.22 and Equation 3.23. The heat exchanger length l_{hx}, also commonly referred to as the heat exchanger depth or thickness, is a derived quantity determined during the sizing process to meet the heat duty requirement at the critical operating point. Other parameters such as the number of microchannels and flat tube width are calculated from the optimization variables and geometric constraints.

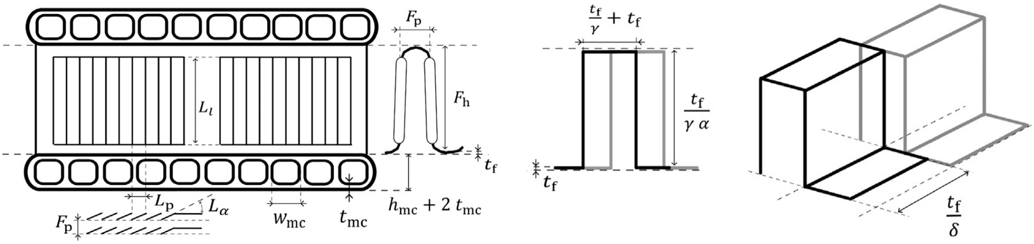

(a) Louvered fins

(b) Offset strip fins

Figure 3.4: Schematic of internal heat exchanger geometry featuring flat-tube microchannels with (a) louvered fins and (b) offset strip fins. Adapted from [36].

Table 3.6: Heat exchanger geometry parameters for flat-tube microchannel topologies. Variables without bounds are solved for during optimization or calculated from other parameters.

Parameter	**Symbol**	**Bounds**	**Unit**
Common Parameters for Both Topologies			
Heat exchanger width	w_{hx}	560	mm
Heat exchanger height	h_{hx}	400–800	mm
Heat exchanger length	l_{hx}	–	mm
Flat tube pitch	p_{tube}	15.0–20.0	mm
Microchannel width	w_{mc}	1.0–2.5	mm
Microchannel wall thickness	t_{mc}	0.2	mm
Microchannel height	h_{mc}	–	mm
Number of microchannels	n_{mc}	–	–
Flat tube height	h_{ft}	3.5–5.0	mm
Flat tube width	w_{ft}	–	mm
Louvered Fins Topology			
Fin pitch	p_{fin}	1.2–3.0	mm
Fin height	h_{fin}	8–16.0	mm
Fin thickness	t_{fin}	0.15	mm
Louver pitch	p_{louver}	1.0–3.0	mm
Louver angle	θ_{louver}	10–35	deg
Normalized louver length	$l_{\mathrm{norm\_louver}}$	0.63–0.96	–
Offset Strip Fins Topology			
Fin pitch	p_{fin}	2.5–5.0	mm
Fin height	h_{fin}	6–18.0	mm
Fin thickness	t_{fin}	0.15	mm
Fin depth	d_{fin}	2.5–12	mm

CFD versus ROM Widely cited experimental work by Nichols [33] showed that inclining a radiator beyond approximately 70° results in significant increases in pressure drop due to flow turning and separation losses. In the reduced-order models presented in Section 3.2 and the subsequent heat exchanger optimization in Section 3.3, the pressure drop due to heat exchanger inclination is not explicitly modeled. This represents an optimistic assumption that neglects potential additional losses due to flow incidence and turning.

In the second part of this thesis (Section 4.2), the effect of heat exchanger inclination and the additional pressure drop due to flow turning are quantified using CFD simulations. The approach is as follows: first, the ROM is verified against CFD for the baseline (0°) configuration where no inclination effects are present. Once this agreement is established, any deviations between ROM and CFD predictions observed at larger inclination angles can be attributed to inclination-specific effects that are captured by CFD but not modeled in the ROM. This comparison strategy allows assessment of whether heat exchangers can be inclined up to 60° without incurring prohibitive aerodynamic penalties. The CFD results will provide inclination correction factors that can be incorporated into the reduced-order model for improved system-level predictions.

3.2. REDUCED-ORDER MODELING FRAMEWORK

3.2.1. OVERVIEW

This section presents the reduced-order models (ROMs) that characterize the performance of each component in the ram air duct: intake, diffuser, heat exchangers, and nozzle. The ROMs serve two main functions in this work. First, they provide the modeling framework for the multi-objective heat exchanger optimization described in Section 3.3. Second, the ROMs allow assessment of system-level ram air duct performance, including total pressure losses, heat transfer, and drag. The ROM predictions are systematically compared to CFD simulations in Section 4.2, providing confidence in the predictive accuracy while identifying modeling limitations that inform future improvements.

The most critical model for this thesis is the heat exchanger model (Subsection 3.2.6), implemented using the in-house finite volume code *HeXacode*. The other component models are needed to compute the boundary conditions for the heat exchangers as functions of mass flow rate and to determine the overall duct performance in terms of drag and thrust.

The remainder of this section is organized as follows. Subsection 3.2.2 first outlines the ram air duct model. Subsection 3.2.3 then presents the intake model, Subsection 3.2.4 describes the diffuser model, Subsection 3.2.5 covers the nozzle model, and Subsection 3.2.6 details the heat exchanger model. Finally, Subsection 3.2.7 discusses the applied fluid models.

3.2.2. RAM AIR DUCT MODEL

The ram air duct, depicted in Figure 3.2, is modeled as a series connection of individual components: intake, diffuser, heat exchangers (condenser and radiator in series), and nozzle. Each component model computes the static and total outlet conditions based on inlet conditions and mass flow rate, enabling sequential evaluation of the complete duct.

The ram air duct model requires input data for operating conditions (Table 3.2 and Table 3.3) and geometric parameters (Table 3.4 and Table 3.6). The individual component models are described in detail in subsequent subsections.

The primary performance metric for the ram air duct is the net drag force D_{net}, which accounts for aerodynamic penalties from the intake and thrust recovery from the nozzle:

$$D_{\text{net}} = D_{\text{int}} + D_{\text{ext}} - T_{\text{noz}} \tag{3.1}$$

where D_{int} is the intake internal drag (Equation 3.5), D_{ext} is the intake external drag (Equation 3.8), and T_{noz} is the nozzle thrust (Equation 3.19). The nozzle thrust accounts for both the internal pressure losses through the duct components and the thermal energy added by the heat exchangers. Each of these terms is computed by the respective component models described in Subsection 3.2.3 and Subsection 3.2.5. This formulation neglects friction drag along the duct walls between components, as these losses are small compared to the other contributions.

3.2.3. INTAKE MODEL

INTRODUCTION

The function of the intake is to supply the required mass flow across the flight envelope while minimizing the effect on the aircraft's drag and minimize total pressure losses over the intake.

Aircraft typically feature flush or scoop intakes, visualized in Figure 3.5a. Flush intakes often feature a NACA duct shape and are integrated into the surface and produce less external drag, but their total pressure recovery is lower as they ingest the incoming boundary layer. They are preferred when the required mass flow is not too high and when minimizing external drag is the priority such as for the intakes to supply ram air for the heat exchangers for the ECS packs [30].
Scoop intakes protrude into the freestream and achieve high total pressure recovery across a wide range of Mach numbers, at the cost of additional external drag. They do not ingest local surface boundary layers and are used when higher mass flow rates are required.

(a) Flush and scoop intakes on a Boeing 787. [57]

(b) Scoop intake beneath the ATR 72's turboprop engine. [58]

Figure 3.5: External air-intake configurations: flush and scoop intakes

MODELING APPROACHES

The E9X features a scoop intake similar to the scoop intake of a turboprop engine in Figure 3.5b. ESDU [59] provides semi-empirical correlations for flush and scoop subsonic intakes allowing the computation of intake drag and total pressure recovery as a function of geometry and operating conditions. According to ESDU [59] consists the drag of a scoop intake of ram drag (related to the ingested momentum), skin friction drag, spillage drag (air bypassing the intake when it operates below design mass flow), and two corrections accounting for the presence of a diverter and the increase of drag near the choking point of the intake.

A key parameter is the mass flow ratio (MFR), defined as the fraction of ingested mass flow relative to the mass flow that would pass through the intake's forward-projected area. The intake geometry provided by Elysian is sized to accommodate a maximum ram-air mass flow of 3.9 kg/s, corresponding to the most demanding heat-rejection condition (TO ISA+35). At this sizing point, the MFR is slightly below but close to unity. At other operating points, the required mass flow is lower and the MFR decreases, leading to upstream flow deceleration and compression. This also increases the external drag, including spillage drag, since the fraction $(1-\mathrm{MFR})$ is not captured by the intake and forced to flow around it. The intake area must therefore be sized for the maximum mass flow while avoiding excessive spillage drag at off-design conditions.

To avoid reproducing existing reduced-order models readily available to Elysian, a surrogate model is developed using data generated by Elysian's 1D *Modelica* model for a ram air duct featuring the ESDU subsonic intake model [59] as applied in [14].

The intake performance is a function of altitude h, freestream Mach number M_∞, and mass flow rate $\dot{m}$. Note that this data is specific to this rectangular intake geometry, which is sufficient as the intake geometry is fixed in this study. However, its performance is important for obtaining the heat exchanger inlet conditions and the overall duct performance as a function of mass flow.

While these correlations provide reasonable estimates for intake performance, future studies would benefit from E9X-specific external drag and total pressure recovery predictions based on the actual aircraft geometry and nacelle integration.

Model Formulation

The intake model is based on curve fits using non-dimensional parameters. The primary correlating variable is the mass flow ratio:

$$\phi = \frac{\dot{m}}{\rho_{\text{in}} v_{\text{in}} A_{\text{int}}} \tag{3.2}$$

where ρ_{in} and v_{in} are the freestream density and velocity, and A_{int} is the intake capture area. This parameter naturally captures spillage effects, with ϕ<1 indicating flow spillage around the intake.

The target variables identified from the dataset are the total pressure ratio, which is constant (i.e., independent of mass flow) for each operating condition with values given in Table 3.7:

$$\pi_t = \frac{P_{t,\text{out}}}{P_{t,\text{in}}} \tag{3.3}$$

Table 3.7: Intake total pressure ratio for different operating conditions.

Altitude h [m]	**Mach Number** M_∞ [-]	**Total Pressure Ratio** π_t [-]
0	0.200	0.9975
7620	0.565	0.9825

The other two fitted variables are the intake outlet Mach number M_{out} and the external drag coefficient $C_{D,\text{ext}}$:

$$C_{D,\text{ext}} = \frac{D_{\text{ext}}}{q_{\text{in}} A_{\text{int}}} \tag{3.4}$$

where the dynamic pressure is defined as $q_{\text{in}} = \frac{1}{2}\rho_{\text{in}} v_{\text{in}}^2$. M_{out} and $C_{D,\text{ext}}$ are fitted using Piecewise Cubic Hermite Interpolating Polynomials (PCHIP) to capture the non-monotonic behavior of $C_{D,\text{ext}}$ without introducing spurious oscillations. The resulting fits achieve $R^2 = 1.00$ and are visualized in Figure 3.6. Figure 3.6a shows that the intake outlet Mach number decreases as the mass flow ratio decreases. This is due to flow deceleration and compression upstream of the intake, which occurs when the mass flow is reduced below the design point (ϕ<1).

Note that complementary to the external drag, the internal drag represents the ingested momentum and can be computed using the derived intake outlet velocity:

$$D_{\text{int}} = \dot{m} v_{\text{out}} \tag{3.5}$$

which can be normalized to an internal drag coefficient $C_{D,\text{int}}$ using the same approach as Equation 3.4.

Both the internal and external drag coefficients are visualized in Figure 3.6b. This shows that external drag increases with mass flow ratio at small mass flow ratios but decreases at moderate to high mass flow ratios due to reduced spillage drag. Internal drag increases with mass flow ratio as more momentum is ingested. Note that in the system model, the net drag is given by Equation 3.1.

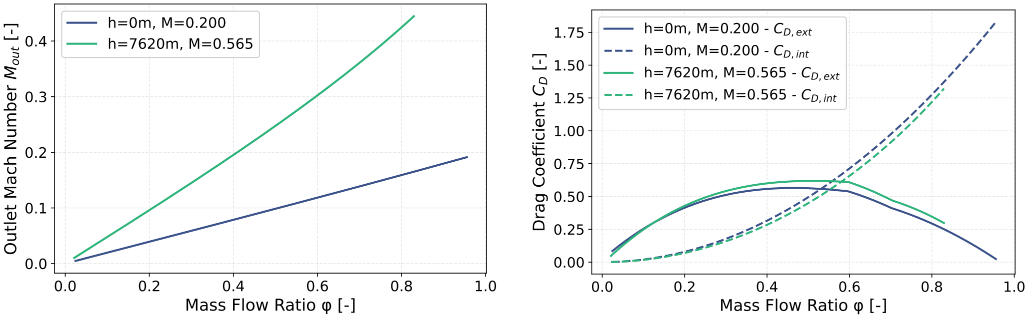

(a) Intake outlet Mach number vs mass flow ratio ϕ.

(b) Internal and external drag coefficient vs mass flow ratio ϕ.

Figure 3.6: Intake performance correlations for 2 altitude h - Mach M combinations covering all operating points.

SOLUTION PROCEDURE

The intake model predicts the intake's outlet flow properties and the drag forces for specified operating conditions $(h, M_\infty, \dot{m})$ and $(P_{t,\text{in}}, T_{t,\text{in}})$. The mass flow ratio ϕ is computed using the intake area with Equation 3.2. The correlations then provide the outlet total pressure using the values in Table 3.7:

$$P_{t,\text{out}} = \pi_t(h, M_\infty) \cdot P_{t,\text{in}} \tag{3.6}$$

the outlet Mach number using the fit in Figure 3.6a:

$$M_{\text{out}} = M_{\text{out}}(h, M_\infty, \phi) \tag{3.7}$$

and the external drag force using the fit in Figure 3.6b:

$$D_{\text{ext}} = C_{D,\text{ext}}(h, M_\infty, \phi) \cdot q_{\text{in}} A_{\text{int}} \tag{3.8}$$

From energy conservation across the intake, total enthalpy is conserved. This implies, when considering air as a perfect gas with constant specific heats, that total temperature is conserved. The complete outlet thermodynamic state is derived from the total conditions and outlet Mach number using the isentropic relations. The density is computed using the ideal gas law and the outlet velocity v_{out} from the outlet Mach number and the computed outlet static temperature. The internal drag can then be computed using Equation 3.5.

This methodology enables accurate prediction of intake outlet variables as well as both the internal and external drag of the intake, thus allowing assessment of the ram air duct drag. The model is verified against the reference *Modelica* intake model from Elysian, which is based on ESDU [59], showing maximum relative errors smaller than 0.02%, thereby demonstrating that both the correlations and thermodynamic relationships are correctly implemented.

3.2.4. DIFFUSER MODEL

INTRODUCTION

The primary function of a diffuser is to convert dynamic pressure (dynamic head) into static pressure, thereby decreasing the velocity magnitude. Decreasing the velocity entering the downstream heat exchangers is beneficial to reduce the pressure drop in the heat exchangers. An additional function of the diffuser is to provide steady and symmetric flow at the diffuser outlet to ensure optimal performance of downstream components like a heat exchanger.

The diffuser performance and exit flow conditions are closely related to the presence of flow separation. By definition, flow in a diffuser experiences an adverse pressure gradient as the static pressure rises in the flow direction, which can lead to flow separation. Regions of stalled separated flow result in lower static pressure recovery, more losses, and typically lead to flow asymmetry, unsteadiness, or both [53].

Diffuser design involves a trade-off. Excessive diffusion or a diffuser that is too short for the required area ratio promotes boundary layer separation, resulting in significant losses of stagnation pressure. Under-diffusing with a long, shallow geometry prevents flow separation but might not result in the desired static pressure recovery and accumulates excessive wall-friction losses with its longer geometry [60]. Longer diffusers also result in more flow non-uniformity due to boundary layer thickening on the wall [52]. Note that boundary layer growth and non-uniformities are amplified under the adverse pressure gradient of diffuser flow [61].

The diffuser performance is characterized by the static pressure recovery coefficient C_p, representing the fraction of inlet dynamic pressure recovered as static pressure rise [62]:

$$C_p = \frac{P_{\text{out}} - P_{\text{in}}}{P_{t,\text{in}} - P_{\text{in}}} \tag{3.9}$$

where P_{in} and P_{out} are the inlet and outlet static pressures, and $P_{t,\text{in}}$ is the inlet total pressure.

Diffuser pressure recovery is independent of Reynolds number for inlet Reynolds numbers greater than 5×10^5, but pressure recovery decreases as the inlet boundary layer thickness increases. Pressure recovery also reduces when the inlet velocity profile is distorted, e.g., wakes and stalled regions entering the diffuser, compared to a uniform velocity profile [63]. Flow entering the diffuser with higher turbulence intensity can handle stronger adverse pressure gradients and hence increases diffuser performance in performance regimes where separation is present [63].

Due to boundary layer blockage, illustrated in Figure 3.7a, the pressure recovery is always lower than the ideal pressure recovery $C_{p,i}$, which is solely a function of the area ratio AR:

$$C_{p,i} = 1 - \frac{1}{\text{AR}^2} \tag{3.10}$$

A 2D rectilinear subsonic diffuser, sketched in Figure 3.7b, can be described with three geometrical parameters: the area ratio $\text{AR} = W_2/W_1$, normalized length N/W_1, and diffuser divergence angle 2θ, with stations 1 and 2 denoting inlet and outlet, respectively. Since only two of these three parameters are independent, diffuser performance is typically described in terms of two parameters.

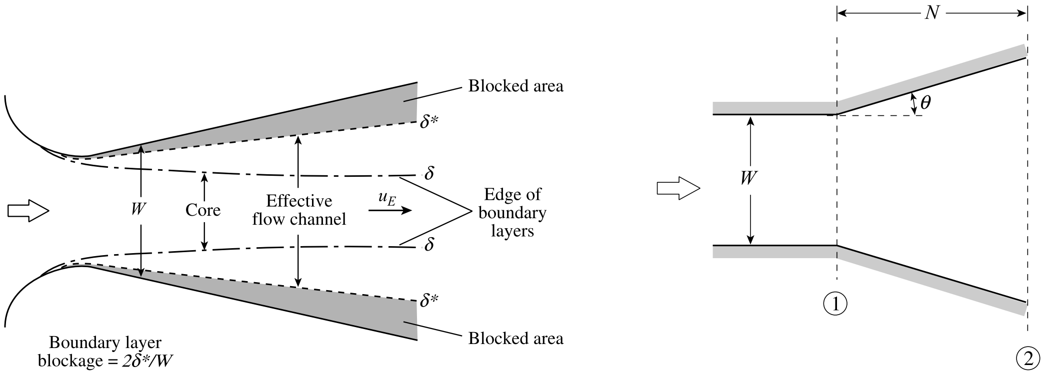

(a) Blockage due to boundary layer displacement thickness δ^* (from Greitzer [61, p. 170], after Kline et al. [64]).

(b) Geometry of 2D straight channel diffuser with area ratio AR = W_2/W_1 [61, p. 167].

Figure 3.7: 2D subsonic diffuser: (a) boundary layer blockage effect and (b) geometric parameters.

Diffuser performance data [53, 62] are typically presented as a function of inlet boundary layer thickness, expressed as the ratio of displacement thickness to inlet height $2\delta_1^*/W_1$, which represents the fraction of diffuser inlet area blocked by the boundary layer.

For the same area ratio, a longer diffuser has lower pressure recovery as a thicker boundary layer develops in the longer diffuser, causing greater blockage to the core flow. At constant area ratio, maximum pressure recovery occur at $2\theta \approx 14°$, which is a widely used design guideline for subsonic diffusers [53].

MODELING APPROACHES

There is extensive literature on subsonic 2D diffusers consisting of experimental data that are widely used in reduced order models. Sovran et al.[62] summarize and establish correlations for rectilinear diffusers with different cross sections, including the experimental data from Reneau [53].

To accurately model a diffuser, one must model the growth of the boundary layer (Figure 3.7a), as the resulting blockage plays a substantial role. The pressure recovery of a diffuser can be reduced to predicting the boundary layer growth [65]. Sovran et al. [62] provide correlations as a function of area ratio for the effective area fractions at the diffuser inlet and outlet for optimal diffusers with highest pressure recovery at fixed non-dimensional length. Note that this approach is limited to the set of optimal diffusers. This method is implemented by Beltrame et al. [11] as a reduced order model of a diffuser as part of a ram air duct housing inclined heat exchangers for an airborne compact organic Rankine cycle. By comparing the model to 2D RANS CFD an improved correlation for the effective area fraction at the diffuser outlet is proposed accounting for the effect of downstream heat exchanger inclination.

A more general approach is to apply a viscous-inviscid coupling method. Kline [64] and Lyrio [66] model an inviscid (potential) core flow and apply integral boundary layer equations to obtain the boundary layer displacement thickness. Fundamental is the modelling of the boundary layer growth as function of pressure gradient, as well as the prediction of flow separation as it has a strong interaction with the rest of the flow. Lyrio's model [66] is able to model unstalled and stalled diffusers by coupling zonal models with a 1D flow model for the potential core and momentum integral equation and an entrainment equation for the boundary layer zone, using correlations for flow detachment and limits for entrainment. This model is accurate in the unsteady separated regimes of transitory and fully developed stall.

Model Formulation

Elysian's TMS sizing [14] modeled the diffuser using only its static pressure recovery and area ratio. This simplified approach is adopted in the present work, as the focus is on heat exchanger modeling and system-level performance. However, the predictive accuracy and limitations of this diffuser model will be assessed using CFD results in Subsection 4.2.3.

The diffuser performance is characterized by the static pressure recovery coefficient C_p, defined in Equation 3.9. The diffuser geometry is fixed as listed in Table 3.4, with a total divergence angle of $2\theta = 9°$, area ratio AR = 4.283, and normalized length $N/W_1 = 20.9$. A larger divergence angle (e.g., $2\theta \approx 14°$) would typically yield higher pressure recovery according to classical diffuser design guidelines [53], but preliminary CFD simulations for this study showed that angles larger than 9° lead to boundary-layer separation for high heat-exchanger inclination geometries. Therefore, a conservative angle of $2\theta = 9°$ is used in all analyses.

For the purpose of heat exchanger optimization, a conservative $C_p = 0.75$ is selected for the reduced-order model, while common diffuser charts [53, 62] suggest $C_p \approx 0.8$–0.9 for the given geometry parameters $(AR, N/W_1)$. The ideal (inviscid, incompressible) pressure recovery is $C_{p,\text{ideal}} = 1 - 1/AR^2 = 0.945$ [62]. It is acknowledged that CFD analysis will likely yield higher C_p values than this conservative choice, but uncertainties regarding propeller slipstream and 3D effects justify this selection. CFD-informed values for C_p are presented in Section 4.2 and listed in Table 4.7.

Solution Procedure

The model ensures conservation of mass and energy through an iterative solution procedure that addresses the interdependency between flow properties. The outlet static pressure is determined by the static pressure recovery C_p from Equation 3.9:

$$P_\text{out} = P_\text{in} + C_p\,(P_{t,\text{in}} - P_\text{in}) \tag{3.11}$$

The fundamental constraints that must be satisfied simultaneously are conservation of mass:

$$\rho_\text{in} v_\text{in} A_\text{in} = \rho_\text{out} v_\text{out} A_\text{out} \tag{3.12}$$

and conservation of energy, where for the adiabatic diffuser process, total enthalpy remains constant:

$$h_\text{t} = h + \frac{v^2}{2} = \text{constant} \tag{3.13}$$

The outlet velocity affects the outlet static temperature through conservation of total enthalpy, which affects density through the equation of state, which in turn determines the outlet velocity through mass conservation. This coupled system is solved iteratively using an incompressible first guess $v_{\text{out}} = v_{\text{in}}/AR$, typically converging within three iterations with mass and energy conservation errors below 10^{-4} relative tolerance. The outlet total pressure is calculated from the converged static conditions.

3.2.5. NOZZLE MODEL

INTRODUCTION

The nozzle converts the pressure energy of the heated air into kinetic energy, thereby producing a thrust force while aiming to minimize additional total pressure losses. In a perfectly expanded subsonic nozzle, losses arise primarily from viscous effects [67]. The nozzle also regulates the mass flow through the duct by setting the effective throat area.

Unlike a diffuser, the nozzle operates under a favorable pressure gradient. This causes the nozzle to act as a natural mixer, progressively smoothing velocity non-uniformities at the exit [61]. For ram air duct applications, subsonic nozzle losses are typically secondary compared to heat exchanger pressure drops, making simplified modeling approaches appropriate for system-level analysis.

MODEL FORMULATION

The nozzle geometry features a fixed width of 0.56 m, consistent with the rectangular duct design. The model determines the nozzle thrust as well as the required nozzle throat area, and thereby the nozzle exit height for each operating point to achieve the specified mass flow. This computed nozzle height serves as the initial geometry input for subsequent CFD simulations.

Flow through the nozzle remains subsonic for all operating conditions encountered in this study. While the model allows for performance computations of a choked nozzle, the nozzle is perfectly expanded for all operating points in this study and thus ensures subsonic expansion to ambient pressure $P_{\text{out}} = P_{\text{amb}}$.

The nozzle performance is characterized by two key parameters. First, total pressure losses are modeled with a nozzle loss factor Y defined by:

$$Y = \frac{P_{t,\text{in}} - P_{t,\text{out}}}{P_{t,\text{in}} - P_{\text{out}}} \tag{3.14}$$

where $P_{t,\text{in}}$ and $P_{t,\text{out}}$ are the inlet and outlet total pressures, and P_{out} is the outlet static pressure.

While some references suggest a fixed nozzle total pressure ratio of, e.g., $P_{t,\text{out}}/P_{t,\text{in}} = 0.99$ [67], a Y-factor approach is adopted in this work with $Y = 0.01$. From Elysian's experience, nozzle losses are relatively small compared to losses in other duct components, particularly the heat exchangers. This was confirmed by CFD results. The Y-factor method allows losses to scale with the available pressure difference $P_{t,\text{in}} - P_{\text{out}}$ rather than with the inlet total pressure alone, providing more realistic loss predictions across varying operating conditions.

Second, boundary layer blockage effects are captured through the discharge coefficient $C_d = 0.988$ [68]. This coefficient, as applied in Equation 3.18, accounts for the reduction in effective mass flow capacity due to boundary layer blockage at the nozzle walls, representing the ratio of actual to ideal mass flow through the geometric throat area. In Section 4.2, CFD-informed values for Y and C_d will be used, as listed in Table 4.7.

SOLUTION PROCEDURE

The model computes the required nozzle area for a specified mass flow and operating conditions. Given inlet total conditions $(P_{t,\mathrm{in}}, T_{t,\mathrm{in}})$, mass flow $\dot{m}$, and ambient back pressure P_{amb}, the solution procedure is as follows.

First, the outlet total pressure is determined using the Y-factor defined in Equation 3.14:

$$P_{t,\mathrm{out}} = P_{t,\mathrm{in}} - Y(P_{t,\mathrm{in}} - P_{\mathrm{amb}}) \tag{3.15}$$

For the adiabatic nozzle, total enthalpy is conserved. Considering air as an ideal gas with constant specific heats, total temperature is conserved:

$$T_{t,\mathrm{out}} = T_{t,\mathrm{in}} \tag{3.16}$$

The exit velocity for subsonic expansion to ambient pressure follows from the isentropic relation:

$$v_{\mathrm{out}} = \sqrt{\frac{2\gamma}{\gamma - 1} R T_{t,\mathrm{out}} \left[1 - \left(\frac{P_{\mathrm{amb}}}{P_{t,\mathrm{out}}} \right)^{\frac{\gamma-1}{\gamma}} \right]} \tag{3.17}$$

where γ is the ratio of specific heats and R is the specific gas constant for air.

In the actual model implementation, the exit velocity is computed by first determining the exit Mach number M_{out} from the isentropic relation and then calculating $v_{\mathrm{out}} = M_{\mathrm{out}}\sqrt{\gamma R T_{\mathrm{out}}}$, which provides equivalent results and allows direct implementation of choked flow conditions. However, Equation 3.17 is presented here as it provides more direct physical insight into the nozzle thrust given in Equation 3.19.

The outlet density is computed from the ideal gas law using ambient pressure and static temperature. The required nozzle area A_{noz} then follows from the corrected mass flow relation using the discharge coefficient C_d:

$$A_{\mathrm{noz}} = \frac{\dot{m}}{C_d \rho_{\mathrm{out}} v_{\mathrm{out}}} \tag{3.18}$$

The nozzle height for the constant width geometry of $w_{\mathrm{noz}} = 0.56$ m is then determined as $h_{\mathrm{noz}} = A_{\mathrm{noz}}/w_{\mathrm{noz}}$, providing the initial nozzle geometry for CFD analysis at each operating point.

For a perfectly expanded nozzle and under the assumption of axial flow alignment, the nozzle produces thrust T_{noz} through momentum addition:

$$T_{\mathrm{noz}} = \dot{m} v_{\mathrm{out}} \tag{3.19}$$

Since the nozzle operates unchoked for all operating points, pressure thrust contributions are not included in the thrust calculation.

Combining Equation 3.17 and Equation 3.19 shows that if total pressure losses in the duct are minimized and sufficient heat is added over the heat exchangers to raise the total temperature, a significant thrust force can be produced that may offset the total drag of the ram air duct. This thrust recovery from heat addition is known as the Meredith effect, as introduced in Subsection 2.1.3.

If the total pressure at the nozzle inlet is lower than the ambient static pressure, natural flow cannot be sustained and a puller fan in the duct would be required to add total pressure and sustain mass flow through the duct.

This methodology provides a computationally efficient nozzle model that enables assessment of nozzle thrust and thereby net ram air duct drag, as well as determination of the required nozzle height for each operating point as input for CFD analysis.

3.2.6. HEAT EXCHANGER MODEL

INTRODUCTION

Heat-exchanger calculations are performed using the in-house Python tool *HeXacode* [36, 37], developed within the TU Delft Propulsion and Power group. *HeXacode* employs a finite-volume formulation that discretizes the heat-exchanger core into control volumes as introduced in Subsection 2.3.1. The tool has been validated against the commercial design software *EchTherm* [69].

As described in Subsection 3.1.3, both heat exchangers considered for this thesis adopt compact flat-tube microchannel topologies with either (i) louvered fins (LF) or (ii) offset-strip fins (OSF). These geometries are defined by the parameters in Table 3.6 and are visualized in Figure 3.4. The objective of the heat-exchanger model is twofold: (i) *Sizing*: determine the geometric parameters required to meet a prescribed heat duty under given inlet conditions; (ii) *Rating*: predict thermal and hydraulic performance for a specified geometry across different operating points.

MODEL FORMULATION

Finite Volume Method *HeXacode* is based on a finite volume approach, where the heat exchanger is discretized into control volumes. These cells represent a portion of the fluids on each side, with the core material acting as a dividing wall. Each cell is assigned a specific heat duty and may vary in size. The first guess of the heat transfer area in each cell is estimated to be proportional to its heat duty. Heat and momentum balance equations are solved for each cell to determine the required heat transfer area and corresponding pressure drop needed to satisfy the imposed local heat duty.

For condensers, the control volume model resolves three thermodynamic regions: superheated vapor, two-phase flow, and subcooled liquid. Each region can be discretized into multiple control volumes. The model works such that the cells of each thermodynamic region are split into constant enthalpy cells. If a thermodynamic region does not exist, the specified cells will be distributed over the other regions. This model can also be used for radiators considering it only has the subcooled region.

The enthalpy drop associated with the control volumes is updated at each iteration based on the estimated pressure drop to ensure that the fluid phase of the cell remains the same. In each cell, local heat transfer and pressure drop coefficients are estimated using specific correlations, depending on the fluid phase and adopted topology. The heat transfer correlations are formulated in terms of the Colburn factor j or Nusselt number Nu, while the pressure drop calculation is based on the estimate of the friction factor f or the pressure gradient. Table 3.8 lists the relevant set of correlations implemented in *HeXacode*.

The local gas-side and working fluid-side heat transfer coefficients are combined to compute the overall heat transfer coefficient of each cell relative to the working fluid area U^n_{wf}. The required cell heat transfer area of the working fluid side is calculated as [36]:

$$A^n_{\mathrm{wf}} = \frac{Q^n}{U^n_{\mathrm{wf}} F^n \, \Delta T^n_{\mathrm{lm}}} \tag{3.20}$$

where $Q^n = \dot{m}\Delta h^n$ is the heat duty in the cell, ΔT^n_{lm} is the local mean logarithmic temperature difference, and F^n is a correction factor that is lower than unity for any flow arrangement different from the pure counter flow and for non-constant temperature heat transfer. Its value depends on the local effectiveness and heat capacity ratio, except in the case of phase change and negligible pressure drop as then the heat capacity ratio is equal to 0 and $F^n = 1$ [36].

Table 3.8: Relevant correlations used in *HeXacode* [36]

Fluid	**Property**	**Reference**
Air	j (Louvered fins) f (Louvered fins) j, f (Offset-strip fins)	Chang and Wang (1997) [54] Chang et al. (2000) [55] Manglik and Bergles (1995) [56]
Working Fluid (single-phase)	Nu f (Laminar) f (Turbulent)	Gnielinski (2013) [70] Shah (2003, Ch. 7) [27] Colebrook–White (VDI, 2010) [71]
Working Fluid (condensation)	Nu dP/dZ	Shah (2019) [72] Del Col et al. (2013) [73]

Sizing and Rating Modes *HeXacode* supports two operating modes: *sizing* and *rating*. In sizing mode, the required heat transfer area is computed to satisfy a specified heat duty for given inlet temperatures, pressures, and mass flow rates on both the hot and cold sides. The frontal area is provided as input, and the length of the heat exchanger core is iteratively adjusted until the relative change in total required heat transfer area between successive iterations falls below a defined threshold.

For the flat-tube microchannel topologies considered in this study, this means that *HeXacode* determines the necessary core length l_{hx} to meet the heat duty for the prescribed inlet conditions and fixed frontal area defined by the air-side width w_{hx} and height h_{hx}. The resulting length is directly related to the number and size of the microchannels. It is computed as [36]:

$$l_{\text{hx}} = t_{\text{mc}} + \left(\sum_{n=0}^{N_{\text{cells}}} A_{\text{wf}}^{n} \right) \frac{p_{\text{tube}}(w_{\text{mc}} + t_{\text{mc}})}{2 w_{\text{hx}} h_{\text{hx}} (w_{\text{mc}} + h_{\text{mc}})} \tag{3.21}$$

where p_{tube} is the longitudinal flat-tube pitch, w_{mc} and h_{mc} are the microchannel width and height, and t_{mc} is the microchannel wall thickness.

The sizing calculation outputs the full heat exchanger geometry, its total mass, and the pressure drops on both fluid sides. Once the geometry is known, either from sizing or when given directly for rating, *HeXacode* computes the heat-exchanger mass by analytically evaluating the metal volume of all geometric features and applying the density of aluminium as the heat-exchanger material.

In rating mode, *HeXacode* predicts the heat duty and pressure losses for a fully specified geometry (frontal area and length) under given inlet boundary conditions. The internal solution procedure is similar to sizing mode.

Figure 3.8 summarizes the inputs and outputs of both modes. In sizing mode, the required length l_{hx} is determined to meet a target heat duty $\dot{Q}$, while in rating mode the thermal performance and pressure losses are evaluated for a prescribed geometry. The working-fluid inlet conditions used in this study are listed in Table 3.3, and the air-side inlet conditions are provided by the ram-air duct model as functions of ambient conditions and ram air duct mass flow. Both modes return the outlet conditions of each fluid, e.g., temperature, pressure, vapor quality.

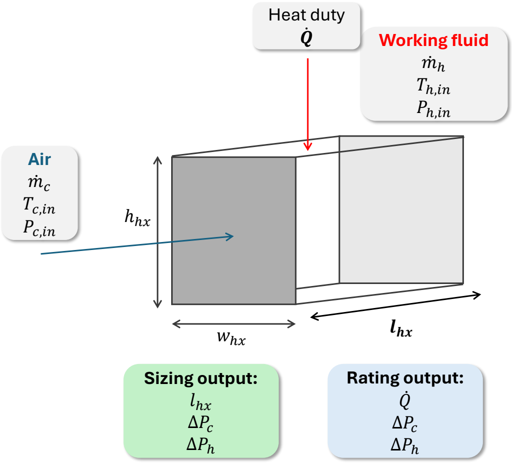

Figure 3.8: Schematic of *HeXacode* inputs and outputs for both sizing and rating modes.

APPLICATION IN THIS WORK

Both sizing and rating modes are used in the multi-point optimization described in Section 3.3. In addition, rating mode is employed to generate the calibration curves required to tune the energy and momentum source terms of the porous zone for the CFD model, as described in Subsection 3.4.5. *HeXacode* is treated as a black-box: no core functionalities were developed nor modified, and it is used by wrapping around it.

However, a few minor adjustments were implemented. During optimization it was observed that certain non-converged or non-physical solutions were not detected by *HeXacode*'s rating functionality. These cases were identifiable because the code returned the provided first guess for the heat duty together with seemingly valid values for almost all other output quantities. This behavior is problematic in the optimization, as the rating function is iterated until the prescribed heat duty is met, and such cases may incorrectly appear as valid individuals in the optimization process.

To improve convergence detection, additional warning flags were introduced and proved to be effective filters:

- If the resulting heat duty differs by less than 1% from its target value (i.e., the input or first guess), *and* the ratio of required to actual heat transfer area exceeds 10%, a warning is raised. This clearly indicates a non-converged solution.

- If the computed lengths of the finite-volume cells contain `NaN` values, a warning is raised. In these cases, the code returns heat-exchanger performance and flow properties, but the `NaN` cell lengths indicate that the rating procedure did not converge.

It should be noted that *HeXacode* rating computations for condensers with minimal subcooling appear to suffer from convergence difficulties. This is visible in Figure 3.25a, where no data points are present in the low-mass-flow region immediately following the quasi-constant wall-temperature plateau.

Discretization Study

As *HeXacode* employs a finite volume method, discretizing the heat exchangers into control volumes for each thermodynamic region, it is important to perform a discretization study on the key optimization metrics:

- **Air-side pressure drop:** Minimized as part of the heat exchanger optimization.
- **Heat duty:** Constrained across all operating points in the multi-point optimization.
- **Hot-side pressure drop:** Although constrained, it was found to be non-limiting and is therefore of secondary importance in terms of convergence. However, significant inconsistencies between sizing and rating mode are observed, which might be relevant for future studies.
- **Sizing–rating consistency:** Discrepancies between rating and sizing were observed. Consistency between sizing and rating modes in relevant performance quantities is important, particularly as the sizing mode is used for the design point (typically TO ISA+35), while the other operating points are evaluated in rating mode.
- **Computational cost:** Relevant especially in rating mode, which inherently solves iteratively. Moreover, rating mode is used within an iterative loop in single-component optimization to adjust the mass flow rate until the heat duty equality constraint is satisfied.

Sizing–Rating Consistency Table 3.9 quantifies the sizing–rating inconsistencies for the selected discretization, which was determined from the convergence studies discussed subsequently (Figure 3.9 and Figure 3.10). Regarding heat transfer, the condenser shows sizing–rating inconsistencies up to 4.5%, with an average of 2.3%. While these fall within modeling uncertainty, they correspond to heat transfer deviations exceeding 1 kW. The radiator, in contrast, demonstrates excellent heat transfer consistency. For cold-side (air) pressure drop, both heat exchangers are sufficiently consistent. The hot-side pressure drop shows the largest discrepancy for the condenser (up to 7.9%), which is attributed to the complex two-phase flow across its three thermodynamic regions (desuperheating, condensation, subcooling). The radiator, involving only subcooling, exhibits generally much lower inconsistencies. This discrepancy in hot-side pressure drop is acknowledged but does not affect the current optimization, as the constraint on hot-side pressure drop was never active. However, this behavior may be relevant for future applications of *HeXacode*.

Table 3.9: Sizing–rating inconsistencies for both heat exchangers

Heat Exchanger	**N$_{cells}$**	**Sizing–Rating Inconsistencies [%]**		
		Heat Transfer $\dot{Q}$	Cold Side ΔP_c	Hot Side ΔP_h
Condenser	[3,4,3]	0.1–4.5%	0.1–0.9%	1.3–7.9%
Radiator	[10]	0.0–0.2%	0.4–1.0%	0.2–1.2%

Condenser Discretization Study A representative condenser geometry has been selected from an initial baseline (no inclination) multi-point optimization. Figure 3.9 shows the sensitivity of key performance metrics to the discretization level across multiple operating points, including non-uniform discretizations (e.g.,[1,2,1]). The selected discretization for this study is $N_{\text{cells}} = [N_{\text{dsh}}, N_{\text{cond}}, N_{\text{sc}}] = [3,4,3]$, to balance numerical accuracy, primarily in terms of heat duty and air-side pressure drop, with computational cost in Figure 3.9a.

At [3,4,3], heat duty errors in Figure 3.9b remain below 2% across all operating points, which is acceptable given overall modeling uncertainties and the sizing-rating inconsistencies in Table 3.9.

The error in cold-side pressure drop in Figure 3.9c consistently decreases with increased mesh resolution, with diminishing improvements beyond the selected point. For the selected point, errors are generally below 3%. In contrast, Figure 3.9d shows that hot-side pressure drop exhibits larger errors, though these do not limit the optimization as this constraint is not active, as discussed previously.

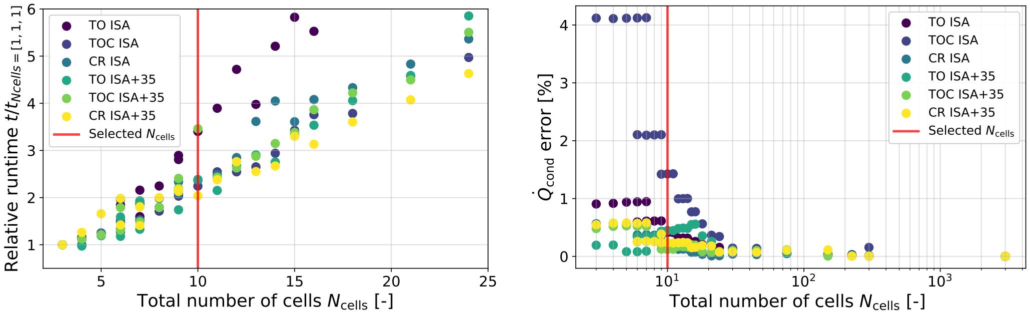

(a) Relative runtime $t/t_{N_{\text{cells}}=[1,1,1]}$

(b) Heat duty $\dot{Q}_{\text{cond}}$ error

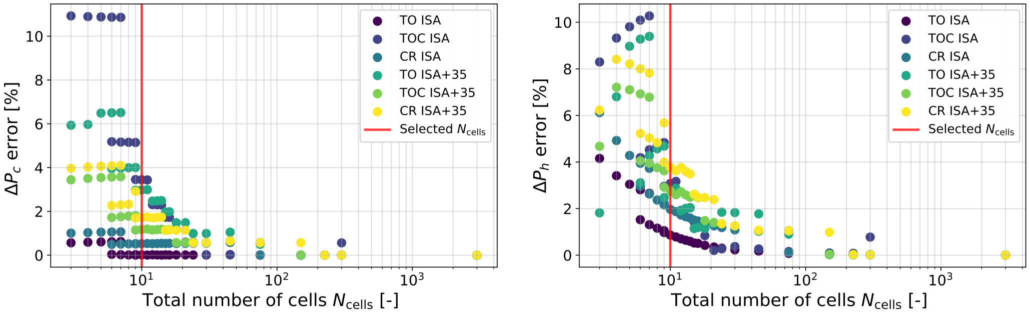

(c) Cold-side ΔP_c error

(d) Hot-side ΔP_h error

Figure 3.9: Discretization study for the condenser as a function of total number of FV cells N_{cells} in *HeXacode* for multiple operating points. Errors are relative to the finest discretization.

Radiator Discretization Study A discretization study was also conducted for a representative radiator geometry obtained from an initial coupled multi-point optimization for the baseline (non-inclined) case. Figure 3.10 shows the convergence behavior of key metrics across increasing levels of discretization in the single subcooled region. The selected discretization is $N_{\text{cells}} = [N_{\text{sc}}] = [10]$ to balance accuracy in terms of heat duty and air side pressure drop, and computational cost indicated in Figure 3.10a. While heat duty predictions converge rapidly, the cold-side pressure drop requires finer discretization to reach error levels of order 2% and hence comparable to the accuracy for the condenser. Although Figure 3.10a indicates only a modest increase in computational time with finer discretization, this does not fully reflect the actual computational cost when using the MEG-50 coolant. As will be further discussed in Figure 3.2.7, evaluating the thermophysical properties of MEG-50 is considerably more expensive, typically an order of magnitude higher, making it important to carefully consider the radiator's discretization.

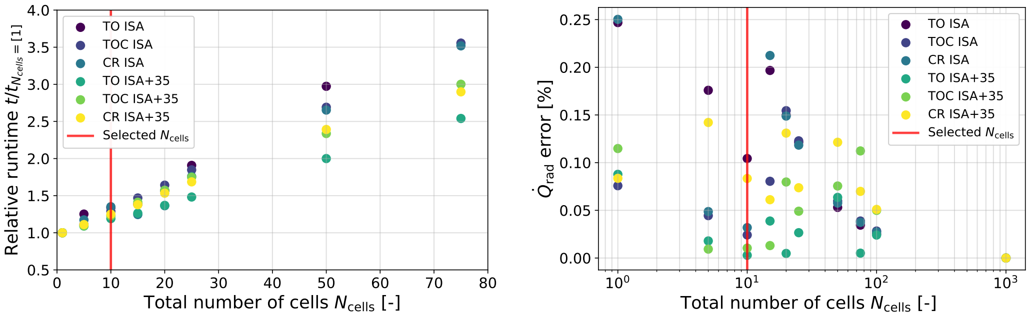

(a) Relative runtime $t/t_{N_{\text{cells}}=[1]}$

(b) Heat duty $\dot{Q}_{\text{rad}}$ error

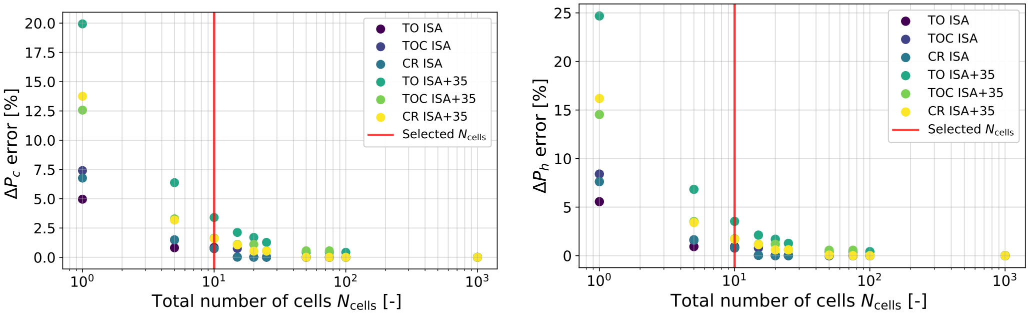

(c) Cold-side ΔP_c error

(d) Hot-side ΔP_h error

Figure 3.10: Discretization study for the radiator as a function of total number of FV cells N_{cells} in *HeXacode* for multiple operating points. Errors are relative to the finest discretization.

3.2.7. FLUID MODEL

INTRODUCTION

In order to evaluate thermodynamic and transport properties of working fluids and air in *HeXacode*, different fluid models have been used. Air is assumed to be dry in this work, while in reality there is some moisture in the air, particularly at ISA+35 conditions. The dry air assumption is conservative as moist air has more cooling power due to a higher specific heat capacity C_p.

THERMODYNAMIC LIBRARIES

Two fluid models are used: the open-source *Coolprop* library [74, 75] using the Helmholtz Equation of State (HEOS) formulation, and the *REFPROP* library developed by the National Institute of Standards and Technology (NIST) [76]. *REFPROP* is widely regarded as the industrial standard due to its highly accurate multi-parameter equations of state. While being computationally more expensive and license-restricted, it provides higher fidelity for working fluids, e.g., refrigerants. *REFPROP* is used via the Python wrapper for *Coolprop*.

For this project, *REFPROP* is available and accuracy of thermodynamic properties is prioritized over potential computational efficiency. Hence *REFPROP* is selected as the primary model for the considered working fluids, i.e., refrigerant R1234yf and coolant MEG-50. For air it was verified that both models produced practically the same results hence for air the computationally cheaper *Coolprop* is selected.

Table 3.10: The considered fluids and selected thermodynamic models applied in this work.

Fluid	**Application**	**Thermodynamic Model**
Air	Cold side (condenser and radiator)	*Coolprop* HEOS [74, 75]
R1234yf	Refrigerant (condenser)	*REFPROP* [76]
MEG-50	Coolant (radiator)	*REFPROP* [76] + correlations [77]

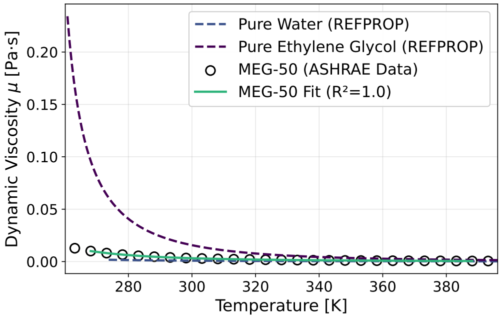

(a) Dynamic viscosity μ.

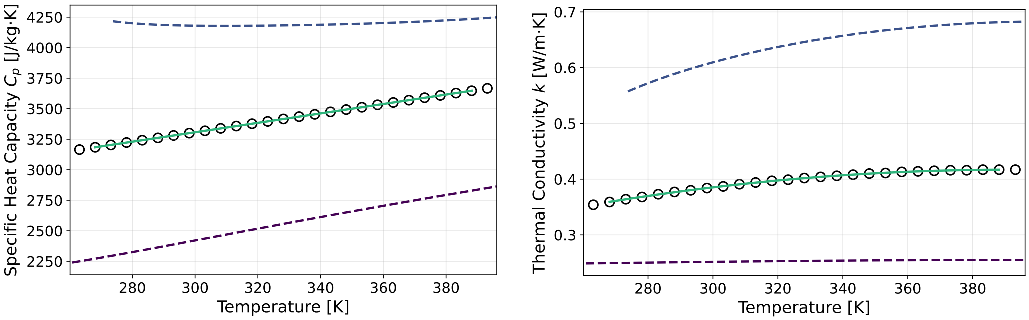

(b) Specific heat capacity C_p.

(c) Thermal conductivity k.

Figure 3.11: Polynomial fits of MEG-50 transport properties as a function of temperature, based on ASHRAE data [77]. Curves for pure water and pure ethylene glycol from *REFPROP* are included for reference.

Coolant-Specific Modeling

Correlations for Transport Properties The radiator's coolant MEG-50, a 50% by mass mono-ethylene glycol (MEG)–water mixture, is not fully supported by *REFPROP* for transport properties due to limitations in mixture transport correlations for aqueous solutions with molar concentrations greater than 5%.

To overcome this limitation, a *REFPROP* wrapper has been created for the FluidModel class in *HeXacode*, allowing to still used the *REFPROP* backend to compute thermodynamic state variables such as temperature, pressure and enthalpy. Meanwhile, the transport properties specific heat capacity c_p, thermal conductivity k and dynamic viscosity μ are computed using polynomial fits as function of temperature derived from experimental data from the American Society of Heating, Refrigerating & Air Conditioning Engineers (ASHRAE) [77]. The transport properties of the liquid are assumed to be a function of temperature only at this relatively low pressure of 3 bar (Table 3.3b).

Figure 3.11 shows the fitted transport properties for MEG-50 in comparison to *REFPROP* values for pure water and pure ethylene glycol, as well as the experimental MEG-50 data from ASHRAE [77]. The resulting correlations cover the temperature range of the coolant during this project. The fits provide good accuracy compared to the ASHRAE data [77], with R^2 values exceeding 0.99 for all properties.

Enthalpy-Temperature Lookup Table The inverse thermodynamic problem $T = f(h,P)$ solved by *REFPROP* was found to be numerically unstable and computationally expensive for the MEG-50 mixture. This severely limited optimization performance, as each evaluation of the sizing and rating functions require repeated enthalpy-to-temperature inversions. To circumvent this, a pressure-specific lookup table was precomputed for MEG-50, mapping enthalpy as a function of temperature at a fixed pressure. The forward relation $h = f(T,P)$ is evaluated once over a temperature range of 270.0 to 385.0 K at $P = 300$ kPa, with a resolution smaller than 0.03 K. A linear interpolator is then used at runtime to compute $T(h)$.

Although the hot-side system pressure is fixed at 3 bar as presented in Table 3.3b, it can locally deviate due to pressure losses along the hot side flow path. The impact of pressure variation on enthalpy is expected to be small for a liquid. This assumption is verified by comparing $h(T)$ curves at nearby pressures. For a deviation of ±5 kPa around the hot side system pressure of 300 kPa, the resulting error in enthalpy remains below 0.3%, which is within the current modeling accuracy, also given that hot side pressure drop and thus the hot side pressure variation is in the order of 0.5 kPa as can be seen for ΔP_h for the optimal radiators in Table A.2 and Table A.3 in Appendix A.

3.3. HEAT EXCHANGER OPTIMIZATION

3.3.1. INTRODUCTION

This section presents the heat exchanger optimization framework employing NSGA-II for multi-objective, multi-point optimization applied to the condenser and radiator heat exchangers within the E9X ram air duct. The optimization employs the reduced-order models developed in Section 3.2 to efficiently explore the design space across the multiple operating points defined in Section 3.1.

The heat exchangers and ram air duct are part of the TMS visualized in Figure 2.5. Ideally, one would optimize the heat exchangers simultaneously with the thermodynamic cycle. Beltrame et al. [37] developed a design methodology for a compact Organic Rankine Cycle (ORC) unit for Waste Heat Recovery (WHR) and showed that optimization of HX geometry together with thermodynamic cycle parameters, although computationally more expensive, yields significant performance improvements. On the other hand, Beltrame et al. [11] concluded that optimal HX design is driven by pressure loss minimization and can be decoupled from optimal duct design.

To limit the design space and computational resources, and acknowledging that Elysian has their own *Modelica*-based thermodynamic cycle and component calculation methods, this project focuses on heat exchanger optimization. Two optimization strategies are employed: single heat exchanger optimization and sequential coupled optimization, which captures the coupling between the series arrangement of the condenser and radiator. The key differences between these modes are: (i) single mode iterates on mass flow to meet heat duty requirements exactly through equality constraints, while coupled radiator mode uses prescribed mass flow from the condenser with inequality constraints, and (ii) single mode requires nested iteration loops to converge inlet conditions and mass flow, while coupled radiator mode evaluates performance directly with fixed inlet conditions from the upstream condenser.

This section is organized as follows. First, Subsection 3.3.2 defines the optimization problem including design variables, objectives, and constraints. Subsection 3.3.3 then describes the NSGA-II algorithm implementation. Subsequently, Subsection 3.3.4 and Subsection 3.3.5 present the single and sequential coupled optimization formulations, respectively. Subsection 3.3.6 verifies the implementation, and finally Subsection 3.3.7 introduces performance metrics for design selection from Pareto fronts.

3.3.2. OPTIMIZATION PROBLEM DEFINITION

DESIGN VARIABLES

The design vector for each HX topology formally contains all geometrical parameters defining the heat exchanger, including parameters held constant during optimization. This ensures that the entire geometry is fully specified. However, only the parameters with variable bounds listed in Table 3.6 are actually optimized.

The heat exchanger width w_{hx} is fixed at 0.56 m, while the height h_{hx} is determined by the selected inclination angle as presented in Table 3.5. The heat exchanger length l_{hx} is determined by sizing at the most critical operating point (TO ISA+35), for which the ram air duct requires the maximum mass flow of 3.9 kg/s supplied by the intake. This sizing condition defines the geometry used for all other operating points in the multi-point evaluation.

The complete geometry vectors are defined as:

$$\mathbf{x}_{\mathrm{LF}}^{\mathrm{T}} = \begin{bmatrix} w_{\mathrm{hx}} & h_{\mathrm{hx}} & p_{\mathrm{tube}} & w_{\mathrm{mc}} & t_{\mathrm{mc}} & h_{\mathrm{mc}} & n_{\mathrm{mc}} & h_{\mathrm{ft}} & w_{\mathrm{ft}} & p_{\mathrm{fin}} \\ h_{\mathrm{fin}} & t_{\mathrm{fin}} & p_{\mathrm{louver}} & \theta_{\mathrm{louver}} & l_{\mathrm{norm\_louver}} & & & & & \end{bmatrix} \tag{3.22}$$

$$\mathbf{x}_{\mathrm{OSF}}^{\mathrm{T}} = \begin{bmatrix} w_{\mathrm{hx}} & h_{\mathrm{hx}} & p_{\mathrm{tube}} & w_{\mathrm{mc}} & t_{\mathrm{mc}} & h_{\mathrm{mc}} & n_{\mathrm{mc}} & h_{\mathrm{ft}} & w_{\mathrm{ft}} & p_{\mathrm{fin}} \\ h_{\mathrm{fin}} & t_{\mathrm{fin}} & d_{\mathrm{fin}} & & & & & & & \end{bmatrix} \tag{3.23}$$

OBJECTIVE FUNCTIONS

Multi-Objective Formulation The optimization has two competing objectives: minimizing heat exchanger mass and minimizing air-side pressure drop, subject to heat duty constraints at all operating points listed in Table 3.3.

Although the ram air duct model described in Section 3.2 would enable single-objective optimization of net ram air duct drag, a multi-objective formulation is preferred for several reasons. First, the Pareto front reveals the mass-pressure drop trade-off and design trends that a single optimum cannot reveal, providing insight into the design space and enabling selection of different designs based on specific criteria. Second, uncertainties exist particularly in the semi-empirical intake model and thereby in the external drag calculation. Moreover, the influence of heat exchanger inclination on internal pressure losses, which affects nozzle thrust and ultimately net drag, has not yet been assessed. Third, since the ram air duct geometry is fixed and only heat exchanger geometry varies, the optimization focuses on heat exchanger-level objectives (mass and pressure drop) rather than system-level net drag.

Weight Allocation The objective air-side pressure drop is computed using a weighted sum over all operating points. The determination of appropriate weights for each operating point is addressed below.

Initially, weights were considered based on the product of propeller shaft power and mission-phase duration obtained from Elysian's performance model. This approach reflects electrical energy consumption during each flight segment but significantly underestimates cooling requirements during descent. In this phase, shaft power is very low, since the aircraft is nearly gliding, and the battery and electric power unit (EPU) generate correspondingly small heat loads. However, the E9X thermal management system (TMS) is deliberately designed to leverage the thermal inertia of the battery. Even when heat loads are low during descent, the cooling system continues to extract heat so that the battery temperature is reduced prior to landing. This ensures that fast charging can begin immediately after arrival. As a result, the cooling demand in descent is comparable to that in cruise and must be weighted accordingly.

To capture this behavior, the multi-point weights are based on an equivalent cooling energy, defined as the product of the total cooling power (sum of condenser and radiator heat duties) and the duration of each mission segment. For each operating point $j \in \Omega$, this quantity is defined as:

$$E_j = \left(Q_{\mathrm{cond},j} + Q_{\mathrm{rad},j}\right) \Delta t_j \tag{3.24}$$

where Δt_j is the effective mission time fraction assigned to j. The mission times Δt for each phase are listed in Table 3.1, and the heat duties Q_{cond} and Q_{rad} are given in Table 3.3. To include hot-day conditions in the objective function, a split of 90%–10% between ISA and ISA+35 conditions is assumed within each phase, such that $\Delta t_j = 0.9\,\Delta t$ for ISA points and $\Delta t_j = 0.1\,\Delta t$ for ISA+35 points.

The normalized weight of operating point j is then obtained as:

$$w_j = \frac{E_j}{\sum\limits_{k\in\Omega} E_k} \tag{3.25}$$

The resulting set of weights, which sum to unity, is provided in Table 3.11. While this weight allocation is physically motivated by cooling requirements, it should be noted that any choice of weights is inherently arbitrary and affects the resulting Pareto-optimal designs.

Table 3.11: Normalized weights w_j allocated to each operating point $j \in \Omega$, based on total cooling energy and assuming a 90%–10% split between ISA and ISA+35 conditions

Operating Point j	Weight w_j
TO ISA	0.0335
TOC ISA	0.2929
CR ISA	0.3286
TOD ISA	0.2346
TO ISA+35	0.0042
TOC ISA+35	0.0359
CR ISA+35	0.0409
TOD ISA+35	0.0293
Total	**1.0000**

CONSTRAINTS

The optimization is subject to several constraints. First, the heat duty requirements must be satisfied at all operating points listed in Table 3.3. Moreover, the hot-side pressure drop ΔP_h is limited to a maximum $\Delta P_{h,\max}$ of 5% of the corresponding inlet pressure to ensure minimal impact on overall system performance. The lower and upper bounds for the design vector are given in Table 3.6.

Additional constraints were investigated but ultimately excluded from the optimization formulation for the following reasons:

- **Air-side pressure drop limits:** Under extreme off-design conditions (e.g.,TO ISA+35), the air-side pressure drop may exceed the available ram pressure, resulting in zero net flow through the heat exchanger. This would require auxiliary components such as a fan, adding complexity, mass, and potential windmilling drag. While this constraint was not explicitly enforced during optimization, designs with high pressure drop at specific operating points naturally lead to higher values in the weighted pressure drop objective. Therefore, such designs are inherently penalized. Moreover, for unconstrained inclination angles, this constraint was often infeasible and would prematurely exclude relevant design trends. As a result, this constraint is best evaluated during post-processing of the optimization results.

- **Maximum HX length (l_{hx}):** Excessively long heat exchangers are undesirable due to increased weight and integration challenges. The length l_{hx} is a derived quantity obtained during the sizing step of the optimization, based on the geometry (design vector) and the selected critical operating point used as the sizing condition (e.g., TO ISA+35). This constraint was removed to avoid obscuring trends for smaller inclination angles, which feature reduced vertical height and therefore require longer lengths to achieve the required heat transfer area. Imposing a strict limit would unfairly penalize such configurations and mask important design trends. The suitability of resulting HX lengths is instead assessed during post-processing.

- **Coolant freezing constraint:** A lower bound on the working fluid outlet temperature was initially introduced to prevent freezing. However, during extensive multi-point simulations, no design violated this condition. The constraint was therefore removed to simplify the problem formulation.

3.3.3. MULTI-OBJECTIVE OPTIMIZATION ALGORITHM

The optimization employs the NSGA-II algorithm [50], a well-established evolutionary algorithm for multi-objective constrained problems, using the *PyMoo* library in Python. This genetic algorithm approach is preferred over gradient-based methods for several reasons: (i) gradient-based algorithms are inherently limited for multi-objective problems, (ii) analytical gradients are unavailable for the objectives and constraints, and (iii) numerical gradient computation becomes prohibitively expensive given the large number of design variables and nonlinear constraints [3].

To accelerate the computationally intensive optimization, the problem was parallelized using Python's *multiprocessing* library, distributing the evaluation of candidate solutions across available CPU cores. With seven CPU cores available, typical speedups of approximately 6× were achieved compared to serial evaluation, significantly reducing the overall optimization runtime.

3.3.4. SINGLE HEAT EXCHANGER OPTIMIZATION

OVERVIEW

The single component optimization mode is applied to both the condenser and radiator as standalone heat exchangers within the ram air duct. This mode serves a dual purpose: (1) generating Pareto-optimal condenser designs for use in the sequential coupled optimization, and (2) establishing a performance benchmark for uncoupled condenser and radiator configurations.

The optimization problem is multi-objective and multi-operating-point, seeking to minimize the heat exchanger mass and the air-side pressure drop, weighted over eight operating points representing standard and hot-day conditions. Each candidate geometry undergoes nested iterations, where for each operating point, the air-side mass flow rate is varied until the required heat duty is met within a numerical tolerance. This creates a nonlinear coupling between geometry, mass flow rate, HX inlet conditions (through the intake-diffuser model), and the heat exchanger's performance.

The intake-diffuser model captures the pressure recovery through the intake and diffuser, and thus the air-side inlet conditions for the heat exchanger, as functions of mass flow rate. The change of HX inlet static temperature and pressure with mass flow is relatively small, so one might consider excluding this effect when one is interested in heat exchanger performance alone. However, (i) the same model is used to compute the internal and external drag using the intake model so it is already implemented, (ii) while changes are small, for nozzle thrust computation an accurate prediction of the total pressure loss through the intake and diffuser is desired.

MATHEMATICAL FORMULATION

The multi-objective optimization problem is formulated as:

$$\min_{\mathbf{x}} \mathbf{F}(\mathbf{x}) = \begin{bmatrix} m_{\text{hx}}(\mathbf{x}) \\ \sum_{j\in\Omega} w_j \, \Delta P_{c,j}(\mathbf{x}) \end{bmatrix} \tag{3.26}$$

subject to the constraints:

$$Q_{j,\text{achieved}}(\mathbf{x}, \dot{m}^*_{c,j}) = Q_{j,\text{required}} \qquad \forall j \in \Omega \tag{3.27}$$

$$\Delta P_{h,j}(\mathbf{x}) \leq \Delta P_{h,\max} \qquad \forall j \in \Omega \tag{3.28}$$

$$\mathbf{lb} \leq \mathbf{x} \leq \mathbf{ub} \tag{3.29}$$

where $\mathbf{x}$ denotes the design vector given in Equation 3.22 and Equation 3.23 depending on the louvered or offset strip fin topology, Ω is the set of all operating points, w_j are the weigts listed in Table 3.11.

The first objective $m_{\text{hx}}(\mathbf{x})$ corresponds to the total heat exchanger mass, while the second represents a weighted sum of cold-side pressure drops across all operating points. All objective functions are normalized using appropriate reference values so that both objectives have comparable magnitudes(i.e., $(\mathcal{O}(1))$. This normalization improves NSGA-II performance by preventing large scale differences between objectives from distorting the crowding-distance metric, thereby maintaining a more balanced exploration of the Pareto front. All constraints are collected into a constraint vector $\mathbf{G}(\mathbf{x}) \leq \mathbf{0}$, following standard multi-objective optimization formulations.

The mass flow rate $\dot{m}^*_{c,j}$ is not part of the design vector but is internally computed iteratively during optimization to satisfy the heat duty equality constraint, requiring an additional iterative loop to compute the heat exchanger inlet pressure and temperature as functions of mass flow.

SOLUTION PROCEDURE

Figure 3.12 illustrates the solution procedure for single heat exchanger optimization. For each candidate design vector $\mathbf{x}$ proposed by NSGA-II, the procedure begins with sizing at the critical operating point j_{crit} (typically TO ISA+35) using the maximum mass flow of 3.9 kg/s. This determines the heat exchanger length l_{hx} and mass m_{hx}.

With the geometry fixed, the algorithm loops over all remaining operating points. For each operating point $j \neq j_{\text{crit}}$, nested iteration is employed. The outer loop iterates on the inlet conditions: the ram air duct model computes HX inlet static pressure $P_{c,\text{in},j}$ and temperature $T_{c,\text{in},j}$ as functions of mass flow rate. The inner loop adjusts the air mass flow rate $\dot{m}_{c,j}$ using *HeXacode* in rating mode until the achieved heat duty matches the required value within tolerance ε. Once both loops converge, the ram air duct model computes the aerodynamic forces (intake drag and nozzle thrust) and the results for operating point j are stored.

After evaluating all operating points, the objectives $\mathbf{F} = \{m_{\text{hx}}, \sum_j w_j \Delta P_{c,j}\}$ and constraints $\mathbf{G}$ are computed and returned to NSGA-II for the next generation.

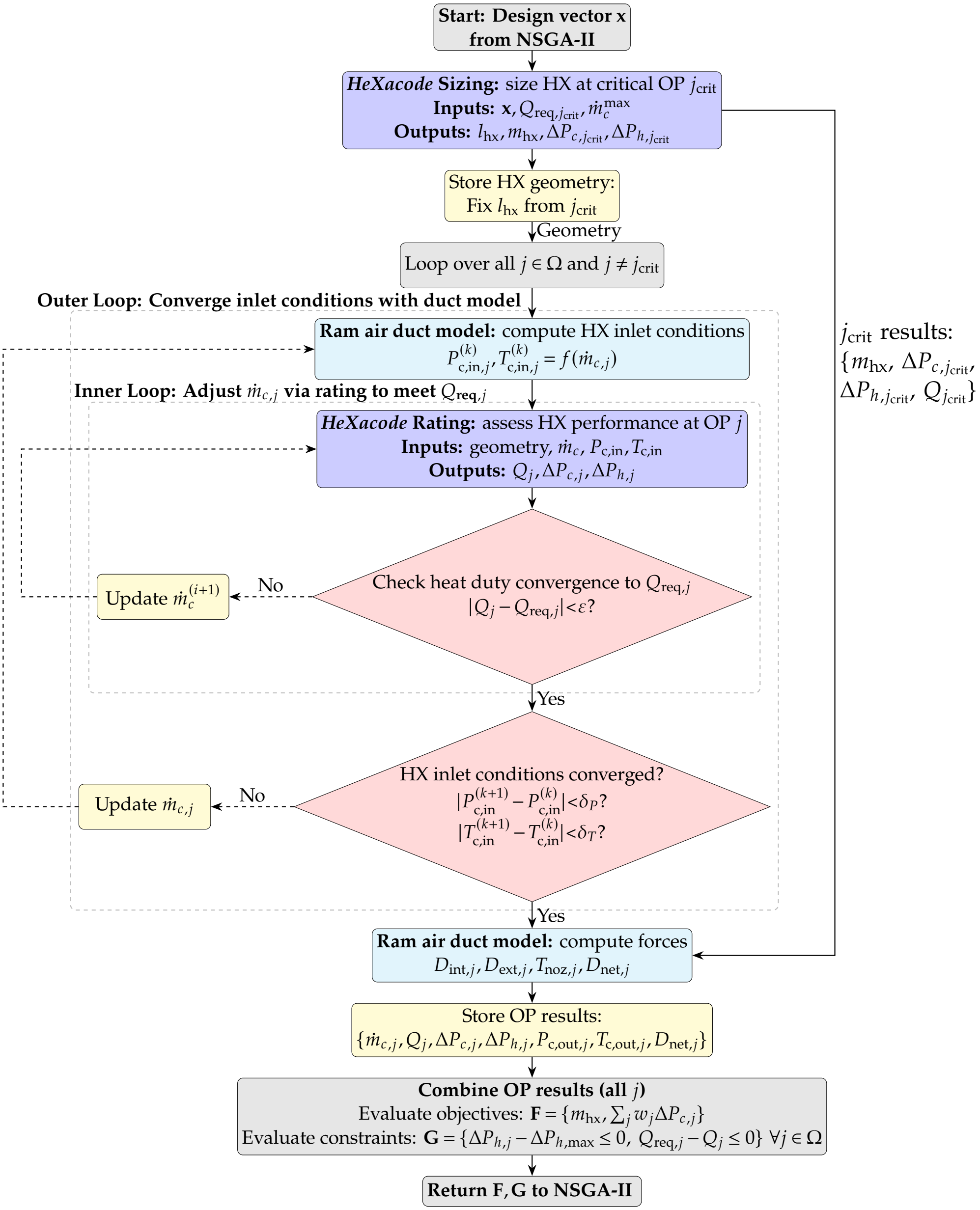

Figure 3.12: Single heat exchanger optimization workflow. Sizing at j_{crit} defines geometry; rating at remaining operating points uses nested iteration (inner: mass flow to meet heat duty; outer: inlet conditions with duct model).

3.3.5. SEQUENTIAL COUPLED OPTIMIZATION

OVERVIEW

The sequential coupled optimization captures the physical arrangement of the condenser and radiator in series within the E9X ram air duct. The condenser is optimized first using the single heat exchanger optimization described in Subsection 3.3.4, yielding a Pareto front. A representative set of designs spanning this Pareto front is then selected, and for each selected condenser design, a separate radiator optimization is performed, yielding a corresponding radiator Pareto front. The final system-level Pareto front is obtained by combining all condenser-radiator pairs and filtering for Pareto-optimal solutions with respect to the total system objectives.

Unlike the condenser, the radiator is not required to meet the heat duty exactly. Instead, the optimization enforces an inequality constraint ensuring that the radiator rejects at least the required heat at each operating point. This reflects the design philosophy where overcooling is acceptable for the radiator, as rejecting more heat does not significantly influence the overall performance of the liquid TMS.

This sequential coupling strategy maintains computational efficiency while capturing the coupling between components. This is particularly important as *HeXacode* computations with MEG-50 as working fluid is an order of magnitude slower than with refrigerant, and the sequential approach avoids iterating on mass flow to match the radiator heat duty exactly. However, the sequential approach does not guarantee a global system-level optimum, as the condenser is optimized without knowledge of how the radiator will respond to its outlet conditions. True simultaneous optimization would require significantly higher computational cost and is beyond the scope of this work.

MATHEMATICAL FORMULATION

In the sequential coupled optimization, the condenser is optimized identically to the single heat exchanger case described in Subsection 3.3.4. After obtaining the condenser Pareto front, selected designs serve as fixed boundary conditions for the downstream radiator. For each operating point $j \in \Omega$, the radiator receives fixed inlet conditions from the condenser outlet: air-side mass flow $\dot{m}_{c,j}$, static pressure $P_{c,\text{in},j}$, and temperature $T_{c,\text{in},j}$. The design vector $\mathbf{x}_\text{rad}$ contains only radiator geometric variables. The radiator optimization problem is then formulated as:

$$\min_{\mathbf{x}_\text{rad}} \mathbf{F}(\mathbf{x}_\text{rad}) = \begin{bmatrix} m_\text{rad}(\mathbf{x}_\text{rad}) \\ \sum_{j\in\Omega} w_j \, \Delta P_{c,j}(\mathbf{x}_\text{rad}) \end{bmatrix} \tag{3.30}$$

subject to the constraints:

$$Q_{j,\text{required}} - Q_{j,\text{achieved}}(\mathbf{x}_\text{rad}, \dot{m}_{c,j}, P_{c,\text{in},j}, T_{c,\text{in},j}) \leq 0 \qquad \forall j \in \Omega \tag{3.31}$$

$$\Delta P_{h,j}(\mathbf{x}_\text{rad}) \leq \Delta P_{h,\max} \qquad \forall j \in \Omega \tag{3.32}$$

$$\mathbf{lb} \leq \mathbf{x}_\text{rad} \leq \mathbf{ub} \tag{3.33}$$

Here, the radiator is only required to meet or exceed the required heat rejection, with air-side mass flow prescribed by the condenser rather than iteratively adjusted. Overcooling is therefore permitted and not penalized.

The radiator's performance is highly sensitive to the inlet mass flow rate and air temperature provided by the upstream condenser. As such, the critical operating point (i.e., the sizing condition) is not predetermined but emerges from the optimization process. For the radiator in the coupled configuration, this resulted in either TO ISA+35 or CR ISA+35 being selected as the sizing condition, depending on the specific condenser outlet conditions, whereas TO ISA+35 consistently emerged as the sizing condition in the single-component case.

SOLUTION PROCEDURE

Figure 3.13 illustrates the solution procedure for sequential coupled optimization. The key difference from single heat exchanger optimization is that the radiator inlet conditions $\{\dot{m}_{c,j}, P_{c,\text{in},j}, T_{c,\text{in},j}\}$ are prescribed from the selected condenser design and remain fixed for all operating points.

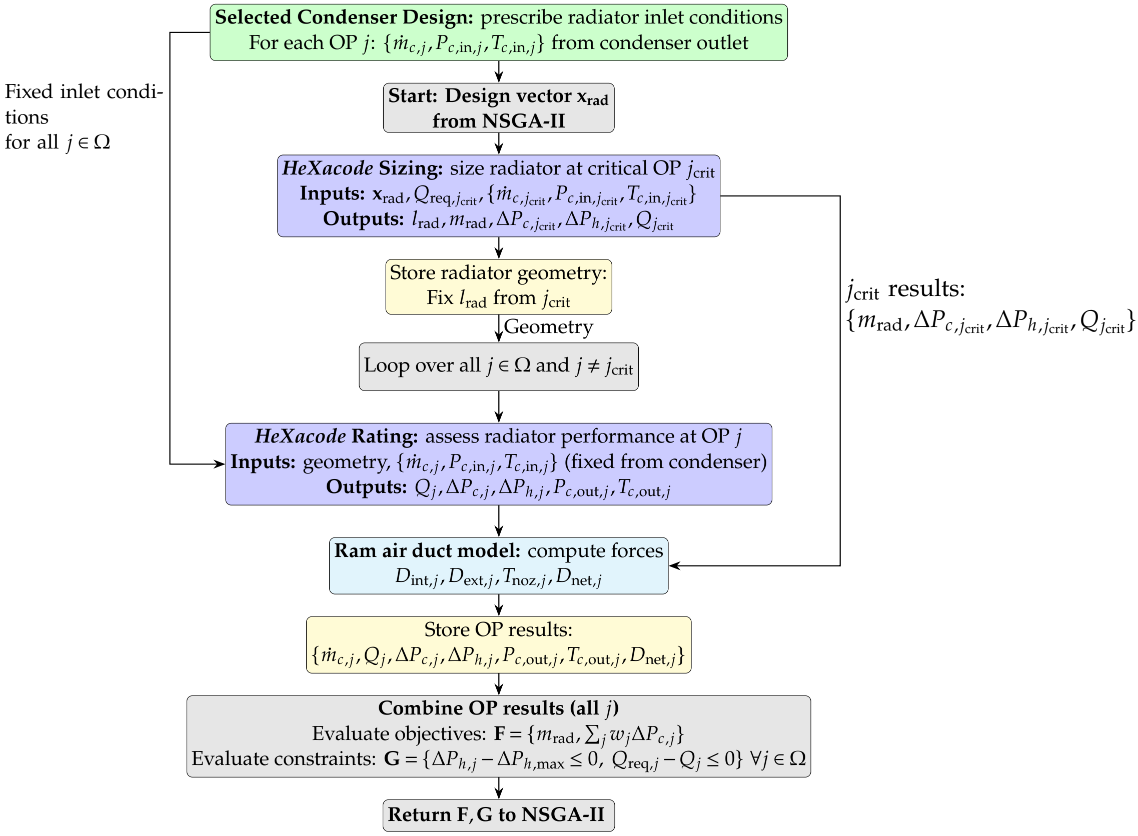

Figure 3.13: Sequential coupled radiator optimization workflow. Selected condenser design provides fixed inlet conditions for all operating points; radiator uses inequality heat duty constraints ($Q_j \geq Q_{\text{req},j}$) permitting overcooling.

For each candidate radiator design vector $\mathbf{x}_\text{rad}$ proposed by NSGA-II, the procedure begins with sizing at the critical operating point j_crit using the fixed inlet conditions from the condenser. This determines the radiator length l_rad and mass m_rad.

With the radiator geometry fixed, the algorithm loops over all remaining operating points. For each operating point $j \neq j_\text{crit}$, *HeXacode* is called in rating mode with the fixed inlet conditions from the condenser. No mass flow iteration is required, as $\dot{m}_{c,j}$ is prescribed. The ram air duct model then computes the aerodynamic forces using the radiator outlet conditions, and the results are stored.

After evaluating all operating points, the objectives $\mathbf{F} = \{m_{\text{rad}}, \sum_j w_j \Delta P_{c,j}\}$ and constraints $\mathbf{G}$ are computed and returned to NSGA-II. Note that the inequality constraint $Q_{j,\text{required}} - Q_{j,\text{achieved}} \leq 0$ permits the radiator to reject more heat than required without penalty.

3.3.6. VERIFICATION OF IMPLEMENTATION

The optimal heat exchanger geometries presented in Table A.1 verify that all design variables respect the lower and upper bounds defined in Table 3.6.

To verify that the coupling between condenser and radiator has been successfully implemented, Table A.2 and Table A.3 demonstrate that for each set of condenser-radiator designs (per inclination angle): (i) the mass flow $\dot{m}_c$ through the condenser and radiator is equal, (ii) the outlet temperature from the condenser $T_{\text{c,out}}$ is the inlet temperature for the radiator $T_{\text{c,in}}$, and (iii) the outlet static pressure of the condenser $P_{\text{c,out}}$ is the inlet static pressure for the radiator $P_{\text{c,in}}$.

3.3.7. PERFORMANCE METRICS AND DESIGN SELECTION

EQUIVALENT BATTERY MASS

The multi-objective optimization results in a Pareto front with the objectives of HX mass and weighted air-side pressure drop. To enable meaningful comparison of designs and facilitate selection from the Pareto front, the pressure drop for each operating point is converted into drag via Equation 3.1 using the ram air duct model. Following the method proposed by Elysian [14], the drag penalty is converted into an equivalent battery mass that must be carried onboard the aircraft. This allows direct comparison between the structural HX mass and the equivalent battery mass due to ram air duct drag.

The equivalent battery mass due to ram air duct drag is computed as [14]:

$$m_{D,\text{eq}} = \frac{1}{e_{\text{bat}}} \int \frac{D_{\text{net}} v_\infty}{\eta_p \eta_{\text{pmad}} \eta_{\text{bat}}} \, dt \tag{3.34}$$

where D_{net} is the net ram air duct drag (Equation 3.1), v_∞ is the freestream velocity, η_p is the propulsive efficiency, η_{pmad} is the power management and distribution efficiency, η_{bat} is the battery efficiency, and e_{bat} is the pack-level battery energy density.

The integrand in Equation 3.34 represents the rate of battery energy consumption required to overcome ram air duct drag, accounting for all conversion losses from stored electrical energy to propulsive power. Integrating over the mission yields the total energy required, which is then converted to equivalent battery mass by dividing by the battery energy density e_{bat}.

For this study, the mission is discretized into four representative flight phases, resulting in the following approximate form of Equation 3.34:

$$m_{D,\text{eq}} \approx \frac{1}{e_{\text{bat}}\, \eta_p\, \eta_{\text{pmad}}\, \eta_{\text{bat}}} \sum_i D_{\text{net},i} \bar{v}_{\infty,i} \Delta t_i \quad \text{for } i \in \{\text{TO}, \text{TOC}, \text{CR}, \text{TOD}\} \tag{3.35}$$

Table 3.1 lists the time spent in each phase Δt_i and the corresponding time-averaged freestream velocity $\bar{v}_{\infty,i}$. Table 3.12 provides the key E9X aircraft and battery parameters used in the calculation.

Table 3.12: Key E9X aircraft and battery parameters used in the equivalent battery mass and modified Breguet range calculations [14]

Parameter	**Value**	**Parameter**	**Value**
Maximum take-off mass (MTOM)	76,000 kg	Maximum lift-to-drag ratio $(L/D)_{\text{max}}$	23
Energy mass (EM)	34,930 kg	Battery efficiency η_{bat}	0.95
Pack-level energy density e_{bat}	360 Wh/kg	PMAD efficiency η_{pmad}	0.96
Usable energy density e_{us}	324 Wh/kg	Propulsive efficiency η_p	0.87

The summation in Equation 3.35 is computed for the nominal mission flown under ISA conditions, as the battery mass sizing is based on this scenario [14]. It is assumed that each flight phase can be represented by a single operating point from Table 3.2 and a corresponding time-averaged freestream velocity in Table 3.1. It is acknowledged that dividing the mission profile over more segments would be more accurate, but this approach is deemed appropriate for the present optimization study, particularly as this method is used to compare different designs among each other rather than assess absolute performance. The climb phase is approximated with TOC and descent with TOD. Both are defined at cruise altitude and Mach number, although in reality altitude and flight velocity vary during these phases, which influences the performance as well.

TOTAL EQUIVALENT SYSTEM MASS

Knowing the equivalent battery mass due to ram air duct drag, the selection metric is the total equivalent HX system mass, i.e., the sum of the structural mass of the HX and the equivalent battery mass from Equation 3.35:

$$m_{\text{total,hx}} = m_{\text{hx}} + m_{D,\text{eq}} \tag{3.36}$$

For the series configuration, $m_{\text{hx}} = m_{\text{cond}} + m_{\text{rad}}$ represents the combined structural mass of both heat exchangers, and $m_{D,\text{eq}}$ accounts for the equivalent battery mass penalty from the total ram air duct drag (including pressure losses through both heat exchangers in series). For single-heat-exchanger configurations, m_{hx} and $m_{D,\text{eq}}$ correspond to that individual component.

IMPACT ON AIRCRAFT RANGE

To assess the impact of saving weight by carefully selecting ram air duct and heat exchanger designs, the resulting increase in usable aircraft range ΔR_{max} can be computed using a modified Breguet range equation for battery-electric aircraft [78, 14]:

$$\Delta R_{\text{max}} = \eta_{\text{bat}}\,\eta_{\text{pmad}}\,\eta_p\,e_{\text{us}}\,\frac{1}{g}\left(\frac{L}{D}\right)_{\text{max}}\left(\frac{\Delta\text{EM}}{\text{MTOM}}\right) \tag{3.37}$$

where g is the gravitational acceleration, $(L/D)_{\text{max}}$ is the maximum lift-to-drag ratio, ΔEM is the change in energy (or empty) mass, and MTOM is the maximum take-off mass. All parameters are listed in Table 3.12.

In this thesis, ΔEM represents the total equivalent system mass savings: when an improved design reduces the total equivalent system mass by $\Delta m_{\text{total,hx}}$ from Equation 3.36 (accounting for both structural mass and aerodynamic penalties), this mass saving can be allocated to additional batteries, giving $\Delta\text{EM} = \Delta m_{\text{total,hx}}$.

Figure 3.14 illustrates the resulting relationship between changes in empty mass and the corresponding improvements in aircraft range for the E9X based on Equation 3.37.

Equation 3.37 considers the case where weight budget is allocated for the installation of additional batteries. It is important to note that this calculation is valid under the assumption that the energy carried by the additional battery mass is used solely to extend the cruise phase, without altering the energy allocations for taxiing, take-off, go-around, and to compensate for the inefficiencies during climb and diversion climb. Furthermore, it does not account for any snowball effect resulting from the mass increase itself [14].

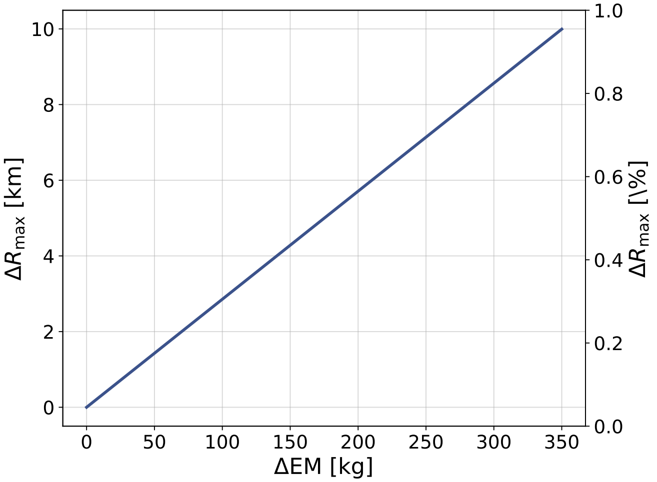

Figure 3.14: Increase in E9X range as a function of empty mass reduction, based on Equation 3.37.

3.4. CFD METHODOLOGY

3.4.1. INTRODUCTION

The goal is to develop and verify a CFD methodology to represent the macroscopic effects of heat exchangers, specifically pressure drop and heat transfer, within the ram air duct. Heat exchangers are modeled using a porous media approach that employs momentum and energy source terms, avoiding the computational expense of resolving the detailed fin geometry. This CFD methodology is subsequently applied in Section 4.2 to compare predictions against the reduced-order model (Section 3.2), assess ROM accuracy, identify modeling limitations, and quantify the effect of heat exchanger inclination.

All porous media model calibration coefficients are provided in Appendix B, while comprehensive CFD results across different operating points and inclination angles are presented in Section 4.2, with additional detailed results in Appendix D.

The remainder of this section is organized as follows. First, Subsection 3.4.2 describes the ram air duct geometries considered. Subsection 3.4.3 then presents the mesh generation strategy and mesh convergence study. Subsequently, Subsection 3.4.4 details the solver configuration and boundary conditions. Finally, Subsection 3.4.5 describes the porous media modeling approach for representing heat exchangers.

3.4.2. GEOMETRY

The ram air duct geometry is modeled in 2D using *Ansys DesignModeler*, where the geometries for the CFD analysis are generated. A baseline configuration, depicted in Figure 3.2, is defined using the fixed parameters listed in Table 3.4. For each inclination case, the duct geometry is updated according to the respective heat exchanger inclination and resulting heat exchanger length obtained from the optimization results (Section 4.1), resulting in the set of geometries used in this CFD study shown in Figure 3.3.

The nozzle height, and therefore area, remains the primary geometric degree of freedom. A first estimate for the required nozzle area is taken from the nozzle model described in Subsection 3.2.5, which predicts the area needed to accommodate the mass flow required to satisfy the heat duty constraints in Table 3.3. A sweep of nozzle outlet area has been performed such that a sweep of mass flows is obtained.

3.4.3. MESH

MESH STRATEGY

A 2D unstructured quad-dominant mesh is created using *Ansys Meshing* for the ram air duct geometries visualized in Figure 3.3. While formally unstructured, the mesh consists predominantly of flow-aligned quad elements, which reduces mesh-induced numerical diffusion. In the transition regions connecting the diffuser to the condenser and the radiator to the nozzle, an unstructured mesh consisting of triangles is used to accommodate the geometric changes. This approach allows a consistent mesh strategy to be applied across all geometries.

To accurately resolve the boundary layer near no-slip walls, inflation layers with a first cell height of 1.5×10^{-5} m and a growth rate of 1.2 are applied. This first cell height is selected to ensure $y^+ < 1$, enabling the use of low-Reynolds number wall treatment with the k–ω SST turbulence model. The y^+ distribution shown in Figure 3.15 indicates that local y^+ values near the nozzle exit reach a maximum of 1.8 over a small region due to high local velocities, while the domain-wide average remains $y^+ = 0.35$.

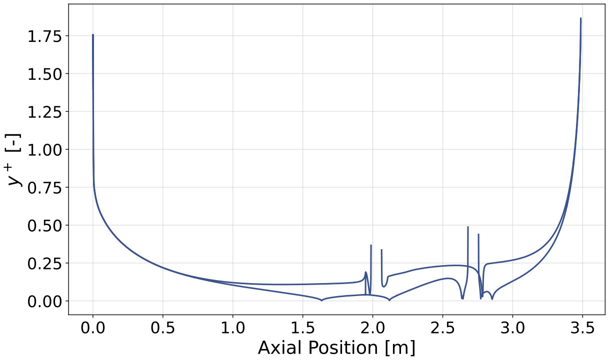

Figure 3.15: Normalized wall distance y^+ distribution along the duct for $\alpha = 60°$ at CR ISA.

The heat exchangers are modeled as porous zones as further outlined in Subsection 3.4.5. In similar studies [11, 13], a uniform but relatively coarse mesh based on a representative elementary volume (REV), equivalent to one flat-tube pitch for the flat-tube heat exchanger topology, is used within the porous region. In contrast, this work applies the same mesh resolution inside the porous zones as in the surrounding duct, following the approach of [34]. This refined strategy better captures flow features induced by inclination and allows the inflation layers to remain continuous across the duct walls, even though slip boundary conditions are applied within the porous zones. The agreement between the CFD model and the ROM presented in Section 4.2 confirms that using a more refined porous-zone mesh, rather than an REV-based mesh, does not negatively affect the consistency between the PMM predictions and those from *HeXacode*.

MESH CONVERGENCE STUDY

A mesh convergence study is performed to ensure that the CFD results are independent of mesh resolution. The analysis focuses on the most challenging geometry, namely the 60° inclination geometry, under cruise ISA conditions. The primary performance metrics evaluated for mesh convergence include (i) the heat duties of both condenser and radiator, (ii) the total pressure loss, which quantifies system losses and forms the basis for developing inclination-dependent pressure-drop correlations, and (iii) the nozzle thrust, which represents the key system-level metric integrating pressure losses, heat addition, and mass flow.

The results of the mesh convergence study are presented in Figure 3.16. It demonstrates that the selected mesh is in the asymptotic convergence region for all performance metrics. If one is interested only in total pressure loss or nozzle thrust, a coarser mesh is acceptable, which is particularly relevant for CFD-based geometry optimization requiring numerous simulations. For this study, the selected mesh does not limit computational resources and also ensures converged solutions for both condenser and radiator heat transfer. Despite significant flow turning and the introduction of source terms in the porous zones, the geometry is sufficiently simple to resolve with a relatively coarse mesh. As further detailed in Appendix C, additional refinement near the nozzle outlet is applied to capture the strong gradients in this region, contributing approximately 200k cells to the total mesh count of 1.2 million cells.

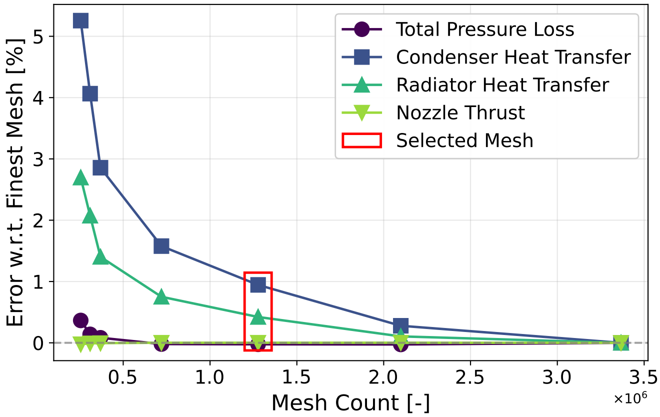

Figure 3.16: Mesh convergence for $\alpha = 60^\circ$ at CR ISA.

3.4.4. SOLVER

Settings Steady-state 2D planar Reynolds-Averaged Navier–Stokes (RANS) simulations are performed using the compressible, pressure-based finite volume solver in *Ansys Fluent 2024 R2*. The coupled scheme and second-order upwind discretization are applied, with gradients discretized using the Least Squares Cell Based method. A pseudo-time stepping method with automatic time step control is employed. The convergence criterion for the simulations is that normalized residuals fall below 10^{-5}. The fluid is dry air, modeled as an ideal gas, with Sutherland's law for the dynamic viscosity. The temperature-dependent specific heat capacity at constant pressure $C_p(T)$ and thermal conductivity $k(T)$ of dry air were obtained from *CoolProp* [74] and fitted to second-order polynomials over the temperature range T = 240–420 K, shown in Figure 3.17. The resulting coefficients are listed in Table 3.13.

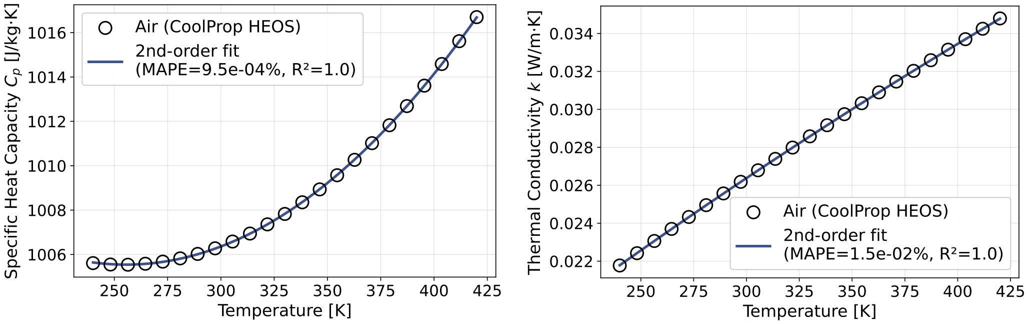

(a) Specific heat capacity $C_p(T)$ fit.

(b) Thermal conductivity $k(T)$ fit.

Figure 3.17: Temperature-dependent second-order polynomials implemented in *Ansys Fluent* for air properties obtained using *CoolProp* over the range T = 240–420 K with the coefficients in Table 3.13.

Table 3.13: Polynomial coefficients for air properties implemented in *Ansys Fluent*. The correlations follow $\phi(T) = a_0 + a_1 T + a_2 T^2$, where ϕ represents either C_p [J/(kg·K)] or k [W/(m·K)], valid for $T = 240$–420 K.

Property	a_0	a_1	a_2
C_p [J/(kg·K)]	1.03237×10^{3}	-2.10041×10^{-1}	4.11186×10^{-4}
k [W/(m·K)]	7.89665×10^{-4}	9.62215×10^{-5}	-3.64078×10^{-8}

Turbulence Modeling RANS simulations are performed using the k–ω SST [79] turbulence model, which is selected due to its superior performance in wall-bounded flows with adverse pressure gradients compared to other linear eddy-viscosity models. This model has also been used in several related studies of ducts with heat exchangers modeled as porous zones [11, 13, 31, 34, 42, 45, 46]. Some works employ the Spalart–Allmaras model instead [20, 44].

While higher-fidelity turbulence modeling approaches such as Reynolds Stress Models (RSMs) could, in principle, capture turbulence anisotropy more accurately, they are not considered for this work. The quantities of interest, pressure drop and heat transfer, are dominated by macroscopic effects modeled by the source terms. In this context, additional turbulence model fidelity would not meaningfully improve predictive accuracy and would only increase computational cost.

To accurately resolve the boundary layer near no-slip walls, inflation layers are applied such that the normalized wall distance $y^+ < 1$, as described in Subsection 3.4.3. This enables the use of a low-Reynolds number wall treatment with the k–ω SST turbulence model.

Boundary Conditions The boundary conditions at the walls are set to be adiabatic and no-slip, except for the walls of the porous zone, where a slip condition is imposed. This is because flow resistance within the porous region is already accounted for via momentum source terms in the governing equations. At the inlet, a total pressure and total temperature boundary condition is applied for each operating point, along with a commonly used value for turbulence intensity of 5%. It is acknowledged that the ram air duct, located in the propeller slipstream, likely experiences higher turbulence intensity. However, the CFD methodology achieves accurate agreement with reduced-order model predictions, and observed discrepancies are attributable to other modeling aspects rather than the inlet turbulence specification. The sensitivity of the results to inlet turbulence intensity, particularly regarding potential for more aggressive (shorter) diffuser designs, remains a topic for future work.

Importantly, the specified inlet total pressure is not the ambient total pressure, but the post-intake value computed using the intake model described in Subsection 3.2.3. The outlet boundary condition is a static pressure outlet corresponding to the ambient static pressure at each operating point. Note that this set of boundary conditions implies that the mass flow rate, inlet static pressure, and outlet total pressure are outputs of the simulation. Mass flow sweeps are performed by varying the outlet area, i.e., varying the nozzle height in this 2D simulation. The complete set of numerical boundary conditions is provided in Table 3.14 corresponding to the operating points in Table 3.2.

Table 3.14: CFD boundary conditions at the duct inlet and outlet. Inlet values correspond to post-intake total conditions, while outlet pressure corresponds to the ambient static pressure at the operating points listed in Table 3.2

Operating Point	$P_{t,\text{inlet}}$ [Pa]	$T_{t,\text{inlet}}$ [K]	P_{outlet} [Pa]
TO ISA	103,934	290.45	101,300
CR ISA	45,877	253.85	37,600

3.4.5. POROUS MEDIA MODELING OF HEAT EXCHANGERS

INTRODUCTION

In this work, the method proposed by Missirlis et al. [41] is used, i.e.,the Darcy–Forchheimer pressure drop law in its anisotropic formulation together with a heat transfer model in the form of a Nusselt–Reynolds–Prandtl number correlation. This approach allows modeling of the macroscopic effects of heat exchangers by means of a porous media model (PMM), avoiding the need to mesh and resolve the geometrical details of the heat exchanger core.

The porous media coefficients must be calibrated such that the porous zone reproduces the same pressure drop and heat transfer characteristics of the actual heat exchanger. The finite-volume heat exchanger tool *HeXacode*, introduced in Subsection 3.2.6, was employed in rating mode to generate reference data across the expected operating envelope. The coefficients are heat exchanger and operating point specific. All PMM calibration coefficients for momentum source terms, energy source terms, and wall temperature correlations are provided in Appendix B.

VELOCITY FORMULATION

Two different velocity formulations exist in porous media modeling: physical velocity (also called interstitial velocity) and superficial velocity. Physical velocity is the actual flow velocity within the void space of the porous region, while superficial velocity is defined as the volumetric flow rate divided by the total cross-sectional area, including both solid and void parts. This implies that superficial velocity neglects the area reduction and resulting flow acceleration through the porous medium, and is therefore lower than physical velocity.

The relationship between the two velocities is governed by the porosity ϵ, defined as the ratio of void volume to total volume, or equivalently the ratio of free flow area to frontal area:

$$\epsilon = \frac{A_{\text{free flow}}}{A_{\text{frontal}}} \tag{3.38}$$

where $A_{\text{free flow}}$ is the cross-sectional area available for fluid flow and A_{frontal} is the total geometric cross-sectional area. Porosity is a number between 0 and 1, where values near 1 indicate high permeability. Porosity is computed internally by *HeXacode* from the fin and tube geometrical parameters.

By mass conservation, the flow must accelerate through the reduced free flow area. The relationship between superficial and physical velocity is expressed as [80]:

$$v_{\text{superficial}} = \epsilon \cdot v_{\text{physical}} \tag{3.39}$$

Figure 3.18 illustrates the difference between superficial and physical velocity in the porous medium model, where physical velocity captures the velocity increase proportional to the inverse of the porosity $1/\epsilon$ according to Equation 3.39.

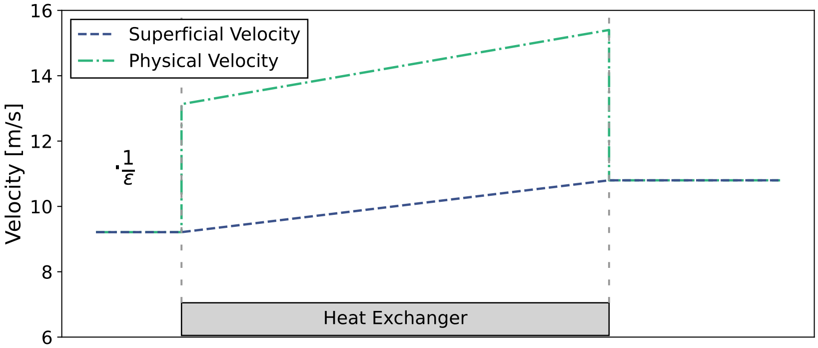

Figure 3.18: Illustration of superficial and physical velocity in the porous medium model, where physical velocity captures the velocity increase proportional to the inverse of the porosity $1/\epsilon$ according to Equation 3.39.

The superficial velocity formulation is the default in *Fluent*, partly because experimental pressure drop correlations are typically based on superficial (inlet) velocity, as that is the only velocity that can be directly measured. If one aims to replicate experimental data, the superficial velocity formulation is often appropriate. However, with the superficial formulation, entrance and exit acceleration effects are not naturally captured in the simulation, as the flow does not instantaneously accelerate upon entering the porous region.

Physical Velocity Formulation

In this work, the physical velocity formulation is chosen for two reasons. First, it naturally captures entrance and exit effects, which are essential for accurate pressure drop predictions. Second, the source term coefficients are calibrated with *HeXacode* using local flow quantities (e.g., Reynolds number) based on physical velocity. Using physical velocity maintains consistency between the CFD implementation and the calibration procedure. Implementation details are discussed in Subsection *Implementation in Fluent*.

MOMENTUM SOURCE TERM

Formulation The generic form of the volumetric momentum source term in the flow direction is given by the Darcy–Forchheimer equation [41]:

$$S_m = -\left(\frac{\mu}{K}v + C_2\frac{1}{2}\rho v^2\right) \tag{3.40}$$

Here μ is the dynamic viscosity and ρ the local fluid density, both computed by the CFD solver. The velocity v is the local velocity in the porous zone, either the superficial or physical velocity depending on the velocity formulation. The parameters $1/K$ and C_2 are calibration coefficients, where $1/K$ represents the viscous resistance (Darcy term), while C_2 is the inertial resistance coefficient associated with form drag. Together, these parameters determine the pressure drop characteristics of the porous zone.

In two dimensions, this formulation is expressed as a matrix equation:

$$\begin{bmatrix} S_x \\ S_y \end{bmatrix} = -\left(\mu \begin{bmatrix} \frac{1}{K_{xx}} & 0 \\ 0 & \frac{1}{K_{yy}} \end{bmatrix} \mathbf{v} + \frac{1}{2}\rho \begin{bmatrix} C_{2,xx} & 0 \\ 0 & C_{2,yy} \end{bmatrix} |\mathbf{v}|\, \mathbf{v} \right) \tag{3.41}$$

where the permeability and inertial resistance coefficients are aligned with the principal axes of the porous medium and rotated into the global (x, y) frame when the heat exchanger is inclined.

To enforce one-dimensional flow through the heat exchanger, the resistance perpendicular to the main flow direction is taken three orders of magnitude higher than the main flow direction, i.e., $\frac{1}{K_{yy}} = 1000 \cdot \frac{1}{K_{xx}}$ and $C_{2,yy} = 1000 \cdot C_{2,xx}$. This is in line with Fluent's recommendations [80] and other work [11, 13, 31]. As a consequence, the porous region acts as a flow straightener, forcing streamlines to align with the (inclined) heat-exchanger axis. This behavior is clearly visible in the streamline plots for inclination angles $\alpha = 30°$ and $\alpha = 60°$ in Figure D.7b and Figure D.8b in Appendix D.

Since *HeXacode* is a one-dimensional code, it only provides calibration data for the main flow direction source term. Missirlis et al. [41] have experimentally determined off-diagonal components of this matrix to capture the effect of flow entering under an angle, which might be particularly relevant for the first part of the heat exchanger where the flow is not yet aligned with the heat exchanger core. However, this is beyond the capabilities of the one-dimensional *HeXacode*, and therefore one-dimensional air flow through the heat exchanger is assumed. Consequently, the PMM does not fully capture incidence losses at the heat exchanger entrance, where flow misalignment with the fin geometry causes additional pressure losses due to secondary flows and local flow disturbances. These effects are expected to be confined to a short entrance region due to the flow-straightening behavior of the closely spaced fins.

The effect of temperature on pressure loss is accounted for through the temperature-dependent parameters, i.e., the dynamic viscosity and density in Equation 3.41. However, this assumption neglects the presence of indirect effects of temperature-dependent viscosity on the flow distribution and form drag [45].

Calibration The momentum source term was calibrated using the static pressure drop predicted by *HeXacode*. *HeXacode* computes the air-side pressure drop using Equation 2.5. For the PMM calibration, only the core friction contribution of the heat exchanger pressure drop is considered, while other contributions (e.g., entrance and exit effects) are excluded. This approach resulted in the best agreement between *HeXacode* rating (with all pressure drop contributions) and CFD PMM during verification. The rationale is that entrance and exit effects are directly resolved by the CFD solver, and momentum effects are inherently included through density variation in the solver.

The calibration procedure consists of a regression of *HeXacode* data for density, viscosity, and velocity against the quadratic Darcy–Forchheimer form, yielding the viscous resistance $1/K_{xx}$ and inertial resistance $C_{2,xx}$ coefficients in Equation 3.41. Note that the average flow properties in the heat exchanger are used, which on the air side is simply the arithmetic mean between the HX inlet and outlet. Figure 3.19 visualizes how the momentum source term coefficients are fitted by sweeping over a three-dimensional grid of heat exchanger air inlet conditions in *HeXacode*.

In *HeXacode* rating mode, three air-side inputs are specified for a fixed geometry: mass flow rate $\dot{m}_c$, inlet static pressure $P_{\mathrm{c,in}}$, and inlet static temperature $T_{\mathrm{c,in}}$, as visualized in Figure 3.8. The ranges of input conditions were chosen to be representative of the operating point under consideration and are listed, together with the coefficients, in Appendix B.

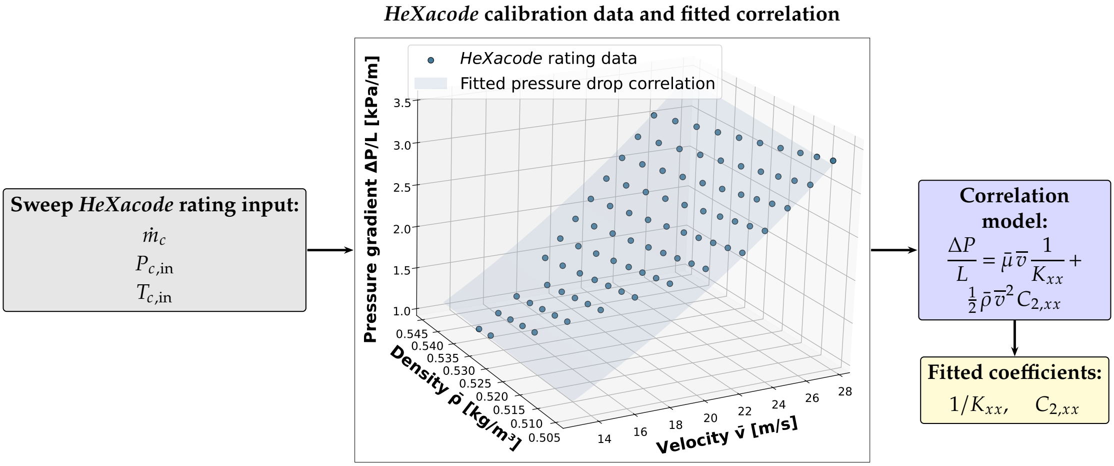

Figure 3.19: Calibration method for the coefficients of the momentum source term. Adapted from [12].

The accuracy of the fitted correlations is assessed by comparing the predicted pressure drop values against the *HeXacode* reference data across the entire calibration grid. The model error, defined as the relative difference between correlation predictions and reference values, quantifies how well the Darcy–Forchheimer correlation reproduces *HeXacode* results. Figure 3.20 shows the absolute relative model error distribution across the three-dimensional input grid of mass flow, inlet temperature, and inlet static pressure.

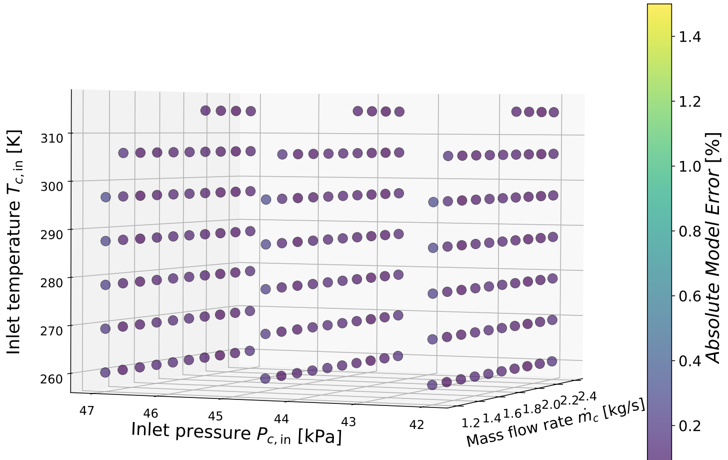

Figure 3.20: Absolute model error distribution for the radiator for the pressure drop correlation fit for baseline CR ISA (mean error 0.40%).

The fitted correlation achieves an absolute mean model error below 0.5% for both condenser and radiator, meaning that the pressure drop can be approximated very accurately with the Darcy–Forchheimer correlation as a function of local velocity, density, and dynamic viscosity.

Figure 3.20 also shows that for some rating points no rating results were obtained due to overly constraining inlet conditions (i.e., small mass flow combined with high inlet temperature resulting in insufficient cooling power), where *HeXacode* could not converge to a solution. This region also exhibits the largest modeling errors, corresponding to the lowest mass flows.

The resulting coefficients can be found in Appendix B. Note that the calibration range provided in Appendix B represents the complete 3D grid, but as shown in Figure 3.20, this does not mean for each combination of inlet variables a rating solution and thus calibration point exists.

The general conclusion is that the pressure drop fit is very accurate. Hence, any discrepancies between CFD and *HeXacode* will be related to how flow properties are locally computed and how appropriate this correlation is, as it is based on average flow properties, thereby implicitly assuming a linear trend across the single air cell in *HeXacode*. The order of magnitude of error is similar for other heat exchanger geometries and calibrations using different hot-side conditions.

ENERGY SOURCE TERM

Formulation While more advanced heat transfer models exist, such as coupled ϵ-NTU approaches [45], this work opts to reproduce the heat exchanger performance from *HeXacode* in CFD by using a Nusselt correlation as a function of Reynolds and Prandtl numbers. Such correlations can often be found for different heat transfer applications [81]. The heat transfer coefficient is derived from this correlation and used to compute the volumetric energy source term.

The generic form of the volumetric energy source term is:

$$S_e = \frac{k}{d_{\mathrm{eq}}}\, a\, \mathrm{Re}^b\, \mathrm{Pr}^c\, (T_{\mathrm{wall}} - T)\, \beta_{\mathrm{HX}} \tag{3.42}$$

Here k denotes the thermal conductivity of air, T the local air temperature, and Re and Pr the local Reynolds and Prandtl numbers, respectively. All these local flow quantities are computed by the CFD solver. The other variables are calibration inputs, where β_{HX} and d_{eq} represent the heat exchanger surface compactness and equivalent hydraulic diameter, respectively, i.e., heat exchanger geometry-dependent parameters. The coefficients a, b, and c are fitted from *HeXacode* rating data, while T_{wall} is the prescribed wall temperature of the heat exchanger.

Figure 3.21 shows the computation flow of the energy source term: local flow properties (ρ, μ, Pr, $k(T)$, T) are computed by the CFD solver and determine the Reynolds number, Nusselt number, local heat transfer coefficient, and resulting volumetric energy source term S_e. The coefficients a, b, and c and the wall temperature T_{wall} are obtained from calibration with *HeXacode*, while the equivalent hydraulic diameter d_{eq} and surface compactness β_{HX} are heat exchanger geometry parameters. This heat transfer coefficient coming from the Nusselt correlation is then multiplied by the compactness β_{HX} and temperature difference $(T_{\mathrm{wall}} - T)$ to obtain the local energy source term.

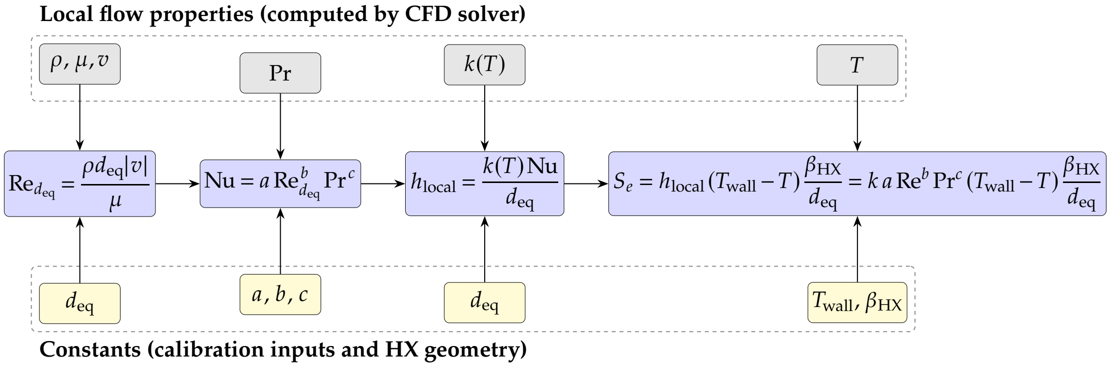

Figure 3.21: Computation flow of the energy source term S_e. Adapted from [41].

Calibration The energy source term coefficients were obtained by fitting a Nusselt correlation against *HeXacode* rating outputs. The calibration targets the local heat transfer coefficient h, expressed as:

$$h = \frac{k}{d_{eq}} a\,\mathrm{Re}^{b}\,\mathrm{Pr}^{c} \tag{3.43}$$

using the average flow properties on the air side.

The calibration procedure is visualized in Figure 3.22, which illustrates how the energy source term coefficients are fitted by sweeping over a three-dimensional grid of heat exchanger air inlet conditions in *HeXacode*. Similar to the momentum calibration, the three air-side inputs are mass flow rate ($\dot{m}_c$), inlet static pressure ($P_{c,in}$), and inlet static temperature ($T_{c,in}$). The ranges of input conditions were chosen to be representative of the operating point under consideration and are listed, together with the coefficients, in Appendix B.

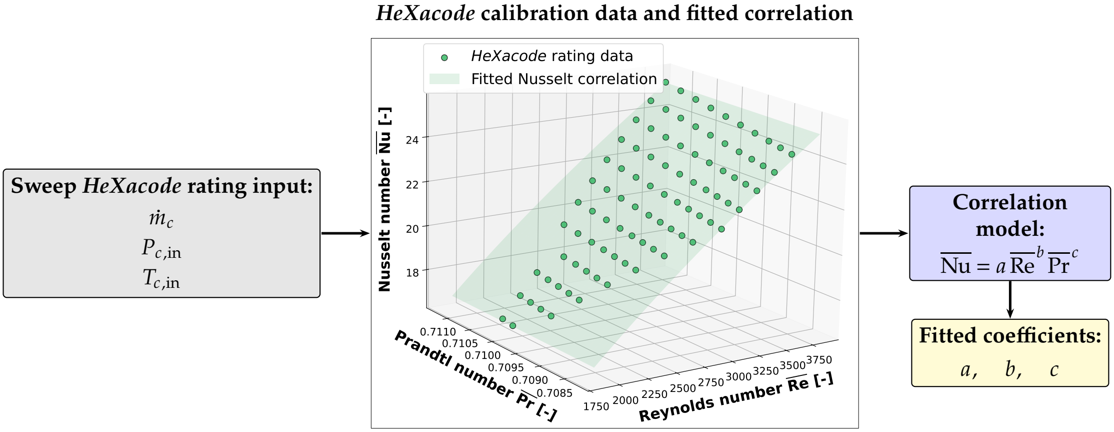

Figure 3.22: Calibration method for the coefficients of the energy source term. Adapted from [12].

The coefficient bounds used in the nonlinear regression were defined as $a \in [10^{-6}, 10]$, $b \in [0.2, 1.5]$, and $c \in [0.25, 0.50]$. These limits constrain the fitted parameters to physically meaningful ranges consistent with established Nusselt number correlations commonly found in heat transfer textbooks [81]. While it would be possible to fix one or more exponents based on known theoretical or empirical relations, the chosen bounds resulted in good agreement between the *HeXacode* and CFD model.

Air-Side Discretization: HeXacode vs. PMM

A fundamental difference exists between *HeXacode* and the PMM regarding air-side discretization for cross-flow heat exchangers. In *HeXacode*, the hot side is discretized with multiple finite volume cells, while the air side is a single cell with linear temperature distribution. In contrast, CFD resolves the nonlinear air-side temperature field spatially. Calibration uses arithmetic mean properties from *HeXacode*'s single air cell inlet and outlet.
This linearization can lead to discrepancies between predictions, as observed in the *Verification* subsection, particularly for the radiator.

The accuracy of the fitted Nusselt correlation is assessed by comparing the predicted Nusselt numbers against the *HeXacode* reference data across the calibration grid. The model error, defined as the relative difference between correlation predictions and reference values, quantifies how well the Nusselt correlation reproduces the results from *HeXacode*. Figure 3.23 shows the absolute relative model error distribution across the three-dimensional input grid of mass flow, inlet temperature, and inlet static pressure.

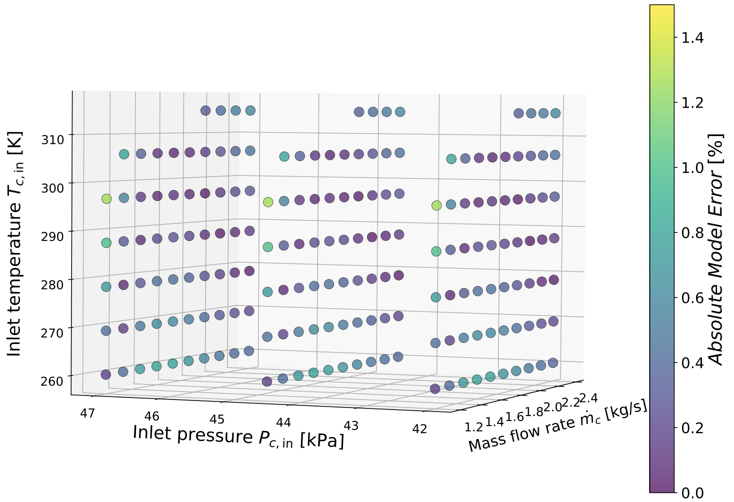

Figure 3.23: Absolute model error distribution for the radiator for the Nusselt correlation fit for baseline CR ISA (mean error 0.08%).

The fitted correlation achieves an absolute mean model error below 0.1% for both condenser and radiator, meaning that the heat transfer coefficient can accurately be approximated with this Nusselt correlation as a function of Reynolds and Prandtl numbers. Similar to Figure 3.20, Figure 3.23 also shows that for some rating points *HeXacode* could not converge to a solution.

The general conclusion is that the heat transfer coefficient (or Nusselt number) fit is very accurate. Hence, any discrepancies between CFD and *HeXacode* will be related to how flow properties are locally computed, how the Nusselt correlation is used to compute the energy source term, and how appropriate this correlation is, as it is based on average flow properties, thereby implicitly assuming a linear trend across the single air cell. The order of magnitude of error is similar for other heat exchanger geometries and calibrations using different hot-side conditions.

WALL TEMPERATURE

Motivation An integral part of the energy source term is the wall temperature T_{wall}, which appears explicitly in the energy source term formulation in Equation 3.42 and represents the temperature at the heat transfer surface. It is an input for the simulation as shown in Figure 3.21. This temperature is not constant throughout the various operating points. It varies with operating conditions as a function of different hot-side conditions (as shown in Table 3.3), and also depends on air-side conditions, primarily mass flow rate and inlet temperature.

A fundamental difference exists between *HeXacode* and the CFD model when considering a cross-flow heat exchanger configuration. In *HeXacode*, only the hot side is discretized with multiple cells while the air side is approximated with only a linear temperature distribution between inlet and outlet. This is inherently different from CFD, where the non-linear temperature variation is resolved spatially. For the current cross-flow configuration with the horizontal tube arrangement, this also implies that the wall temperature distribution is only resolved in *HeXacode* in the width axis of the heat exchanger, which is the axis that is out-of-plane and not modeled in the current 2D CFD model. For that reason, a single wall temperature is specified, which is obtained from *HeXacode* by means of a finite volume cell length-averaged value:

$$T_{\text{wall}} = \frac{\sum (T^n_{\text{wall}} \cdot L^n)}{\sum L^n} \tag{3.44}$$

where n denotes the finite volume cell index. Note that in *HeXacode*, cell lengths are determined to keep enthalpy difference constant throughout the cells, hence this is effectively an enthalpy-based average.

This approach results in a spatially uniform wall temperature in the CFD model. While this may appear as a limitation, it is important to recognize that *HeXacode* itself does not resolve spatial wall temperature variation along the air flow direction due to its single-cell air-side discretization in the cross-flow configuration. Therefore, the constant wall temperature assumption in CFD is consistent with *HeXacode*.

Figure 3.24 shows the spatial distribution of wall temperature along the hot-side flow direction computed by *HeXacode* for the baseline heat exchanger designs at ISA operating points. The solid lines represent the cell-wise temperature distribution, while the dashed lines indicate the length-weighted average wall temperature used as input for the PMM.

Notably, the condenser wall temperature shown in Figure 3.24a is not necessarily more uniform than the radiator wall temperature. One might expect the condensation process to maintain a nearly constant wall temperature due to the isothermal nature of phase change at constant pressure, resulting in a more uniform distribution for the condenser. However, when desuperheating and subcooling regions are also present alongside condensation, the wall temperature can exhibit significant spatial variation.

In contrast, the radiator in Figure 3.24b shows a linear decrease in wall temperature as it consists of subcooling only. This observation is important for understanding the relative performance of the PMM between the condenser and the radiator, as will be discussed in Subsection *Verification*. It suggests that the assumption of a spatially uniform wall temperature may be equally limiting for both heat exchangers, rather than being particularly problematic for the radiator alone.

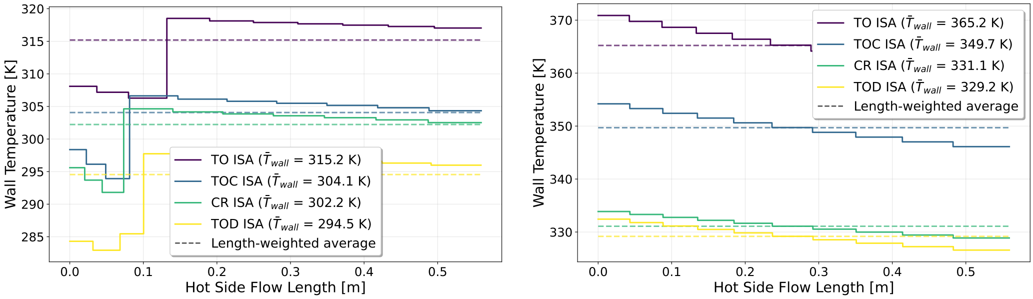

(a) Condenser (desuperheating and condensing).

(b) Radiator (subcooling only).

Figure 3.24: Spatial distribution of wall temperature along the hot-side flow direction computed by *HeXacode* for baseline heat exchanger designs at ISA operating points. The hot-side flow length corresponds to the out-of-plane dimension in the cross-flow configuration with $w_{\mathrm{hx}} = 0.56$ m.

Sensitivity Analysis To quantify the sensitivity of T_{wall} to operating conditions, a parametric study was conducted for the baseline heat exchanger designs. *HeXacode* rating calculations were performed over a three-dimensional grid of air-side inlet conditions spanning representative ranges for the CR ISA operating point. It became apparent that inlet pressure has negligible effect. This can also be observed from the very similar error trends in Figure 3.20 and Figure 3.23 across different inlet pressures. Therefore, only the effects of mass flow rate and inlet static temperature are plotted in Figure 3.25.

The effect of mass flow rate is present in Figure 3.25, but changes remain relatively small near the design point. Note that the trends are not particularly linear for the condenser, partially because the wall temperature depends on the distribution of thermodynamic regions (desuperheating, condensing, subcooling), which in turn depends on the heat transfer. Particularly at lower mass flow rates, where the condenser operates predominantly in the condensing region with no or minimal subcooling, the wall temperature variation with mass flow is small. In general, the effect of inlet temperature is more significant. This effect is particularly relevant for the condenser-radiator series configuration, as the condenser outlet temperature directly determines the radiator inlet conditions.

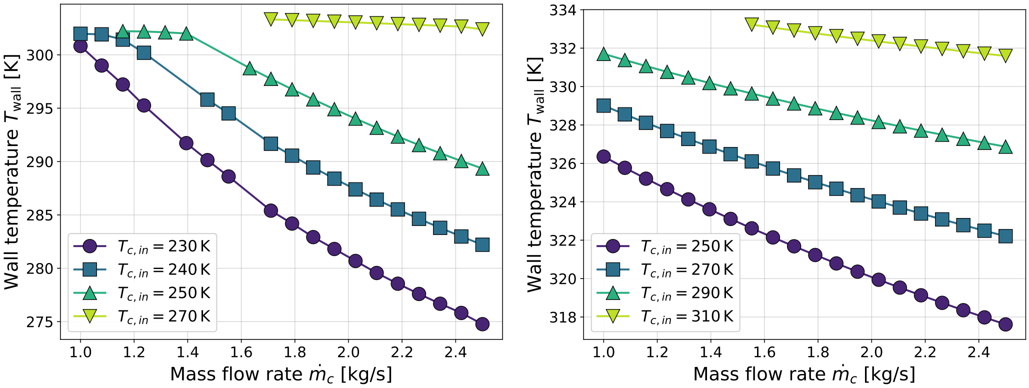

(a) Condenser

(b) Radiator

Figure 3.25: Sensitivity of wall temperature to mass flow rate and inlet static temperature for (a) the baseline condenser and (b) radiator at CR ISA conditions.

Modeling Approaches Based on the sensitivity analysis, two modeling approaches are distinguished depending on whether the inlet conditions are known a priori or vary significantly during operation.

Method 1: Constant Wall Temperature. For cases where both inlet temperature and mass flow rate are known a priori and remain approximately constant, a single constant value for T_{wall} can be used without significant loss of accuracy. This simplified approach is applicable when the heat exchanger operates at or near a single known design point, where the inlet conditions are well-defined and variations are small. Under these circumstances, the length-averaged wall temperature from *HeXacode* at the design condition provides a suitable constant boundary condition for the porous media model. This particularly holds for a condenser operating at a design point where condensation dominates with minimal desuperheating and subcooling, corresponding to the quasi-constant region in Figure 3.25a at lower mass flow rates. The verification results in Figure 3.27 confirm that the constant wall temperature is sufficiently accurate near the design point, but show significant deviation in heat transfer at higher mass flow rates when substantial subcooling occurs.

This constant wall temperature approach is effectively equivalent to stating that if the inlet conditions are known and fixed, the source term will reproduce the expected heat transfer. However, once the operating conditions deviate significantly from the calibration point, the prediction becomes inaccurate. In such cases, the formulation is only valid when the inlet conditions remain consistent with those assumed during calibration, making it essentially no more general than prescribing a constant volumetric heat source term $\dot{Q}/V$, which would be a simpler implementation for the CFD user.

Method 2: Variable Wall Temperature Correlation. When inlet conditions vary during operation, a correlation approach is required to capture the wall temperature dependence on operating conditions. Note that this correlation is specific to each operating point, as the hot-side conditions and hence the wall temperature vary between operating points according to Table 3.3. Depending on which inlet conditions vary significantly, two sub-cases are distinguished:

- **Univariate correlation for condenser:** When the inlet temperature remains nearly constant and only the mass flow rate varies, a univariate correlation is sufficient. This applies to the condenser, where the inlet conditions are set by the diffuser outlet and show negligible temperature variation with mass flow at these relatively low Mach numbers. For such conditions, the average wall temperature can be expressed as a polynomial function of mass flow rate $\dot{m}_c$:

  $$T_{\mathrm{wall}} = \sum_{i=0}^{n} c_i \, \dot{m}_c^{\,i} \tag{3.45}$$

  where c_i are regression coefficients determined for each operating point, and n is the polynomial order selected to provide an accurate fit while avoiding oscillations associated with higher-order terms. Higher-order terms are required for the condenser due to the non-monotonic behavior of wall temperature with respect to mass flow rate. As visualized in Figure 3.25a, the wall temperature remains nearly constant at lower mass flow rates where condensation dominates, but decreases significantly at higher mass flow rates where subcooling becomes more substantial. Typically, polynomial orders of $n = 4$–6 are used.

  Alternative fitting functions such as piecewise linear fits or lookup tables could provide greater accuracy. However, these would require defining and compiling a custom User Defined Function (UDF) in *Fluent* for each operating point and heat exchanger design. The polynomial correlation approach is deemed sufficiently accurate while offering greater flexibility and ease of implementation when switching between heat exchanger designs and operating points.

- **Bivariate correlation for radiator:** When both mass flow rate and inlet air temperature vary significantly, a bivariate correlation is required. This applies to the radiator, the second heat exchanger in series, whose inlet conditions are determined by the condenser outlet. If the condenser operates differently than predicted, experiencing enhanced or reduced heat transfer, its outlet temperature will deviate from nominal values. These deviations alter the inlet air temperature entering the radiator, such that the radiator wall temperature depends on both mass flow rate and inlet temperature.

  Accordingly, the radiator wall temperature is expressed as a function of both the mass flow rate $\dot{m}_c$ and the inlet air temperature $T_{\mathrm{c,in}}$:

  $$T_{\mathrm{wall}} = t_0 + t_1 \dot{m}_c + t_2 \dot{m}_c^2 + t_3 T_{\mathrm{c,in}} + t_4 T_{\mathrm{c,in}}^2 + t_5 \dot{m}_c \, T_{\mathrm{c,in}} \tag{3.46}$$

  In the CFD model, the inlet temperature $T_{\mathrm{c,in}}$ is obtained by taking a mass-average at the radiator inlet section. Unlike the condenser, the radiator exhibits an almost linear decrease of wall temperature with increasing mass flow rate at constant inlet temperature, as shown in Figure 3.25b. Consequently, higher-order polynomial terms are not required and this compact bivariate form provides an accurate representation. As will be demonstrated in Figure 3.28, a single correlation per operating point successfully captures the simultaneous variations of mass flow rate and inlet air temperature across a wide range of operating conditions.

Calibration The coefficients c_i in Equation 3.45 and t_i in Equation 3.46 are operating-point-specific and must be determined separately for each operating point, as they implicitly capture the hot-side thermal boundary conditions that vary between operating points according to Table 3.3. The coefficients are fitted simultaneously with the momentum and energy source term calibrations described previously. The fitted coefficients for all operating points can be found in Appendix B.

IMPLEMENTATION IN *FLUENT*

The porous media model was implemented in *Ansys Fluent* with the following key considerations:

- The momentum source terms were applied using the default porous zone model in *Ansys Fluent*. The energy source term was implemented as a custom source term to the energy equation.

- Two porous zones were defined, representing the condenser and radiator respectively, with their own respective source terms and coefficients given in Appendix B. Note that the source terms depend on the hot-side operating conditions (Table 3.3), so depending on the required accuracy, separate calibrations may be needed for each operating point.

- The porous zone effective thermal conductivity was explicitly set equal to the conductivity of air (Table 3.13), to avoid solid conduction in the porous zone and ensure that all heat transfer is captured by the volumetric source term. Note that *Fluent*'s default [80] is a porosity-based average of the thermal conductivity of the fluid and the solid medium, but that gave poor correlation.

- The inclination of the heat exchanger by an angle α is introduced by rotating the Darcy–Forchheimer resistance frame of the porous zone from the global (x, y) axes to the local porous axes (x', y') using the 2D transformation matrix:

  $$\begin{bmatrix} x' \\ y' \end{bmatrix} = \begin{bmatrix} \cos\alpha & \sin\alpha \\ -\sin\alpha & \cos\alpha \end{bmatrix} \begin{bmatrix} x \\ y \end{bmatrix}$$

  ensuring that both the principal viscous and inertial resistance directions in *Ansys Fluent* are aligned with the physically inclined heat exchanger core and thus with the true flow-resistance direction of the exchanger.

- In line with discrepancies in pressure drop observed in previous HX PMM calibration studies using *HeXacode* [11, 12], noticeable differences were also found between *HeXacode* and *Fluent*'s PMM results. During extensive verification efforts, the author concluded that *Fluent* likely evaluates the momentum source terms using the superficial velocity coefficients, even when the physical velocity option is selected. This behavior implies that the resistance coefficients provided to *Fluent* should, in principle, be fitted based on superficial velocity. However, to maintain consistency with the physical-velocity-based calibration approach adopted in this work, the computed momentum source coefficients were rescaled accordingly.

Momentum Source Term Scaling Correction

Fluent likely evaluates momentum source terms using superficial velocity coefficients even when the physical velocity option is selected. To maintain consistency with the physical-velocity-based calibration from *HeXacode*, the momentum source coefficients are rescaled using the velocity relationship in Equation 3.39:

$$\left(\frac{1}{K}\right)_{\text{superficial}} = \left(\frac{1}{K}\right)_{\text{physical}} \cdot \frac{1}{\epsilon} \tag{3.47}$$

$$(C_2)_{\text{superficial}} = (C_2)_{\text{physical}} \cdot \frac{1}{\epsilon^2} \tag{3.48}$$

where ϵ is the porosity.

- In 2D *Fluent* simulations, the out-of-plane depth is 1 m. To obtain physically meaningful quantities from the 2D analysis, all cross-section-dependent results (e.g., mass flow, heat transfer) were scaled by the actual duct width, i.e., $w_{\text{hx}} = 0.56$ m.

MODEL LIMITATIONS AND ASSUMPTIONS

- *Ansys Fluent* will, by default, solve the standard transport equations for turbulence quantities in the porous medium [80]. In this default approach, turbulence in the medium is treated as though the solid medium has no effect on turbulence generation or dissipation rates. This assumption may be reasonable if the PMM's porosity is quite large and the geometric scale of the medium does not interact with the scale of turbulent eddies. However, if the heat exchanger geometry scale is comparable to the turbulent eddy scale, turbulence effects should be actively suppressed in the simulation [38].

  This work uses the default approach, as the focus is on calibrating source terms to achieve good agreement with *HeXacode*. Moreover, implementing turbulence suppression would require data from advanced simulations or experiments that are unavailable, as only the one-dimensional *HeXacode* is used for calibration.

- Heat conduction within the porous block is neglected. The thermal conductivity of the porous zone is explicitly set to that of air to avoid nonphysical solid conduction. This results in good agreement between PMM and *HeXacode*.

- The validity of the PMM coefficients is restricted to the operating point used for calibration in *HeXacode*. It was observed that pressure drop and, to a lesser extent, energy source term coefficients were quite similar across calibrations with different operating points, as listed in Appendix B. One might therefore use a single set of coefficients for all operating point simulations. However, the specified wall temperature T_{wall} depends on the actual heat transfer and the hot-side conditions, which vary according to Table 3.3. This also holds for the more advanced T_{wall} correlations.

- The CFD model does not capture incidence losses due to flow misalignment with the heat exchanger fins at the heat exchanger inlet, as the fin geometry is not explicitly modeled with a PMM. When flow enters the heat exchanger at an angle relative to the fin orientation, additional pressure losses occur, including secondary flows and potential local flow separation, that are not represented by the calibrated Darcy-Forchheimer coefficients. This limitation is particularly relevant for the entrance region of the heat exchanger. Missirlis et al. [41] demonstrated that off-diagonal terms in the resistance matrix can capture such effects, but determining these coefficients is beyond the capabilities of the one-dimensional *HeXacode*.

In practice, compact heat exchangers with closely spaced fins act as effective flow straighteners, rapidly aligning the flow with the fin orientation once inside the core. The high perpendicular resistance (e.g., $K_{yy} = 1000 \cdot K_{xx}$) used in the model reflects this flow-straightening behavior. Therefore, incidence effects are expected to be confined to a short entrance region and have only a small effect on the pressure drop, except potentially at very large inclination angles. By definition, this methodology is not able to fully predict the maximum possible inclination angle as it does not capture this incidence loss.

In contrast, the CFD methodology does resolve several other loss mechanisms, including: (i) flow turning losses in the tilted duct sections where flow redirects to follow the inclined geometry; (ii) flow turning within the heat exchanger as the high perpendicular resistance forces flow alignment with the HX axis, dissipating transversal momentum; (iii) viscous and inertial core friction losses along the main flow direction through the calibrated Darcy-Forchheimer momentum source terms; (iv) entrance and exit losses due to sudden contraction and expansion at the porous zone boundaries through the physical velocity formulation; (v) viscous losses along duct walls; and (vi) mixing losses throughout the domain wherever flow non-uniformities exist.

VERIFICATION

Introduction The PMM methodology has been developed through extensive verification efforts for different heat exchanger geometries and specifications (porosities, lengths, pressure drop and heat transfer characteristics). The verification is structured in two stages to systematically verify both the source term formulations and the wall temperature modeling approach:

1. **Source term verification with constant wall temperature**: The momentum and energy source terms are verified by comparing CFD results against *HeXacode* rating calculations for prescribed inlet conditions. A constant wall temperature, extracted as a length-averaged value from *HeXacode* for each operating point, is used. This verifies the fundamental source term implementation and calibration methodology.

2. **Wall temperature correlation verification**: The univariate and bivariate wall temperature correlations developed in Equation 3.45 and Equation 3.46 are verified by sweeping over a range of mass flow rates and inlet temperatures. This demonstrates the ability of the correlations to adapt to off-design conditions where a constant wall temperature assumption would fail.

The verification methodology employs a 2D straight duct with slip walls and a single porous zone representing the heat exchanger. By prescribing inlet mass flow and total temperature together with outlet static pressure boundary conditions, the *HeXacode* rating conditions can be replicated in *Fluent*, enabling direct comparison between the models.

This simplified setup isolates the PMM performance for verification. Once verified, this provides confidence that when more complex conditions are introduced (e.g., a diffuser upstream, heat exchanger inclination, or series configurations), the PMM will accurately represent heat exchanger behavior.

Verification at Design Point with Constant Wall Temperature Table 3.15 presents the verification results in terms of heat transfer and pressure drop for both the baseline (no inclination) and the 60° inclined configuration across four operating points. The magnitude of the observed discrepancies is deemed acceptable for system-level modeling, particularly considering the inherent uncertainties of the correlations and models used within *HeXacode*, as well as the discretization convergence in *HeXacode* and the sizing-rating inconsistencies discussed in Subsection 3.2.6.

The analysis of the discrepancies in Table 3.15 is as follows:

- The pressure drop is in general in good agreement, as the absolute differences are negligible. The observed deviations can be understood through the different modeling approaches. The momentum source term coefficients are fitted considering only the pressure drop due to core friction. However, the *HeXacode* rating model uses the full pressure drop expression in Equation 2.5, with empirical correlations for entrance and exit effects. Therefore, when entrance and exit effects become more significant (i.e., for heat exchangers with small length l_{hx} and low porosity ϵ such as the 60° inclined configuration), larger deviations between PMM CFD and *HeXacode* in terms of pressure drop are expected. This does not necessarily indicate greater error, as *HeXacode* also uses empirical correlations for entrance and exit effects. However, the absolute pressure drop differences remain well within acceptable modeling accuracies for system-level analysis. This behavior is consistent with earlier verification efforts during this work while developing the methodology, where the error tends to zero for longer heat exchangers with higher porosities. Note that this verifies the methodology improvements applied in this work compared to previous work [11, 12], where the average pressure drop variations were on the order of 5%.

- Regarding heat transfer, the condenser demonstrates very good agreement with *HeXacode* across all operating points, while the radiator exhibits systematic overprediction of 2–6%, even though the Nusselt correlations for both the condenser and radiator had calibration errors below 0.1%, as shown in Figure 3.23. The physical mechanisms underlying this condenser-radiator accuracy difference are discussed in detail in a subsequent paragraph.

- Heat transfer shows larger deviations for shorter heat exchangers with smaller porosity, also due to entrance and exit effects (local accelerations, changing flow properties) in the CFD that are not captured in the same way by *HeXacode*'s lumped approach.

- If heat transfer deviates, it also affects the pressure drop. For the same mass flow rate, increased heat transfer leads to lower density and higher velocities, inducing higher pressure drop and thereby amplifying pressure drop deviations.

- The heat transfer deviations also exhibit sensitivity to operating point. Deviations are larger at operating points with higher mass flow rates (e.g., TO ISA).

Table 3.15: Verification of PMM CFD against *HeXacode* rating model for baseline and 60° inclined configurations with constant T_{wall}. Comparison is presented for four operating points. Note the different heat exchanger lengths l_{hx} and porosities ϵ between configurations. MAE and MAPE denotes the mean absolute (percentage) error across all operating points for each configuration.

Configuration	Operating Point	$\dot{m}$ [kg/s]	$\dot{\mathbf{Q}}$ **[W]**			$\boldsymbol{\Delta}$**P [Pa]**		
			HeXacode	*CFD PMM*	Δ	*HeXacode*	*CFD PMM*	Δ
Baseline case $w_{\text{hx}} = 560$ mm, $h_{\text{hx}} = 400$ mm								
	Condenser: $l_{\text{hx}} = 217$ mm, $\epsilon = 0.77$							
Condenser	TO ISA	2.144	45 680	45 411	−0.6%	282	279	−1.1%
	TOC ISA	1.619	71 100	71 660	+0.8%	380	384	+1.0%
	CR ISA	1.461	62 900	63 070	+0.3%	325	326	+0.3%
	TOD ISA	1.513	55 000	54 653	−0.6%	334	335	+0.3%
	Radiator: $l_{\text{hx}} = 187$ mm, $\epsilon = 0.75$							
Radiator	TO ISA	2.144	97 843	103 162	+5.4%	393	400	+1.8%
	TOC ISA	1.619	74 642	78 062	+4.6%	563	570	+1.2%
	CR ISA	1.461	45 855	46 854	+2.2%	464	461	−0.6%
	TOD ISA	1.513	52 715	54 953	+4.2%	478	479	+0.2%
			MAPE = 2.3% Max = +5.4%			MAPE = 0.8% Max = +1.8%		
60° inclination case $w_{\text{hx}} = 560$ mm, $h_{\text{hx}} = 800$ mm								
	Condenser: $l_{\text{hx}} = 67$ mm, $\epsilon = 0.61$							
Condenser	TO ISA	2.228	45 680	44 487	−2.6%	184	190	+3.3%
	TOC ISA	1.667	71 180	70 559	−0.9%	233	253	+8.6%
	CR ISA	1.502	62 900	62 237	−1.1%	195	215	+10.3%
	TOD ISA	1.596	55 000	53 644	−2.5%	212	230	+8.5%
	Radiator: $l_{\text{hx}} = 84$ mm, $\epsilon = 0.68$							
Radiator	TO ISA	2.228	100 531	106 720	+6.2%	182	186	+2.2%
	TOC ISA	1.667	77 294	80 947	+4.7%	246	255	+3.7%
	CR ISA	1.502	46 977	48 885	+4.1%	207	226	+9.2%
	TOD ISA	1.596	56 564	59 109	+4.5%	216	241	+11.6%
			MAPE = 3.3% Max = +6.2%			MAPE = 7.2% Max = +11.6%		

Significance of Deviations for System-Level Performance To assess the system-level significance of the discrepancies between *HeXacode* rating results and PMM predictions in Table 3.15, the reduced-order model of the ram air duct (Section 3.2) is used. The nozzle model (Subsection 3.2.5) enables computation of how heat transfer and pressure drop variations across the heat exchangers affect nozzle thrust for the baseline geometry.

Figure 3.26 demonstrates that the relative thrust deviations are typically smaller than 1%, corresponding to maximum absolute deviations below 5 N per duct. This represents an order of magnitude reduction in relative terms compared to the heat transfer and pressure drop discrepancies observed in Table 3.15. Total pressure deviations have a larger influence on thrust than heat transfer variations. The sensitivity is more pronounced at TO ISA due to the higher ambient pressure and mass flow compared to cruise conditions, combined with a smaller absolute thrust value that amplifies percentage-wise deviations. Moreover, at cruise conditions the intake total pressure loss represents a smaller fraction of total system pressure loss (Figure 4.24), such that internal flow total pressure deviations have a proportionally larger effect on net ram duct performance.

While a 5 N thrust deviation per duct may appear small in absolute terms, its impact becomes significant when considering net drag. Since thrust is the primary contributor to net drag and net drag has a much smaller magnitude than thrust, small thrust deviations translate to proportionally large net drag variations. A single-duct thrust deviation of 5 N already leads to measurable differences in net drag (Table 4.9) and the resulting equivalent battery mass and total equivalent system mass (Table 4.10). Similarly, for the complete E9X configuration with eight ram air ducts, an accumulated thrust deviation of $8 \times 5 = 40$ N is significant when compared to the net drag values in Table 4.6.

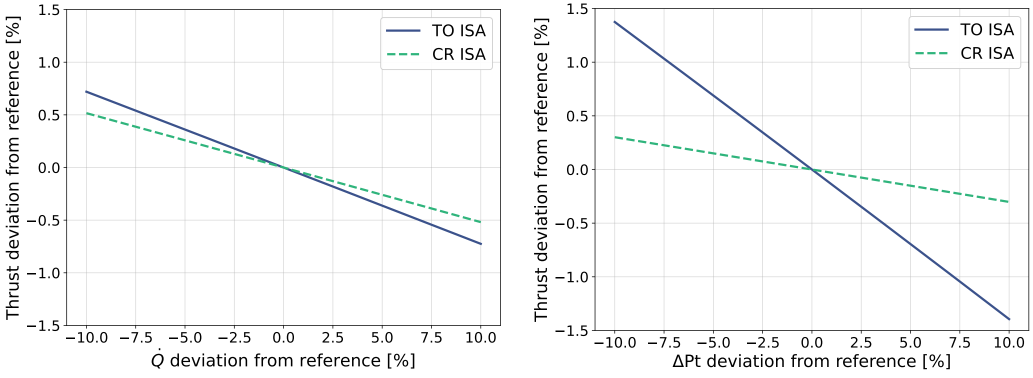

(a) Effect of HX heat duty $\dot{Q}$ variation on nozzle thrust for constant P_t and $\dot{m}_c$.

(b) Effect of HX total pressure loss ΔP_t variation on nozzle thrust for constant T_t and $\dot{m}_c$.

Figure 3.26: Sensitivity of nozzle thrust to performance deviations of the PMM heat exchanger model to assess system-level impact of deviations in Table 3.15. Evaluated using the nozzle model in Subsection 3.2.5.

It should be emphasized that this sensitivity analysis is indicative only, as the simplified approach does not capture the coupled, nonlinear interactions between heat transfer, pressure drop, and thrust. For instance, when the condenser heat duty is overpredicted, the required mass flow decreases to meet the thermal load, which in turn reduces pressure drop while also directly affecting thrust through the lower mass flow rate. Conversely, an increased heat duty at constant mass flow would generally cause higher pressure drop due to lower air density and higher flow velocities, leading to greater frictional losses. These coupled effects are not captured in the present decoupled sensitivity study, which varies heat duty and pressure drop independently around the reference condition.

Nevertheless, this analysis demonstrates that achieving the PMM accuracy levels shown in Table 3.15 is essential for reliable system-level performance predictions, as deviations propagate significantly to net drag and equivalent battery mass.

Physical Explanation of Condenser-Radiator Heat Transfer Accuracy Difference The verification results in Table 3.15 show markedly different heat transfer predictive accuracy between the condenser and radiator: the condenser demonstrates good agreement (MAPE <1%), whereas the radiator systematically overpredicts heat transfer by 2–6%. This occurs despite both Nusselt correlations having calibration errors below 0.1% (Figure 3.23). This discrepancy can be attributed to fundamental differences in how air-side temperature variation is modeled.

For cross-flow heat exchangers, *HeXacode* uses a single air control volume with a linear temperature distribution between inlet and outlet. CFD explicitly resolves the nonlinear spatial temperature field. For flows with nonlinear temperature rise, the spatial integral of locally evaluated heat transfer coefficients does not equal the bulk-evaluated coefficient multiplied by mean temperature difference. This effect is amplified by temperature-dependent transport properties ($k(T)$, $\mu(T)$, $\Pr(T)$), which are evaluated locally in CFD but at bulk conditions in *HeXacode*, resulting in higher predicted heat transfer in CFD.

This modeling difference affects the radiator more significantly than the condenser. For the condenser, the majority of heat duty occurs during the condensation region where the hot-side temperature is isothermal due to phase change, resulting in a relatively uniform wall temperature profile for the largest portion of heat transfer. The driving temperature difference $\Delta T = T_{\text{wall}} - T_{\text{air}}$ therefore varies primarily due to air heating, creating relatively limited spatial variation that *HeXacode*'s single air cell can adequately capture. For the radiator, both wall temperature (varying along the hot-side flow due to subcooling) and air temperature (varying along the air-side flow) change significantly, resulting in greater spatial variation in the driving temperature difference. This increased nonlinearity in the ΔT field is not adequately captured by *HeXacode*'s single control volume approach, while CFD resolves the in-plane nonlinear air temperature field, leading to the observed overprediction.

Importantly, the CFD predicting higher heat transfer does not indicate PMM inaccuracy, but rather reflects the combined limitations of *HeXacode*'s single air-side control volume approach and the current single-zone PMM implementation in capturing spatial temperature variation for cross-flow configurations. The 2–6% radiator overprediction is deemed acceptable for system-level analysis. A multi-porous-zone approach with vertical tubes allowing spatially varying wall temperatures could improve accuracy, but given the acceptable current agreement and practical constraints (increased complexity, potential buoyancy effects in the condenser), this methodological extension is not pursued in this work but is recommended for future work.

Verification at Off-Design Conditions with Wall Temperature Correlations The previous verification demonstrated that the momentum and energy source terms accurately reproduce *HeXacode* results when operating at or near the design point with a known constant wall temperature. This section verifies the wall temperature correlations developed in Equation 3.45 and Equation 3.46, which enable the PMM to adapt to off-design conditions where the wall temperature varies with operating conditions. The verification is performed by comparing *HeXacode* rating results against CFD PMM predictions across a sweep of mass flow rates at the CR ISA operating point. For the radiator, an additional sweep of inlet temperatures is performed to verify the bivariate correlation.

Condenser: Univariate Wall Temperature Correlation Figure 3.27 shows the verification of the univariate wall temperature correlation for the condenser. Near the design point for CR ISA (corresponding to $\dot{m}_c = 1.46$ kg/s and $T_{\text{wall}} = 302.2$ K), both the constant wall temperature approach and the univariate correlation in Equation 3.45 provide good agreement with *HeXacode*. However, as visualized in Figure 3.27a, the wall temperature decreases significantly at higher mass flow rates due to increased subcooling in the condenser. This variation results in substantial deviations in heat transfer predictions when using a constant wall temperature, as shown in Figure 3.27b. The univariate correlation successfully captures this variation, maintaining good agreement with *HeXacode* across the entire mass flow range.

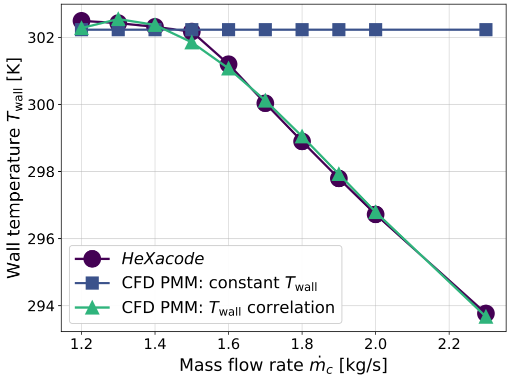

(a) Wall temperature T_{wall} (MAE= 0.14 K, Max. dev.= 0.32 K)

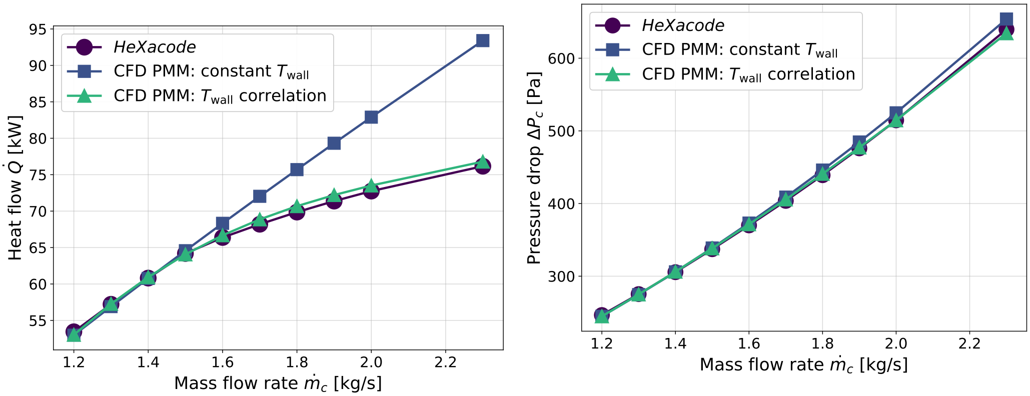

(b) Heat duty $\dot{Q}$ (MAPE= 0.69%, Max. dev.= 1.17%).

(c) Condenser pressure drop ΔP_c (MAPE= 0.46%, Max. dev.= 0.83%).

Figure 3.27: Verification of PMM baseline condenser at CR ISA with univariate wall temperature correlation: $T_{\text{wall}} = \sum_{i=0}^{n} c_i \, \dot{m}_c^i$.

The pressure drop results in Figure 3.27c show good agreement for both approaches. The pressure drop is indirectly coupled to heat transfer through two mechanisms. First, temperature-dependent density and viscosity appear explicitly in the momentum source term (Equation 3.41). Second, higher heat transfer increases air temperature, reducing air density and thereby increasing velocity for a given mass flow rate (via continuity), which in turn increases pressure drop through both viscous and inertial terms. However, this coupling is relatively weak. Therefore, even significant heat transfer deviations at off-design conditions have only minor influence on pressure drop predictions. If one is solely interested in pressure drop, the wall temperature variation can be neglected.

Note that Figure D.1j, Figure D.2j and Figure D.5j in Appendix D further verify this methodology for condensers inside the ram air duct across different operating points and different inclination angles.

Radiator: Bivariate Wall Temperature Correlation Figure 3.28 shows the verification of the bivariate wall temperature correlation for the radiator given by Equation 3.46. The single bivariate correlation successfully captures the simultaneous variations in both mass flow rate and inlet temperature. The wall temperature is predicted with good accuracy, demonstrating that the correlation successfully adapts to varying inlet conditions.

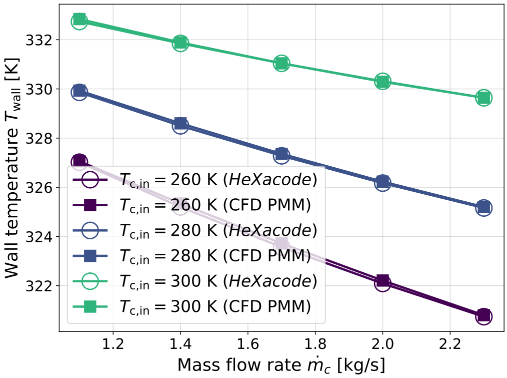

(a) Wall temperature T_{wall} (MAE= 0.07 K, Max. dev.= 0.15 K)

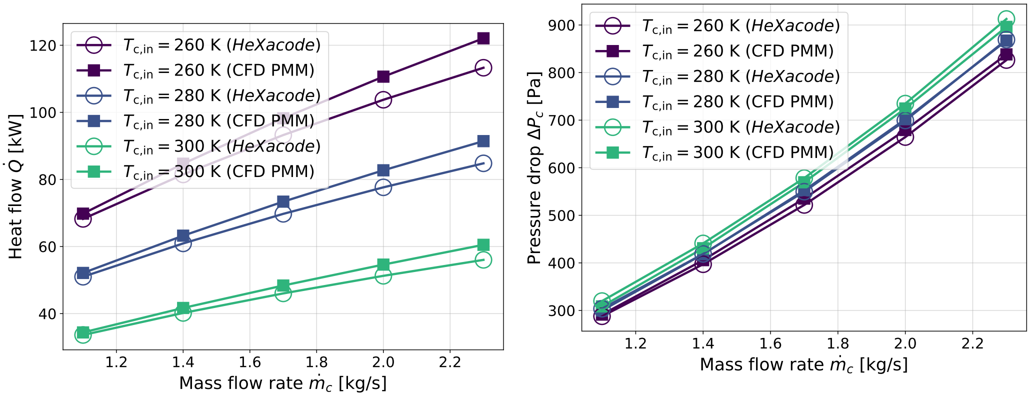

(b) Heat flow $\dot{Q}$ (MAPE= 4.81%, Max. dev.= 8.01%)

(c) Radiator pressure drop ΔP_c (MAPE= 1.49%, Max. dev.= 3.51%)

Figure 3.28: Verification of PMM baseline radiator at CR ISA with bivariate wall temperature correlation: $T_{\text{wall}} = t_0 + t_1 \dot{m}_c + t_2 \dot{m}_c^2 + t_3 T_{\text{c,in}} + t_4 T_{\text{c,in}}^2 + t_5 \dot{m}_c T_{\text{c,in}}$.

Similar to the constant wall temperature verification in the previous section, the radiator shows consistent overprediction of heat transfer of approximately 5%, as shown in Figure 3.28b. *This overprediction persists across the range of operating conditions, confirming*

that it is a fundamental modeling difference rather than a calibration error. The pressure drop agreement shown in Figure 3.28c remains good. Note that Figure D.1l, Figure D.2l and Figure D.5l in Appendix D further verify this methodology for radiators inside the ram air duct across different operating points and different inclination angles.
The ability of the bivariate correlation to capture variations in both mass flow rate and inlet temperature is essential for modeling heat exchangers in series, where the condenser outlet conditions directly determine the radiator inlet conditions. This verification demonstrates that the proposed correlation approach enables the PMM to adapt to off-design conditions that deviate from the calibration point.

Conclusions The porous media model methodology has been verified across a range of operating conditions for both constant wall temperature and variable wall temperature correlation approaches. The key findings are:

- **Source term accuracy:** The momentum and energy source terms accurately reproduce *HeXacode* predictions for both heat transfer and pressure drop. Larger deviations are observed for heat exchangers with shorter lengths and lower porosities, where entrance and exit effects become more significant. The condenser shows good agreement (MAPE <1%), while the radiator exhibits systematic overprediction in terms of heat transfer of approximately 5% due to fundamental differences in how air-side temperature fields are resolved between *HeXacode*'s single-cell model and CFD's spatial discretization.

- **Constant wall temperature approach:** A constant wall temperature extracted from *HeXacode* provides acceptable accuracy when operating at or near the design point. However, for such cases, prescribing a constant volumetric heat source term $\dot{Q}/V$ would be equally accurate and simpler to implement. The constant wall temperature approach fails to accurately predict heat transfer at off-design conditions where wall temperature varies significantly with operating conditions, though pressure drop predictions remain reasonably accurate.

- **Wall temperature correlations:** The univariate correlation for the condenser (as a function of mass flow rate) and the bivariate correlation for the radiator (as a function of mass flow rate and inlet temperature) successfully enable the PMM to adapt to off-design conditions. The correlations predict wall temperature with high accuracy and maintain good agreement in heat transfer and pressure drop predictions across a wide range of operating conditions. While lookup tables could provide similar or better accuracy, the polynomial correlation approach offers practical advantages in *Fluent*, as correlations can be directly specified without requiring custom User Defined Function (UDF) compilation for each operating point and heat exchanger design, providing greater flexibility when switching between configurations.

The verified PMM methodology provides a computationally efficient approach to model heat exchanger performance in CFD while maintaining acceptable accuracy for system-level performance assessment. This methodology is applied to simulate the condenser-radiator series configuration within the ram air duct geometry in Section 4.2.

4

RESULTS AND DISCUSSION

This chapter presents the results of this thesis and is structured as follows. First, Section 4.1 presents the heat exchanger optimization results from the multi-point multi-objective optimization. Subsequently, Section 4.2 discusses the CFD results, including ROM-CFD comparisons and quantification of heat exchanger inclination-induced pressure losses.

4.1. HEAT EXCHANGER OPTIMIZATION

4.1.1. INTRODUCTION

This section presents the results of the multi-objective, multi-point optimization of flat-tube microchannel condensers and radiators for the E9X thermal management system. Following the methodology in Section 3.3, a sequential coupled optimization is performed: the condenser is optimized first, and its outlet conditions define the inlet state for the radiator. Two system-level objectives are minimized: total heat exchanger mass and weighted air-side pressure drop across multiple operating points. Note that optimized geometries from this section are later analyzed using CFD in Section 4.2 to assess inclination-induced losses not captured by the reduced-order model. Detailed geometry and performance results from all optimizations are provided in Appendix A.

This section is organized as follows. Subsection 4.1.2 analyzes the coupled condenser–radiator system, examining the impact of fin topology (Offset Strip Fins versus Louvered Fins) and inclination angle (0° to 60°). Subsection 4.1.3 then presents independent optimization of each heat exchanger to isolate design trends and quantify how upstream condenser conditions constrain radiator performance. Finally, Subsection 4.1.4 compares two system architectures: series configuration (both heat exchangers per duct) versus separate-duct configuration (independent ducts for each component).

4.1.2. COUPLED OPTIMIZATION

This subsection discusses the results of the coupled condenser–radiator optimization in a series layout.

FIN TOPOLOGY

This section compares the performance of two air-side fin topologies for flat-tube microchannel heat exchangers: Offset Strip Fins (OSF) and Louvered Fins (LF). Both fin types enhance heat transfer through repeated boundary-layer disruption, but they differ in their heat-transfer and pressure-drop characteristics, as captured by the correlations listed in Table 3.8. To isolate the effect of fin geometry, the comparison is performed at 0° inclination, ensuring identical inlet conditions and frontal area.

The optimization results in Figure 4.1a show that OSF consistently outperform LF across the entire Pareto front. Because all designs are constrained to meet the same heat-duty requirement, the only remaining difference is the aerodynamic penalty associated with achieving that heat transfer. For the same combined condenser–radiator mass, OSF yield substantially lower weighted air-side pressure drop than LF, primarily due to lower average friction factors at comparable inlet Reynolds numbers [37].

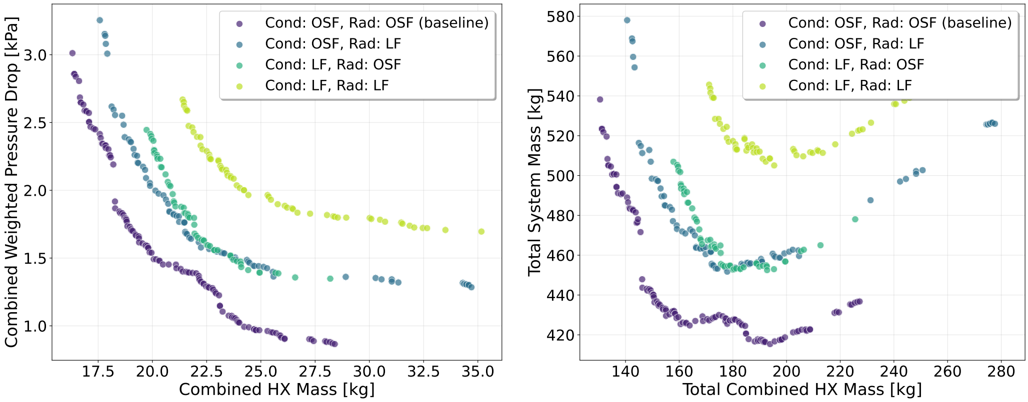

(a) Weighted pressure drop versus combined HX mass (sum of condenser and radiator).

(b) Total equivalent system mass versus total combined HX mass (eight ram air ducts).

Figure 4.1: Comparison of heat-exchanger fin topologies: Offset Strip Fins (OSF) and Louvered Fins (LF).

The literature supports this observation. Baglieri [82] concluded, using the same underlying correlations, that the optimal fin topology is problem-dependent and dictated by objectives and constraints, with no universally superior fin type. Similarly, Beltrame et al. [37] found that OSF outperform LF in terms of pressure drop at equal mass for an airborne ORC waste-heat recovery system application, while LF can yield lighter designs if higher air-side pressure drops are acceptable. These studies highlight that the preferred fin topology is determined by boundary and operating conditions, as well as allowable pressure loss.

The system-level implications become evident when the equivalent battery mass due to ram air drag is included. Figure 4.1b shows that, when scaled to all eight ram air ducts of the E9X, OSF reduce the total equivalent system mass by approximately 100 kg. Using the modified Breguet range equation in Equation 3.37, this corresponds to a range increase of roughly 3 km (+0.4%). Although modest, this benefit arises solely from the air-side fin topology and demonstrates that fin selection has a non-negligible system-level impact.

Finally, it is important to recognize that both OSF and LF predictions rely on the semi-empirical correlations listed in Table 3.8. While widely used, these correlations originate from older experiments and may not perfectly represent modern fin designs. Absolute performance values should therefore be interpreted with caution, and the relative superiority of OSF over LF observed here is specific to these correlations and the boundary conditions of this study.

Nevertheless, the present analysis clearly demonstrates that optimizing fin topology can yield significant system-level performance gains. Under the boundary conditions and thermal constraints of this study, OSF offer a markedly better balance between heat transfer enhancement and pressure loss than LF. For this reason, OSF are adopted as the air-side fin topology for all subsequent analyses.

HEAT EXCHANGER INCLINATION

Sequential coupled optimizations of the condenser and radiator were performed for the inclination angles listed in Table 3.5, resulting in different effective heat-exchanger heights h_{hx}. Each optimization corresponds to a full condenser–radiator system with inclination $\alpha = 0°, 15°, 30°, 45°, 60°$. The resulting Pareto fronts in Figure 4.2 show how the trade-off between combined HX mass and weighted pressure drop evolves with inclination, and how this translates to total equivalent system mass.

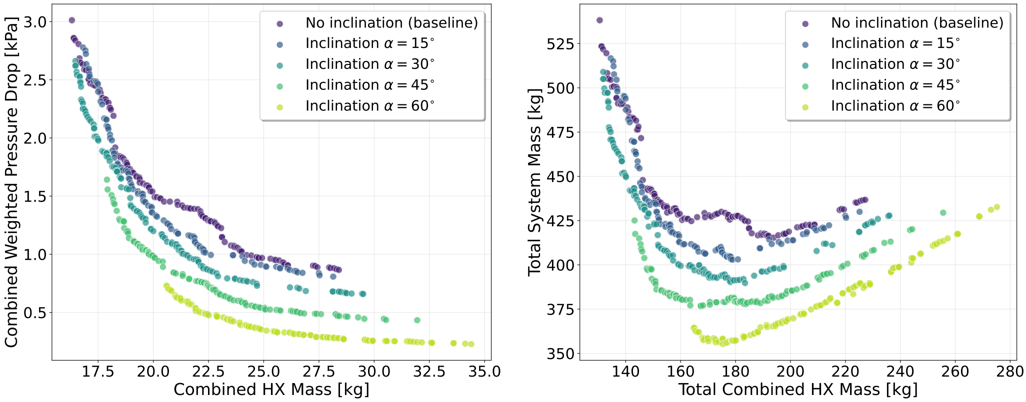

(a) Weighted pressure drop versus combined HX mass (sum of condenser and radiator).

(b) Total equivalent system mass versus total HX mass (eight ducts).

Figure 4.2: Effect of heat-exchanger inclination on coupled condenser–radiator optimization.

Figure 4.2 shows that increasing inclination leads to designs with consistently lower weighted pressure drop and lower total equivalent system mass. The observed trend can be explained from first principles. Inclining the heat exchanger increases its effective frontal area according to:

$$A_{\mathrm{frontal}} = \frac{A}{\cos(\alpha)} \tag{4.1}$$

which reduces the inlet velocity for a given mass flow. Because the upstream intake and diffuser boundary conditions (static pressure, temperature, and mass flow) are identical across inclination angles, the inlet velocity follows from combining mass conservation with the equation of state:

$$v_{\mathrm{in,HX}} = \frac{\dot{m}_c}{\rho A_{\mathrm{frontal}}} \approx \frac{\dot{m}_c R T_{\mathrm{c,in}}}{P_{\mathrm{c,in}} A_{\mathrm{frontal}}} \tag{4.2}$$

For the same mass flow, an increase in A_{frontal} lowers the inlet velocity. Since air-side pressure losses scale approximately with v^2, the pressure drop decreases significantly.

The nonlinear $1/\cos(\alpha)$ dependence in Equation 4.1 magnifies this effect at higher inclination angles. Figure 4.3 shows this explicitly: the condenser inlet velocity at CR ISA drops significantly as inclination increases, enabling the optimizer to select denser fins at acceptable pressure drop.

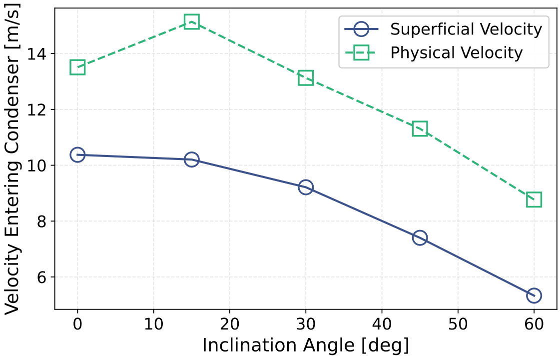

Figure 4.3: Velocity entering the condenser for optimum designs at CR ISA. Increasing inclination reduces inlet velocity, enabling denser fin configurations.

At first sight, these results might suggest that increasing the inclination angle indefinitely is beneficial. However, this neglects a crucial aerodynamic mechanism not captured by the reduced-order model: pressure losses induced by flow turning and incidence onto an inclined core. Classical experimental data by Nichols [33] demonstrate that beyond approximately 70°, inclination and resulting flow separation cause exponential increases in total pressure loss. This effect is visualized in Figure 4.23b.

These turning and incidence losses are not included in the present reduced-order model and therefore not included in the optimization results in this section. This effect is partially assessed with CFD in Section 4.2, which shows that no fundamental pressure loss penalty emerges up to 60°. Consequently, the trends observed in this section, namely decreasing weighted pressure drop and decreasing total equivalent system mass with increasing inclination, remain valid.

Selecting from Figure 4.2b the design that minimizes total equivalent system mass for each inclination yields the results in Table 4.1. Notably, the structural HX mass does not decrease with inclination angle, for example the combined HX mass at 60° is higher than at 45°. However, the aerodynamic penalty (and therefore the equivalent battery mass) decreases strongly with increasing inclination, so the total equivalent system mass still reaches its minimum at 60°.

Table 4.1: System-level performance metrics for optimum configurations at different inclination angles.

Parameter	**0°**	**15°**	**30°**	**45°**	**60°**
Combined HX mass [kg]	193.9	178.8	183.4	167.4	175.4
Combined weighted pressure drop [kPa]	0.993	1.015	0.811	0.843	0.513
Equivalent battery mass [kg]	221.5	224.1	206.3	209.5	179.9
Total equivalent system mass [kg]	**415.4**	**402.9**	**389.8**	**376.9**	**355.3**

The heat exchanger geometry characteristics in Table 4.2 show several consistent trends. First, the porosity generally decreases with inclination angle. Lower inlet velocity allows the optimizer to choose denser fins without incurring excessive pressure losses. Moreover, the HX core length decreases with inclination angle. Higher inclination increases the effective frontal area, which allows the heat duty to be met with a shorter core length. Combined, the reduction in porosity and the shortening of the core result in progressively more compact heat exchangers at higher inclination angles. Compactness values β_{hx} lie in the range 700–800 m^{-1}, confirming that all designs fall within the definition of compact heat exchangers [28].

Table 4.2: Optimized condenser and radiator characteristics for different inclination angles.

Parameter	0°		15°		30°		45°		60°	
	Cond.	Rad.	Cond.	Rad.	Cond.	Rad.	Cond.	Rad.	Cond.	Rad.
Mass [kg]	12.54	11.70	10.75	11.61	11.34	11.59	9.99	10.93	10.43	11.49
Weighted pressure drop [Pa]	410	583	468	548	358	453	410	433	255	259
Porosity ϵ [–]	0.768	0.751	0.674	0.722	0.701	0.732	0.655	0.669	0.608	0.678
Heat transfer area compactness β_{hx} [m^{-1}]	653	754	802	778	769	791	785	786	808	804
w_{hx} [mm]	560	560	560	560	560	560	560	560	560	560
h_{hx} [mm]	400.0	400.0	414.2	414.2	461.9	461.9	565.7	565.7	800.0	800.0
l_{hx} [mm]	217.4	187.4	136.0	164.0	138.4	148.5	98.6	112.2	67.4	83.6

THERMAL ANALYSIS FOR 60° INCLINATION

This subsection examines the thermal performance for the optimum configuration with 60° inclination, as identified in Table 4.1. Table 4.3 summarizes the resulting condenser and radiator performance across all operating points. At each operating point, the condenser meets its heat duty requirement exactly, while the radiator exceeds its required heat duty under ISA conditions by up to 30%. This oversizing leads to higher radiator pressure drops at these operating points, as either a lower mass flow or reduced fin density would be sufficient under those conditions.

This behavior results from the series architecture and optimization setup: at each operating point, the ram-air mass flow is determined by matching the condenser's heat duty constraint. This fixed mass flow is then forced through to the radiator, which causes it to overperform except at its own design point (TO ISA+35).

Table 4.3: Coupled condenser–radiator performance for the 60° optimum configuration.

OP	$\dot{m}_c$ [kg/s]	Q_{cond} [kW]	Q_{rad} [kW]	$\Delta P_{c,\mathrm{cond}}$ [kPa]	$\Delta P_{c,\mathrm{rad}}$ [kPa]	D_{int} [N]	D_{ext} [N]	T_{noz} [N]	D_{net} [N]
TO ISA	2.228	45.60 (0.0%)	100.35 (+30.3%)	0.184	0.182	76.6	83.3	138.6	17.6
TOC ISA	1.667	71.10 (0.0%)	77.30 (+20.8%)	0.232	0.246	85.4	248.4	294.0	22.1
CR ISA	1.502	62.90 (0.0%)	46.98 (+20.5%)	0.195	0.201	69.1	237.5	265.7	30.5
TOD ISA	1.595	55.00 (0.0%)	56.55 (+2.8%)	0.211	0.216	78.1	244.0	278.1	31.1
TO ISA+35	3.900	58.20 (0.0%)	81.00 (0.0%)	0.566	0.504	266.5	6.0	169.1	103.4
TOC ISA+35	2.990	82.00 (0.0%)	71.25 (+6.0%)	0.717	0.692	327.7	248.1	506.4	69.4
CR ISA+35	2.682	73.20 (0.0%)	42.34 (+3.1%)	0.592	0.559	260.6	270.0	462.2	68.4
TOD ISA+35	2.435	64.60 (0.0%)	43.02 (+4.9%)	0.501	0.473	213.2	271.9	428.7	56.4

The temperature–heat flow rate (T–$\dot{Q}$) diagrams in Figure 4.4 illustrate the thermal interaction within the series arrangement. Incoming ram air first absorbs heat from the refrigerant in the condenser, cooling the battery, followed by additional heating from the coolant in the downstream radiator, cooling the EPU. This configuration leverages the fact that the coolant operates at a significantly higher temperature than the refrigerant, allowing the same ram air stream to act as a common thermal sink for both heat exchangers. The series setup inherently leads to thermal coupling between the components: the ram air outlet temperature of the condenser becomes the inlet temperature for the radiator, and the mass flow required to meet the condenser's heat duty sets the conditions under which the radiator must operate. As a result, the radiator tends to overperform at operating points other than its design point, as seen in Table 4.3.

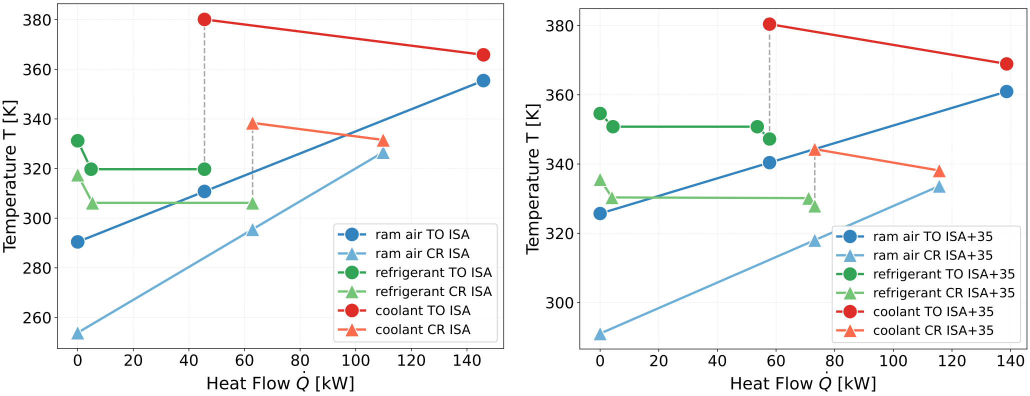

(a) ISA conditions.

(b) ISA+35 conditions.

Figure 4.4: Temperature–heat flow rate (T–$\dot{Q}$) diagrams for multiple operating points for the ram air duct with condenser and radiator in series.

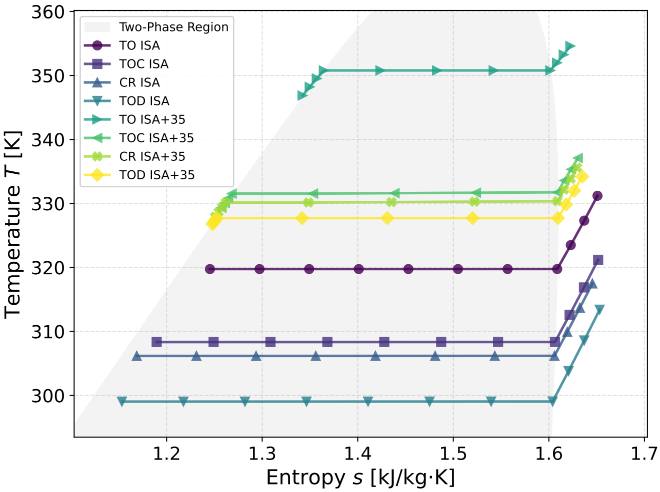

Figure 4.5: T–s diagram of the condenser for the 60° optimum configuration across all operating points.

The temperature–entropy diagram of the condenser, shown in Figure 4.5, provides further insight into the refrigerant-side behavior. Under ISA conditions, the refrigerant undergoes desuperheating and partial condensation, exiting the condenser with nonzero vapor quality. Under ISA+35 conditions, full condensation is achieved along with some degree of subcooling. While full condensation is generally preferred for improved heat transfer efficiency, the presence of two-phase refrigerant at the condenser outlet under ISA conditions is acceptable in this system architecture, as the downstream expansion valve, shown in Figure 2.5, is designed to accommodate two-phase flow.

These results highlight a key characteristic of the coupled series architecture: both temperature and mass flow are shared between components, creating tight interdependency. The optimization successfully accounts for this coupling, yielding condenser–radiator designs and mass flows that satisfy the thermal performance requirements across all operating points.

4.1.3. Standalone Optimization

This subsection presents the results of the standalone condenser and radiator optimizations, in which each heat exchanger is analyzed independently within the ram air duct. This decoupled setup allows for detailed investigation of geometry and performance trends and enables assessment of the influence of upstream condenser conditions on downstream radiator behavior. Detailed geometric and performance data for the standalone optimal configurations are provided in Appendix A.

Standalone Condenser

The condenser is the upstream component in the series configuration and thus forms the basis for the radiator optimization discussed in Subsection 4.1.2. Its Pareto front is already available from the coupled optimization as part of Figure 4.2. In this subsection, the condenser results are analyzed in isolation to identify condenser-specific performance and design trends. Similar to the conclusions for the coupled optimization regarding inclination, Figure 4.6 shows that increasing the heat exchanger inclination systematically reduces the weighted air-side pressure drop and overall equivalent system mass.

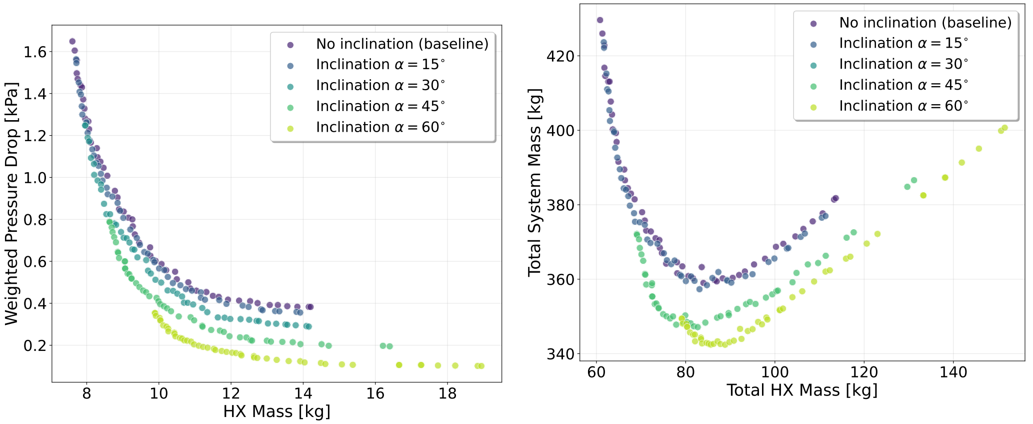

(a) Weighted pressure drop versus condenser mass.

(b) Total equivalent system mass versus condenser mass (eight ducts).

Figure 4.6: Standalone condenser optimization results.

The associated geometry trends are shown in Figure 4.7. At larger inclination angles, the optimizer can reduce porosity and increase surface area compactness. The lower inlet velocity alleviates pressure drop, enabling denser fin structures that improve heat transfer per unit volume.

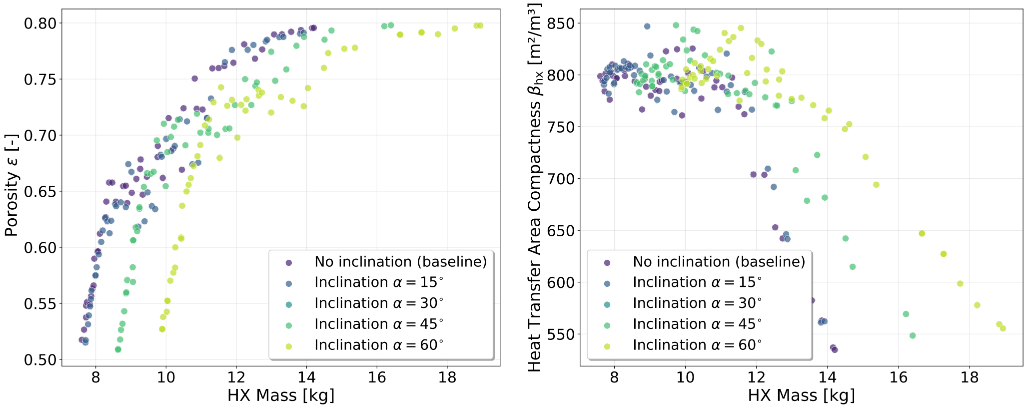

(a) Porosity ϵ

(b) Heat-transfer surface-area compactness β_{hx}

Figure 4.7: Geometric characteristics from the standalone condenser optimization.

Figure 4.8 analyzes pressure drop and net drag across all operating points for the optimal standalone condenser designs at $\alpha = 60°$. The weighted pressure drop in Figure 4.8a shows a dominant contribution from ISA pressure drops due to the weight allocation listed in Table 3.11. The Pareto fronts across different operating points exhibit similar trends, with ISA+35 conditions showing the largest absolute variations due to higher ram air mass flows. As seen in Figure 4.8a, the shape of the pressure drop curves remains largely consistent across operating points. This suggests that optimizing for the most critical condition, typically TO ISA+35, also yields near-optimal performance for other operating points. Consequently, the number of operating points included in the optimization could potentially be reduced without significantly compromising accuracy, thereby improving computational efficiency.

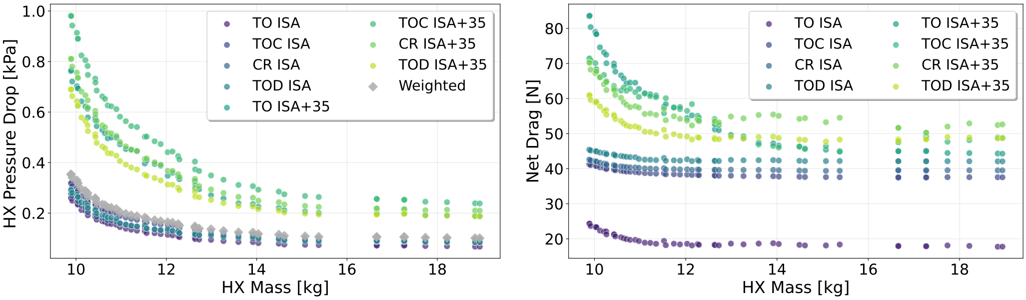

(a) HX pressure drop

(b) Net drag

Figure 4.8: Pressure drop and net drag vs condenser mass across all operating points from the standalone condenser optimization with $\alpha = 60°$.

The net drag trends in Figure 4.8b largely follow those of the pressure drop in Figure 4.8a but reveal important distinctions. Notably, the TO ISA+35 curve exhibits a noticeable drop in net drag at higher HX masses, falling below the curves of other operating points. This behavior contrasts with Figure 4.8a, where all operating points remain distinctly separated. The discrepancy highlights that net drag accounts for additional system-level effects, including external drag. As a result, optimizing solely for pressure drop may overlook these effects, potentially leading to slightly different Pareto-optimal designs when net drag is used as the objective.

The thermal behavior of the condenser in standalone mode is identical to that in the coupled configuration, shown in Figure 4.4 and Figure 4.5. However, the selected optimal design differs. Here, the condenser is chosen to minimize the standalone equivalent system mass without considering the radiator. In contrast, the coupled optimization minimizes the total equivalent system mass of both condenser and radiator.

Table 4.4 summarizes the performance across all operating points for the selected standalone optimum at 60°.

Table 4.4: Standalone condenser performance at 60° inclination (all operating points).

OP	$\dot{m}_c$ [kg/s]	Q_{cond} [kW]	ΔP_c [kPa]	D_{int} [N]	D_{ext} [N]	T_{noz} [N]	D_{net} [N]
TO ISA	2.126	45.60 (0.0%)	0.140	69.7	83.7	134.2	19.2
TOC ISA	1.618	71.10 (0.0%)	0.183	80.4	245.4	286.9	38.8
CR ISA	1.460	62.90 (0.0%)	0.154	65.3	234.4	259.5	40.2
TOD ISA	1.483	55.00 (0.0%)	0.157	67.4	236.1	260.9	42.7
TO ISA+35	3.900	58.20 (0.0%)	0.461	266.5	6.0	210.5	62.0
TOC ISA+35	2.923	82.00 (0.0%)	0.568	312.2	255.8	507.7	60.3
CR ISA+35	2.622	73.20 (0.0%)	0.469	248.7	270.7	462.6	56.8
TOD ISA+35	2.375	64.60 (0.0%)	0.394	202.5	271.9	423.2	51.2

STANDALONE RADIATOR

In the coupled series configuration, the radiator geometry is influenced by the upstream condenser outlet conditions, the ram air mass flow required to satisfy the condenser heat duty, and the overall system-level trade-off that includes both heat exchangers. To isolate radiator-specific behavior and quantify the impact of the condenser–radiator interaction, a separate standalone radiator optimization was performed at the same inclination angle of 60°. This enables a direct comparison between (i) a radiator optimized independently (standalone), and (ii) a radiator constrained by upstream condenser performance in the coupled configuration.

The Pareto front from the standalone radiator optimization is compared to the coupled radiator results in Figure 4.9. In the coupled setup, the radiator receives preheated air from the condenser, while in the standalone case, it directly receives ambient ram air. The substantially lower inlet air temperature in the standalone case increases the available temperature difference across the radiator, enhancing its thermal driving potential. As a result, the standalone radiator can achieve the same heat rejection with a smaller mass flow rate and less surface area, leading to significant lower pressure drop (Figure 4.9a), and shorter cores, higher porosity, and lower surface area compactness, clearly visible in Figure 4.9b–Figure 4.9d.

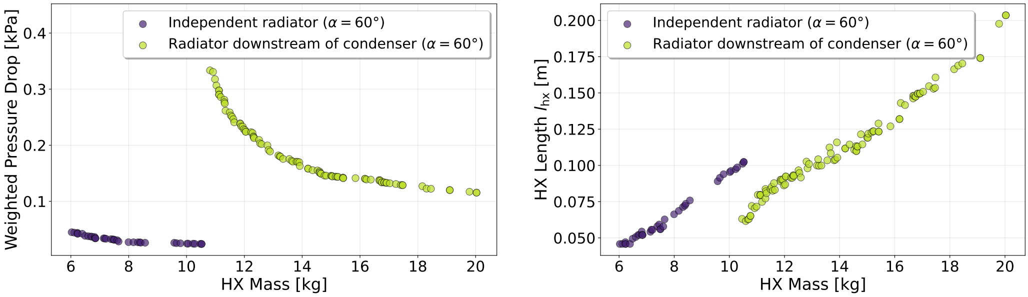

(a) Mass versus weighted pressure drop.

(b) Mass versus heat exchanger core length.

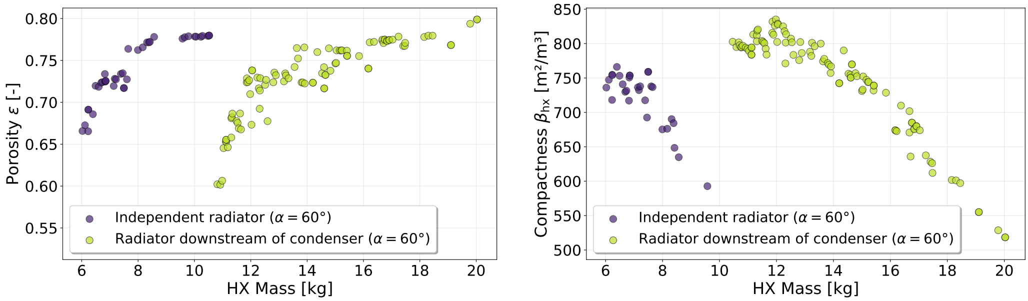

(c) Mass versus core porosity.

(d) Mass versus surface area compactness.

Figure 4.9: Comparison of radiator optimization results for standalone and condenser-constrained configurations at $\alpha = 60°$.

The performance of the optimal standalone radiator is presented in Table 4.5. Unlike the coupled radiator, which overperforms at off-design points due to fixed mass flow from the condenser (Table 4.3), the standalone radiator meets its heat duty exactly at all operating points. This is achieved through optimized mass flow selection for each condition. The pressure drop in the standalone case is significantly lower than in the coupled configuration. The standalone configuration's freedom to select its own ram air mass flow allows the optimizer to choose lower mass flows, which in turn reduces pressure losses. Compared to the coupled results in Table 4.3, the standalone radiator consistently achieves lower mass flows and pressure drops.

Table 4.5: Standalone radiator performance at 60° inclination (all operating points).

OP	$\dot{m}_c$ [kg/s]	Q_{rad} [kW]	ΔP_c [kPa]	D_{int} [N]	D_{ext} [N]	T_{noz} [N]	D_{net} [N]
TO ISA	1.538	77.00 (0.0%)	0.052	36.4	80.4	104.9	11.9
TOC ISA	0.900	64.00 (0.0%)	0.047	24.7	174.6	169.1	30.1
CR ISA	0.630	39.00 (0.0%)	0.028	12.1	132.4	117.0	27.4
TOD ISA	0.638	39.00 (0.0%)	0.028	12.4	133.7	118.3	27.8
TO ISA+35	3.900	81.00 (0.0%)	0.279	266.5	6.0	224.4	48.1
TOC ISA+35	1.949	67.20 (0.0%)	0.167	135.0	266.0	359.3	41.6
CR ISA+35	1.311	41.00 (0.0%)	0.086	60.4	229.9	243.9	46.3
TOD ISA+35	1.262	41.00 (0.0%)	0.081	55.9	225.4	235.4	45.9

The thermal behavior of the standalone radiator is shown in the T–$\dot{Q}$ diagrams in Figure 4.10. Compared to the coupled case in Figure 4.4, the ram air stream in the standalone configuration exhibits a significantly larger temperature rise, despite the radiator having the same or lower heat duty than in the coupled case. This effect is primarily due to the lower mass flows (Table 4.5) for a similar heat load. Note that the coolant-side (hot side) temperature profiles remain nearly identical across both configurations, as the hot-side inlet conditions are fixed.

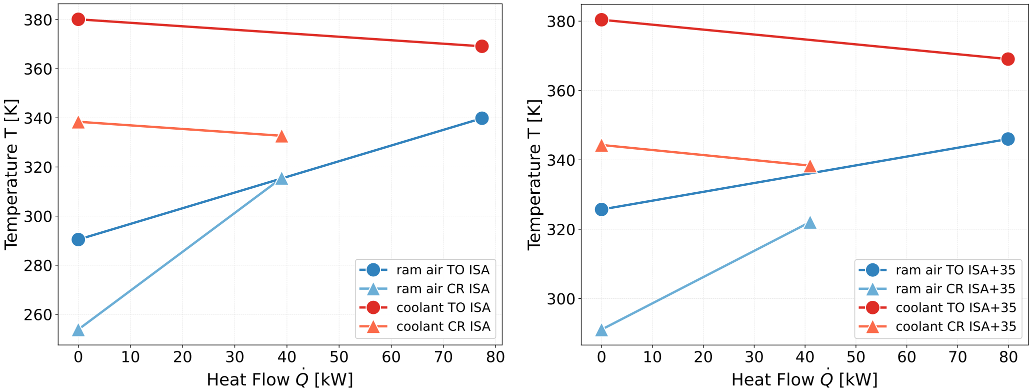

(a) ISA conditions.

(b) ISA+35 conditions.

Figure 4.10: T–$\dot{Q}$ diagrams for the standalone radiator in the ram air duct. Compared to the coupled configuration, the standalone radiator operates with a colder air inlet and therefore achieves a larger air-side temperature rise.

4.1.4. ARCHITECTURE COMPARISON: SERIES VS. SEPARATE DUCTS

The preceding sections analyzed the condenser and radiator both in isolation and in the coupled series configuration. This subsection compares two complete thermal management system (TMS) architectures, consistent with the study in [14]:

1. **Series architecture**: 8 ram air ducts, each containing a condenser followed by a radiator in series.
2. **Separate-duct architecture**: 16 ducts in total: eight dedicated condenser ducts and eight dedicated radiator ducts, with each heat exchanger optimized independently.

To enable a system-level comparison, the internal drag, external drag, and nozzle thrust are listed in Table 4.6, along with the resulting net drag defined in Equation 3.1 for each operating point. The series configuration data comes from Table 4.3, while for the separate-duct configuration, the net drag is obtained by summing the standalone condenser and standalone radiator values from Table 4.4 and Table 4.5.

Table 4.6 shows a clear trade-off between the two architectures. The series configuration benefits from using only eight ducts, which reduces the total frontal area. As a result, external drag is significantly lower, by nearly 50% under ISA conditions, and the equivalent battery mass is correspondingly reduced. However, the radiator in the series setup receives preheated air from the upstream condenser, which reduces the available temperature difference. To meet the same heat load, the radiator must compensate with a larger heat transfer surface area, resulting in heavier geometry inducing higher pressure losses.

In contrast, the separate-duct architecture supplies each heat exchanger with ambient ram air and allows full freedom in mass flow selection. This results in shorter and lighter individual components with lower pressure drop over the radiator, achieving a 22% reduction in total heat exchanger mass (175.4 kg vs. 137.6 kg). However, this benefit comes at the cost of doubling the number of intakes from 8 to 16, which substantially increases frontal area, external drag, and total intake pressure losses. Consequently, the equivalent battery mass increases dramatically, ultimately leading to significantly higher total equivalent system mass.

Quantitatively, the series architecture results in 213 kg less system mass compared to the separate-duct configuration, representing a 37% reduction (355.3 kg vs. 568.1 kg), despite having heavier heat exchangers.

Table 4.6: Architecture comparison at 60° inclination for eight ram air ducts. Series: 8 ducts with condenser–radiator in series. Separate: 8 condenser ducts + 8 radiator ducts.

OP	**Series**				**Separate**			
	D_{int} [N]	D_{ext} [N]	T_{noz} [N]	D_{net} [N]	D_{int} [N]	D_{ext} [N]	T_{noz} [N]	D_{net} [N]
TO ISA	612.8	666.4	1108.8	140.8	848.8	1312.8	1912.8	248.8
TOC ISA	683.2	1987.2	2352.0	176.8	840.8	3360.0	3648.0	551.2
CR ISA	552.8	1900.0	2125.6	244.0	619.2	2934.4	3012.0	540.8
TOD ISA	624.8	1952.0	2224.8	248.8	638.4	2958.4	3033.6	564.0
TO ISA+35	2132.0	48.0	1352.8	827.2	4264.0	96.0	3479.2	880.8
TOC ISA+35	2621.6	1984.8	4051.2	555.2	3577.6	4174.4	6936.0	815.2
CR ISA+35	2416.8	3991.2	4350.4	824.8	2472.8	4004.8	5652.0	824.8
TOD ISA+35	1705.6	2175.2	3429.6	451.2	2067.2	3978.4	5268.8	776.8
Total HX mass [kg]	**175.4**				**137.6**			
Equivalent battery mass [kg]	**179.9**				**430.5**			
Total eq. system mass [kg]	**355.3**				**568.1**			

It is important to note that these results are *indicative*. The intake geometry used in this analysis was optimized by Elysian for the series configuration and was not redesigned for the separate-duct layout. The resulting intake area, flow capacity, and pressure recovery are thus likely suboptimal for the separate-duct case. A fair comparison would require dedicated optimization of the intake geometry.

Furthermore, component masses beyond the heat exchangers themselves are not included in the current mass breakdown. Since the separate-duct configuration requires twice the number of ducts, including these additional components would further increase its mass penalty, making the present comparison conservative in favor of the separate-duct architecture.

Finally, only the series configuration will be further examined in the CFD study in Section 4.2. For each inclination angle, the optimal heat exchanger geometries listed in Table 4.2 will be used. These simulations will capture effects such as flow turning and potential separation, which are not included in the reduced-order model used in this section.

4.2. CFD AND ROM ANALYSIS

4.2.1. INTRODUCTION

This section evaluates the performance of optimized heat exchangers in the ram air duct using CFD simulations, following the methodology described in Section 3.4. For each inclination angle (0°, 15°, 30°, 45°, and 60°), the corresponding optimized geometries from Subsection 4.1.2 are analyzed with CFD. The geometric details are provided in Table 4.2 and Appendix A. The PMM methodology introduced in Subsection 3.4.5 is used throughout, with corresponding PMM coefficients listed in Appendix B.

The primary objectives are to assess ROM predictive capability and to quantify pressure losses due to heat exchanger inclination. The ROM-based optimization in Section 4.1 indicated that larger inclination angles improve system-level performance by reducing frontal velocity and therefore pressure losses. However, these results assumed no additional inclination-induced losses. Since experimental studies [33] show that inclination can introduce significant additional losses at high angles, the present CFD analysis quantifies these effects for the current geometry. While the ROM does not capture inclination losses, the CFD simulations partially resolve them (excluding incidence losses at the heat exchanger entrance).

This section is organized as follows. Subsection 4.2.2 determines ROM model coefficients directly from CFD results, allowing verification and correction of originally assumed values. Subsection 4.2.3 then compares ROM and CFD predictions for the baseline (0°) configuration to verify the ROM and establish a reference for inclined cases. Subsection 4.2.4 presents flow field visualizations illustrating key physical features across inclination angles. Subsection 4.2.5 quantifies inclination-induced pressure losses and develops a correction factor to capture these effects. Finally, Subsection 4.2.6 incorporates this correction factor into the ROM and evaluates system performance across all operating points for two diffuser pressure recovery coefficients.

4.2.2. ROM COEFFICIENT CALIBRATION USING CFD

The reduced-order model (ROM) of the ram-air duct, introduced in Section 3.2, relies on three model coefficients to characterize the diffuser and nozzle performance: the diffuser static pressure recovery coefficient C_p, the nozzle loss factor Y, and the nozzle discharge coefficient C_d.

During the heat exchanger optimization, fixed values for these coefficients were assumed. This section compares those assumptions with values derived from CFD simulations to verify their accuracy and adjust ROM inputs where necessary. The updated coefficients are used for ROM–CFD comparisons throughout this chapter.

BASELINE COEFFICIENT COMPARISON

Table 4.7 compares the ROM assumptions to CFD-derived coefficients for the baseline geometry (i.e., uninclined heat exchangers). The CFD analysis shows that the coefficients are largely insensitive to operating point, with low standard deviations across the simulated mass flow ranges. The nozzle loss factor Y is the only coefficient that exhibits noticeable dependence on mass flow rate.

The CFD results confirm that the assumed ROM values for Y and C_d are already close to the actual duct performance. The low magnitude of Y indicates that nozzle losses are relatively minor. For the diffuser, a conservative value of $C_p = 0.75$ was used during optimization to account for possible 3D effects and non-uniform inlet conditions from a upstream propeller, effects not captured in the present CFD model. Based solely on the internal flow geometry, the CFD results support a higher diffuser static pressure recovery of $C_p = 0.90$.

Table 4.7: Comparison of ROM assumptions and CFD-derived coefficients for the baseline geometry ($\alpha = 0°$).

Coefficient	**ROM Assumption**	**CFD (TO ISA)**	**CFD (CR ISA)**	**CFD-informed Value**
Mass flow range [kg/s]	–	[1.45, 2.87]	[1.27, 2.34]	–
C_p (Equation 3.9)	0.75	$0.9005 \pm 0.3\%$	$0.8998 \pm 0.3\%$	**0.900**
Y (Equation 3.14)	0.01	$0.0061 \pm 7.9\%$	$0.0060 \pm 3.8\%$	**0.006**
C_d (Equation 3.18)	0.988	$0.9872 \pm 0.1\%$	$0.9864 \pm 0.1\%$	**0.987**

EFFECTS OF INCLINATION ON ROM COEFFICIENTS

Table 4.8 presents CFD-derived ROM coefficients for the CR ISA condition across various inclination angles. Each case was evaluated over a similar mass flow sweep as in the baseline case. The diffuser region includes both the horizontal and inclined portions upstream of the condenser, while the nozzle region includes the flow downstream of the radiator. Consequently, the effects of inclination are, for now, incorporated into the coefficients C_p and Y.

Table 4.8: CFD-derived ROM coefficients for inclined heat exchanger configurations (CR ISA).

Coefficient	$\alpha = 0°$	$\alpha = 15°$	$\alpha = 30°$	$\alpha = 45°$	$\alpha = 60°$
Mass flow range [kg/s]	[1.27, 2.34]	[1.28, 2.25]	[1.28, 2.29]	[1.28, 2.26]	[1.30, 2.33]
C_p	$0.8998 \pm 0.3\%$	$0.8866 \pm 0.4\%$	$0.8805 \pm 0.4\%$	$0.8873 \pm 0.3\%$	$0.8698 \pm 0.5\%$
Y	$0.0060 \pm 3.8\%$	$0.0067 \pm 5.1\%$	$0.0071 \pm 3.2\%$	$0.0076 \pm 0.4\%$	$0.0078 \pm 1.7\%$
C_d	$0.9864 \pm 0.1\%$	$0.9890 \pm 0.1\%$	$0.9890 \pm 0.1\%$	$0.9891 \pm 0.1\%$	$0.9888 \pm 0.1\%$

With increasing inclination, the diffuser static pressure recovery C_p decreases slightly, while the nozzle loss factor Y increases. These trends are expected, as inclined geometries introduce flow turning and additional pressure losses. The discharge coefficient C_d remains essentially unchanged.

To isolate the effect of inclination in the following ROM–CFD comparisons, the baseline CFD-informed ROM coefficients from Table 4.7 will be used consistently for all inclination angles for the remainder of this section.

4.2.3. COMPARISON OF ROM AND CFD MODELS

This section compares the results of the reduced-order model (ROM) with those of the CFD model for the baseline configuration. The comparison serves three purposes. First, it verifies the predictive accuracy of the ROM. Second, it highlights systematic deviations that indicate potential improvements to the ROM or limitations in the PMM methodology. Third, by establishing close agreement for the baseline configuration, any deviations observed in the inclined cases can be attributed directly to inclination effects, providing the foundation for the pressure-drop analysis presented later in this chapter.

The comparison consists of two parts: (i) a mass-flow sweep of key performance variables, and (ii) a component-wise evaluation of total pressure losses including axial (station-wise) distributions at a representative mass flow near the design point.

System-Level Performance Comparison

Figure 4.11 shows the ratio of CFD to ROM predictions for key performance quantities under CR ISA conditions. The ROM accurately predicts duct performance quantities, while the heat exchanger results further verify the PMM modeling approach in CFD. Specifically, the PMM implementation in CFD reproduces condenser heat transfer with high accuracy, while the radiator shows a consistent deviation of approximately 2–6% relative to the ROM. This aligns with findings during PMM verification in Subsection 3.4.5. Consequently, the total temperature rise across the duct is also slightly overpredicted in CFD, with the overprediction increasing slightly with mass flow.

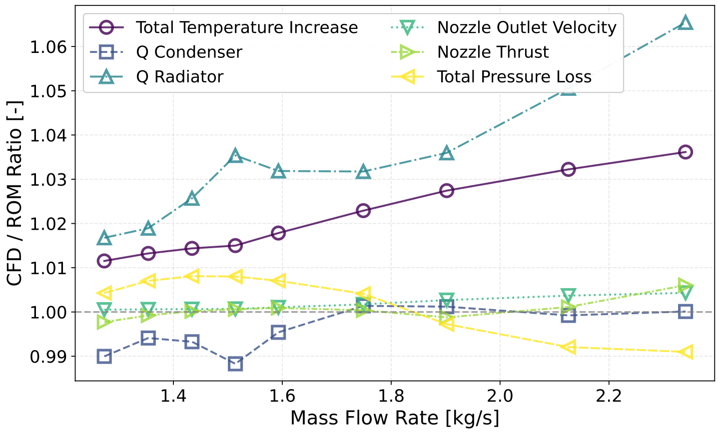

Figure 4.11: Comparison of key performance variable ratios (CFD/ROM) as a function of mass flow rate at CR ISA conditions for the baseline geometry ($\alpha = 0°$).

The total pressure loss, computed from the diffuser inlet to the nozzle outlet (excluding the intake), is predicted within about 1%. The pressure loss and total temperature rise determine the nozzle outlet velocity (Equation 3.17) and, consequently, the nozzle thrust (Equation 3.19). The deviations in thrust prediction are significantly smaller, consistent with the sensitivity analysis in Figure 3.26, which showed that nozzle thrust is relatively insensitive to small variations in stagnation properties.

Additional mass flow sweeps for both TO ISA and CR ISA conditions are presented in Appendix D, specifically in Figure D.1 and Figure D.2. The trends observed for TO ISA are similar to those for CR ISA.

Component-Wise Total Pressure Losses

This subsection evaluates the accuracy of the ROM in predicting total pressure losses for individual duct components. Figure 4.12 presents relative and absolute deviations in component-wise pressure losses. As shown in Figure 4.12a, the ROM matches CFD predictions within 5% for all components except the diffuser, where it overpredicts losses by roughly 30%. In absolute terms (Figure 4.12b), this corresponds to an offset of approximately 20 Pa that increases with mass flow.

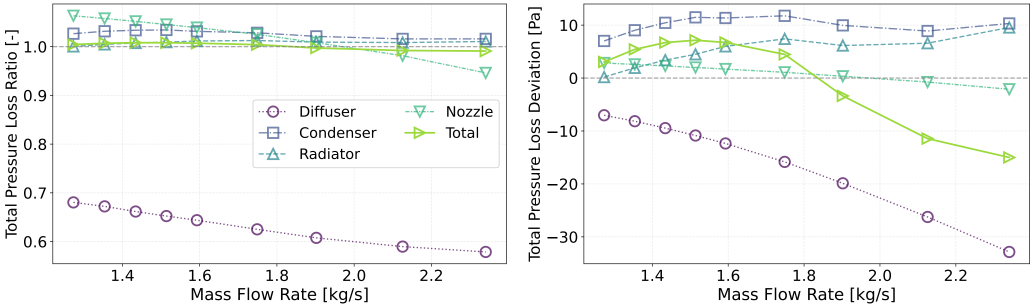

(a) Relative deviation (CFD/ROM ratio)

(b) Absolute deviation (CFD – ROM)

Figure 4.12: Total pressure loss comparison between ROM and CFD for a mass flow sweep at CR ISA conditions for the baseline geometry ($\alpha = 0°$).

Diffuser Discrepancy The diffuser model used in the ROM described in Subsection 3.2.4 is one-dimensional and does not account for boundary layer growth. The diffuser outlet pressure is computed using a static pressure recovery coefficient (Equation 3.11), and the outlet velocity is obtained via mass conservation based on the geometric area ratio (Equation 3.12). The total pressure at the diffuser outlet is then computed from these static quantities. Because the ROM does not account for boundary layer blockage, it underpredicts the outlet velocity, underpredicts the outlet total pressure, and consequently overpredicts the diffuser total pressure loss.

In contrast, the CFD model captures boundary layer growth, which reduces the effective flow area and more accurately predicts the losses in the diffuser. To illustrate this effect, the geometric diffuser area ratio is 4.283 (Table 3.4), while mass-averaged CFD results at the CR ISA design point indicate an effective area ratio of 3.763—a reduction of approximately 12% due to blockage. This causes the ROM to underpredict the diffuser outlet velocity by a similar fraction. Boundary layer growth and associated flow blockage are illustrated by the diffuser velocity profiles in Figure 4.13.

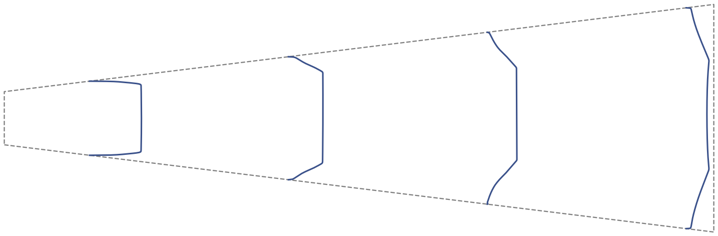

Figure 4.13: Velocity profiles in the diffuser computed by CFD at design point for CR ISA for the baseline geometry ($\alpha = 0°$).

Although the diffuser accounts for the largest component-level deviation, its contribution is still small in the overall pressure budget: approximately 1.8% of the total pressure loss (including the intake) and approximately 3.4% of the internal pressure loss (excluding the intake).

Heat Exchanger Pressure Losses Part of the diffuser discrepancy is compensated by slightly lower heat exchanger losses in the ROM compared to CFD. Because the ROM underpredicts the diffuser outlet velocity, it also slightly underpredicts the velocity entering the condenser and therefore the downstream condenser pressure losses. The effect is smaller for the radiator since it is downstream of the condenser. Deviations in the condenser and radiator pressure losses remain below 1%.

These trends are clearly visible in the axial distributions of total pressure (Figure 4.14) and velocity (Figure 4.15). The CFD results exhibit the expected detailed nonlinear spatial variations, while the ROM accurately captures the mean axial behavior throughout all component stations. CFD predicts a higher velocity entering the condenser, as seen in Figure 4.15, resulting from the diffuser blockage effect discussed above.

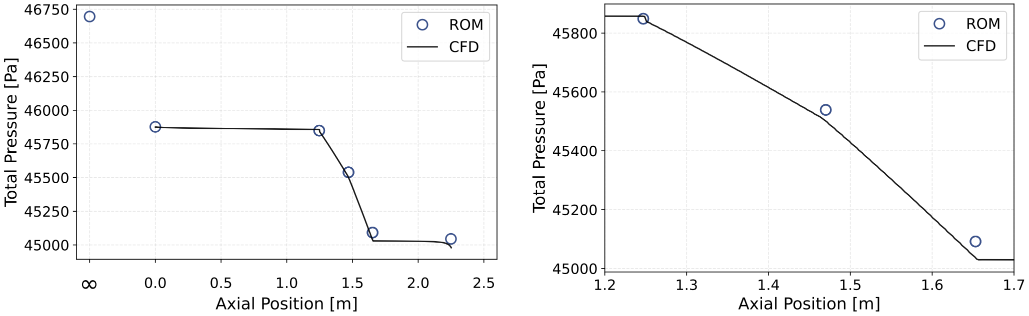

(a) Full duct

(b) Condenser and radiator detail

Figure 4.14: Axial distribution of total pressure from mass-averaged CFD values and ROM predictions at CR ISA for the baseline geometry ($\alpha = 0°$).

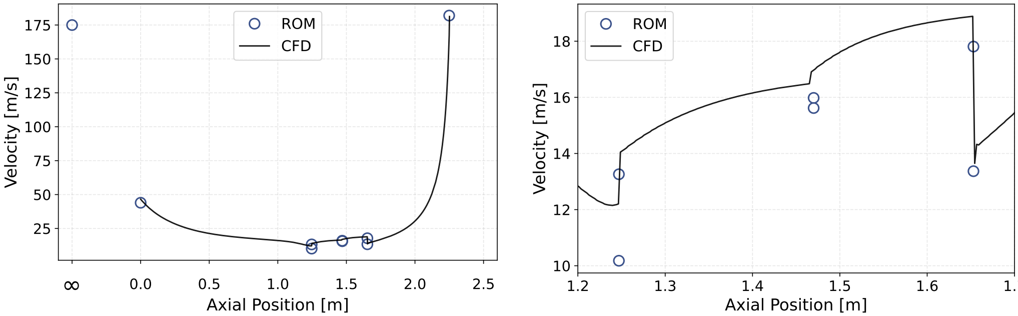

(a) Full duct

(b) Condenser and radiator detail

Figure 4.15: Axial distribution of velocity from mass-averaged CFD values and ROM predictions at CR ISA for the baseline geometry ($\alpha = 0°$).

More detailed axial comparisons near the design point are provided in Appendix D: Figure D.3 for TO ISA and Figure D.4 for CR ISA.

DRAG COMPARISON

The net ram air duct drag is defined by Equation 3.1. Figure 4.16 and Figure 4.17 show the drag components and net drag as functions of mass flow for TO ISA and CR ISA, respectively. Since the CFD model resolves only the internal flow, external drag is taken directly from the ROM for both ROM and CFD comparisons (Equation 3.8). The internal drag matches closely because it depends on the inlet boundary conditions and intake area, which are identical across both models. Therefore, the deviations in net drag arise primarily from discrepancies in nozzle thrust prediction. The nozzle thrust deviations were shown to be small in Figure 4.11, with absolute errors below 3 N.

For TO ISA (Figure 4.16), the relative deviation in net drag (and hence thrust) is larger compared to CR ISA (Figure 4.17). At TO ISA, lower total pressure losses across the intake are present (Figure 4.24), resulting in a larger relative effect of deviations in internal pressure losses on thrust. Moreover, the drag components have lower magnitude at TO ISA, making deviations in thrust have a more significant effect on net drag.

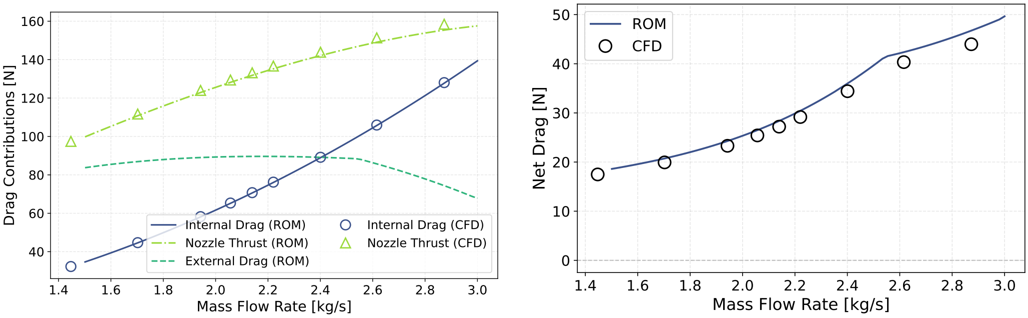

(a) Drag contributions

(b) Net drag

Figure 4.16: Drag as a function of mass flow for TO ISA for the baseline geometry ($\alpha = 0°$). Drag: MAE = 1.45 N (4.68%), max error = 2.88 N (9.31%).

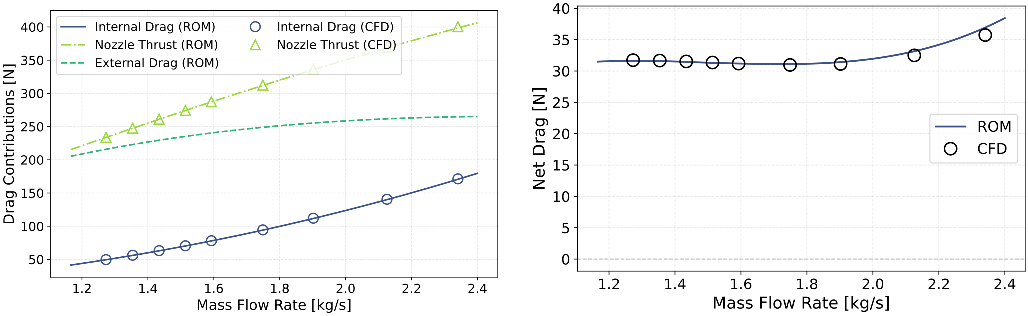

(a) Drag contributions

(b) Net drag

Figure 4.17: Drag as a function of mass flow for CR ISA for the baseline geometry ($\alpha = 0°$). Drag: MAE = 0.29 N (0.63%), max error = 1.10 N (2.4%).

SUMMARY: ROM VS CFD

The ROM accurately captures the internal pressure losses of the ram air duct for the baseline configuration. Despite fundamental differences in modeling approaches, the ROM reproduces key system-level metrics—including total pressure loss, heat transfer, and net drag—within 1–5% deviation from CFD. The remaining discrepancies are small and systematic, primarily arising from the following modeling differences:

- **Diffuser boundary layer growth:** The ROM employs a 1D diffuser model using a constant pressure recovery coefficient, while CFD captures boundary layer growth that reduces the effective flow area by approximately 12%. This causes the ROM to overpredict diffuser losses by roughly 30% in relative terms (approximately 20 Pa absolute), though this represents only 1.8% of total pressure loss of the duct (including the intake).
- **Non-uniform flow distribution:** The ROM assumes uniform, one-dimensional axial flow throughout all duct components, while CFD resolves spatial variations in velocity and other flow properties. These non-uniformities are especially pronounced at the diffuser outlet and condenser inlet due to boundary layer growth and adverse pressure gradients.
- **PMM calibration and averaging:** The PMM coefficients used in both ROM and CFD were calibrated using flow-averaged data from *HeXacode* assuming linear profiles. While fitting errors are small (typically <0.5%), this calibration neglects spatial variation of air properties within the heat exchanger. Additionally, the CFD applies a constant wall temperature across the HX length (due to the 2D domain and cross-flow configuration), which affects energy source term accuracy, particularly in the radiator where consistent 2–6% overprediction is observed.
- **Model coefficient sensitivity:** The ROM uses constant model coefficients for the diffuser and nozzle, while CFD reveals mild mass-flow sensitivity (Table 4.7).

Notably, errors tend to partially cancel: the ROM overpredicts diffuser losses but underpredicts heat exchanger losses due to the lower inlet velocities. Consequently, any deviations observed in the inclined cases can be attributed to inclination effects rather than inherent ROM inaccuracies. These comparisons confirm the ROM's predictive accuracy and form the basis for the inclined-case pressure-loss analysis presented next. The analysis demonstrates that the ROM is an accurate and computationally efficient alternative to CFD, provided that appropriate model coefficients are used.

4.2.4. ANALYSIS OF FLOW FIELD IN THE DUCT

To complement the quantitative ROM–CFD comparisons presented earlier, this subsection highlights key flow features observed in the CFD simulations. Full contour plots of velocity, total pressure, static pressure, total temperature, and streamlines for $\alpha = 0°$, 30°, and 60° are provided in Appendix D in Section D.3. Here, for brevity, only the baseline (0°) and most inclined (60°) configurations are shown.

Figure 4.18 compares the streamlines for the baseline and 60° cases. As shown in Figure 4.18a, the baseline configuration exhibits fully attached flow throughout the duct. Even at $\alpha = 60°$ (Figure 4.18b), the flow remains attached, confirming that the inclined heat exchanger does not induce separation in the duct. The porous media strongly straightens the flow through the heat exchanger core, resulting in noticeable flow turning at the entrance and again after the radiator when the flow realigns with the duct axis.

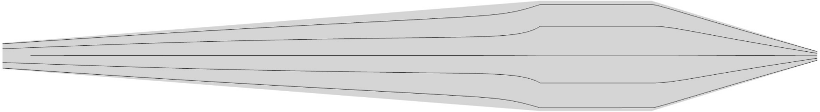

(a) Baseline ($\alpha = 0°$)

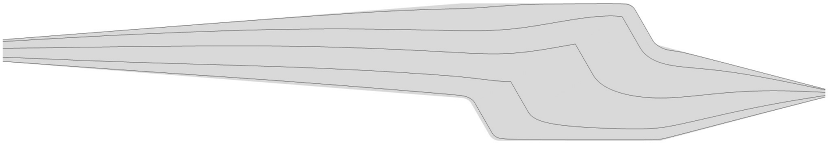

(b) 60° inclined configuration

Figure 4.18: Comparison of streamlines for baseline and 60° inclination at CR ISA design point.

The velocity magnitude contours in Figure 4.19 illustrate the effect of the diffuser and the inclined core on the flow field. Both the baseline (Figure 4.19a) and 60° case (Figure 4.19b) show progressive boundary layer thickening in the diffuser and non-uniform velocity entering the condenser. These non-uniformities increase with inclination but, as shown in the ROM–CFD comparison, have only a minor influence on the overall thermal performance of the heat exchangers.

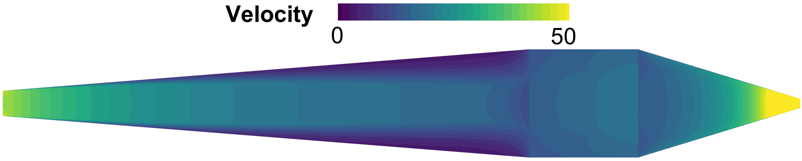

(a) Baseline ($\alpha = 0°$)

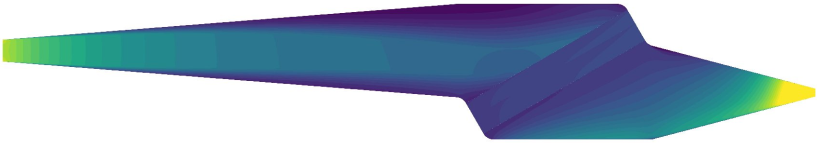

(b) 60° inclined configuration

Figure 4.19: Velocity magnitude ([m/s]) contours comparing baseline and 60° inclination at CR ISA design point.

Finally, Figure 4.20 shows the total pressure distribution. The baseline case (Figure 4.20a) exhibits markedly larger total pressure loss across the entire duct, resulting in substantially lower total pressure at the nozzle outlet. Although some additional losses appear in the diffuser and tilted inlet section for the 60° configuration (Figure 4.20b), the overall pressure drop is much smaller than for the baseline.

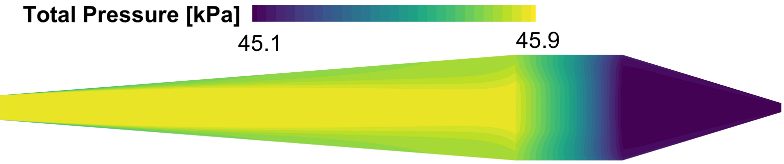

(a) Baseline ($\alpha = 0°$)

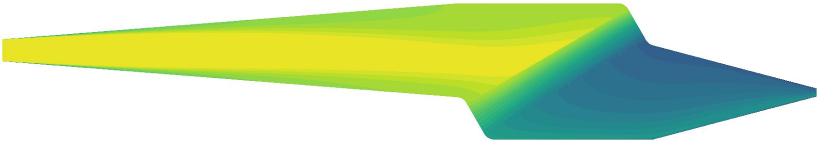

(b) 60° inclined configuration

Figure 4.20: Total pressure contours comparing baseline and 60° inclination at CR ISA design point.

Overall, the contour plots confirm that (i) the flow remains attached even at $\alpha = 60°$, (ii) diffuser-induced and inclination-induced non-uniformities do not severely degrade heat exchanger thermal performance, and (iii) higher inclination angles substantially reduce total pressure losses in the duct, although some additional losses due to inclination are observed.

4.2.5. QUANTIFICATION OF HEAT EXCHANGER INCLINATION PRESSURE LOSSES

The key question addressed in this section is whether heat exchanger inclination introduces a significant pressure drop penalty beyond what the ROM predicts. As shown in Figure 4.2, the optimization results indicate increasing performance benefits with greater heat exchanger inclination. However, these analyses did not account for additional pressure losses due to inclination effects or the potential for flow separation. Having verified the ROM for the baseline (uninclined) configuration in Subsection 4.2.3, CFD is now used to quantify inclination-specific effects by comparing ROM predictions (which do not model inclination losses) against CFD results (which capture flow turning and other inclination-induced losses). Note that, as discussed in Subsection 3.4.5, the PMM does not fully model incidence losses that occur at the entrance of an inclined heat exchanger.

SYSTEM-LEVEL PERFORMANCE

The complete results across all inclination angles are provided in Appendix D, shown in Figure D.5. Figure 4.21a shows that, in general, total pressure loss decreases at higher inclination angles, as concluded from the optimization results in Figure 4.2. However, the deviation between ROM predictions (solid lines) and CFD results (markers) increases at larger inclination angles. This growing discrepancy indicates that inclination introduces additional pressure losses not captured by the ROM, and these inclination-specific losses increase with angle despite the overall trend of decreasing absolute pressure loss.

The net drag shown in Figure 4.21b remains largely unaffected up to 60°. Combined, this suggests that inclination angles up to 60° are feasible, as there is no significant increase in drag, provided that the flow remains attached in the duct.

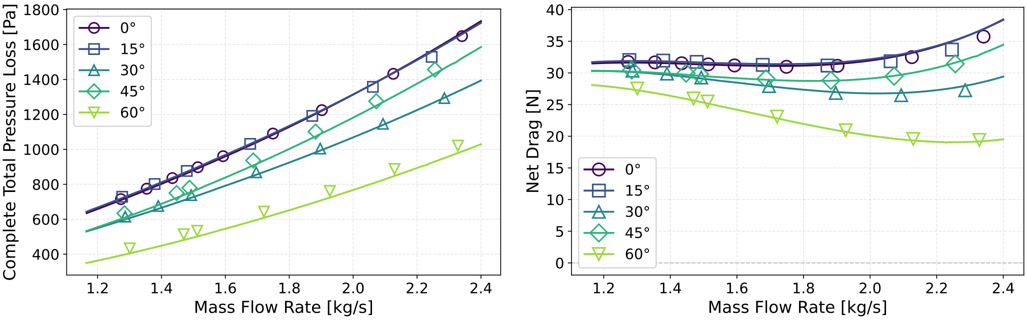

(a) Total pressure loss in the ram air duct

(b) Net drag

Figure 4.21: Total pressure loss and net drag as functions of mass flow rate under CR ISA conditions for various inclination angles. Solid lines: ROM predictions; Markers: CFD results.

Component-Level Pressure Drop Analysis

While Figure 4.21a shows the overall pressure loss trend, a component-by-component comparison of ROM predictions and CFD results reveals where inclination effects are most significant. The largest ROM–CFD discrepancies due to inclination occur in the condenser and nozzle regions. Note that the condenser pressure drop includes the tilted region between the diffuser and the condenser, and the nozzle region includes the tilt-back section downstream of the radiator.

Figure 4.22a shows a clear increase in the ROM–CFD deviation for the condenser at higher inclination angles, with CFD predicting higher losses than ROM. Similarly, Figure 4.22b demonstrates that the ROM–CFD discrepancy in nozzle pressure drop increases systematically with inclination, although the absolute deviations are smaller compared to the condenser in Figure 4.22a.

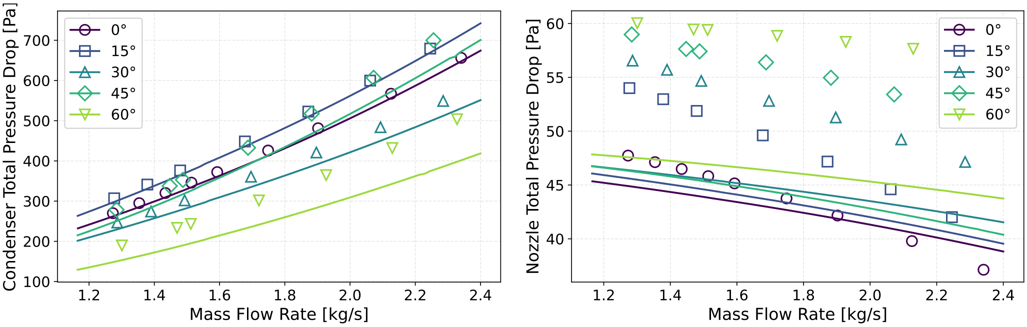

(a) Condenser pressure drop (includes tilted inlet region)

(b) Nozzle pressure drop (includes tilt-back region)

Figure 4.22: Component-level pressure drops under CR ISA conditions in the ram air duct regions most affected by heat exchanger inclination. Solid lines: ROM predictions; Markers: CFD results.

The remaining duct components show minimal sensitivity to inclination. Since the ROM does not model inclination effects, close agreement between ROM predictions (solid lines) and CFD results (markers) across different inclination angles indicates that inclination-induced losses are negligible for that component. For the diffuser (Figure D.5m in Appendix D), the baseline ROM–CFD discrepancy remains consistent across all inclination angles, indicating that the discrepancy is not related to inclination but rather to other modeling differences. For the radiator (Figure D.5p in Appendix D), ROM and CFD show good agreement across all inclination angles, with minimal variation, confirming negligible inclination sensitivity.

These observations reveal that inclination-induced pressure losses primarily arise in the tilted entry region upstream of and within the condenser, and in the tilted nozzle region downstream of the radiator. The radiator itself shows minimal sensitivity to inclination, as it receives flow that has already been aligned by the condenser.

INCLINATION CORRECTION FACTOR DEVELOPMENT

Figure 4.23a shows the CFD/ROM total pressure loss ratio evaluated in two ways: for the complete ram air duct (intake, diffuser, heat exchangers, and nozzle), and excluding the diffuser (tilted regions, heat exchangers, and nozzle only). Error bars represent the range across the simulated mass flows.

The complete duct case shows significant sensitivity in the CFD/ROM ratio with mass flow. In contrast, excluding the diffuser results in consistently higher CFD/ROM ratios with notably lower sensitivity to mass flow.

This difference is attributed to limitations in the ROM's diffuser model, as discussed in Subsection 4.2.3. The simplified 1D diffuser overpredicts pressure losses, particularly at high mass flows, thereby inflating the denominator of the CFD/ROM ratio. This can lead to underestimation of inclination penalties. By excluding the diffuser while retaining the tilted region between the diffuser and the condenser, a more physically representative estimate of inclination-induced losses is obtained. For this reason, the duct excluding the diffuser is used to develop an inclination correction factor.

Figure 4.23b shows this data, shifted to unity at $\alpha = 0°$, forming a multiplicative factor that quantifies the pressure drop penalty due to inclination. Nichols' experimental data [33] is included for reference. Differences are expected due to geometric variations, the absence of heat transfer in Nichols' tests, and other modeling assumptions.

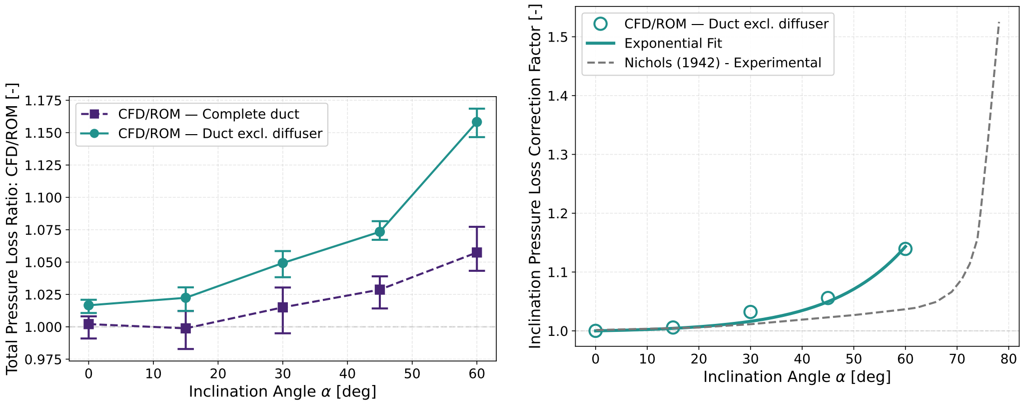

(a) CFD/ROM total pressure loss ratio across inclination angles with error bars showing mass flow variation

(b) Inclination correction factor and Nichols [33] experimental data

Figure 4.23: CFD/ROM pressure loss ratio analysis for various inclination angles.

Inclination Correction Factor

The correction factor is fitted with an exponential function:

$$f(\alpha) = 1 + 0.002361 \left(e^{0.068706\alpha} - 1\right) \tag{4.3}$$

where α is the inclination angle in degrees. This captures the exponential pressure loss increase with inclination and is valid for $0° \leq \alpha \leq 60°$. Extrapolation beyond this range is not recommended due to uncertainty.

The correction factor in Equation 4.3 is applied as a multiplier to the baseline heat exchanger pressure drop:

$$\Delta P_{\text{inclined}} = f(\alpha) \cdot \Delta P_{\text{baseline}} \tag{4.4}$$

where $\Delta P_{\text{inclined}}$ is the pressure drop at inclination angle α, and $\Delta P_{\text{baseline}}$ is the baseline pressure drop at $\alpha = 0°$. This enables the ROM to incorporate inclination effects.

It is important to note that this correction factor is specific to the current configuration and should be interpreted as indicative, not universal. While Nichols' study involved a single, unheated heat exchanger, this work considers two heat exchangers (condenser and radiator) in series, with geometry and performance varying across inclination angles (e.g., height, depth, pressure drop, and heat transfer characteristics).

Several modeling and configuration-specific factors require careful interpretation of the derived correction factor. First, incidence losses at the heat exchanger entrance are not fully captured by the PMM, as discussed in Subsection 3.4.5. Second, as shown in Table 3.15, the PMM methodology showed increased deviation from *HeXacode* for pressure drop predictions in short, low-porosity heat exchangers during verification. Although the PMM's physical velocity formulation does model entrance and exit effects, *HeXacode* employs semi-empirical correlations for these losses, and the deviation between the two approaches becomes more pronounced for shorter heat exchangers where entrance and exit effects are proportionally larger. Since optimization at higher inclination angles yields progressively shorter heat exchangers with lower porosity, the observed pressure drop increase may partially reflect this geometry-dependent PMM-HeXacode deviation rather than purely inclination-induced losses. Third, the inclination strategy results in longer ram air ducts at higher angles (Figure 3.3), incurring additional viscous losses along the extended wetted surface area that are not explicitly quantified in this work. The derived correlation implicitly accounts for these configuration-specific factors and should not be generalized to arbitrary heat exchanger designs. Future work should isolate these effects through parametric studies with controlled heat exchanger geometry.

4.2.6. Evaluation of Ram Air Duct Performance Using Inclination-Informed ROM

Having verified ROM accuracy (Subsection 4.2.3) and determined that 60° inclination yields optimal performance, the ROM is now extended to incorporate the CFD-derived inclination correction factor. The correction factor introduced in Equation 4.3 is applied to all ROM predictions to account for inclination-induced losses that are not captured by the original model. This approach assumes that the correction factor, derived under CR ISA conditions, is valid across all operating points.

As shown in Figure 4.23, for an inclination of $\alpha = 60°$, the CFD/ROM pressure drop ratio reaches approximately 1.16, indicating a 16% increase in total pressure loss through the heat exchanger region. This factor is now applied uniformly across all operating points in the ROM evaluation.

PREDICTED PERFORMANCE ACROSS ALL OPERATING POINTS

Table 4.9: ROM-predicted aerodynamic performance at $\alpha = 60°$ for all operating points, comparing models without and with inclination correction.

Operating Point	**No Inclination Corr.** ($C_p = 0.75$)			**Inclination Corr.** ($C_p = 0.75$)			**Inclination Corr.** ($C_p = 0.90$)		
	T_{nozzle} [N]	D_{net} [N]	ΔP_{tot} [kPa]	T_{nozzle} [N]	D_{net} [N]	ΔP_{tot} [kPa]	T_{nozzle} [N]	D_{net} [N]	ΔP_{tot} [kPa]
TO ISA	142.5	17.3	0.807	140.5	19.3	0.865	144.3	15.5	0.755
TOC ISA	312.3	21.5	1.534	310.9	22.9	1.610	313.2	20.6	1.486
CR ISA	276.7	30.0	1.416	275.7	31.0	1.478	277.3	29.4	1.378
TOD ISA	291.7	30.5	1.468	290.6	31.7	1.535	292.5	29.8	1.422
TO ISA+35	171.3	101.1	1.916	155.7	116.8	2.082	190.2	82.3	1.694
TOC ISA+35	509.4	68.4	3.044	500.7	77.2	3.269	519.9	58.0	2.766
CR ISA+35	465.1	68.4	2.625	459.0	74.5	2.810	471.9	61.7	2.415
TOD ISA+35	431.2	56.1	2.335	426.6	60.6	2.491	435.8	51.4	2.171

Table 4.9 summarizes the ROM-predicted performance across all operating points, incorporating the inclination correction factor. Results are shown for $C_p = 0.75$ for with and without inclination correction factor, and for $C_p = 0.9$ with correction factor. This allows to (i) quantify the effect of the inclination factor and thus heat exchanger inclination , and (ii) the impact of diffuser modeling assumptions. Thermal performance of the heat exchangers is omitted for brevity, but this analysis is done at the design point.
Both inclining and lower diffuser static pressure recovery increase the total pressure losses, resulting in lower thrust and higher net drag. This effect becomes more pronounced at the higher mass flow conditions associated with ISA+35 conditions.

Using the methodology outlined in Subsection 3.3.7, the equivalent battery mass and total equivalent system mass are computed using the net drag values in Table 4.9. The results are listed in Table 4.10. Comparing the ROM predictions without inclination correction and with correction at $C_p = 0.75$ shows that the additional pressure loss due to inclination increases the equivalent battery mass by only 7.4 kg (+7%), as seen in Table 4.10. This confirms that the aerodynamic penalty from HX inclination is relatively modest in terms of its impact on overall equivalent system mass. In contrast, the difference between $C_p = 0.75$ and $C_p = 0.90$ leads to a reduction of approximately 12 kg in equivalent battery mass, highlighting that assumptions in diffuser modeling have a larger effect on system-level performance than the inclination-induced losses.

Table 4.10: System-level comparison at 60° inclination: HX-optimized configuration versus ROM predictions with inclination correction.

Parameter	**ROM** ($C_p = 0.75$)	**ROM Inclined** ($C_p = 0.75$)	**ROM Inclined** ($C_p = 0.90$)
Combined HX mass [kg]	175.4	175.4	175.4
Equivalent battery mass [kg]	176.4	183.8	171.9
Total equivalent system mass [kg]	**351.8**	**359.2**	**347.3**

COMPONENT-WISE PRESSURE LOSS BREAKDOWN

The bar plots in Figure 4.24 illustrate the component-wise contributions to the total pressure loss of the ram air duct for the diffuser pressure coefficients $C_p = 0.90$ and $C_p = 0.75$, respectively. These results show that the diffuser becomes a dominant contributor to the total pressure loss at the lower value of C_p, in some cases reaching the same order of magnitude as the losses across the heat exchangers. This behavior is particularly evident at operating points corresponding to higher mass flow rates. Although the inclination of the heat exchangers introduces additional pressure losses, these remain relatively modest.

Figure 4.24 shows that the intake contributes significantly to the total pressure loss of the duct. The intake performance is modeled using semi-empirical correlations from ESDU [59], as described in Subsection 3.2.3, with a total pressure ratio given in Table 3.7. For the TO ISA+35 operating point, the total pressure loss in the duct approaches the available ram air dynamic pressure, given in Table 3.2. If the losses exceed the available ram pressure at any point, a puller fan would be required to maintain the desired mass flow through the system. This is ideally avoided, as it would increase system mass, increase system complexity, and add windmilling drag during all other operating points. A future study should therefore include CFD simulations of the intake in combination with the internal duct to capture interaction effects and more accurately assess both the external drag and the intake total pressure loss.

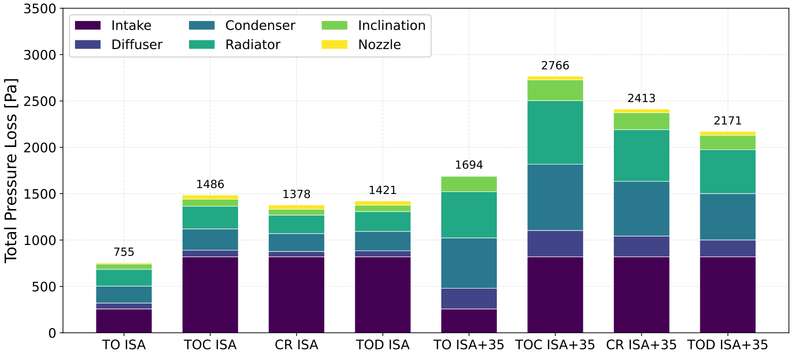

(a) $C_p = 0.90$

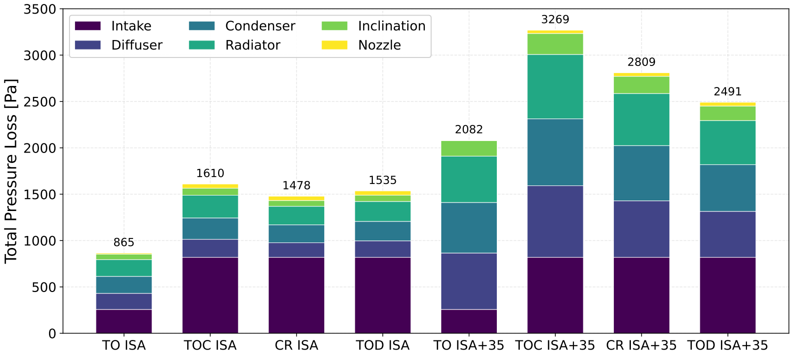

(b) $C_p = 0.75$

Figure 4.24: Total pressure loss breakdown by component for two diffuser static pressure recovery C_p values.

5

CONCLUSIONS AND RECOMMENDATIONS

This chapter presents the conclusions and recommendations of this thesis and is structured as follows. The conclusions in Section 5.1 aim to answer the research questions listed in Section 2.5, after which recommendations for future work are presented in Section 5.2.

5.1. CONCLUSIONS

METHODOLOGY

- A multi-objective, multi-point optimization framework was successfully developed using *HeXacode* and the NSGA-II genetic algorithm, enabling efficient exploration of the heat exchanger design space while satisfying thermal requirements across eight operating points spanning the E9X mission profile.

- A sequential coupled optimization strategy was implemented to maintain physical consistency between the condenser and radiator by propagating outlet conditions from the condenser (mass flow rate, static pressure, and temperature) as inlet boundary conditions for the radiator. This approach captures the coupling while maintaining computational efficiency compared to simultaneous optimization.

- The optimization framework identifies the true system-level optimum that balances structural weight and aerodynamic penalties by evaluating the total equivalent system mass, i.e., the sum of structural heat exchanger mass and an equivalent battery mass needed to compensate for ram air duct drag (Equation 3.35).

- A porous media modeling (PMM) methodology for RANS CFD was implemented and verified, representing heat exchangers through calibrated momentum and energy source terms in simplified 2D ram air duct geometries. Several methodological improvements are presented: (i) enhanced pressure drop calibration that addresses systematic deviations observed in earlier work [11, 12, 13], and (ii) wall temperature correlations enabling accurate off-design heat transfer predictions.

- The calibrated porous media model reproduces heat exchanger pressure drops within 1% of *HeXacode* predictions for the baseline, with discrepancies up to 10% for shorter, denser cores where entrance and exit effects are more significant. Heat transfer predictions show excellent agreement for the condenser (within 1%), while the radiator exhibits a systematic 2–6% overprediction due to fundamental differences between *HeXacode*'s single-cell discretization and CFD's spatially resolved temperature profiles.

- The reduced-order model accurately predicts system-level metrics including total pressure loss, heat transfer, and net drag within 1–5% of CFD predictions for the baseline configuration. The largest discrepancies arise from the simplified diffuser model, which does not account for flow blockage due to boundary layer growth, resulting in underprediction of diffuser outlet velocity and corresponding overprediction of total pressure losses.

LEARNINGS

- Offset strip fins (OSF) consistently outperform louvered fins (LF) for the boundary conditions and thermal constraints of this study, achieving the same heat transfer requirements with substantially lower air-side pressure drop, primarily due to lower average friction factors at comparable inlet Reynolds numbers. Selecting OSF over LF reduces total system mass by approximately 100 kg across all eight ram air duct. This demonstrates that fin topology selection has non-negligible system-level impact despite being a component-level design choice.

- Heat exchanger inclination from $\alpha = 0°$ to 60° increases effective frontal area by a factor of $1/\cos(\alpha)$, reducing inlet velocity and enabling denser fin configurations without excessive pressure loss penalties. Optimized designs at higher inclination angles feature progressively lower porosities and shorter core lengths.

- Increasing inclination from 0° to 60° reduces total system mass (heat exchanger mass plus equivalent battery mass to overcome drag) by 60.1 kg, representing approximately 16% system mass reduction. The structural heat exchanger mass does not decrease monotonically with inclination, but the aerodynamic penalty decreases significantly to yield lower net system mass.

- CFD simulations reveal that inclination introduces additional pressure losses due to flow turning within the duct. These losses remain modest even at 60° inclination, with attached flow maintained throughout the operating range. A pressure loss correction factor was developed from CFD data and incorporated into the ROM. However, incidence losses at the heat exchanger inlet due to flow misalignment with fins are not captured by the PMM. These losses are expected to become relevant at larger inclination angles.

- Two TMS architectures were compared: a series configuration with eight ram air ducts each containing both condenser and radiator, and a separate-duct configuration with 16 total ducts (eight for condensers, eight for radiators). In the series configuration, the radiator receives preheated air from the condenser outlet, requiring larger heat transfer area to achieve the same heat rejection, resulting in suboptimal radiator performance. Moreover, the radiator is often oversized when constrained by the condenser outlet mass flow rate. This results in excess heat rejection capacity and corresponding pressure drop penalties. Despite these thermal coupling disadvantages, the series configuration reduces total equivalent system mass by 213 kg (-37%) compared to the separate-duct architecture. This advantage arises primarily from having only half the number of ram air ducts, thereby reducing frontal area and external drag.

- The intake represents a significant source of total pressure loss (Figure 4.24), highlighting the importance of intake design, integration, and external aerodynamics for overall system performance.

- The combined effects of heat exchanger topology selection (OSF), inclination optimization (60°), and series-architecture choice yield cumulative equivalent system mass savings of approximately 326 kg, demonstrating the significant system-level impact of integrated heat exchanger and TMS architecture optimization. The mass reduction corresponds to approximately 10 km (+1%, Figure 3.14) nominal range increase, representing a meaningful performance gain for battery-electric aircraft where every kilogram directly impacts range and payload capacity.

5.2. RECOMMENDATIONS FOR FUTURE WORK

MODELING

- Integrate heat exchanger optimization with Elysian's full-system *Modelica* model, including ram air duct components, thermal loops, and hot-side components. As demonstrated by Beltrame et al. [36], combined thermodynamic cycle and heat exchanger optimization can yield significant performance improvements. Computational cost can be reduced by developing surrogate models for heat exchanger performance, enabling more extensive design space exploration and integration with higher-level aircraft design tools.

- Extend the sequential coupled optimization to simultaneous integrated optimization of both heat exchangers to identify the global system optimum. While the sequential approach enforces physical coupling (mass flow continuity and condenser outlet conditions as radiator inlet) with computational efficiency, simultaneous optimization may reveal additional design space regions not accessible through sequential optimization.

- Apply gradient-based local optimization following genetic algorithm optimization to refine convergence to local optima with higher precision. Many optimized geometries feature design variables near their bounds but not within rounding accuracy of the maximum values, suggesting potential for further refinement through local search methods.

- Include humidity effects in heat exchanger optimization and CFD simulations. Humid air has higher specific heat capacity than dry air, providing additional cooling capacity. Neglecting humidity in the present analysis is conservative, but explicit modeling would improve prediction accuracy and potentially reveal opportunities for heat exchanger mass reduction.

- For future CFD studies the heat transfer modeling approach can be selected based on simulation objectives. The simplest approach specifies uniform volumetric heat sources independent of operating conditions, or velocity/mass-flow-dependent source terms. An intermediate approach, as employed in this work, uses Nusselt number-based correlations with the proposed wall temperature correlations as input, enabling off-design predictions by capturing mass flow and temperature dependencies. However, if the primary objective is pressure drop or thrust prediction, simpler constant heat flux models may be sufficient, as heat transfer has only secondary effects on pressure drop (Figure 3.27c) and relatively small effects on thrust predictions (Figure 3.26a). In this study, the condenser heat transfer showed predictable behavior across operating conditions. This suggests that for the radiator, simpler univariate correlations (wall temperature as function of mass flow only) calibrated from coupled condenser-radiator simulations might be sufficient, rather than the bivariate correlations (mass flow and inlet temperature) developed here. However, for more advanced duct geometries with greater flow non-uniformities, the bivariate correlation approach may prove essential. For highest accuracy, advanced porous media models such as those by Yakinthos et al. [45] can resolve both hot and cold fluid streams simultaneously at increased computational cost.

- If more accurate modeling of radiator heat transfer is required (beyond the current 2–6% overprediction), a multi-zone porous media approach could be implemented by dividing the heat exchanger into multiple zones with spatially varying wall temperatures. However, in 2D this approach is only viable for specific heat exchanger flow arrangements. The current cross-flow configuration with horizontal tubes results in wall temperature variation along the heat exchanger width (hot-side flow direction), which corresponds to the out-of-plane dimension in the 2D CFD model. To implement a multi-zone approach, the heat exchanger would require a vertical tube arrangement where wall temperature varies within the CFD plane, enabling multiple porous zones with distinct wall temperatures. This configuration change may introduce practical challenges related to space constraints and buoyancy effects in the condenser and should be evaluated against the acceptable accuracy already achieved.

- Improve the predictive accuracy of the reduced-order model by implementing a more sophisticated diffuser model that accounts for boundary layer blockage effects. The current diffuser model does not capture the reduction in effective flow area due to boundary layer displacement thickness, leading to underprediction of diffuser outlet velocity and corresponding overprediction of total pressure losses. Two approaches could address this limitation: (i) implement semi-empirical and/or CFD-informed corrections such as an area correction factor, as demonstrated by Beltrame et al. [11], or (ii) for more general applicability across diverse geometries and operating conditions, adopt a viscous-inviscid coupling method such as that proposed by Lyrio [66], which couples inviscid core flow with integral boundary layer equations to predict displacement thickness and flow separation, though at increased model complexity and computational cost.

Design and CFD Investigations

- Investigate the observed discrepancies in condensation behavior. The thermal diagrams (Figure 4.5) indicate incomplete condensation at ISA conditions where Elysian's models predicted complete condensation. These discrepancies require further investigation to ensure accurate thermal performance predictions.

- Extend the CFD analysis to include ISA+35 hot-day conditions, which are critical TMS sizing cases. This would: (i) verify that heat duties can be met during extreme thermal conditions, particularly for TO ISA+35 which typically serves as the sizing point, and (ii) quantify pressure drops to assess whether a ram air duct fan can be avoided, thereby saving weight, reducing system complexity, and eliminating windmilling drag during other flight phases.

- Apply the CFD methodology to more representative duct geometries with curved walls, either in 2D or 3D. The present 2D rectangular duct represents a simplification to enable methodology development, but actual aircraft ducts feature complex shapes optimized for the available volume in the nacelle.
- Investigate flow attachment and uniformity at high inclination angles in a more representative 3D duct to verify there is no fundamental pressure drop penalty and to ensure thermal performance is not degraded by flow separation or maldistribution. In this study, CFD results showed no fundamental flow separation in the duct up to 60°. In case of flow separation at high inclination angles:
  - Consider guide vanes if flow separation becomes problematic, as investigated by Sain et al. [40]. The trade-off between reduced turning losses and increased wetted surface area and thus friction losses should be quantified to determine net benefit.
  - Investigate curved fin designs for high inclination angles to promote flow turning and potentially reduce pressure losses compared to conventional straight fin heat exchangers, as demonstrated by Patrão et al. [52]. This may enable even higher inclination angles or further pressure drop reductions.
- Isolate inclination-specific pressure losses through parametric CFD studies with controlled heat exchanger geometry. The derived inclination correction factor may combine true inclination losses with: (i) entrance/exit effects that become more pronounced for shorter, low-porosity heat exchangers (which result from optimization at higher inclination angles), and (ii) increased viscous losses along extended wetted surface area as duct length increases with inclination angle.
- Perform 3D CFD simulations including external aerodynamics and propeller-nacelle integration to capture effects not present in 2D analysis, such as propeller slipstream-induced flow non-uniformities (e.g., swirl) and intake-nacelle integration effects. These effects may significantly alter intake and diffuser performance, as well as external drag predictions.
- Investigate intake integration strategies on the aircraft, as the intake represents the largest source of total pressure loss (Figure 4.24). Optimizing intake design and location is critical for overall ram air duct performance and drag minimization.
- Experimental validation of the selected ram air duct design with inclined heat exchangers is recommended rather than relying solely on simulations. Experiments could also quantify incidence losses at the heat exchanger inlet, which are not captured by the current PMM approach. Furthermore, once Elysian selects specific heat exchangers for the E9X, the current CFD methodology can be directly applied if manufacturer data or experimental measurements become available. Measured characteristics would then replace the empirical correlations used in this study.

Appendix

A

Heat Exchanger Optimization Results

A.1. Coupled Optimization

Table A.1: Heat exchanger geometry parameters for optimized condenser and radiator configurations for condenser-radiator in series configuration at different inclination angles. Design variables correspond to optimization inputs with bounds, while derived parameters are calculated from the optimized designs.

Parameter	**Symbol**	**LB**	**UB**	**0°**		**15°**		**30°**		**45°**		**60°**	
				Cond.	Rad.	Cond.	Rad.	Cond.	Rad.	Cond.	Rad.	Cond.	Rad.
Geometry vector inputs (design variables)													
Heat exchanger width	w_{hx} [mm]	560	560	560	560	560	560	560	560	560	560	560	560
Heat exchanger height	h_{hx} [mm]	400	800	400.0	400.0	414.2	414.2	461.9	461.9	565.7	565.7	800.0	800.0
Flat tube pitch	p_{tube} [mm]	15.0	20.0	16.6	19.0	19.0	15.4	16.7	16.6	16.2	16.8	15.2	19.5
Flat tube height	h_{ft} [mm]	3.5	5.0	3.5	3.7	3.5	3.6	3.6	3.5	4.9	4.9	4.6	4.7
Microchannel width	w_{mc} [mm]	1.0	2.5	1.0	1.0	1.0	1.0	1.0	1.0	1.0	1.0	1.0	1.0
Microchannel wall thickness	t_{mc} [mm]	0.2	0.2	0.2	0.2	0.2	0.2	0.2	0.2	0.2	0.2	0.2	0.2
Fin pitch (OSF)	p_{fin} [mm]	2.5	5.0	3.2	2.7	2.5	2.6	2.5	2.5	2.5	2.5	2.5	2.5
Fin height (OSF)	h_{fin} [mm]	6.0	18.0	15.2	15.1	9.3	12.2	11.0	12.8	11.5	12.5	8.8	12.5
Fin thickness (OSF)	t_{fin} [mm]	0.15	0.15	0.15	0.15	0.15	0.15	0.15	0.15	0.15	0.15	0.15	0.15
Fin depth (OSF)	d_{fin} [mm]	2.5	12.0	11.7	10.1	11.7	11.0	11.6	9.3	3.7	5.0	2.6	2.9
Derived parameters (solved or calculated)													
Heat exchanger length	l_{hx} [mm]	–	–	217.4	187.4	136.0	164.0	138.4	148.5	98.6	112.2	67.4	83.6
Number of microchannels	n_{mc} [–]	–	–	181	156	113	134	115	123	82	90	55	69
Flat tube width	w_{ft} [mm]	–	–	217.4	187.4	136.0	164.0	138.4	148.5	98.6	112.2	67.4	83.6
Hydraulic diameter	d_{eq} [mm]	–	–	4.7	4.0	3.4	3.7	3.6	3.7	3.3	3.4	3.0	3.4
Porosity	ε [–]	–	–	0.77	0.75	0.67	0.72	0.70	0.73	0.66	0.67	0.61	0.68
Heat transfer area compactness	β_{hx} [$\mathrm{m}^2/\mathrm{m}^3$]	–	–	653	754	802	778	769	791	785	786	808	804
Mass	m_{hx} [kg]	–	–	12.5	11.7	10.8	11.6	11.3	11.6	10.0	10.9	10.4	11.5

Table A.2: Optimized condenser and radiator performance for different inclination angles under ISA conditions.

Parameter	**Unit**	**0°**		**15°**		**30°**		**45°**		**60°**	
		Cond.	Rad.	Cond.	Rad.	Cond.	Rad.	Cond.	Rad.	Cond.	Rad.
General performance											
Mass	[kg]	12.53	11.70	10.75	11.61	11.34	11.59	9.99	10.93	10.43	11.49
Weighted pressure drop	[kPa]	0.410	0.583	0.468	0.548	0.358	0.453	0.410	0.433	0.255	0.259
TO ISA											
$\dot{m}_c$	[kg/s]	2.146	2.146	2.177	2.177	2.203	2.203	2.159	2.159	2.228	2.228
$T_{c,\text{in}}$	[K]	290.43	311.54	290.42	311.24	290.42	310.99	290.43	311.41	290.42	310.76
$T_{c,\text{out}}$	[K]	311.54	356.41	311.24	355.75	310.99	355.31	311.41	356.13	310.76	355.43
ΔT_c	[K]	21.11	44.87	20.82	44.51	20.57	44.32	20.98	44.72	20.34	44.67
$P_{c,\text{in}}$	[kPa]	103.763	103.481	103.758	103.439	103.754	103.510	103.761	103.470	103.750	103.566
$P_{c,\text{out}}$	[kPa]	103.481	103.087	103.439	103.071	103.510	103.203	103.470	103.172	103.566	103.384
ΔP_c	[kPa]	0.283	0.394	0.320	0.368	0.245	0.307	0.291	0.298	0.184	0.182
ΔP_h	[kPa]	0.154	0.265	0.163	0.250	0.160	0.271	0.125	0.185	0.107	0.197
D_{internal}	[N]	71.0	71.0	73.1	73.1	74.8	74.8	71.9	71.9	76.6	76.6
D_{external}	[N]	83.6	83.6	83.5	83.5	83.4	83.4	83.6	83.6	83.3	83.3
T_{nozzle}	[N]	132.0	128.3	132.5	129.3	136.0	135.2	131.9	131.2	138.6	142.2
D_{net}	[N]	22.6	26.3	24.0	27.2	22.2	23.0	23.6	24.3	21.2	17.6
Q	[kW]	45.60	97.11	45.60	97.69	45.60	98.42	45.60	97.38	45.60	100.35
ΔQ	[%]	+0.0	+26.1	+0.0	+26.9	+0.0	+27.8	0.0	+26.5	+0.0	+30.3
T_{wall}	[K]	315.19	365.22	315.28	365.23	315.29	365.08	315.17	366.12	315.09	366.20
TOC ISA											
$\dot{m}_c$	[kg/s]	1.620	1.620	1.651	1.651	1.664	1.664	1.636	1.636	1.667	1.667
$T_{c,\text{in}}$	[K]	253.79	297.46	253.79	296.64	253.78	296.31	253.79	297.03	253.78	296.24
$T_{c,\text{out}}$	[K]	297.46	343.24	296.64	342.38	296.31	342.04	297.03	342.79	296.24	342.31
ΔT_c	[K]	43.67	45.78	42.85	45.74	42.53	45.73	43.24	45.76	42.46	46.07
$P_{c,\text{in}}$	[kPa]	45.683	45.303	45.675	45.239	45.672	45.338	45.679	45.302	45.672	45.439
$P_{c,\text{out}}$	[kPa]	45.303	44.739	45.239	44.704	45.338	44.896	45.302	44.885	45.439	45.193
ΔP_c	[kPa]	0.380	0.564	0.437	0.535	0.335	0.442	0.377	0.417	0.232	0.246
ΔP_h	[kPa]	0.397	0.346	0.416	0.327	0.408	0.355	0.320	0.241	0.280	0.258
D_{internal}	[N]	80.6	80.6	83.8	83.8	85.1	85.1	82.2	82.2	85.4	85.4
D_{external}	[N]	245.6	245.6	247.4	247.4	248.2	248.2	246.5	246.5	248.4	248.4
T_{nozzle}	[N]	284.8	296.0	288.7	300.5	292.3	306.1	286.9	300.7	294.0	311.6
D_{net}	[N]	41.4	30.2	42.5	30.7	41.0	27.2	41.8	28.0	39.8	22.1
Q	[kW]	71.10	74.68	71.10	76.04	71.10	76.62	71.08	75.34	71.09	77.30
ΔQ	[%]	+0.0	+16.7	+0.0	+18.8	+0.0	+19.7	+0.0	+17.7	+0.0	+20.8
T_{wall}	[K]	304.07	349.69	304.02	349.60	304.04	349.47	303.80	350.39	304.18	350.51
CR ISA											
$\dot{m}_c$	[kg/s]	1.462	1.462	1.489	1.489	1.499	1.499	1.475	1.475	1.502	1.502
$T_{c,\text{in}}$	[K]	253.80	296.61	253.80	295.83	253.80	295.55	253.80	296.24	253.80	295.49
$T_{c,\text{out}}$	[K]	296.61	327.26	295.83	326.65	295.55	326.43	296.24	326.96	295.49	326.59
ΔT_c	[K]	42.81	30.65	42.03	30.82	41.75	30.88	42.44	30.72	41.69	31.10
$P_{c,\text{in}}$	[kPa]	45.720	45.395	45.714	45.339	45.711	45.424	45.717	45.400	45.711	45.516
$P_{c,\text{out}}$	[kPa]	45.395	44.931	45.339	44.899	45.424	45.060	45.400	45.060	45.516	45.315
ΔP_c	[kPa]	0.325	0.464	0.375	0.440	0.288	0.364	0.317	0.340	0.195	0.201
ΔP_h	[kPa]	0.374	0.500	0.392	0.473	0.384	0.513	0.302	0.350	0.265	0.372
D_{internal}	[N]	65.5	65.5	68.0	68.0	68.9	68.9	66.7	66.7	69.1	69.1
D_{external}	[N]	234.5	234.5	236.6	236.6	237.3	237.3	235.5	235.5	237.5	237.5
T_{nozzle}	[N]	257.9	263.7	261.4	267.8	264.2	272.0	259.7	267.5	265.7	276.2
D_{net}	[N]	42.2	36.4	43.1	36.8	42.0	34.3	42.5	34.7	41.0	30.5
Q	[kW]	62.90	45.09	62.90	46.17	62.90	46.59	62.90	45.57	62.92	46.98
ΔQ	[%]	+0.0	+15.6	+0.0	+18.4	+0.0	+19.5	+0.0	+16.8	+0.0	+20.5
T_{wall}	[K]	302.23	331.09	302.19	330.99	302.21	330.90	302.00	331.52	302.36	331.56
TOD ISA											
$\dot{m}_c$	[kg/s]	1.515	1.515	1.514	1.514	1.525	1.525	1.512	1.512	1.595	1.595
$T_{c,\text{in}}$	[K]	253.80	289.94	253.80	289.95	253.80	289.69	253.80	290.00	253.79	288.11
$T_{c,\text{out}}$	[K]	289.94	324.57	289.95	324.30	289.69	324.07	290.00	324.45	288.11	323.35
ΔT_c	[K]	36.14	34.63	36.15	34.35	35.89	34.38	36.20	34.45	34.32	35.24
$P_{c,\text{in}}$	[kPa]	45.708	45.373	45.708	45.332	45.706	45.417	45.709	45.384	45.689	45.478
$P_{c,\text{out}}$	[kPa]	45.373	44.895	45.332	44.890	45.417	45.051	45.384	45.037	45.478	45.262
ΔP_c	[kPa]	0.335	0.479	0.376	0.442	0.289	0.366	0.324	0.347	0.211	0.216
ΔP_h	[kPa]	0.431	0.515	0.465	0.484	0.456	0.525	0.353	0.359	0.294	0.384
D_{internal}	[N]	70.4	70.4	70.3	70.3	71.3	71.3	70.1	70.1	78.1	78.1
D_{external}	[N]	238.5	238.5	238.4	238.4	239.2	239.2	238.3	238.3	244.0	244.0
T_{nozzle}	[N]	263.8	271.5	263.0	271.1	266.0	275.5	263.2	272.9	278.1	291.0
D_{net}	[N]	45.0	37.4	45.7	37.6	44.5	35.0	45.2	35.5	44.0	31.1
Q	[kW]	55.00	52.76	55.00	52.32	55.00	52.73	55.00	52.40	55.00	56.55
ΔQ	[%]	+0.0	+35.3	+0.0	+34.1	+0.0	+35.2	+0.0	+34.4	+0.0	+45.0
T_{wall}	[K]	294.55	329.18	295.46	329.32	295.48	329.23	294.88	329.81	293.64	329.51

Table A.3: Optimized condenser and radiator performance for different inclination angles under ISA+35 conditions.

Parameter	**Unit**	**0°**		**15°**		**30°**		**45°**		**60°**	
		Cond.	Rad.	Cond.	Rad.	Cond.	Rad.	Cond.	Rad.	Cond.	Rad.
General performance											
Mass	[kg]	12.53	11.70	10.75	11.61	11.34	11.59	9.99	10.93	10.43	11.49
Weighted pressure drop	[kPa]	0.410	0.583	0.468	0.548	0.358	0.453	0.410	0.433	0.255	0.259
TO ISA+35											
$\dot{m}_c$	[kg/s]	3.900	3.900	3.900	3.900	3.900	3.900	3.900	3.900	3.900	3.900
$T_{c,\text{in}}$	[K]	325.61	340.42	325.61	340.42	325.61	340.42	325.61	340.42	325.61	340.42
$T_{c,\text{out}}$	[K]	340.42	360.99	340.42	360.99	340.42	360.99	340.42	360.99	340.42	360.99
ΔT_c	[K]	14.81	20.57	14.81	20.57	14.81	20.57	14.81	20.57	14.81	20.57
$P_{c,\text{in}}$	[kPa]	103.291	102.378	103.291	102.272	103.291	102.538	103.291	102.345	103.291	102.725
$P_{c,\text{out}}$	[kPa]	102.378	101.207	102.272	101.203	102.538	101.665	102.345	101.447	102.725	102.220
ΔP_c	[kPa]	0.913	1.171	1.019	1.069	0.753	0.873	0.946	0.898	0.566	0.504
ΔP_h	[kPa]	0.051	0.254	0.054	0.245	0.051	0.261	0.042	0.176	0.037	0.175
D_{internal}	[N]	266.5	266.5	266.5	266.5	266.5	266.5	266.5	266.5	266.5	266.5
D_{external}	[N]	6.0	6.0	6.0	6.0	6.0	6.0	6.0	6.0	6.0	6.0
T_{nozzle}	[N]	185.8	34.0	176.7	26.5	195.1	118.4	177.5	78.3	203.3	169.1
D_{net}	[N]	86.6	238.5	95.8	246.0	77.3	154.1	94.9	194.2	69.2	103.4
Q	[kW]	58.20	81.00	58.20	81.00	58.20	81.00	58.20	81.00	58.20	81.00
ΔQ	[%]	+0.0	+0.0	+0.0	+0.0	+0.0	+0.0	+0.0	+0.0	+0.0	+0.0
T_{wall}	[K]	345.03	368.24	344.82	368.22	344.85	368.15	345.01	368.95	345.45	369.34
TOC ISA+35											
$\dot{m}_c$	[kg/s]	2.924	2.975	2.975	2.975	3.017	3.017	2.946	2.946	2.990	2.990
$T_{c,\text{in}}$	[K]	290.80	318.68	290.79	318.19	290.78	317.80	290.79	318.47	290.79	318.05
$T_{c,\text{out}}$	[K]	318.68	342.20	318.19	341.67	317.80	341.25	318.47	342.02	318.05	341.71
ΔT_c	[K]	27.88	23.52	27.40	23.48	27.02	23.45	27.68	23.55	27.26	23.66
$P_{c,\text{in}}$	[kPa]	45.112	44.006	45.075	43.832	45.050	44.107	45.095	43.930	45.074	44.357
$P_{c,\text{out}}$	[kPa]	44.006	42.494	43.832	42.421	44.107	42.936	43.930	42.759	44.357	43.666
ΔP_c	[kPa]	1.106	1.512	1.244	1.411	0.944	1.171	1.166	1.171	0.717	0.692
ΔP_h	[kPa]	0.096	0.356	0.101	0.336	0.099	0.365	0.078	0.249	0.068	0.265
D_{internal}	[N]	312.5	312.5	324.2	324.2	333.9	333.9	317.5	317.5	327.7	327.7
D_{external}	[N]	255.6	255.6	249.8	249.8	244.9	244.9	253.2	253.2	248.1	248.1
T_{nozzle}	[N]	494.3	455.7	496.3	460.0	511.6	486.2	492.2	465.8	512.6	506.4
D_{net}	[N]	73.8	112.4	77.7	114.0	67.2	92.6	78.4	104.8	63.1	69.4
Q	[kW]	82.00	69.27	82.00	70.35	82.00	71.24	82.00	69.87	82.00	71.25
ΔQ	[%]	+0.0	+3.1	+0.0	+4.7	+0.0	+6.0	+0.0	+4.0	+0.0	+6.0
T_{wall}	[K]	318.26	348.84	318.13	348.72	318.03	348.56	318.21	349.38	318.11	349.52
CR ISA+35											
$\dot{m}_c$	[kg/s]	2.624	2.624	2.672	2.672	2.705	2.705	2.646	2.646	2.682	2.682
$T_{c,\text{in}}$	[K]	290.86	318.60	290.85	318.08	290.84	317.74	290.85	318.36	290.85	317.99
$T_{c,\text{out}}$	[K]	318.60	334.08	318.08	333.64	317.74	333.35	318.36	333.89	317.99	333.67
ΔT_c	[K]	27.74	15.48	27.23	15.56	26.90	15.61	27.51	15.53	27.14	15.68
$P_{c,\text{in}}$	[kPa]	45.271	44.351	45.244	44.206	45.227	44.438	45.260	44.295	45.242	44.650
$P_{c,\text{out}}$	[kPa]	44.351	43.130	44.206	43.063	44.438	43.490	44.295	43.349	44.650	44.090
ΔP_c	[kPa]	0.920	1.221	1.038	1.143	0.789	0.948	0.965	0.945	0.592	0.559
ΔP_h	[kPa]	0.089	0.446	0.094	0.418	0.092	0.454	0.073	0.309	0.063	0.329
D_{internal}	[N]	248.9	248.9	258.7	258.7	265.4	265.4	253.3	253.3	260.6	260.6
D_{external}	[N]	270.7	270.7	270.1	270.1	269.7	269.7	270.4	270.4	270.0	270.0
T_{nozzle}	[N]	452.8	424.9	456.2	430.0	468.1	449.0	452.6	433.2	468.2	462.2
D_{net}	[N]	66.8	94.7	72.5	98.8	67.1	86.1	71.1	90.6	62.4	68.4
Q	[kW]	73.20	40.89	73.20	41.84	73.20	42.52	73.20	41.36	73.20	42.34
ΔQ	[%]	+0.0	-0.3	+0.0	+2.0	+0.0	+3.7	+0.0	+0.9	+0.0	+3.3
T_{wall}	[K]	317.55	337.97	317.42	337.86	317.33	337.74	317.50	338.29	317.40	338.35
TOD ISA+35											
$\dot{m}_c$	[kg/s]	2.383	2.383	2.422	2.422	2.450	2.450	2.399	2.399	2.435	2.435
$T_{c,\text{in}}$	[K]	290.90	317.85	290.89	317.42	290.89	317.11	290.90	317.67	290.89	317.26
$T_{c,\text{out}}$	[K]	317.85	335.20	317.42	334.80	317.11	334.53	317.67	335.05	317.26	334.81
ΔT_c	[K]	26.95	17.35	26.53	17.38	26.22	17.42	26.77	17.38	26.37	17.55
$P_{c,\text{in}}$	[kPa]	45.382	44.601	45.366	44.472	45.353	44.675	45.376	44.556	45.359	44.858
$P_{c,\text{out}}$	[kPa]	44.601	43.561	44.472	43.500	44.675	43.868	44.556	43.759	44.858	44.385
ΔP_c	[kPa]	0.782	1.040	0.894	0.972	0.678	0.806	0.820	0.797	0.501	0.473
ΔP_h	[kPa]	0.141	0.433	0.171	0.409	0.167	0.443	0.132	0.303	0.116	0.322
D_{internal}	[N]	203.9	203.9	210.8	210.8	215.9	215.9	206.7	206.7	213.2	213.2
D_{external}	[N]	271.9	271.9	271.9	271.9	271.8	271.8	271.9	271.9	271.9	271.9
T_{nozzle}	[N]	416.7	398.9	419.7	403.1	429.4	418.1	416.8	405.4	430.0	428.7
D_{net}	[N]	59.1	76.9	62.9	79.6	58.4	69.7	61.9	73.2	55.1	56.4
Q	[kW]	64.60	41.62	64.60	42.39	64.60	42.99	64.60	41.98	64.58	43.02
ΔQ	[%]	+0.0	+1.5	+0.0	+3.4	+0.0	+4.9	+0.0	+2.4	+0.0	+4.9
T_{wall}	[K]	315.99	339.13	323.72	339.05	323.75	338.94	323.65	339.48	324.01	339.54

A.2. Standalone Optimization

Table A.4: Geometry parameters for the standalone condenser and radiator optimized at 60° inclination.

Parameter	**Unit**	**LB**	**UB**	**Cond.**	**Rad.**
Geometry vector inputs (design variables)					
Heat exchanger width	w_{hx} [mm]	560	560	560.0	560.0
Heat exchanger height	h_{hx} [mm]	800	800	800.0	800.0
Flat tube pitch	p_{tube} [mm]	15.0	20.0	16.2	19.7
Flat tube height	h_{ft} [mm]	3.5	5.0	3.5	4.7
Microchannel width	w_{mc} [mm]	1.0	2.5	1.0	1.0
Microchannel wall thickness	t_{mc} [mm]	0.2	0.2	0.2	0.2
Fin pitch (OSF)	p_{fin} [mm]	2.5	5.0	2.5	2.7
Fin height (OSF)	h_{fin} [mm]	6.0	18.0	10.5	12.1
Fin thickness (OSF)	t_{fin} [mm]	0.15	0.15	0.15	0.15
Fin depth (OSF)	d_{fin} [mm]	2.5	12.0	2.5	2.8
Derived parameters (solved or calculated)					
Heat exchanger length	l_{hx} [mm]	–	–	77.9	45.8
Number of microchannels	n_{mc} [–]	–	–	64	38
Flat tube width	w_{ft} [mm]	–	–	77.9	45.8
Hydraulic diameter	d_{eq} [mm]	–	–	3.3	3.6
Porosity	ε [–]	–	–	0.70	0.67
Heat transfer area compactness	β_{hx} [m^2/m^3]	–	–	836	747
Mass	m_{hx} [kg]	–	–	11.1	6.1

Table A.5: Standalone optimized condenser performance for all operating points at 60° inclination.

Operating Point	$\dot{m}_c$ [kg/s]	$T_{c,\text{in}}$ [K]	$T_{c,\text{out}}$ [K]	ΔT_c [K]	$P_{c,\text{in}}$ [kPa]	$P_{c,\text{out}}$ [kPa]	ΔP_c [kPa]	ΔP_h [kPa]	D_{int} [N]	D_{ext} [N]	T_{noz} [N]	D_{net} [N]	Q [kW]	ΔQ [%]	T_{wall} [K]
TO ISA	2.126	290.43	311.74	21.31	103.766	103.626	0.140	0.160	69.7	83.7	134.2	19.2	45.60	+0.0	315.2
TOC ISA	1.618	253.79	297.53	43.75	45.684	45.501	0.183	0.406	80.4	245.4	286.9	38.8	71.10	+0.0	303.9
CR ISA	1.460	253.80	296.68	42.88	45.720	45.566	0.154	0.383	65.3	234.4	259.5	40.2	62.90	+0.0	302.0
TOD ISA	1.483	253.80	290.71	36.91	45.715	45.559	0.157	0.455	67.4	236.1	260.9	42.7	55.00	+0.0	295.4
TO ISA+35	3.900	325.61	340.42	14.80	103.290	102.829	0.461	0.052	266.5	6.0	210.5	62.0	58.20	+0.0	344.8
TOC ISA+35	2.923	290.80	318.70	27.90	45.111	44.544	0.568	0.167	312.2	255.8	507.7	60.3	82.00	+0.0	325.8
CR ISA+35	2.622	290.86	318.61	27.75	45.271	44.802	0.469	0.157	248.7	270.7	462.6	56.8	73.20	+0.0	324.9
TOD ISA+35	2.375	290.90	317.95	27.05	45.385	44.992	0.394	0.145	202.5	271.9	423.2	51.2	64.60	+0.0	316.0
Weighted pressure drop: 0.199 kPa															

Table A.6: Standalone optimized radiator performance for all operating points at 60° inclination.

Operating Point	$\dot{m}_c$ [kg/s]	$T_{c,\text{in}}$ [K]	$T_{c,\text{out}}$ [K]	ΔT_c [K]	$P_{c,\text{in}}$ [kPa]	$P_{c,\text{out}}$ [kPa]	ΔP_c [kPa]	ΔP_h [kPa]	D_{int} [N]	D_{ext} [N]	T_{noz} [N]	D_{net} [N]	Q [kW]	ΔQ [%]	T_{wall} [K]
TO ISA	1.538	290.44	340.13	49.69	103.846	103.794	0.052	0.341	36.4	80.4	104.9	11.9	77.00	+0.0	344.9
TOC ISA	0.900	253.83	324.57	70.74	45.818	45.771	0.047	0.454	24.7	174.6	169.1	30.1	64.00	+0.0	323.0
CR ISA	0.630	253.84	315.46	61.62	45.848	45.820	0.028	0.660	12.1	132.4	117.0	27.4	39.00	+0.0	310.1
TOD ISA	0.638	253.84	314.70	60.86	45.847	45.819	0.028	0.670	12.4	133.7	118.3	27.8	39.00	+0.0	309.5
TO ISA+35	3.900	325.61	346.21	20.60	103.290	103.011	0.279	0.331	266.5	6.0	224.4	48.1	81.00	+0.0	367.5
TOC ISA+35	1.949	290.96	325.23	34.27	45.551	45.385	0.167	0.471	135.0	266.0	359.3	41.6	67.20	+0.0	331.2
CR ISA+35	1.311	291.03	322.12	31.09	45.732	45.646	0.086	0.590	60.4	229.9	243.9	46.3	41.00	+0.0	323.9
TOD ISA+35	1.262	291.04	323.34	32.30	45.743	45.662	0.081	0.576	55.9	225.4	235.4	45.9	41.00	+0.0	324.9
Weighted pressure drop: 0.044 kPa															

B

POROUS MEDIA MODEL COEFFICIENTS

Table B.1: Summary of geometry (common to both operating points), reference data, calibration ranges, and fitted PMM coefficients for both heat exchangers for baseline: **0° inclination**

(a) Condenser

Parameter	**TO ISA**	**CR ISA**
Geometry		
w_{HX} [mm]	560	
h_{HX} [mm]	400	
l_{HX} [mm]	217.4	
ε [–]	0.7681	
d_{eq} [m]	0.0047	
β_{HX} [m^2]	652.9	
Reference rating data		
$\dot{m}_c$ [kg/s]	2.146	1.462
$P_{\mathrm{c,in}}$ [Pa]	103,763	45,720
$T_{\mathrm{c,in}}$ [K]	290.4	253.8
$\dot{Q}$ [kW]	45.60	62.90
ΔP_c [Pa]	283	325
ΔT_s [K]	21.1	42.8
T_{wall} [K]	315.2	302.2
Calibration range		
$\dot{m}_c$ [kg/s]	1.5–3.0	1.2–2.4
$P_{c,\mathrm{in}}$ [kPa]	100–105	42–47
$T_{c,\mathrm{in}}$ [K]	285–305	250–275
Source term coefficients		
$1/k_{xx,\mathrm{phys}}$ [m^{-2}]	2.761e+06	2.898e+06
$C_{2,\mathrm{phys}}$ [–]	10.356	9.879
$1/k_{xx,\mathrm{sup}}$ [m^{-2}]	3.594e+06	3.773e+06
$C_{2,\mathrm{sup}}$ [–]	17.551	16.743
a [–]	0.274	0.286
b [–]	0.566	0.561
c [–]	0.426	0.442
Wall-temperature correlation coefficients		
c_0 [K]	210.78	215.08
c_1 [K·s/kg]	270.78	181.76
c_2 [K·(s/kg)^2]	-274.12	-131.71
c_3 [K·(s/kg)^3]	135.96	39.06
c_4 [K·(s/kg)^4]	-33.02	-4.21
c_5 [K·(s/kg)^5]	3.13	0
c_6 [K·(s/kg)^6]	0	0
Calibration range (wall temperature correlation)		
$\dot{m}_c$ [kg/s]	1.5–3.0	1.2–3.0
$P_{c,\mathrm{in}}$ [Pa]	103,763	45,720
$T_{c,\mathrm{in}}$ [K]	290.4	253.8

(b) Radiator

Parameter	**TO ISA**	**CR ISA**
Geometry		
w_{HX} [mm]	560	
h_{HX} [mm]	400	
l_{HX} [mm]	187.4	
ε [–]	0.7508	
d_{eq} [m]	0.0040	
β_{HX} [m^2]	753.5	
Reference rating data		
$\dot{m}_c$ [kg/s]	2.146	1.462
$P_{\mathrm{c,in}}$ [Pa]	103,481	45,395
$T_{\mathrm{c,in}}$ [K]	311.5	296.6
$\dot{Q}$ [kW]	97.11	45.09
ΔP_c [Pa]	394	464
ΔT_s [K]	44.9	30.7
T_{wall} [K]	301.2	303.5
Calibration range		
$\dot{m}_c$ [kg/s]	1.5–3.0	1.25–2.4
$P_{c,\mathrm{in}}$ [kPa]	100–105	42–47
$T_{c,\mathrm{in}}$ [K]	290–340	260–315
Source term coefficients		
$1/k_{xx,\mathrm{phys}}$ [m^{-2}]	3.984e+06	4.237e+06
$C_{2,\mathrm{phys}}$ [–]	12.873	12.110
$1/k_{xx,\mathrm{sup}}$ [m^{-2}]	5.306e+06	5.642e+06
$C_{2,\mathrm{sup}}$ [–]	22.836	21.482
a [–]	0.308	0.319
b [–]	0.553	0.548
c [–]	0.412	0.393
Wall-temperature correlation coefficients		
t_0 [K]	354.97	317.88
t_1 [K·s/kg]	-23.18	-23.86
t_2 [K·(s/kg)^2]	0.55	0.58
t_3 [–]	0.04	0.05
t_4 [1/K]	8.60e-05	4.50e-05
t_5 [s/kg]	0.05	4.50e-05

Table B.2: Summary of geometry (common to both operating points), reference data, calibration ranges, and fitted PMM coefficients for both heat exchangers for **15° inclination**

(a) Condenser

Parameter	**TO ISA**	**CR ISA**
Geometry		
w_{HX} [mm]	560	
h_{HX} [mm]	414.2	
l_{HX} [mm]	136.0	
ε [–]	0.674029	
d_{eq} [m]	0.0034	
β_{HX} [m^2]	801.7	
Reference rating data		
$\dot{m}_c$ [kg/s]	2.177	1.489
$P_{\mathrm{c,in}}$ [Pa]	103,758	45,714
$T_{\mathrm{c,in}}$ [K]	290.42	253.80
$\dot{Q}$ [kW]	45.60	62.90
ΔP_c [Pa]	320	375
ΔT_s [K]	20.82	42.03
T_{wall} [K]	315.28	302.19
Calibration range		
$\dot{m}_c$ [kg/s]	1.5–3.0	1.2–2.4
$P_{c,\mathrm{in}}$ [kPa]	100–105	42–47
$T_{c,\mathrm{in}}$ [K]	285–305	250–275
Source term coefficients		
$1/k_{xx,\mathrm{phys}}$ [m^{-2}]	4.961e+06	5.230e+06
$C_{2,\mathrm{phys}}$ [–]	12.820	11.991
$1/k_{xx,\mathrm{sup}}$ [m^{-2}]	7.360e+06	7.759e+06
$C_{2,\mathrm{sup}}$ [–]	28.219	26.394
a [–]	0.282	0.296
b [–]	0.555	0.549
c [–]	0.447	0.454
Wall-temperature correlation coefficients		
c_0 [K]	-123.25	579.36
c_1 [K·s/kg]	1193.90	-958.94
c_2 [K·(s/kg)^2]	-1322.88	1327.47
c_3 [K·(s/kg)^3]	763.67	-937.74
c_4 [K·(s/kg)^4]	-241.96	357.09
c_5 [K·(s/kg)^5]	39.84	-70.07
c_6 [K·(s/kg)^6]	-2.66	5.57
Calibration range (wall temperature correlation)		
$\dot{m}_c$ [kg/s]	1.5–3.0	1.25–3.0
$P_{c,\mathrm{in}}$ [Pa]	103,481	45,395
$T_{c,\mathrm{in}}$ [K]	311.5	296.6

(b) Radiator

Parameter	**TO ISA**	**CR ISA**
Geometry		
w_{HX} [mm]	560	
h_{HX} [mm]	414.2	
l_{HX} [mm]	164.0	
ε [–]	0.721633	
d_{eq} [m]	0.0037	
β_{HX} [m^2]	778.4	
Reference rating data		
$\dot{m}_c$ [kg/s]	2.177	1.489
$P_{\mathrm{c,in}}$ [Pa]	103,439	45,339
$T_{\mathrm{c,in}}$ [K]	311.24	295.83
$\dot{Q}$ [kW]	97.69	46.17
ΔP_c [Pa]	368	440
ΔT_s [K]	44.51	30.82
T_{wall} [K]	365.23	330.99
Calibration range		
$\dot{m}_c$ [kg/s]	1.5–3.0	1.25–2.4
$P_{c,\mathrm{in}}$ [kPa]	100–105	42–47
$T_{c,\mathrm{in}}$ [K]	290–340	260–315
Source term coefficients		
$1/k_{xx,\mathrm{phys}}$ [m^{-2}]	4.461e+06	4.715e+06
$C_{2,\mathrm{phys}}$ [–]	11.991	11.225
$1/k_{xx,\mathrm{sup}}$ [m^{-2}]	6.182e+06	6.534e+06
$C_{2,\mathrm{sup}}$ [–]	23.027	21.556
a [–]	0.302	0.313
b [–]	0.551	0.545
c [–]	0.415	0.388
Wall-temperature correlation coefficients		
t_0 [K]	356.44	310.76
t_1 [K·s/kg]	-23.15	-28.01
t_2 [K·(s/kg)^2]	0.54	1.02
t_3 [–]	0.04	0.14
t_4 [1/K]	8.90e-05	-1.48e-04
t_5 [s/kg]	0.05	0.07

Table B.3: Summary of geometry (common to both operating points), reference data, calibration ranges, and fitted PMM coefficients for both heat exchangers for **30° inclination**

(a) Condenser

Parameter	**TO ISA**	**CR ISA**
Geometry		
w_{HX} [mm]	560	
h_{HX} [mm]	461.9	
l_{HX} [mm]	138.4	
ε [–]	0.701366	
d_{eq} [m]	0.0036	
β_{HX} [m^2]	769.3	
Reference rating data		
$\dot{m}_c$ [kg/s]	2.203	1.499
$P_{\mathrm{c,in}}$ [Pa]	103,754	45,711
$T_{\mathrm{c,in}}$ [K]	290.42	253.80
$\dot{Q}$ [kW]	45.60	62.90
ΔP_c [Pa]	245	288
ΔT_s [K]	20.57	41.75
T_{wall} [K]	315.29	302.21
Calibration range		
$\dot{m}_c$ [kg/s]	1.5–3.0	1.2–2.4
$P_{c,\mathrm{in}}$ [kPa]	100–105	42–47
$T_{c,\mathrm{in}}$ [K]	285–305	250–275
Source term coefficients		
$1/k_{xx,\mathrm{phys}}$ [m^{-2}]	4.686e+06	4.901e+06
$C_{2,\mathrm{phys}}$ [–]	11.695	10.917
$1/k_{xx,\mathrm{sup}}$ [m^{-2}]	6.682e+06	6.987e+06
$C_{2,\mathrm{sup}}$ [–]	23.774	22.192
a [–]	0.303	0.317
b [–]	0.549	0.543
c [–]	0.465	0.461
Wall-temperature correlation coefficients		
c_0 [K]	63.31	638.51
c_1 [K·s/kg]	653.11	-1138.39
c_2 [K·(s/kg)^2]	-678.58	1548.66
c_3 [K·(s/kg)^3]	360.04	-1080.04
c_4 [K·(s/kg)^4]	-101.78	407.70
c_5 [K·(s/kg)^5]	14.25	-79.53
c_6 [K·(s/kg)^6]	-0.74	6.30
Calibration range (wall temperature correlation)		
$\dot{m}_c$ [kg/s]	1.5–3.0	1.25–3.0
$P_{c,\mathrm{in}}$ [Pa]	103,481	45,395
$T_{c,\mathrm{in}}$ [K]	311.5	296.6

(b) Radiator

Parameter	**TO ISA**	**CR ISA**
Geometry		
w_{HX} [mm]	560	
h_{HX} [mm]	461.9	
l_{HX} [mm]	148.5	
ε [–]	0.731683	
d_{eq} [m]	0.0037	
β_{HX} [m^2]	791.0	
Reference rating data		
$\dot{m}_c$ [kg/s]	2.203	1.499
$P_{\mathrm{c,in}}$ [Pa]	103,510	45,424
$T_{\mathrm{c,in}}$ [K]	310.99	295.55
$\dot{Q}$ [kW]	98.42	46.59
ΔP_c [Pa]	307	364
ΔT_s [K]	44.32	30.88
T_{wall} [K]	365.08	330.90
Calibration range		
$\dot{m}_c$ [kg/s]	1.5–3.0	1.25–2.4
$P_{c,\mathrm{in}}$ [kPa]	100–105	42–47
$T_{c,\mathrm{in}}$ [K]	290–340	260–315
Source term coefficients		
$1/k_{xx,\mathrm{phys}}$ [m^{-2}]	4.601e+06	4.862e+06
$C_{2,\mathrm{phys}}$ [–]	14.046	13.157
$1/k_{xx,\mathrm{sup}}$ [m^{-2}]	6.288e+06	6.645e+06
$C_{2,\mathrm{sup}}$ [–]	26.236	24.575
a [–]	0.324	0.336
b [–]	0.546	0.540
c [–]	0.419	0.392
Wall-temperature correlation coefficients		
t_0 [K]	356.05	320.25
t_1 [K·s/kg]	-22.98	-23.21
t_2 [K·(s/kg)^2]	0.54	0.56
t_3 [–]	0.04	0.03
t_4 [1/K]	8.90e-05	7.70e-05
t_5 [s/kg]	0.05	0.06

Table B.4: Summary of geometry (common to both operating points), reference data, calibration ranges, and fitted PMM coefficients for both heat exchangers for **45° inclination**

(a) Condenser

Parameter	**TO ISA**	**CR ISA**
Geometry		
w_{HX} [mm]	560	
h_{HX} [mm]	565.7	
l_{HX} [mm]	98.6	
ε [–]	0.654491	
d_{eq} [m]	0.0033	
β_{HX} [m^2]	784.5	
Reference rating data		
$\dot{m}_c$ [kg/s]	2.159	1.475
$P_{\mathrm{c,in}}$ [Pa]	103,761	45,717
$T_{\mathrm{c,in}}$ [K]	290.43	253.80
$\dot{Q}$ [kW]	45.60	62.90
ΔP_c [Pa]	291	317
ΔT_s [K]	20.98	42.44
T_{wall} [K]	315.17	302.00
Calibration range		
$\dot{m}_c$ [kg/s]	1.5–3.0	1.2–2.4
$P_{c,\mathrm{in}}$ [kPa]	100–105	42–47
$T_{c,\mathrm{in}}$ [K]	285–305	250–275
Source term coefficients		
$1/k_{xx,\mathrm{phys}}$ [m^{-2}]	5.750e+06	5.466e+06
$C_{2,\mathrm{phys}}$ [–]	40.319	41.124
$1/k_{xx,\mathrm{sup}}$ [m^{-2}]	8.785e+06	8.351e+06
$C_{2,\mathrm{sup}}$ [–]	94.124	96.003
a [–]	0.356	0.373
b [–]	0.555	0.550
c [–]	0.449	0.454
Wall-temperature correlation coefficients		
c_0 [K]	-111.81	544.24
c_1 [K·s/kg]	1183.73	-851.58
c_2 [K·(s/kg)^2]	-1337.16	1193.36
c_3 [K·(s/kg)^3]	788.16	-850.58
c_4 [K·(s/kg)^4]	-255.51	325.93
c_5 [K·(s/kg)^5]	43.17	-64.25
c_6 [K·(s/kg)^6]	-2.97	5.13
Calibration range (wall temperature correlation)		
$\dot{m}_c$ [kg/s]	1.5–3.0	1.25–3.0
$P_{c,\mathrm{in}}$ [Pa]	103,481	45,395
$T_{c,\mathrm{in}}$ [K]	311.5	296.6

(b) Radiator

Parameter	**TO ISA**	**CR ISA**
Geometry		
w_{HX} [mm]	560	
h_{HX} [mm]	565.7	
l_{HX} [mm]	112.2	
ε [–]	0.668717	
d_{eq} [m]	0.0034	
β_{HX} [m^2]	785.5	
Reference rating data		
$\dot{m}_c$ [kg/s]	2.159	1.475
$P_{\mathrm{c,in}}$ [Pa]	103,470	45,400
$T_{\mathrm{c,in}}$ [K]	311.41	296.24
$\dot{Q}$ [kW]	97.38	45.57
ΔP_c [Pa]	298	340
ΔT_s [K]	44.72	30.72
T_{wall} [K]	366.12	331.52
Calibration range		
$\dot{m}_c$ [kg/s]	1.5–3.0	1.25–2.4
$P_{c,\mathrm{in}}$ [kPa]	100–105	42–47
$T_{c,\mathrm{in}}$ [K]	290–340	260–315
Source term coefficients		
$1/k_{xx,\mathrm{phys}}$ [m^{-2}]	5.184e+06	5.404e+06
$C_{2,\mathrm{phys}}$ [–]	29.994	29.197
$1/k_{xx,\mathrm{sup}}$ [m^{-2}]	7.752e+06	8.082e+06
$C_{2,\mathrm{sup}}$ [–]	67.074	65.291
a [–]	0.358	0.371
b [–]	0.547	0.541
c [–]	0.416	0.392
Wall-temperature correlation coefficients		
t_0 [K]	344.26	322.07
t_1 [K·s/kg]	-22.19	-22.36
t_2 [K·(s/kg)^2]	0.86	0.52
t_3 [–]	0.13	0.03
t_4 [1/K]	-6.10e-05	7.40e-05
t_5 [s/kg]	0.05	0.06

Table B.5: Summary of geometry (common to both operating points), reference data, calibration ranges, and fitted PMM coefficients for both heat exchangers for **60° inclination**

(a) Condenser

Parameter	**TO ISA**	**CR ISA**
Geometry		
w_{HX} [mm]	560	
h_{HX} [mm]	800.0	
l_{HX} [mm]	67.4	
ε [–]	0.607704	
d_{eq} [m]	0.0030	
β_{HX} [m^2]	808.5	
Reference rating data		
$\dot{m}_c$ [kg/s]	2.228	1.502
$P_{\mathrm{c,in}}$ [Pa]	103,750	45,711
$T_{\mathrm{c,in}}$ [K]	290.42	253.80
$\dot{Q}$ [kW]	45.60	62.92
ΔP_c [Pa]	184	195
ΔT_s [K]	20.34	41.69
T_{wall} [K]	315.09	302.36
Calibration range		
$\dot{m}_c$ [kg/s]	1.5–3.0	1.2–2.4
$P_{c,\mathrm{in}}$ [kPa]	100–105	42–47
$T_{c,\mathrm{in}}$ [K]	285–305	250–275
Source term coefficients		
$1/k_{xx,\mathrm{phys}}$ [m^{-2}]	6.655e+06	6.368e+06
$C_{2,\mathrm{phys}}$ [–]	60.342	61.354
$1/k_{xx,\mathrm{sup}}$ [m^{-2}]	1.095e+07	1.048e+07
$C_{2,\mathrm{sup}}$ [–]	163.393	166.135
a [–]	0.384	0.401
b [–]	0.550	0.543
c [–]	0.459	0.461
Wall-temperature correlation coefficients		
c_0 [K]	261.55	641.77
c_1 [K·s/kg]	93.78	-1137.59
c_2 [K·(s/kg)^2]	-31.51	1532.94
c_3 [K·(s/kg)^3]	-33.31	-1059.80
c_4 [K·(s/kg)^4]	30.74	396.97
c_5 [K·(s/kg)^5]	-9.22	-76.91
c_6 [K·(s/kg)^6]	0.96	6.05
Calibration range (wall temperature correlation)		
$\dot{m}_c$ [kg/s]	1.5–3.0	1.25–3.0
$P_{c,\mathrm{in}}$ [Pa]	103,481	45,395
$T_{c,\mathrm{in}}$ [K]	311.5	296.6

(b) Radiator

Parameter	**TO ISA**	**CR ISA**
Geometry		
w_{HX} [mm]	560	
h_{HX} [mm]	800.0	
l_{HX} [mm]	83.6	
ε [–]	0.677671	
d_{eq} [m]	0.0034	
β_{HX} [m^2]	803.8	
Reference rating data		
$\dot{m}_c$ [kg/s]	2.228	1.502
$P_{\mathrm{c,in}}$ [Pa]	103,566	45,516
$T_{\mathrm{c,in}}$ [K]	310.76	295.49
$\dot{Q}$ [kW]	100.35	46.98
ΔP_c [Pa]	182	201
ΔT_s [K]	44.67	31.10
T_{wall} [K]	366.20	331.56
Calibration range		
$\dot{m}_c$ [kg/s]	1.5–3.0	1.25–2.4
$P_{c,\mathrm{in}}$ [kPa]	100–105	42–47
$T_{c,\mathrm{in}}$ [K]	290–340	260–315
Source term coefficients		
$1/k_{xx,\mathrm{phys}}$ [m^{-2}]	5.497e+06	5.604e+06
$C_{2,\mathrm{phys}}$ [–]	51.309	50.830
$1/k_{xx,\mathrm{sup}}$ [m^{-2}]	8.111e+06	8.270e+06
$C_{2,\mathrm{sup}}$ [–]	111.727	110.684
a [–]	0.416	0.431
b [–]	0.540	0.534
c [–]	0.421	0.394
Wall-temperature correlation coefficients		
t_0 [K]	344.77	323.02
t_1 [K·s/kg]	-21.62	-21.72
t_2 [K·(s/kg)^2]	0.85	0.50
t_3 [–]	0.13	0.03
t_4 [1/K]	-7.00e-05	7.30e-05
t_5 [s/kg]	0.05	0.06

C

Mesh Refinement Study

Nozzle Outlet Mesh Refinement

During mesh convergence studies on the baseline (0° inclination) duct geometry, a local mesh-sensitivity issue was identified at the nozzle outlet. Although integrated quantities such as thrust appeared converged, the total pressure field exhibited a clear numerical artifact: a sharp, nonphysical increase in total pressure in the final cells adjacent to the outlet boundary. With insufficient refinement, this even produced a net total pressure increase over the nozzle section, which is physically impossible. This artifact is illustrated in the local flow field and mass-averaged profiles shown in Figure C.1.

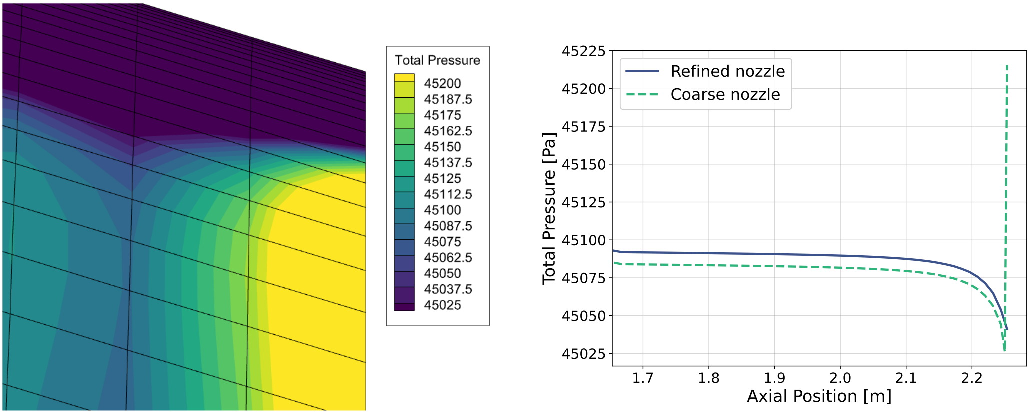

(a) Local total pressure contours.

(b) Mass-averaged total pressure for coarse vs. refined mesh.

Figure C.1: Nonphysical total pressure spike at the nozzle outlet.

This behavior arises from two combined effects. First, the 2D modeling approach imposes a constant duct width, reducing the effective nozzle height compared to the real 3D geometry and amplifying local gradients. Second, the converging nozzle accelerates the flow significantly, producing high velocity and static pressure gradients near the outlet where a static pressure boundary condition is applied. These high gradients, shown in Figure C.2, cannot be resolved on a coarse mesh, causing the solver to generate an artificial rise in total pressure.

To eliminate the numerical artifact, a targeted outlet-edge refinement was introduced in *Ansys Meshing*. A boundary-edge sizing was applied along the nozzle outlet, refining the mesh in the streamwise direction with near-unity aspect ratio and a growth rate. A refinement study was performed to determine the required edge size, as shown in Figure C.3. The selected outlet-edge size of 1.5×10^{-5} m removes the total-pressure spike and produces a smooth, physically consistent distribution as shown in Figure C.1b. Depending on nozzle height, this refinement adds approximately 200,000 cells relative to the unrefined mesh.

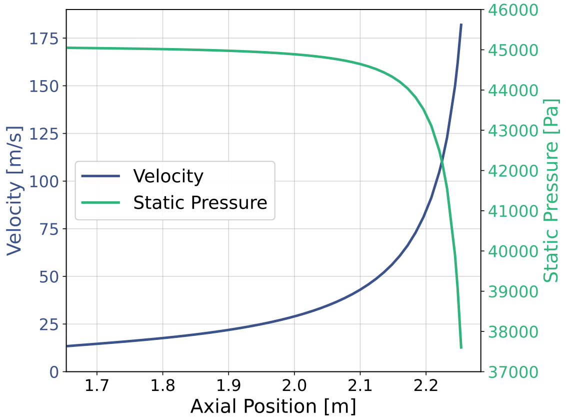

Figure C.2: Mass-averaged velocity and static pressure through the nozzle section.

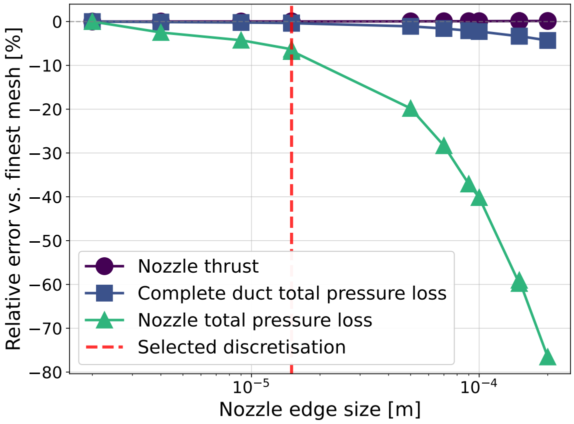

Figure C.3: Mesh refinement study for the nozzle outlet.

The effect of this refinement is quantified in Figure C.1b and Figure C.3. Without refinement, the error in nozzle total-pressure loss is on the order of 100 Pa. With proper refinement, this reduces to below 5 Pa. Notably, the total-pressure loss of the complete duct varies by only about 5% across refinement levels, and nozzle thrust is largely unaffected. This confirms that although integrated performance quantities converge rapidly, accurate outlet resolution is essential when comparing CFD predictions with the reduced-order nozzle model in Subsection 3.2.5.

The selected outlet-edge refinement of 1.5×10^{-5} m is applied uniformly across all heat exchanger inclination cases to ensure consistent mesh quality and enable fair comparison between configurations.

D

CFD Results

D.1. Baseline

D.1.1. Mass Flow Sweep

Operating Point: TO ISA

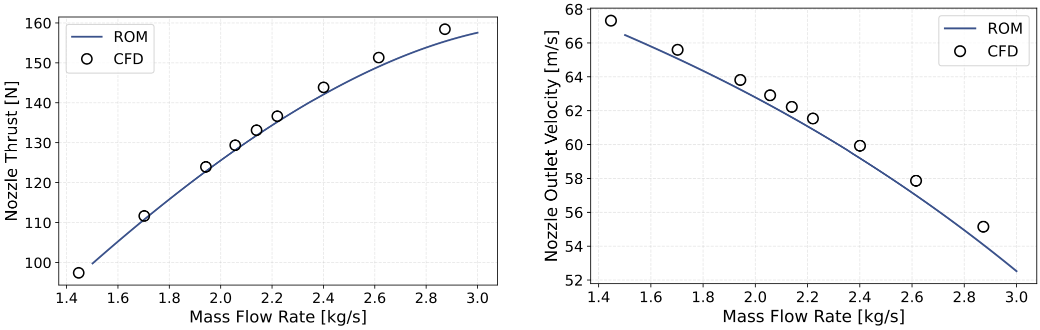

(a) Nozzle thrust

(b) Nozzle outlet velocity

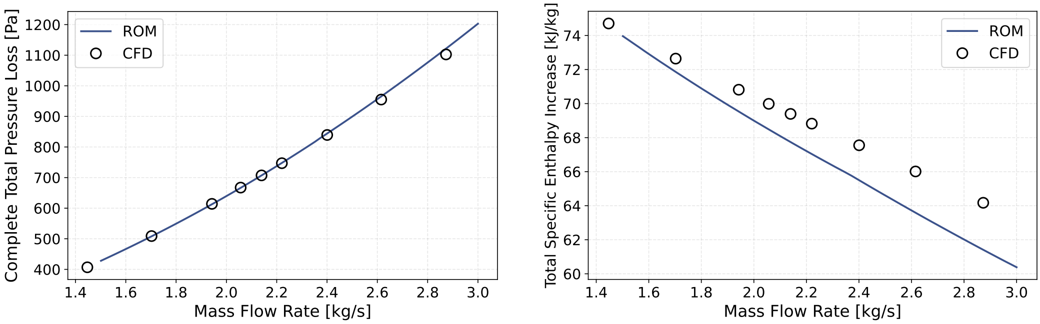

(c) Total pressure loss in the duct

(d) Total specific enthalpy increase in the duct

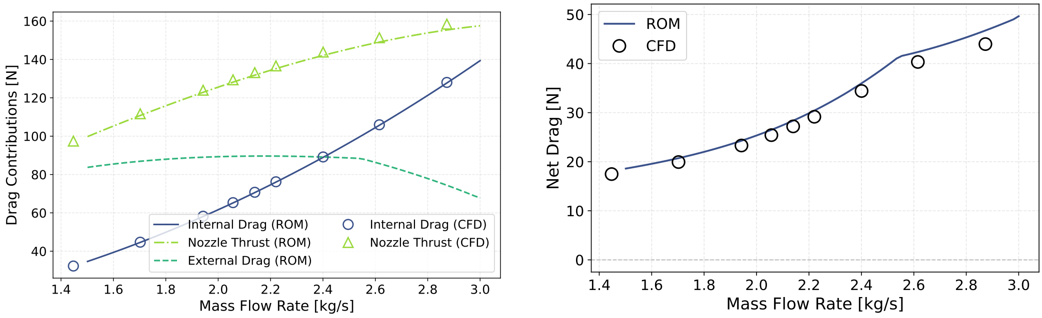

(e) All drag contributions

(f) Net drag

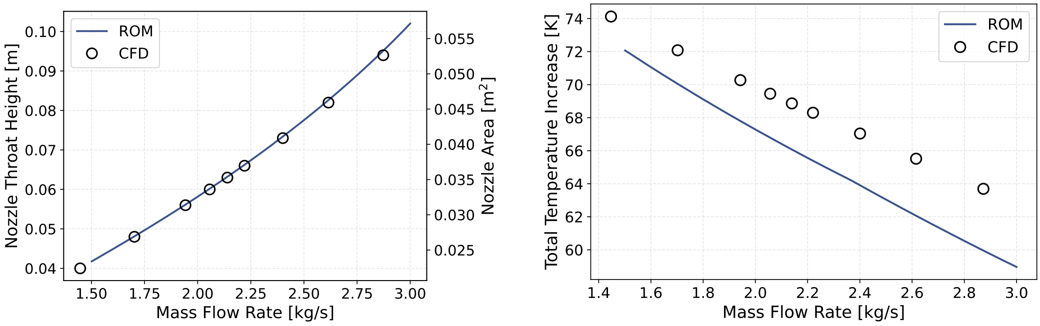

(g) Nozzle throat height and area

(h) Total temperature increase in the duct

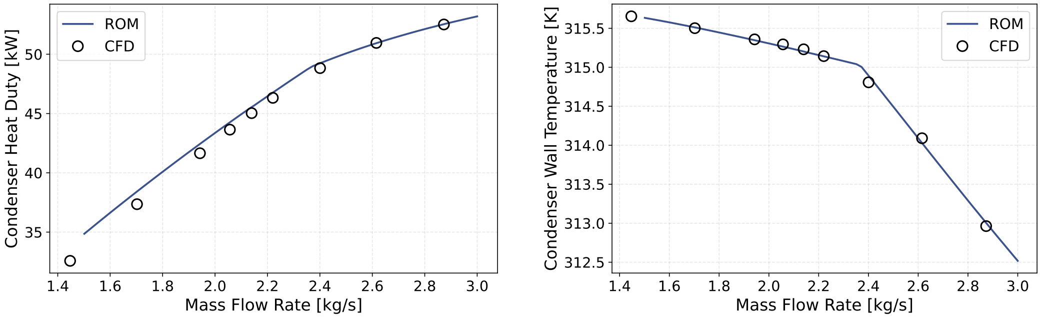

(i) Heat transfer rate in the condenser

(j) Wall temperature in the condenser

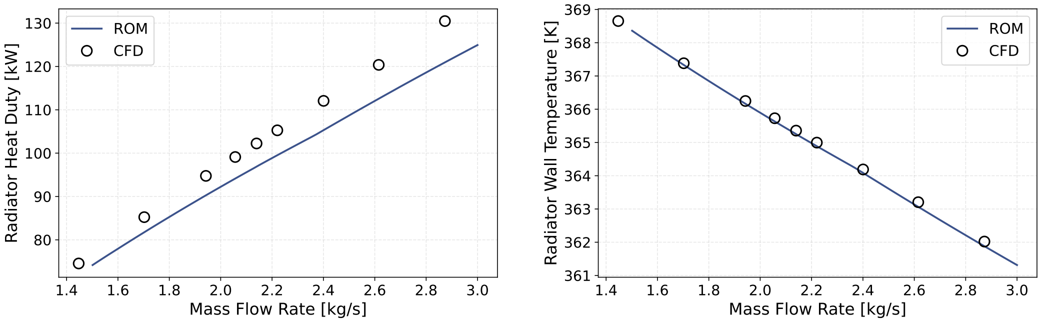

(k) Heat transfer rate in the radiator

(l) Wall temperature in the radiator

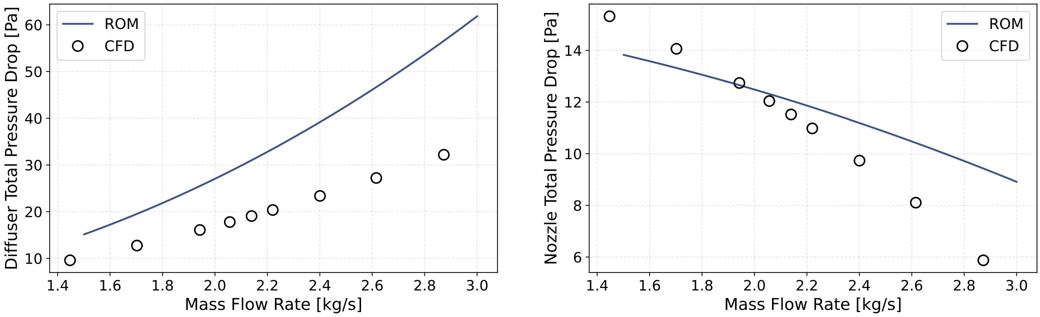

(m) Pressure drop across the diffuser

(n) Pressure drop across the nozzle

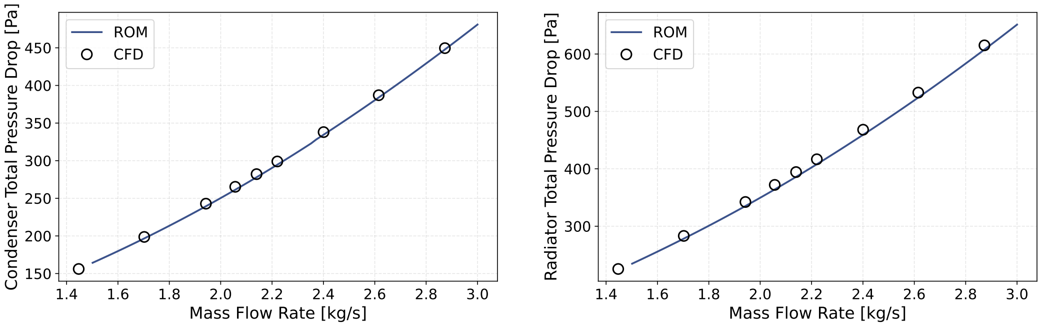

(o) Total pressure drop over the condenser

(p) Total pressure drop over the radiator

Table D.1: Baseline ram air duct comparison for **TO ISA** conditions during a mass flow sweep achieved by adjusting the nozzle throat area, as shown in (g). Results compare the CFD model and the Reduced-Order Model (ROM) predictions.

Operating Point: CR ISA

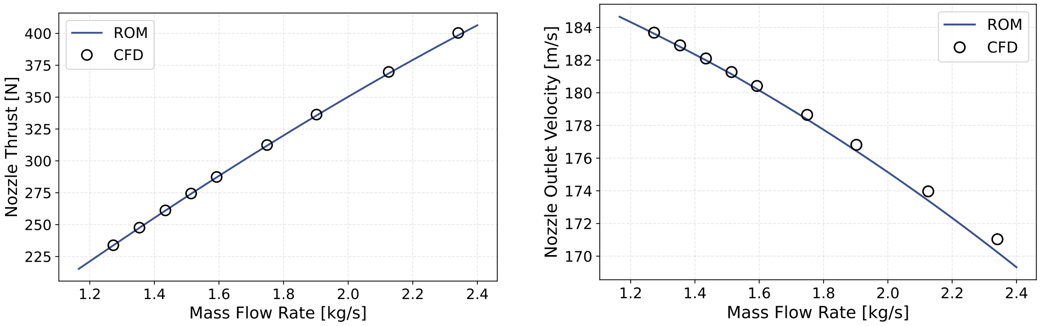

(a) Nozzle thrust

(b) Nozzle outlet velocity

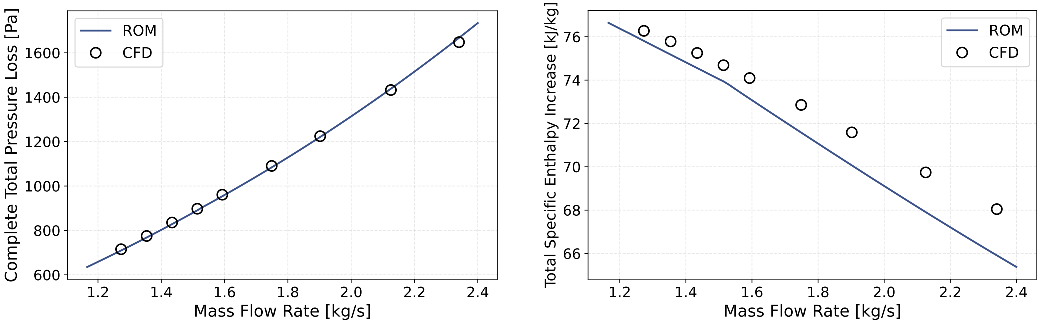

(c) Total pressure loss in the duct

(d) Total specific enthalpy increase in the duct

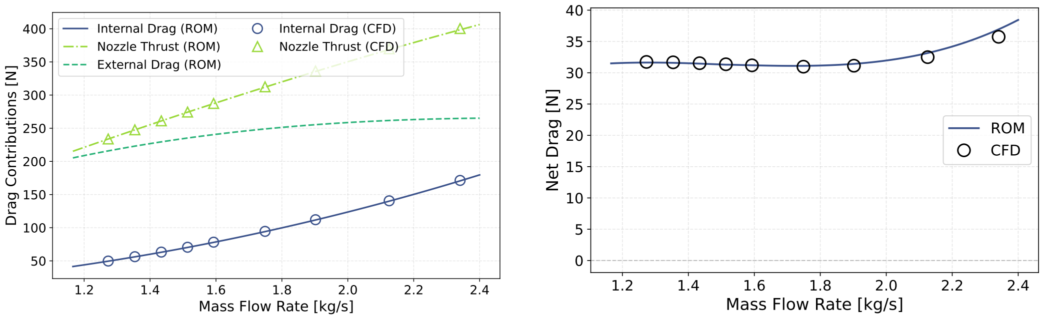

(e) All drag contributions

(f) Net drag

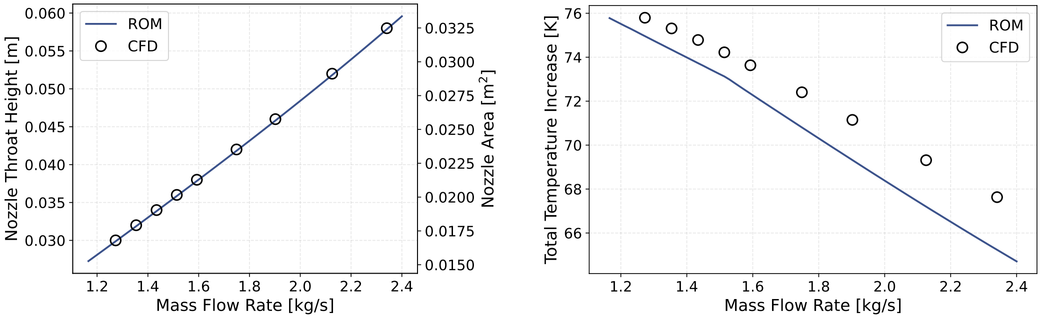

(g) Nozzle throat height and area

(h) Total temperature increase in the duct

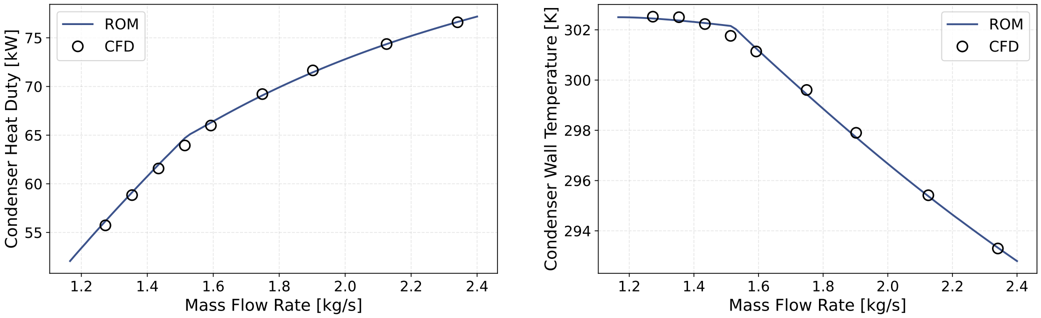

(i) Heat transfer rate in the condenser

(j) Wall temperature in the condenser

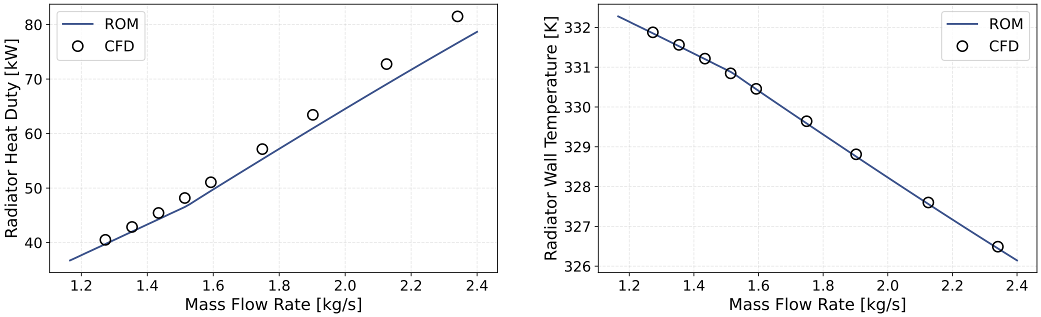

(k) Heat transfer rate in the radiator

(l) Wall temperature in the radiator

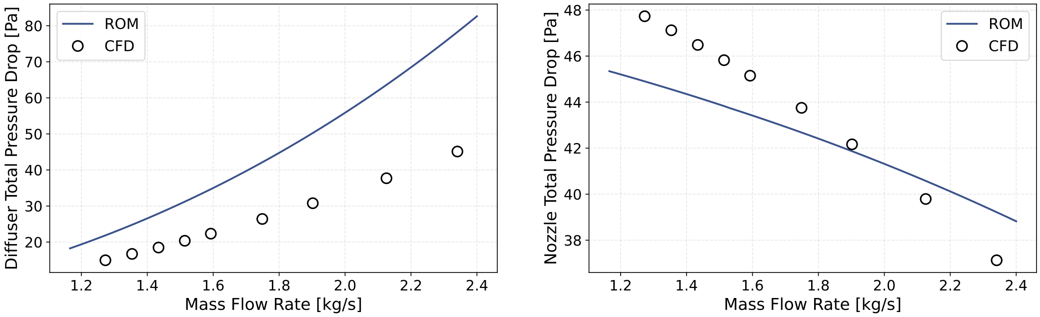

(m) Pressure drop across the diffuser

(n) Pressure drop across the nozzle

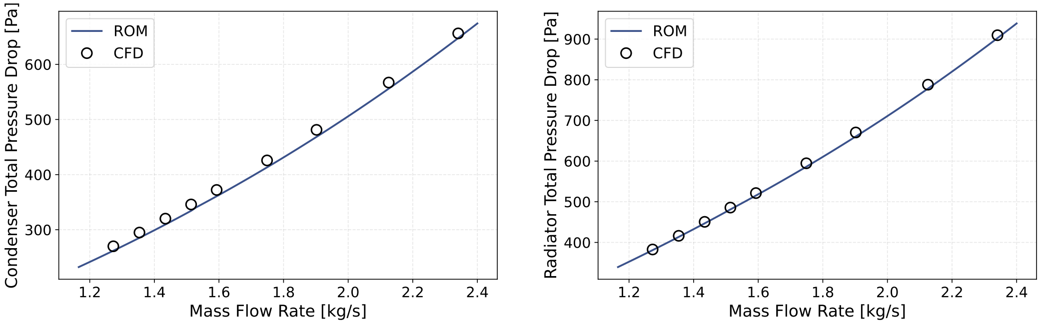

(o) Total pressure drop over the condenser

(p) Total pressure drop over the radiator

Table D.2: Baseline ram air duct comparison for **CR ISA** conditions during a mass flow sweep achieved by adjusting the nozzle throat area, as shown in (g). Results compare the CFD model and the Reduced-Order Model (ROM) predictions.

D.1.2. AXIAL FLOW DISTRIBUTION

To asses the agreement of flow properties along the duct, mass-averaged flow properties along the duct are compared to the ROM predictions corresponding to one mass flow close to the design point, for both TO ISA and CR ISA operating points. Since the ROM also includes the intake, the freestream (∞) is incorporated in the comparison to capture the complete flow development through the system. For some flow properties a zoomed-in view near the heat exchanger (HX) sections are provided.

OPERATING POINT: TO ISA

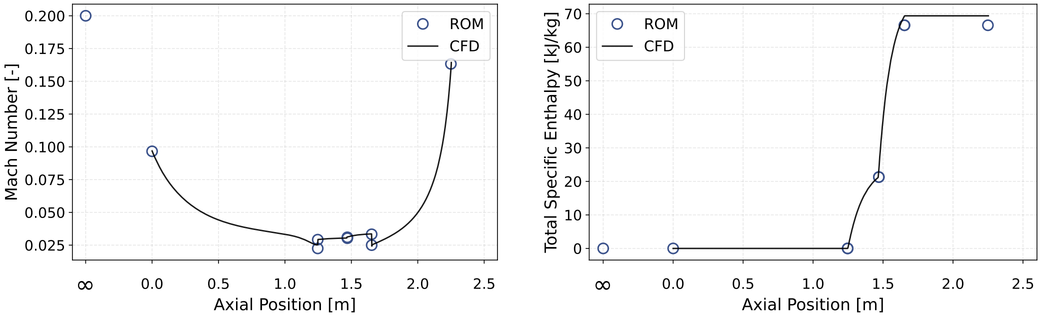

(a) Mach number distribution along the duct

(b) Total specific enthalpy along the duct

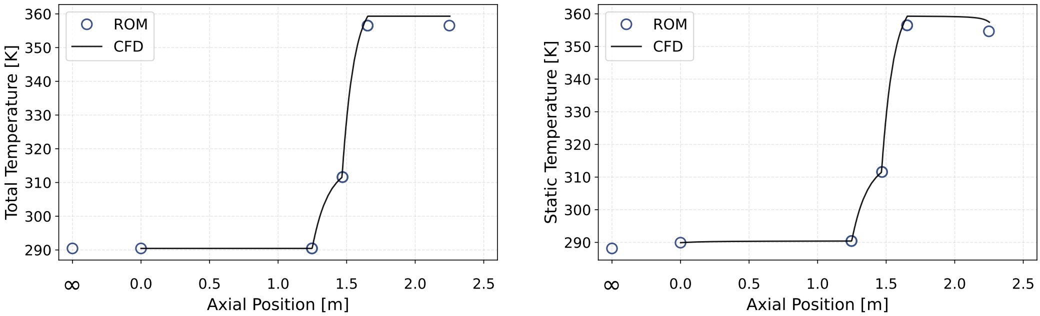

(c) Total temperature variation along the duct

(d) Static temperature variation along the duct

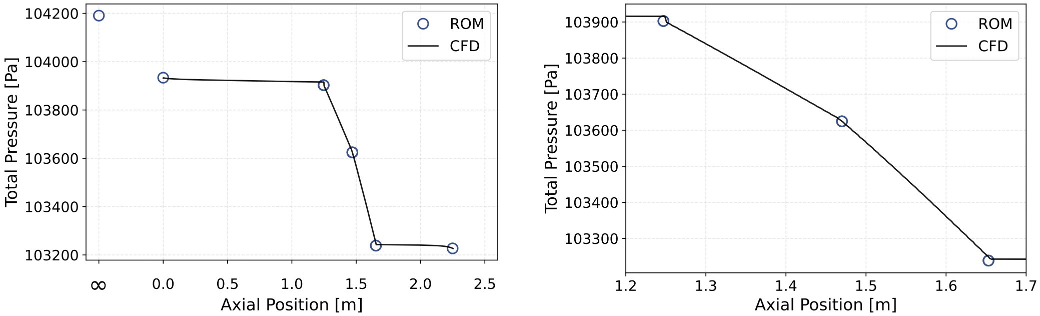

(e) Total pressure distribution along the duct

(f) Zoomed-in total pressure near HX regions

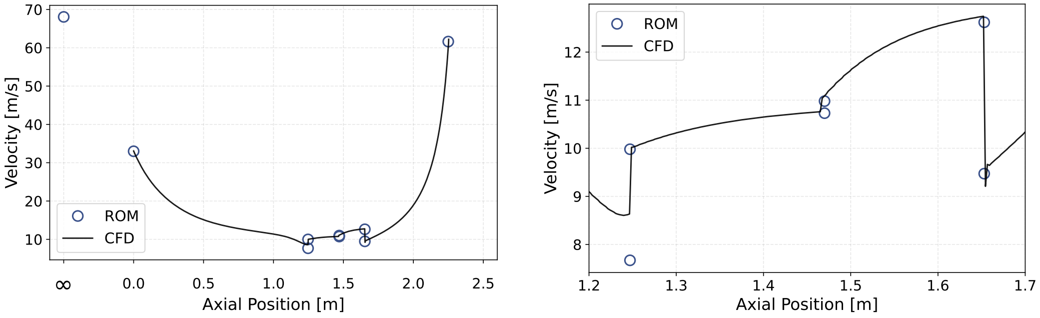

(g) Velocity magnitude along the duct

(h) Zoomed-in velocity near HX regions

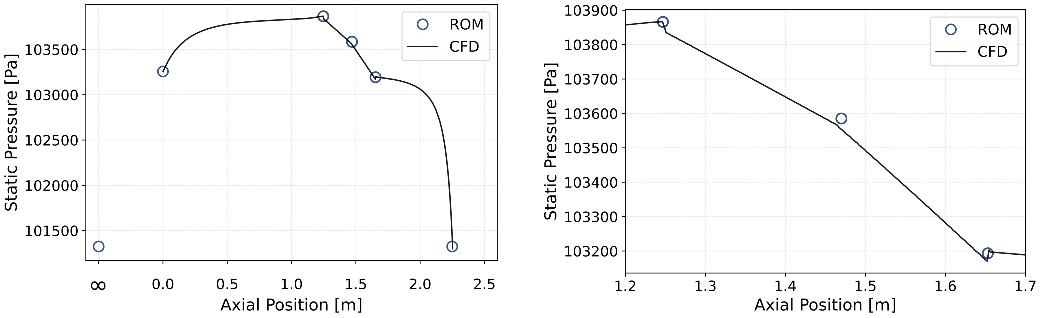

(i) Static pressure distribution along the duct

(j) Zoomed-in static pressure near HX regions

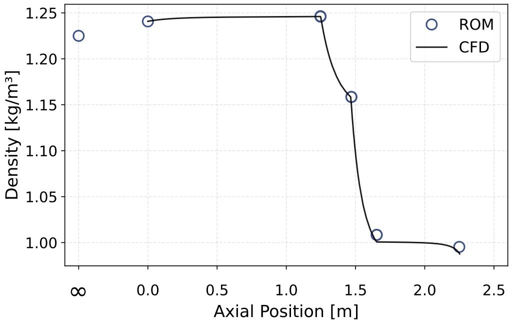

(k) Density variation along the duct

Table D.3: Axial variation of key flow quantities from CFD and ROM predictions for the baseline configuration at **TO ISA**, near the design point corresponding to a mass flow rate of $\dot{m} = 2.140$ kg/s. The CFD results represent mass-flow-averaged quantities along the duct. Zoomed-in views highlight the flow behavior near the condenser and radiator heat exchanger (HX) regions, where the most significant local changes occur.

Operating Point: CR ISA

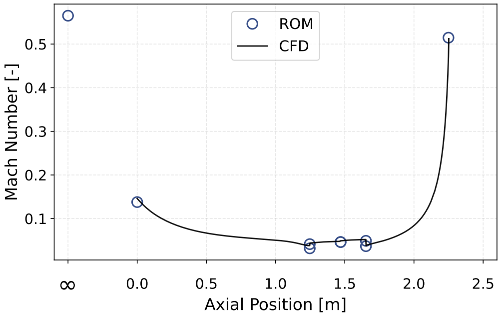

(a) Mach number distribution along the duct

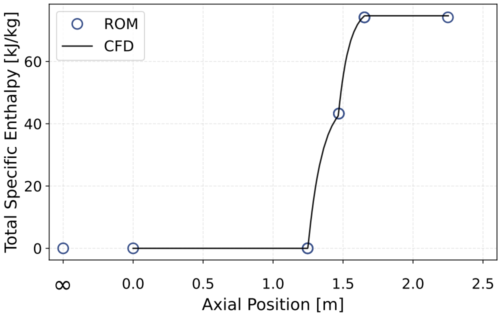

(b) Total specific enthalpy along the duct

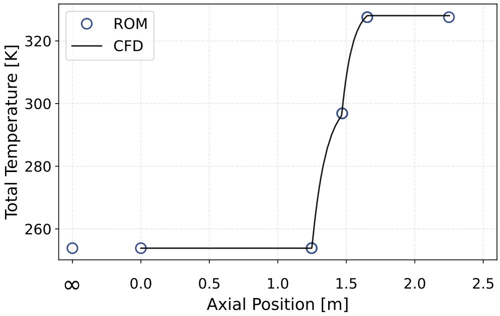

(c) Total temperature variation along the duct

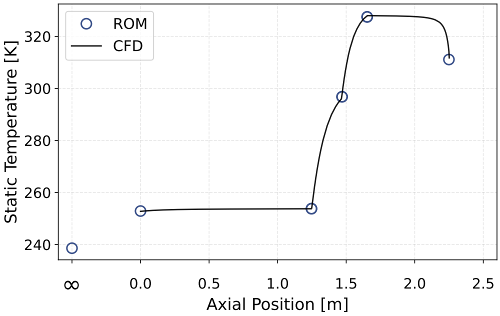

(d) Static temperature variation along the duct

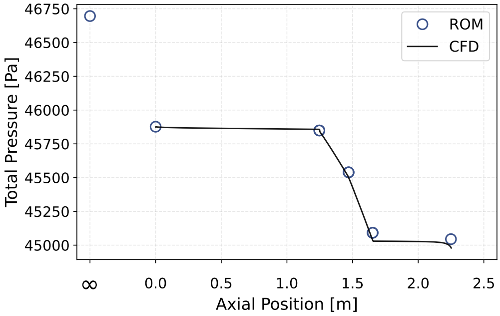

(e) Total pressure distribution along the duct

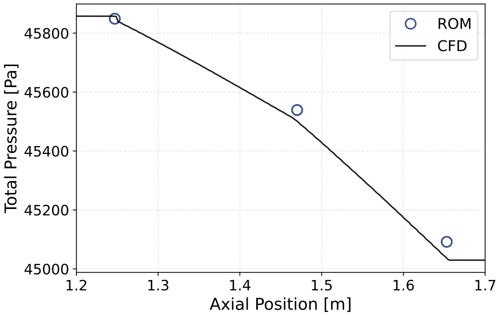

(f) Zoomed-in total pressure near HX regions

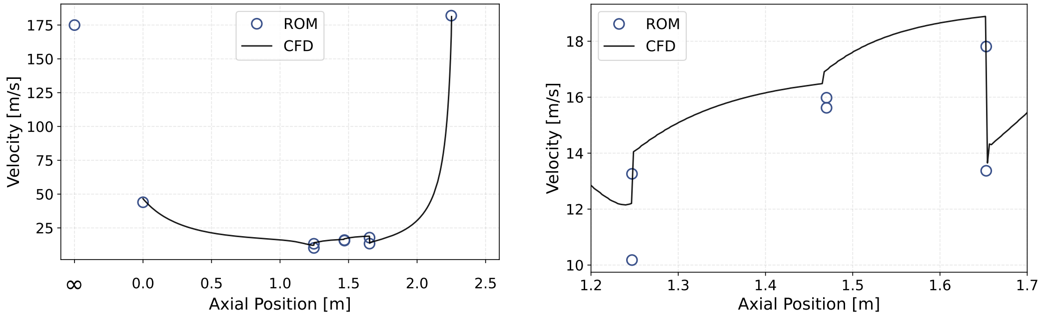

(g) Velocity magnitude along the duct

(h) Zoomed-in velocity near HX regions

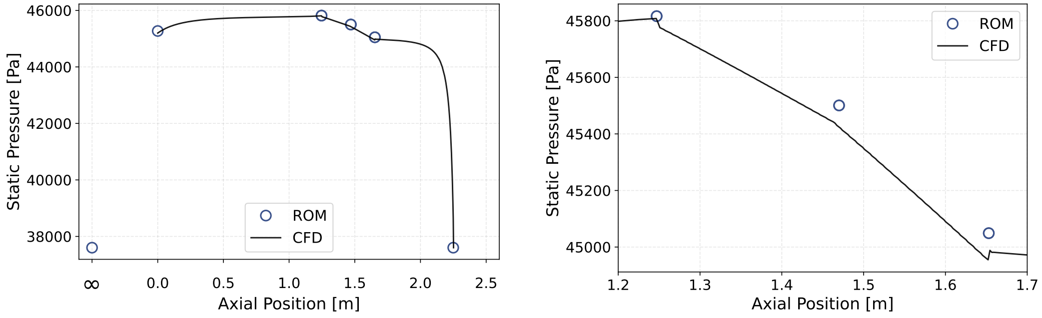

(i) Static pressure distribution along the duct

(j) Zoomed-in static pressure near HX regions

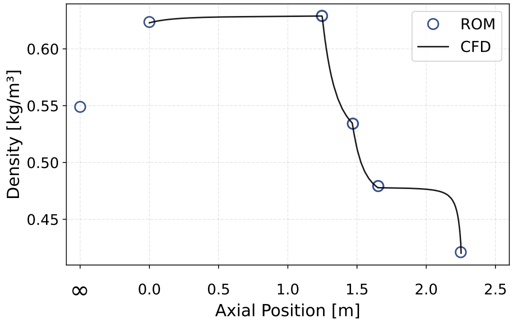

(k) Density variation along the duct

Table D.4: Axial variation of key flow quantities from CFD and ROM predictions for the baseline configuration at **CR ISA**, near the design point corresponding to a mass flow rate of $\dot{m} = 1.514$ kg/s. The CFD results represent mass-flow-averaged quantities along the duct. Zoomed-in views highlight the flow behavior near the condenser and radiator heat exchanger (HX) regions, where the most significant local changes occur.

D.2. ALL INCLINATION ANGLES

OPERATING POINT: CR ISA

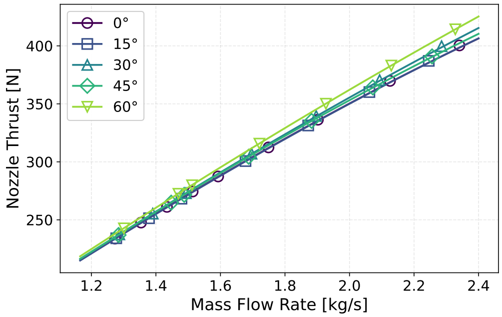

(a) Nozzle thrust

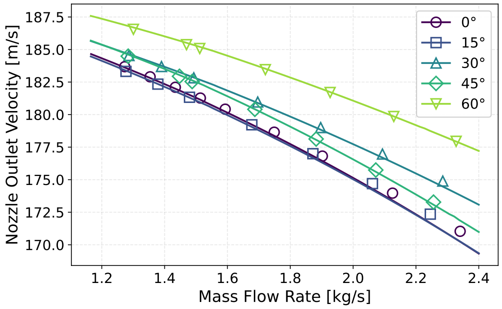

(b) Nozzle outlet velocity

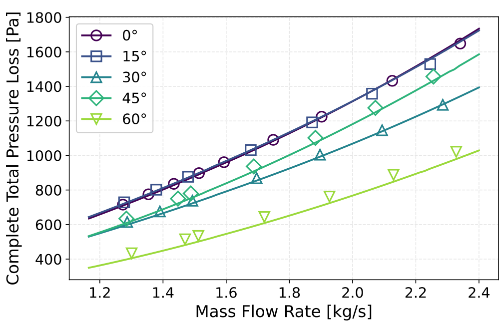

(c) Total pressure loss in the duct

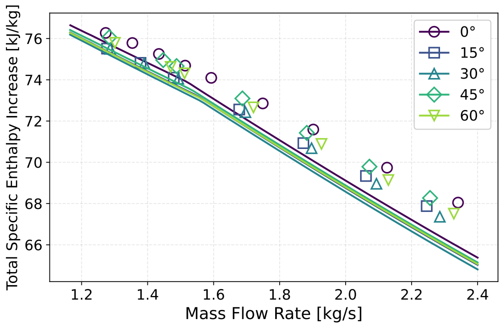

(d) Total specific enthalpy increase in the duct

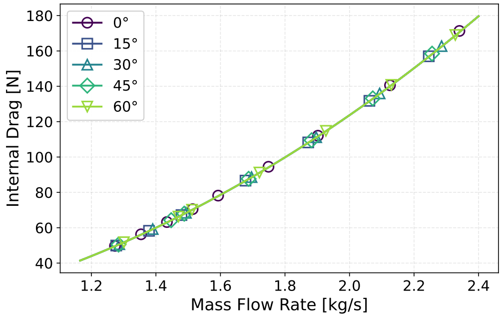

(e) Internal drag

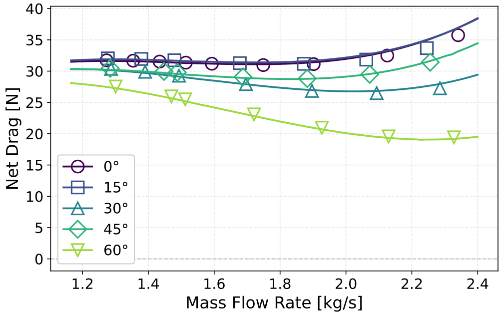

(f) Net drag

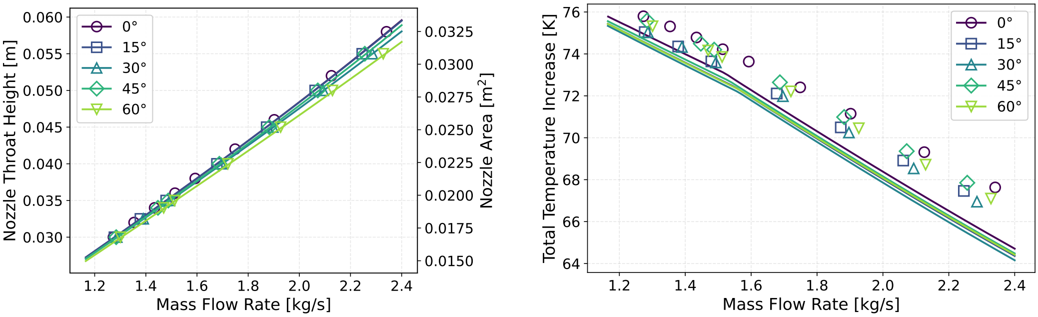

(g) Nozzle throat height and area

(h) Total temperature increase in the duct

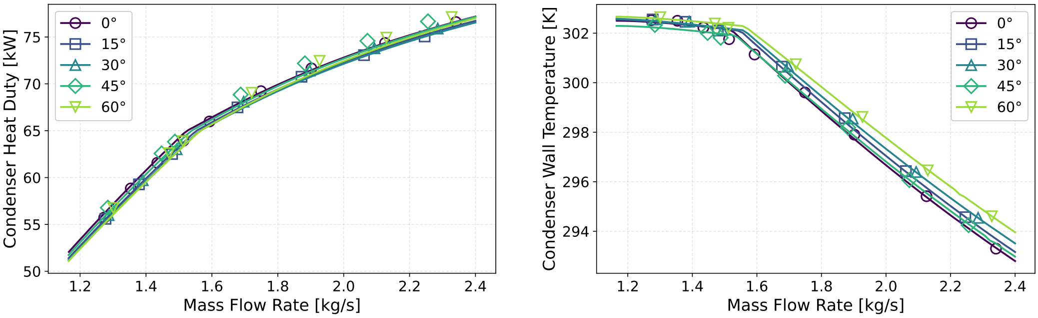

(i) Heat transfer rate in the condenser

(j) Wall temperature in the condenser

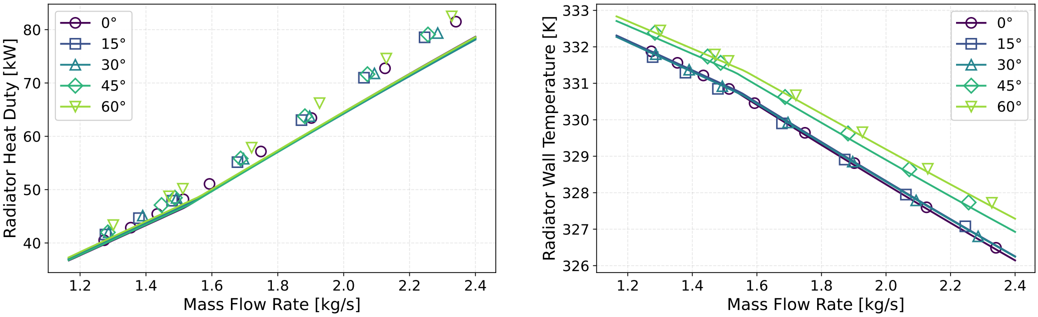

(k) Heat transfer rate in the radiator

(l) Wall temperature in the radiator

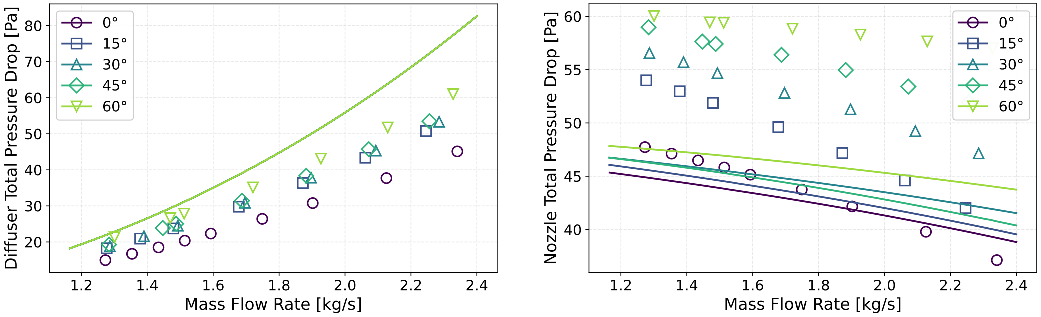

(m) Pressure drop across the diffuser

(n) Pressure drop across the nozzle (includes tilt back region)

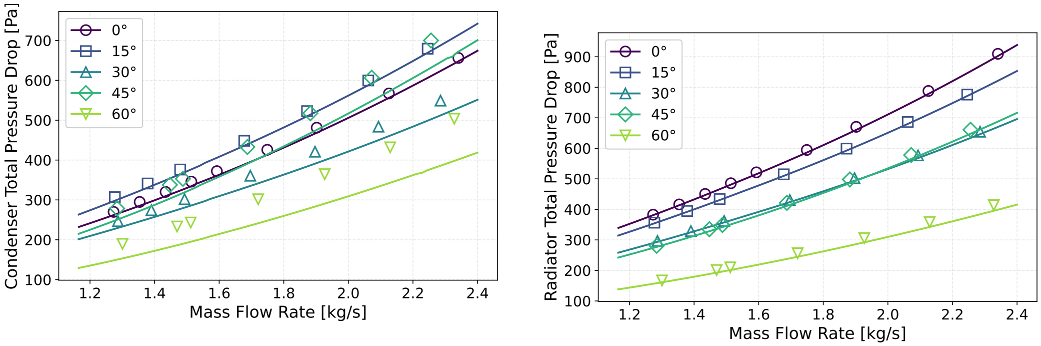

(o) Total pressure drop over the condenser (includes tilt region)

(p) Total pressure drop over the radiator

Table D.5: Ram air duct comparison for **CR ISA** conditions across all inclination angles α during a mass flow sweep achieved by adjusting the nozzle throat area, as shown in (g). Solid lines: ROM predictions; Markers: CFD results.

D.3. CONTOUR PLOTS

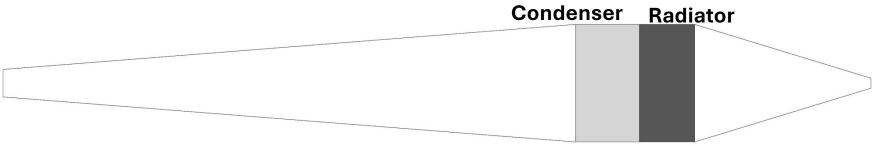

(a) Geometry

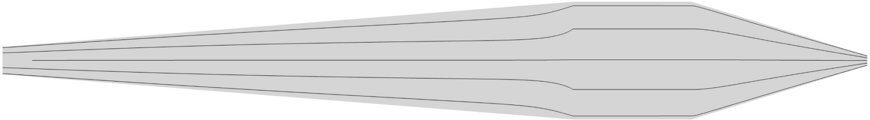

(b) Streamlines

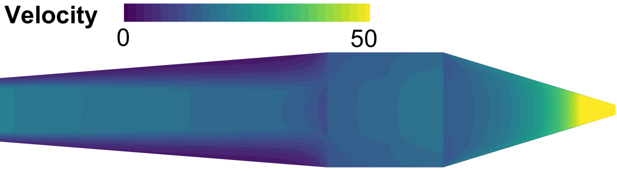

(c) Velocity [m/s]

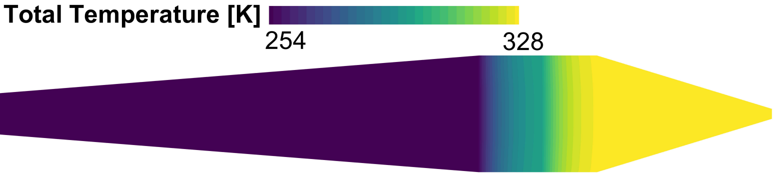

(d) Total temperature

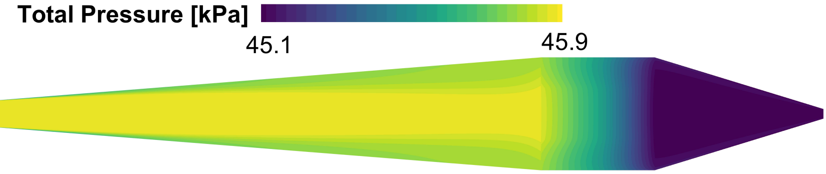

(e) Total pressure

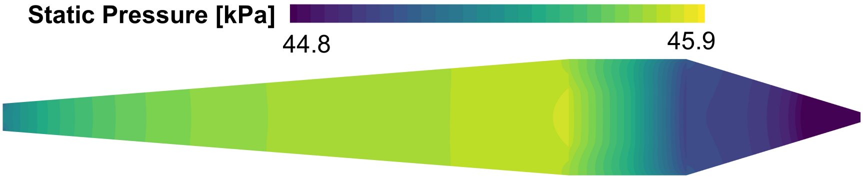

(f) Static pressure

Figure D.6: CFD contour plots for baseline configuration ($\alpha = 0°$) at design-point CR ISA.

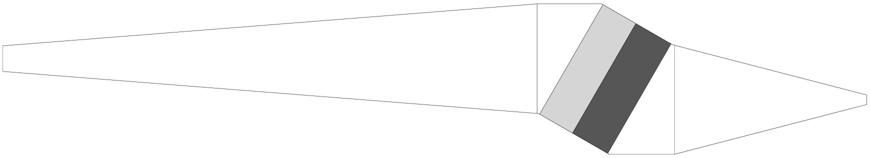

(a) Geometry

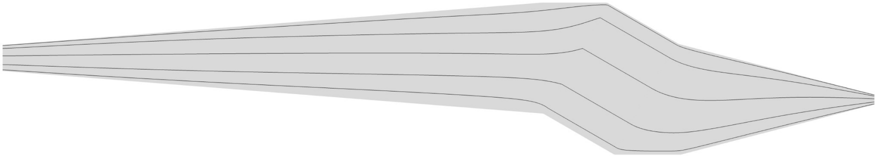

(b) Streamlines

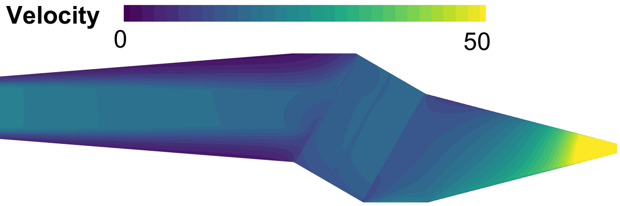

(c) Velocity [m/s]

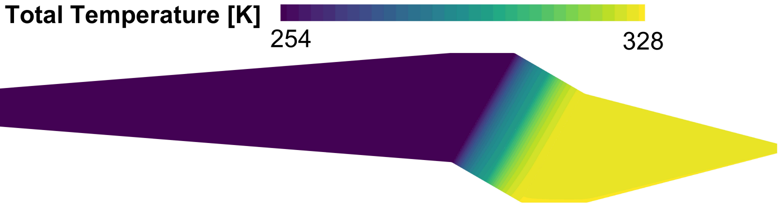

(d) Total temperature

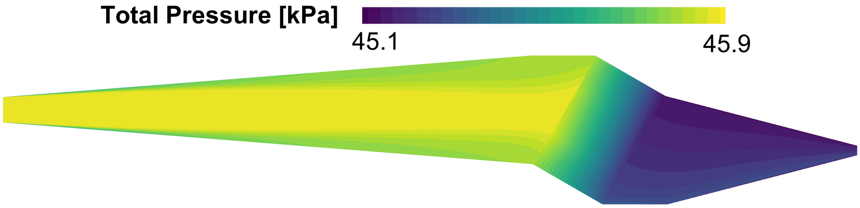

(e) Total pressure

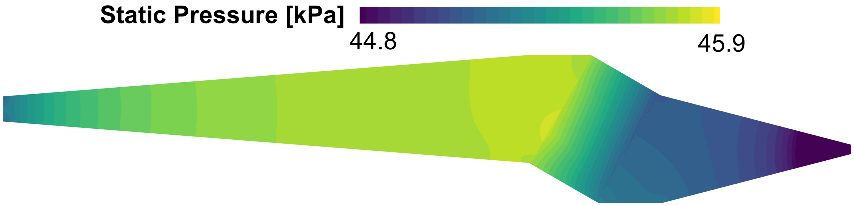

(f) Static pressure

Figure D.7: CFD contour plots for $\alpha = 30°$ inclination configuration at design-point CR ISA.

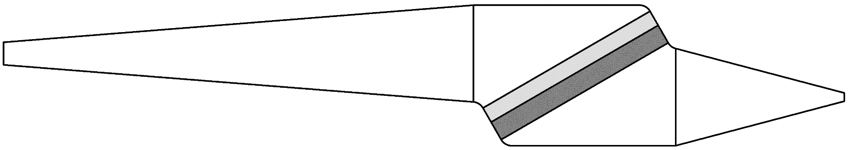

(a) Geometry

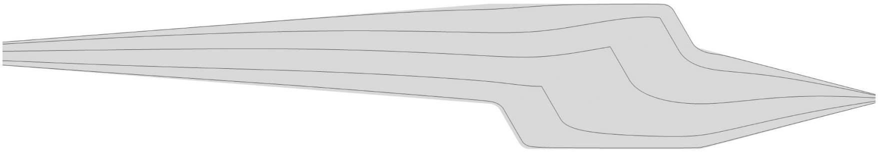

(b) Streamlines

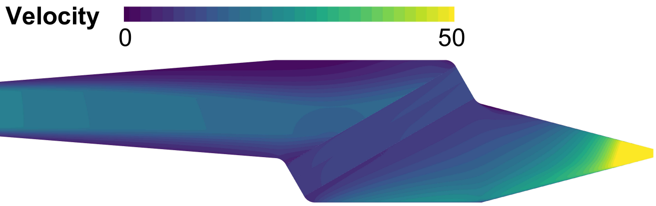

(c) Velocity [m/s]

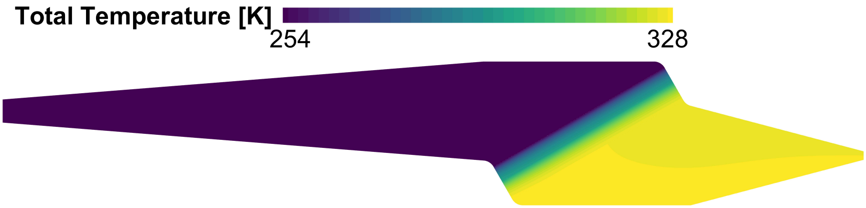

(d) Total temperature

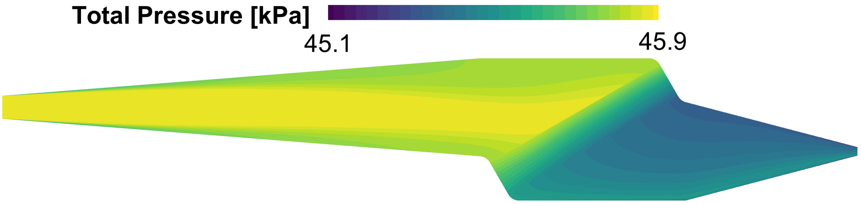

(e) Total pressure

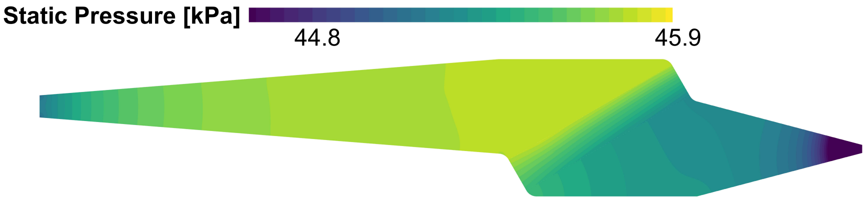

(f) Static pressure

Figure D.8: CFD contour plots for $\alpha = 60^\circ$ inclination configuration at design-point CR ISA.

Bibliography

[1] R. de Vries, R. E. Wolleswinkel, M. F. M. Hoogreef, and R. Vos. “A New Perspective on Battery-Electric Aviation, Part II: Conceptual Design of a 90-Seater”. In: *Proceedings of the AIAA SCITECH 2024 Forum*. Orlando, Florida: American Institute of Aeronautics and Astronautics, 2024. DOI: `10.2514/6.2024-1490`.

[2] H. Ritchie. *What share of global CO emissions come from aviation?* Our World in Data. Accessed: 27-07-2025. 2024. URL: `https://ourworldindata.org/global-aviation-emissions`.

[3] A. Giuffré. “Integrated Design Optimization of Electrically-Driven Vapor Compression Cycle Systems for Aircraft: Powered by High-Speed Centrifugal Compressors”. PhD thesis. Delft University of Technology, 2023. DOI: `10.4233/uuid:b4f6a4a4-2e48-4bbe-9093-3f1368282f63`.

[4] International Energy Agency (IEA). *Aviation*. Tech. rep. International Energy Agency, 2022. URL: `https://www.iea.org/energy-system/transport/aviation`.

[5] *Strategic Research and Innovation Agenda: 2017 Update, Volume 1*. Tech. rep. Advisory Council for Aviation Research and Innovation in Europe (ACARE), 2017.

[6] Clean Sky 2 EU. *Clean Sky 2 First Global Assessment 2020: Technology Evaluator Report*. Technical Report. Available online. May 2021.

[7] R. E. Wolleswinkel, R. de Vries, M. F. M. Hoogreef, and R. Vos. “A New Perspective on Battery-Electric Aviation, Part I: Reassessment of Achievable Range”. In: *Proceedings of the AIAA SCITECH 2024 Forum*. American Institute of Aeronautics and Astronautics, 2024. DOI: `10.2514/6.2024-1489`.

[8] I. Staack, A. Sobron, and P. Krus. “The potential of full electric aircraft for civil transportation: from the Breguet range equation to operational aspects”. In: *CEAS Aeronautical Journal* 12 (2021), pp. 803–819. DOI: `10.1007/s13272-021-00530-w`. URL: `https://doi.org/10.1007/s13272-021-00530-w`.

[9] V. Viswanathan, A. H. Epstein, Y.-M. Chiang, E. Takeuchi, M. Bradley, J. Langford, and M. Winter. “The challenges and opportunities of battery-powered flight”. In: *Nature* 601 (2022), pp. 519–525. DOI: `10.1038/s41586-021-04139-1`. URL: `https://doi.org/10.1038/s41586-021-04139-1`.

[10] R. de Vries, R. E. Wolleswinkel, J. Exalto, P. van den Berg, R. Vos, and M. F. M. Hoogreef. “Conceptual Redesign of a 90-Seater Battery-Electric Aircraft”. In: *Proceedings of the AIAA AVIATION Forum and ASCEND 2025*. Las Vegas, Nevada: American Institute of Aeronautics and Astronautics, 2025. DOI: `10.2514/6.2025-3153`.

[11] F. Beltrame, P. Colonna, and C. M. De Servi. “Optimal Design of Ram Air Cooling Ducts Housing Compact Heat Exchangers for Airborne Thermal Systems”. In: *Journal of the Global Power and Propulsion Society* (2024).

[12] L. J. van Dongen. “Modelling and Design Guidelines for Ram Air Ducts Using the Meredith Effect: Applied to an Organic Rankine Cycle Waste Heat Recovery System”. Master’s Thesis. Delft University of Technology, 2024. URL: `https://resolver.tudelft.nl/uuid:2702f50e-44e6-4369-8807-f38aa6b4c7de`.

[13] K. Wessendorp. “Aerodynamic Optimisation of a Turbofan Bypass Duct with a Heat Exchanger Modelled as a Porous Zone”. Master Thesis. TU Delft, 2025. URL: `https://resolver.tudelft.nl/uuid:1550ddd3-c99f-4224-b552-7d74b183a024`.

[14] A. Giuffré, R. de Vries, R. E. Wolleswinkel, and C. M. De Servi. “Thermal Management System Architecture for the Powertrain of a 90-Seater Battery-Electric Aircraft”. In: *Proceedings of the AIAA AVIATION Forum and ASCEND 2025*. Las Vegas, Nevada: American Institute of Aeronautics and Astronautics, 2025. DOI: `10.2514/6.2025-3207`.

[15] H. Kellermann, M. Lüdemann, M. Pohl, and M. Hornung. “Design and Optimization of Ram Air–Based Thermal Management Systems for Hybrid-Electric Aircraft”. In: *Aerospace* 8.1 (2020), p. 3. DOI: `10.3390/aerospace8010003`.

[16] M. Coutinho, D. Bento, A. Souza, R. Cruz, F. Afonso, F. Lau, A. Suleman, F. R. Barbosa, R. Gandolfi, W. Affonso Junior, F. I. Odaguil, M. F. Westin, R. J. dos Reis, and C. R. da Silva. “A review on the recent developments in thermal management systems for hybrid-electric aircraft”. In: *Applied Thermal Engineering* 227 (2023), p. 120427. DOI: `10.1016/j.applthermaleng.2022.120427`.

[17] F. W. Meredith. *Cooling of Aircraft Engines with Special Reference to Ethylene Glycol Radiators Enclosed in Ducts*. Tech. rep. Aeronautical Research Committee, 1935.

[18] C. K. Sain, J. Hänsel, and S. Kazula. “Conceptual Design of Air and Thermal Management in a Nacelle-Integrated Fuel Cell System for an Electric Regional Aircraft”. In: *AIAA AVIATION 2023 Forum*. San Diego, CA and Online: American Institute of Aeronautics and Astronautics, 2023. DOI: `10.2514/6.2023-3875`.

[19] J. M. Rheaume and C. E. Lents. “Commercial Hybrid Electric Aircraft Thermal Management Sensitivity Studies”. In: *AIAA/IEEE Electric Aircraft Technologies Symposium (EATS)*. 2020, pp. 1–6. DOI: `10.2514/6.2020-3558`.

[20] J. Kirz, A.-R. Hübner, and S. Spinner. *Systematic Numerical Investigations of Heat Exchangers Integrated Behind Propellers of Hybrid-Electric Propulsion Aircraft Configurations*. Tech. rep. German Aerospace Center (DLR): Institute of Aerodynamics and Flow Technology, 2023.

[21] T. A. Harris and I. G. Recant. *Investigation in the 7-By-10 Foot Wind Tunnel of Ducts for Cooling Radiators Within an Airplane Wing*. Special Report NASA/SR-93. Hampton, VA 23681-2199, USA: NASA, Langley Research Center, 1938. URL: `https://ntrs.nasa.gov/citations/20090014718`.

[22] D. Bierman and B. W. Corson. *Model Tests of a Wing-Duct System for Auxiliary Air Supply*. Technical Memorandum NASA/TM-X-57675. Hampton, VA 23681-2199, USA: NASA, Langley Research Center, 1941. URL: `https://ntrs.nasa.gov/citations/19660085318`.

[23] D. R. Chapman. *Investigation of Slipstream Effects on a Wing-inlet Oil-cooler Ducting System of a Twin-engine Airplane in the Ames 40- by 80-foot Wind Tunnel*. Tech. rep. NACA-WR-A-1. Wartime Report. Hampton, VA 23681-2199, USA: NACA, Langley Research Center, 1945. URL: `https://ntrs.nasa.gov/citations/19930093542`.

[24] M. Drela. “Aerodynamics of Heat Exchangers for High-Altitude Aircraft”. In: *Journal of Aircraft* 33.2 (1996), pp. 176–184.

[25] Military Aviation Museum, Virginia Beach. *North American P-51D Mustang (photograph)*. https://www.militaryaviationmuseum.org/aircraft/north-american-p-51d-mustang/. Accessed: 22-08-2025.

[26] C. Graff. *P-51 Mustang: Seventy-Five Years of America's Most Famous Warbird*. Zenith Press, 2015.

[27] R. K. Shah and D. P. Sekulić. *Fundamentals of Heat Exchanger Design*. Hoboken, New Jersey: John Wiley & Sons, Inc., 2003. ISBN: 978-0-471-32171-2.

[28] B. Zohuri. *Compact Heat Exchangers: Selection, Application, Design and Evaluation*. Switzerland: Springer International Publishing, 2017. ISBN: 978-3-319-29835-1. DOI: 10.1007/978-3-319-29835-1.

[29] W. M. Kays and A. L. London. *Compact Heat Exchangers*. 3rd. Krieger Publishing Company, 1984. ISBN: 1-57524-060-2.

[30] A. Giuffré, F. Ascione, P. Colonna, and C. De Servi. "Integrated Design Optimization of Environmental Control Systems for Next-Generation Aircraft". In: *Journal of Aircraft* 62.3 (2025), pp. 498–516. DOI: 10.2514/1.C038093.

[31] M. Musto, N. Bianco, G. Rotondo, F. Toscano, and G. Pezzella. "A Simplified Methodology to Simulate a Heat Exchanger in an Aircraft's Oil Cooler by Means of a Porous Media Model". In: *Applied Thermal Engineering* 94 (2016), pp. 836–845. DOI: 10.1016/j.applthermaleng.2015.10.147.

[32] D. Missirlis, K. Yakinthos, A. Palikaras, K. Katheder, and A. Goulas. "Experimental and Numerical Investigation of the Flow Field Through a Heat Exchanger for Aero-Engine Applications". In: *International Journal of Heat and Fluid Flow* 26 (2005), pp. 440–458. DOI: 10.1016/j.ijheatfluidflow.2004.10.003.

[33] M. R. Nichols. *Investigation of Flow Through an Intercooler Set at Various Angles to the Supply Duct*. Tech. rep. National Advisory Committee for Aeronautics (NACA), 1942.

[34] A. C. Patrao, I. Jonsson, C. Xisto, A. Lundbladh, and T. Grönstedt. "Compact heat exchangers for hydrogen-fueled aero engine intercooling and recuperation". In: *Applied Thermal Engineering* 243 (2024), p. 122538. DOI: https://doi.org/10.1016/j.applthermaleng.2024.122538.

[35] H. Pangborn, A. G. Alleyne, and N. Wu. "A comparison between finite volume and switched moving boundary approaches for dynamic vapor compression system modeling". In: *International Journal of Refrigeration* 53 (May 2015), pp. 101–114. ISSN: 0140-7007. DOI: 10.1016/j.ijrefrig.2015.01.009.

[36] F. Beltrame, P. Colonna, and C. M. De Servi. "Optimal design of aircraft thermal systems and their heat exchangers leveraging a data-driven surrogate model". In: *International Journal of Heat and Mass Transfer* 253 (2025), p. 127502. DOI: 10.1016/j.ijheatmasstransfer.2025.127502.

[37] F. Beltrame, D. Krempus, P. Colonna, and C. M. De Servi. "Reduced Order Modelling of Optimized Heat Exchangers for Maximum Mass-Specific Performance of Airborne ORC Waste Heat Recovery Units". In: *7th International Seminar on ORC Power Systems (ORC2023)*. Seville, Spain: Editorial Universidad de Sevilla, 2023. DOI: 10.12795/9788447227457_93.

[38] Q. Zhu, M. Pishahang, M. Caccia, C. C. Kelsall, A. LaPotin, K. H. Sandhage, and A. Henry. "Validation of the Porous Medium Approximation for Hydrodynamics Analysis in Compact Heat Exchangers". In: *Journal of Fluids Engineering* 144.8 (2022), p. 081403. doi: 10.1115/1.4053174.

[39] C. K. Sain and S. Kazula. "Comparative Assessment of Compact Air Heat Exchangers for Fuel Cell-Powered Electric Aircraft". In: *AIAA AVIATION Forum and ASCEND 2024*. Las Vegas, Nevada, USA: American Institute of Aeronautics and Astronautics, 2024. doi: 10.2514/6.2024-3831.

[40] C. K. Sain, J. Hänsel, and S. Kazula. "Preliminary Design of Air and Thermal Management of a Nacelle-Integrated Fuel Cell System for an Electric Regional Aircraft". In: *2023 IEEE Transportation Electrification Conference & Expo (ITEC)*. Detroit, MI, USA: IEEE, 2023, pp. 1–8. doi: 10.1109/ITEC55900.2023.10187105.

[41] D. Missirlis, S. Donnerhack, O. Seite, C. Albanakis, A. Sideridis, K. Yakinthos, and A. Goulas. "Numerical development of a heat transfer and pressure drop porosity model for a heat exchanger for aero engine applications". In: *Applied Thermal Engineering* 30.11 (2010), pp. 1341–1350. doi: 10.1016/j.applthermaleng.2010.02.010.

[42] H. Maho. "Aerodynamics of wing-integrated ram-air duct for propeller aircraft: A numerical investigation into wing-integrated duct performance and wing-body junction flow". Master Thesis. Delft, The Netherlands: Delft University of Technology, 2025. url: https://resolver.tudelft.nl/uuid:39d98e6c-9e3b-4d4c-86f0-774fef917968.

[43] J. Kirz, A.-R. Hübner, S. Spinner, and K. Weinman. "Application of a Body Force Approach for Numerical Heat Exchanger Simulations within a Hybrid Electric Propulsion Aircraft Concept". In: 2023.

[44] E. J. Adler, A. H. R. Lamkin, and J. R. R. A. Martins. "Aircraft Ducted Heat Exchanger Aerodynamic Shape and Thermal Optimization". In: *ASME Journal of Heat and Mass Transfer* 147.1 (Jan. 2025). doi: 10.1115/1.4066438.

[45] K. Yakinthos, D. Misirlis, Z. Vlahostergios, M. Flouros, S. Donnerhack, and A. Goulas. "Best Strategies for the Development of a Holistic Porosity Model of a Heat Exchanger for Aero Engine Applications". In: *Proceedings of the ASME Turbo Expo 2015: Power for Land, Sea and Air*. Montreal, PQ, Canada, 2015. doi: 10.1115/GT2015-42408.

[46] D. Misirlis, Z. Vlahostergios, M. Flouros, C. Salpingidou, S. Donnerhack, A. Goulas, and K. Yakinthos. "Optimization of Heat Exchangers for Intercooled Recuperated Aero Engines". In: *Aerospace* 4.1 (2017), p. 14. doi: 10.3390/aerospace4010014.

[47] J. Yang, L. Ma, J. Bock, A. M. Jacobi, and W. Liu. "A comparison of four numerical modeling approaches for enhanced shell-and-tube heat exchangers with experimental validation". In: *Applied Thermal Engineering* 65 (2014), pp. 369–383. doi: 10.1016/j.applthermaleng.2014.01.009.

[48] Z. Li, Y. Ding, Q. Liao, M. Cheng, and X. Zhu. "An approach based on the porous media model for numerical simulation of 3D finned-tubes heat exchanger". In: *International Journal of Heat and Mass Transfer* 173 (2021), p. 121226. doi: 10.1016/j.ijheatmasstransfer.2021.121226.

[49] X. Zhao, M. Tokarev, E. A. Hartono, V. Chernoray, and T. Grönstedt. “Experimental Validation of the Aerodynamic Characteristics of an Aero-engine Intercooler”. In: *Journal of Engineering for Gas Turbines and Power* 139.5 (2017), p. 051201. DOI: `10.1115/1.4034964`.

[50] K. Deb, A. Pratap, S. Agarwal, and T. Meyarivan. “A fast and elitist multiobjective genetic algorithm: NSGA-II”. In: *IEEE Transactions on Evolutionary Computation* 6.2 (Apr. 2002), pp. 182–197. DOI: `10.1109/4235.996017`. URL: `http://dx.doi.org/10.1109/4235.996017`.

[51] A. C. Frey, J. Stonham, D. Bosak, C. M. Sangan, and O. J. Pountney. “Radiators in Fuel Cell Powered Aircraft: The Effect of Heat Rejection on Drag”. In: *Applied Thermal Engineering* 274 (2025). DOI: `10.1016/j.applthermaleng.2025.126697`.

[52] A. C. Patrao, I. Jonsson, and C. Xisto. “Compact Heat Exchangers With Curved Fins for Hydrogen Turbofan Intercooling”. In: *ASME Journal of Engineering for Gas Turbines and Power* (2024). DOI: `10.1115/1.4065887`. URL: `https://doi.org/10.1115/1.4065887`.

[53] L. R. Reneau, J. P. Johnston, and S. J. Kline. “Performance and Design of Straight, Two-Dimensional Diffusers”. In: *Journal of Basic Engineering* 89.1 (1967), pp. 141–150. DOI: `10.1115/1.3645776`.

[54] Y.-J. Chang and C.-C. Wang. “A generalized heat transfer correlation for louver fin geometry”. In: *International Journal of Heat and Mass Transfer* 40.3 (1997), pp. 533–544. DOI: `10.1016/0017-9310(96)00116-0`.

[55] Y.-J. Chang, K.-C. Hsu, Y.-T. Lin, and C.-C. Wang. “A generalized friction correlation for louver fin geometry”. In: *International Journal of Heat and Mass Transfer* 43.12 (2000), pp. 2237–2243. DOI: `10.1016/S0017-9310(99)00289-6`.

[56] R. M. Manglik and A. E. Bergles. “Heat transfer and pressure drop correlations for the rectangular offset strip fin compact heat exchanger”. In: *Experimental Thermal and Fluid Science* 10.2 (1995), pp. 171–180. DOI: `10.1016/0894-1777(94)00096-Q`.

[57] J. Paur. *Peek Inside the First Passenger-Ready 787 Dreamliner*. Accessed: 14-08-2025. 2011. URL: `https://www.wired.com/2011/08/peek-inside-the-first-passenger-ready-787-dreamliner/`.

[58] ATR–Aircraft. *EASA Certifies ATR’s Regional Turboprop Aircraft Powered by the New PW127XT-M Engine*. Accessed: 14-08-2025. Oct. 2022. URL: `https://www.atr-aircraft.com/presspost/easa-certifies-atrs-regional-turboprop-aircraft-powered-by-new-pw127xt-m-engine/`.

[59] ESDU 86002. *Drag and pressure recovery characteristics of auxiliary air inlets at subsonic speeds*. Tech. rep. 2004.

[60] S. L. Dixon and C. A. Hall. *Fluid Mechanics and Thermodynamics of Turbomachinery*. 7th. Oxford: Butterworth-Heinemann, 2014. ISBN: 978-0-12-415954-9.

[61] E. M. Greitzer, C. S. Tan, and M. B. Graf. *Internal Flow: Concepts and Applications*. Cambridge: Cambridge University Press, 2004, pp. xviii+445. ISBN: 9780521660452.

[62] G. Sovran and E. D. Klomp. "Experimentally Determined Optimum Geometries for Rectilinear Diffusers with Rectangular, Conical or Annular Cross-Section". In: *Fluid Dynamics of Internal Flow: Proceedings of the Symposium on the Fluid Dynamics of Internal Flow*. Ed. by G. Sovran. Warren, Michigan: General Motors Research Laboratories, 1968.

[63] B. A. Waitman, L. R. Reneau, and S. J. Kline. "Effects of Inlet Conditions on Performance of Two-Dimensional Subsonic Diffusers". In: *Journal of Basic Engineering* 85.4 (1963), pp. 559–568. DOI: `10.1115/1.3656754`.

[64] S. J. Kline and J. P. Johnston. "Diffusers - Flow Phenomena and Design Layers in Internal Flow – Performance Prediction". In: *Advanced Topics in Turbomachinery Technology*. Ed. by D. Japikse. Wilder, VT: Concepts ETI Press, 1986.

[65] A. B. Cocanower, S. J. Kline, and J. P. Johnston. *A Unified Method for Predicting the Performance of Subsonic Diffusers of Several Geometries*. Technical Report PD-10. Stanford, California: Thermosciences Division, Department of Mechanical Engineering, Stanford University, 1965.

[66] A. A. Lyrio, J. H. Ferziger, and S. J. Kline. *An Integral Method for the Computation of Steady and Unsteady Turbulent Boundary Layer Flows, Including the Transitory Stall Regime in Diffusers*. Technical Report PD-23. Stanford, CA: Thermosciences Division, Department of Mechanical Engineering, Stanford University, 1981.

[67] J. D. Mattingly. *Elements of Propulsion: Gas Turbines and Rockets*. AIAA Education Series. Reston, VA: American Institute of Aeronautics and Astronautics, 2006.

[68] A. J. Szaniszlo. "Experimental and Analytical Sonic Nozzle Discharge Coefficients for Reynolds Numbers up to 8×10^6". In: *Journal of Engineering for Power* 97.4 (1975), pp. 521–525. DOI: `10.1115/1.3446050`.

[69] Groupe de Recherche sur les Échangeurs Thermiques (GRETh). *EchTherm*. `https://greth.fr/en/echtherm/`. Accessed: 16-04-2025.

[70] V. Gnielinski. "On heat transfer in tubes". In: *International Journal of Heat and Mass Transfer* 63 (2013), pp. 134–140. DOI: `10.1016/j.ijheatmasstransfer.2013.04.015`.

[71] V. G. V. und Chemieingenieurwesen. *VDI Heat Atlas*. 2nd. Springer, 2010. Chap. L1: Pressure Drop in Single-Phase Flow.

[72] R. K. Shah. "Improved correlation for heat transfer during condensation in conventional and mini/micro-channels". In: *International Journal of Refrigeration* 104 (2019), pp. 283–294. DOI: `10.1016/j.ijrefrig.2018.07.037`.

[73] D. Del Col, A. Bisetto, M. Bortolato, D. Torresin, and L. Rossetto. "Experiments and updated model for two-phase frictional pressure drop inside minichannels". In: *International Journal of Heat and Mass Transfer* 60 (2013), pp. 326–337. DOI: `10.1016/j.ijheatmasstransfer.2013.03.070`.

[74] I. H. Bell, J. Wronski, S. Quoilin, and V. Lemort. "Pure and pseudo-pure fluid thermophysical property evaluation and the open-source thermophysical property library coolprop". In: *Industrial and Engineering Chemistry Research* 53 (6 Feb. 2014), pp. 2498–2508. ISSN: 08885885. DOI: `10.1021/ie4033999`.

[75] *CoolProp: Open-source thermophysical property library*. `https://coolprop.org`.

[76] E. W. Lemmon, I. H. Bell, M. L. Huber, and M. O. McLinden. *NIST Standard Reference Database 23: Reference Fluid Thermodynamic and Transport Properties-REFPROP, Version 10.0, National Institute of Standards and Technology*. 2018. DOI: `https://doi.org/10.18434/T4/1502528`. URL: `https://www.nist.gov/srd/refprop`.

[77] American Society of Heating, Refrigerating & Air Conditioning Engineers. *ASHRAE Fundamentals Handbook 2001 (SI)*. 2001. Chap. 21 Physical Properties of Secondary Coolants (Brines). ISBN: 9781883413880.

[78] R. de Vries, M. F. M. Hoogreef, and R. Vos. "Range Equation for Hybrid-Electric Aircraft with Constant Power Split". In: *Journal of Aircraft* 57.3 (2020). DOI: `10.2514/1.C035734`.

[79] F. R. Menter. *Zonal Two Equation k-omega Turbulence Models for Aerodynamic Flows*. NASA Technical Memorandum NASA-TM-103975. NASA Ames Research Center, 1993. DOI: `10.2514/6.1993-2906`.

[80] ANSYS, Inc. *Ansys Fluent User's Guide*. 2025 R2. Accessed: 20-08-2025. ANSYS, Inc. Canonsburg, PA, USA, July 2025. URL: `https://ansyshelp.ansys.com/public/account/secured?returnurl=/Views/Secured/prod_page.html?pn=Fluent`.

[81] T. L. Bergman, A. S. Lavine, F. P. Incropera, and D. P. DeWitt. *Fundamentals of Heat and Mass Transfer*. 8th. Hoboken, NJ, USA: John Wiley & Sons, 2017. ISBN: 9781118989173.

[82] A. Baglieri. "Plate fin heat exchanger design optimization and mass-specific performance assessment for aerospace applications". Master's thesis. Turin, Italy: Politecnico di Torino, 2023. URL: `https://webthesis.biblio.polito.it/28843/`.